NASA-CR-194390

CONFIDENTIAL
UNTIL SEPTEMBER 15, 1993

OPTICAL DATA STORAGE CENTER

University-Industry Cooperative Research

Annual Report: March 15, 1993

(NASA-CR-194390) RESEARCH STUDIES ON ADVANCED OPTICAL MODULE/HEAD DESIGNS FOR OPTICAL DISK RECORDING DEVICES (Arizona Univ.) 168 p

N94-14981
--THRU--
N94-14997
Unclas

G3/82 0185930

Optical Sciences Center
The University of Arizona
Tucson, Arizona

FROM THE DIRECTOR

This report should reach you approximately one month before our upcoming meeting at the Viscount Suites Hotel in Tucson on April 28. As usual, it begins with summary reports on continuing projects. These are followed by extended reports, primarily in the form of preprints of papers to be published in the future.

We were informed yesterday that the DARPA program on Ultra-High Density Recording has a start date of today, March 19. As many of you know, it has three components — magnetic disks, magnetic tape and optical recording. Sixteen universities and thirteen companies are participating in the total program. The University of Arizona has joined with three companies and three other universities in the optical recording projects, which are primarily directed toward the development of "blue media." First-year costs at Arizona are projected at $686,346; the University will fund approximately one-third of this, while DARPA will fund two-thirds. This should substantially complement and expand our present program.

LaserByte Corporation of Sunnyvale, California, became a Level-3 sponsor of ODSC on December 16, 1992. We welcome them most heartily. Our association was initiated by Frank Whitehead of LaserByte, who graduated from the Optical Sciences Center in 1976. He has been working on optical recording in the San Francisco Bay area for the past decade, first with 3M, then Verbatim and now LaserByte, a new company, started by Ingolf Sander, developing 3.5-inch magneto-optic drives. The major investor is Hyundai. We expect that Frank will attend our upcoming meeting. I hope he will be joined by Ingolf Sander and/or Robert Toda, the President and CEO of LaserByte.

As many of you know, AMC's Optical Product Division has been sold to MOST Inc., which is a subsidiary of Nakamichi Peripherals Inc. It now has a new name — MOST Manufacturing Inc. We expect that Bernard Bell of MMI will attend our meeting. I hope he will be joined by executives from MMI and its parent company. We are encouraging them to join ODSC, of course.

We expect Jim Lemke of Recording Physics to be at our meeting. Several others who have been invited include T.C. Lee of Literal Corp., Dave Campbell of Hewlett-Packard, Tu Chen of Komag, Gordon Knight of Maxoptix, Archie Smith of StorageTek, and others. I expect this to be a particularly interesting meeting. We hope that you can attend and I look forward to hosting your visit.

JJBurke

James J. Burke
March 19, 1993

CONTENTS

SECTION 1. SUMMARY REPORTS

N94-14982

MAGNETO-OPTIC SUPERLATTICE THIN FILMS: FABRICATION, STRUCTURAL AND MAGNETIC CHARACTERIZATION

C.M. Falco, B.N. Engel, R.A. Van Leeuwen and J. Yu

PROGRESS

During this quarter we extended our studies to determine the electronic contribution to the perpendicular interface anisotropy in Co-based multilayers. Using *in situ* Kerr effect measurements, we investigated the influences of different transition metals (TM = Ag, Au, Cu, and Pd) on the magnetic properties of single-crystal Co films grown on Pd (111) and Au (111) surfaces. We reported last quarter the discovery of a large peak in the perpendicular anisotropy when approximately one monolayer of Cu or Ag is deposited on the Co surface.

We now have added a computer-controlled stepper-motor drive to our MBE sample transfer mechanism. The motor allows us to move the sample at a constant velocity from behind a shutter during deposition. The film, therefore, is deposited as a wedge with a linear variation of thickness across the substrate. In this way, we can study a continuous range of coverage on a single sample. The stepper motor also provides the necessary control for precisely positioning the sample in the laser beam for Kerr effect measurements at the different coverages.

Also during this quarter we have continued our work on MnSb alloy films. We have made sputtered Mn_xSb_{1-x} ($x \approx .50$) alloy films using DC triode system with a *3N5* Mn target and *5N* Sb target both bonded to Cu backing plates.* The typical sputtering power for Sb was 60 Watts (15 Watt/in^2) and 120 Watts (30 Watts/in^2) for Mn. Typical system pressure before sputtering was $\approx 1 \times 10^{-7}$ Torr. Normal argon sputtering pressure was 7 mTorr, although samples were made in pressures ranging from 3 mTorr to 20 mTorr. Substrate height varied from 3.63 in. to 7.06 in. Samples were deposited on substrates either at room temperature or $\sim$250 °C. Substrates were normally at ground potential but in some instances also were biased to +55 VDC and to -55 VDC during deposition.

Films of pure Sb and Mn approximately 1000 Å thick were sputtered on carbon and 90° orientated Al_2O_3. Precise measurements of the deposition rates were determined by Rutherford backscattering spectrometry (± 3%) and the film structure was analyzed by x-ray diffraction. Standard Bragg-Brentano θ-2θ x-ray diffraction techniques showed the Sb film to be rhombahedral and polycrystalline with the (001) orientation dominant, although many other orientations were present. Bragg-Brentano spectra of the Mn film consisted of only one small peak possibly attributable to Mn. Subsequent measurements were performed using a Seemann-Bohlin x-ray diffractometer with a glancing angle of incidence of 6° so that the effective film thickness is increased to approximately ten times the

*3N5 means 3 nines 5. It is the way buyers and sellers of materials specify chemical purity. Ed.

actual thickness. This technique showed that the film was polycrystalline α-Mn phase with predominant (330, 411) orientation.

The Mn_xSb_{1-x} films were deposited by rotating the substrates over the sputtering guns and sequentially depositing thin layers of each of the two materials. The sputtering power was set so that the ratio of the thicknesses, t_{Sb}/t_{Mn}, was 2.47. This results in 50 at. % of each material(x = .50). With this setup, arbitrary layer thicknesses can be deposited by simply changing the sample rotation speed. Typical layer thicknesses for Mn was 2.6 Å and for Sb was 6.4 Å. Total films thicknesses were approximately 1000 Å. We have used different substrates to try to influence the growth of the Mn_xSb_{1-x}. These include: glass, Si(111), Si(001), GaAs(110), Al_2O_3, mica and quartz. To determine the effect of different buffer layers on the Mn_xSb_{1-x} films, we deposited polycrystalline films of Mn, Sb and Cu on these same substrates.

Bragg-Brentano x-ray diffraction performed on the MnSb films showed that the films were polycrystalline with two orientations normal to the film plane: (101) and (110). Even though the peak intensities were low, their widths were narrow. Calculations of the crystallite size from the peak widths using the Scherrer equation yielded values between 300 Å and 400 Å. We did not observe any peaks due to Mn_2Sb, Mn or Sb. While the single crystal substrates generally resulted in higher intensity peaks, possibly due to a smoother starting surface, there was no significant difference in the orientation of the films due to different substrates. Films grown on buffer layers of polycrystalline Sb, Mn, and Cu also were not significantly different from each other or from those without buffers. To date, we have systematically varied sputtering rates, sputtering pressure, substrate height, substrate bias, buffer layers, amorphous- or single-crystal substrates, and layer thicknesses. We have not yet found a technique that results in c-axis oriented films.

Ex situ annealing of a film at 300 °C for 5 minutes or 400 °C for 10 minutes in an Ar atmosphere did not change the structure; however the film appearance degraded significantly for the higher temperature. A comparison of x-ray spectra showed little change except that the x-ray intensity increased for the MnSb(101) and decreased for the MnSb(103) peak after annealing.

VSM measurements indicate in-plane magnetization with values of M_s = 2.0 - 2.2 μ_B/Mn atom. This is lower than the bulk value of M_s, which is 3.3 μ_B/Mn atom. Samples deposited on Si had values of 2.2 μ_B/Mn atom, while those samples on glass were 2.0 μ_B/Mn atom. In-plane coercive fields ranged from 100 Oe to 200 Oe. Measurements of polar Kerr rotation yielded typical values of 0.2° regardless of substrate type, while the polar ellipticity, ϵ_k, was much smaller at $\sim$0.02°.

We have recently begun deposition of MnSb by MBE. The work is in preliminary stages and results will be reported next quarter.

PLANS

During the next quarter we will extend our studies of Co interface anisotropy and the Mn/Sb system. We are interested in the magneto-optic and magnetic properties of c-axis oriented MnSb alloy films. Therefore, we will use MBE to produce highly textured films for study. From these high-quality films, we will be able to estimate the fundamental performance limits of the oriented MnSb alloy and, therefore, guide our sputtering studies of more practical media.

N94-14983

CHARACTERIZATION FACILITY FOR MAGNETO-OPTIC MEDIA AND SYSTEMS

M. Mansuripur, H. Fu, S. Gadetsky, S. Sugaya, T.H. Wu, J. Zambuto, R. Gerber, T. Goodman and J.K. Erwin

OBJECTIVES

Objectives of this research are listed below.

Measure the hysteresis loop, Kerr rotation angle, anisotropy energy profile, Hall voltage and magnetoresistance of thin-film magneto-optic media using our loop-tracer. This instrument has a maximum field capability of 21 kOe, and can measure the temperature-dependence of the media's magnetic properties in the range 77 K to 475 K.

Measure the wavelength-dependence of the Kerr rotation angle, θ_k, and ellipticity, ϵ_k, for thin-film media using our magneto-optic Kerr spectrometer (MOKS). The spectrometer operates in the wavelength range 350 nm to 1050 nm.

Measure the dielectric tensor of thin-film and multilayer samples using our variable-angle magneto-optic ellipsometer (VAMOE). This device measures (at the HeNe wavelength of 633 nm) the complex reflection coefficients of the samples at angles of incidence ranging from 26° to 88°. A computer program then estimates the dielectric tensor from the measured coefficients of reflection.

Measure the hysteresis loop, coercivity, remanent magnetization, saturation magnetization, and anisotropy energy constant for thin film magnetic media using vibrating sample magnetometry. The temperature range of our VSM is 77 K to 1000 K, and it has a maximum magnetic field capability of 12 kOe.

Observe small magnetic domains and investigate their interaction with defects using magnetic force microscopy.

Perform static read/write/erase experiments on thin-film magneto-optic media using our static test station. The test station is a polarized-light microscope, modified to include a laser diode, electromagnet, temperature-controlled stage, and a TV camera, all under computer control.

Integrate the existing models of magnetization, magneto-optic effects, coercivity, and anisotropy in an interactive and user-friendly environment. Analyze the characterization data obtained in the various experiments, using this modeling package.

Measure focusing- and tracking-error signals on a static testbed; determine the "feedthrough" for various focusing schemes, investigate the effects of polarization and birefringence, and compare the results with diffraction-based calculations. The testbed has two HeNe lasers (λ_1 = 544 nm, λ_2 = 633 nm), a series of high-NA objectives (0.5 to 0.8), piezoelectric actuators (with better than 0.1 μm positioning accuracy) for driving the sample, CCD camera emulating multi-element detectors, several interchangeable focus-error modules, and in-built shearing and Twyman-Green interferometers for ascertaining beam quality and/or calibrating the focus position.

Measure the birefringence of optical disk substrates using two variable angle ellipsometers. The first system operates at λ = 780 nm and has the capability of both reflection and transmission measurements. The beam in this system has an angle of incidence θ in the range of (0, 70°), and an azimuth of incidence ϕ which can vary continuously from 0 to 360°. The second system operates at λ = 633 nm, is restricted to reflection measurements only, and has an angle of incidence in the range of (20°, 70°). The azimuth of incidence in this system is restricted to two values: 0 and 90°.

PROGRESS

Substrate Birefringence Measurements

A significant fraction of our efforts during the past quarter was devoted to measurements of substrate birefringence. We now have three systems and four people devoted to this project. A complete report on this work appears as Appendix A and soon will be submitted to *Applied Optics*. The following is a brief description of the three systems with emphasis on their main features.

VAE633. This variable-angle ellipsometer operates at the HeNe wavelength of 633 nm, can make reflection measurements only, and is limited in its setting of the azimuth of incidence (ϕ = 0 and ϕ = 90° are the only possibilities). The system originally was built in our laboratory for dielectric tensor measurements for magneto-optic media, and recently was modified for birefringence measurements.

VAE780. This variable-angle ellipsometer operates at λ = 780 nm, has both the reflection and transmission capability, and allows arbitrary settings of the azimuth of incidence (ϕ = 0 - 180°). The system has been designed specifically for measuring birefringence on 3.5 in. and 5.25 in. optical disk substrates.

Commercial ellipsometer. This variable-angle and variable-wavelength ellipsometer was donated to us by Eastman Kodak Company (we thank Dr. Joseph Wrobel of Kodak Research Laboratories for suggesting and facilitating the donation). We have made a minor modification to the system and have begun measuring substrate birefringence at various wavelengths (λ = 400 nm - 800 nm). This work is in the preliminary testing stage and we hope to present its results at the IAB meeting in April.

Ring-Toric Lens for Focus-Error-Detection

Work on the ring-toric lens continued during this quarter. We have fabricated several more lenses and tested them in our static testbed. A report on the progress of this work is included as Appendix B. The upgraded testbed can measure at two wavelengths (red and green HeNe) as well as two polarization directions (parallel and perpendicular to grooves). We have done extensive comparisons between the ring lens scheme of focus error detection and the conventional method of using an astigmatic lens.

Magnetic and Magneto-Optic Characterization of Magneto-Optic Media

Hong Fu has completed a series of studies on thermomagnetic write/erase cycle using the Connection Machine simulations. He will present an invited paper on this subject at the Intermag meeting in Stockholm, April 1993. He is working on a long paper for *Computers in Physics* based on these studies and expects to have the paper ready in time for the next quarterly report.

Sergei Gadetsky, our new research scientist, arrived in December and is engaged in a study of Co/Pd superlattice films produced by Dr. T. Suzuki of IBM Almaden Research Center. His findings are summarized in Appendix C.

PLANS

During our studies of substrate birefringence we have noticed certain curious phenomena related to the relative orientation of incident beam and grooves on the substrate. We plan to look into these phenomena carefully and will try to understand their origins.

The ring-lens studies will continue and we will try to make lenses with smaller ring diameters. We also will investigate the dependence of track-crossing signal and feedthrough on the relative orientation of polarization vector and the groove.

With the graduation of Bruce Bernacki and his departure for Oak Ridge National Laboratory, we will miss one of our highly productive members. New students will be learning to use DIFFRACT and will continue Bernacki's modeling of the optical path in magneto-optic systems.

N94-14984

MeV ION-BEAM ANALYSIS OF OPTICAL DATA STORAGE FILMS

J.A. Leavitt, L.C. McIntyre Jr. and Z. Lin

OBJECTIVES

Our objectives are threefold: 1) to accurately characterize optical data storage films by MeV ion-beam analysis (IBA) for ODSC collaborators; 2) to develop new and/or improved analysis techniques; and 3) to expand the capabilities of the IBA facility itself.

Using $^{1}H^{+}$, $^{4}He^{+}$ and $^{15}N^{++}$ ion beams in the 1.5 MeV to 10 MeV energy range from a 5.5 MV Van de Graaff accelerator, we determine film thickness (in atoms/cm^2), stoichiometry, impurity concentration profiles and crystalline structure by Rutherford backscattering (RBS), high-energy backscattering, channeling, nuclear reaction analysis (NRA) and proton induced X-ray emission (PIXE). Most of these techniques are discussed in detail in the ODSC Annual Report (February 17, 1987), p. 74. The PIXE technique is briefly discussed in the ODSC Annual Report (March 15, 1991), p. 23.

PROGRESS

Film Characterization

From March 1, 1992, to March 1, 1993, we provided a total of 214 equivalent backscattering analyses of thin films provided by ODSC collaborators. Table 1 indicates the distribution.

Table 1. Number of analyses of thin films for ODSC.

Period	Falco	Mansuripur	Zelinski	Armstrong	Totals
3/1/92 - 6/1/92	10	22	---	2	34
6/1/92 - 9/1/92	27	50	21	---	98
9/1/92 - 12/1/92	31	8	6	---	45
12/1/92 - 3/1/93	19	---	18	---	37
3/1/92 - 3/1/93	87	80	45	2	214

For Falco (with Engel, Van Leeuwen, Wiedmann and Yu), we provided channeling analyses of Pd/Co multilayers, backscattering analyses of PdCu, MnSb, NbCuMn, PdCoAu, and CoAgIr films and PIXE analyses of several films containing adjacent mass elements (such as Pd and Ag).

For Mansuripur (with Wu and Shieh), we provided backscattering analyses of 3-layer (and 4-layer) SiN/TbFeCo/SiN/(Al) films to determine stoichiometry and "thickness."

For Zelinski (with Vogt and Weisenbach), we performed channeling studies of $SiO_2/TiO_2(Zn)$ waveguide films to provide stoichiometry, "thickness" and impurities.

For Armstrong (with England), we provided two backscattering analyses of SnS_2 films.

Technique Development

We have continued to develop techniques for increasing sensitivity for quantifying light elements in/on heavy matrices. In this connection: 1) We have published measured ^{4}He-^{10}B, ^{4}He-^{11}B backscattering cross sections for incident ^{4}He energies 1 MeV to 3 MeV (see publications). 2) We have published details of a technique for quantifying ^{10}B and ^{11}B in films using (α,p) nuclear reactions for incident ^{4}He energies near 3 MeV (see publications). 3) Work involving use of (α,p) reactions to quantify ^{14}N has been submitted for publication (see preprint, Appendix A, ODSC Quarterly Report, December 15, 1992). 4) Work involving use of ^{4}He and ^{1}H non-Rutherford backscattering to quantify ^{9}Be in thin films will be reported at the 11th IBA Conference in Hungary, July 1993. 5) We are continuing work on using (α,p) reactions to quantify Al and Si in films. 6) We have recently developed a technique to accurately determine the stoichiometry of SiC films on single crystal Si substrates. The technique uses channeling with incident 3776 keV ^{4}He ions to reduce the Si substrate signal and enhance the C signal. The ^{4}He-C cross section is about seven times Rutherford for this ^{4}He energy. The hydrogen content of the films is determined by the elastic recoil detection (ERD) technique. 7) The PIXE technique is now fully developed. It has been used to analyze more than 2500 samples during the past year. Most of these samples are of biological interest; we have used the PIXE technique on 10 films for ODSC to separate adjacent-mass film components.

Facility Development

We are continuing to work on installing the nuclear microprobe. The goal of this project is to produce analysis beams (^{1}H or ^{4}He) of about 1 μm diameter. This microbeam will be rastered over the sample to determine the lateral distribution of trace elements in features more than a few microns in size. The beamline is nearly complete; we have actually run a beam through the entire length of the apparatus. We have not yet finished installing two high-vacuum pumps. An extended period of testing will follow. We hope to be in operation in late spring 1993. This project is a collaborative effort involving Q. Fernando (University of Arizona, Department of Chemistry) and is partially supported by funds from an NIH Superfund grant (see the ODSC Quarterly Report, September 15, 1997, p. 27).

PLANS

During the next year, we plan: 1) to continue characterizing optical data storage films for ODSC collaborators; 2) to continue our program for developing techniques for quantifying light elements in/on heavy matrices; and 3) to complete construction and testing of the nuclear microprobe.

PUBLICATIONS

1. L.C. McIntyre Jr., J.A. Leavitt, M.D. Ashbaugh, Z. Lin, and J.O. Stoner Jr., "Cross Sections for 170.5° Backscattering of ^{4}He by the Isotopes of Boron for ^{4}He Energies Between 1.0 and 3.3 MeV," Nucl. Instr. Meth. **B64**, 457 (1992).

2. L.C. McIntyre Jr., J.A. Leavitt, M.D. Ashbaugh, Z. Lin, and J.O. Stoner Jr., "Determination of Boron Using the $B(\alpha,p)$C Nuclear Reaction at Incident Energies Near 3 MeV," Nucl. Instr. Meth. **B66**, 221 (1992).

3. Z. Lin, L. C. McIntyre Jr., J.A. Leavitt, M.D. Ashbaugh and R.P. Cox, "Determination of Nitrogen Using the $^{14}N(\alpha,p)^{17}O$ Nuclear Reaction," Nucl. Instr. Meth., in press (1993).

N94-14985

APPLICATION OF HOLOGRAPHIC OPTICAL ELEMENTS TO MAGNETO-OPTIC READ/WRITE HEADS

R.K. Kostuk, E. Campbell and T. Kim

OBJECTIVES

Objectives of this research are to determine the theoretical and practical performance limits of holographic optical elements (HOEs) formed in different recording materials, and to evaluate the application of these components to magneto-optic read/write heads.

PROGRESS

Hologram Characterization, Modeling, and Design

We completed measurements of the refractive index profile of dichromated gelatin emulsions for recording volume holograms. Characterizing the refractive index profile is important for realizing accurate designs using our diffraction models. Measurement techniques based on Brewster angle and Fresnel reflection coefficients were used to determine the emulsion's surface index. An interferometric method with oil index matching was used to determine the bulk refractive index of the emulsion. The experiments showed that the surface index was higher than the bulk index, which contradicts the change expected due to exposure, dehydration, and the resulting airation of the emulsion. We suspect that the emulsion surface collapses during development, forming a layer with higher refractive index. We found some references to experimental data that support this hypothesis, but we would like to confirm this model on our own with additional experiments and SEM analysis. A short proceedings paper summarizing these findings is reproduced in Appendix D.

Gene Campbell is examining the application of volume gratings for polarization and phase components. His model, based on rigorous coupled wave theory, allows the index and permittivity modulation to be varied as a function of emulsion depth. This characterization is necessary for an accurate description of the phase and polarization properties of diffracted fields. Figure 1 shows the calculated phase difference between s-polarized and p-polarized diffracted fields as a function of permittivity modulation for a zero-order beam passing through the grating. As indicated, a permittivity modulation of about 0.17 ($\Delta n \sim 0.0623$) provides a $\lambda/4$ phase delay, and a modulation of 0.27 ($\Delta n \sim 0.10$) produces $\lambda/2$ retardation. Both of these modulation values can be achieved in DCG, and it may be possible to reduce the required index modulation value by forming thicker emulsions. Figure 2 shows the efficiency of a polarization beam splitter (PBS) as a function of grating strength with an interbeam angle of 60° within the emulsion. The grating strength is defined as the product of $\Delta\epsilon d/\lambda$. To achieve a grating strength of 1.2 to make the PBS with $\lambda = 0.50$ μm and $d = 8.3$ μm, an index modulation of 0.027 is needed, which can be realized in DCG.

We also examined the effect of saturation on the efficiency properties of volume gratings during this period. The model used for a saturated refractive index modulation is

$$n(\vec{r}) = N_o[1 - \exp(-E(\vec{r})/E_o)] \ ,$$

where $n(\vec{r})$ is the saturated index modulation, N_o is a proportionality constant, $E(\vec{r})$ is the grating exposure, and E_o is a saturation constant. (This model also was used by workers at Solymar's group at Oxford.) Figure 3 shows the efficiency with a saturation constant of 1000 mJ/cm², and N_o of 0.5. Some of the important consequences of saturation is that the TE efficiency does not go to zero, and the non-oscillatory efficiency function for the TM polarized field. The more commonly quoted results of Kogelnik have TE and TM polarized fields that have a $\sin^2$ dependence on increasing modulation and thickness. This difference will greatly influence the design of many types of polarization beam splitters.

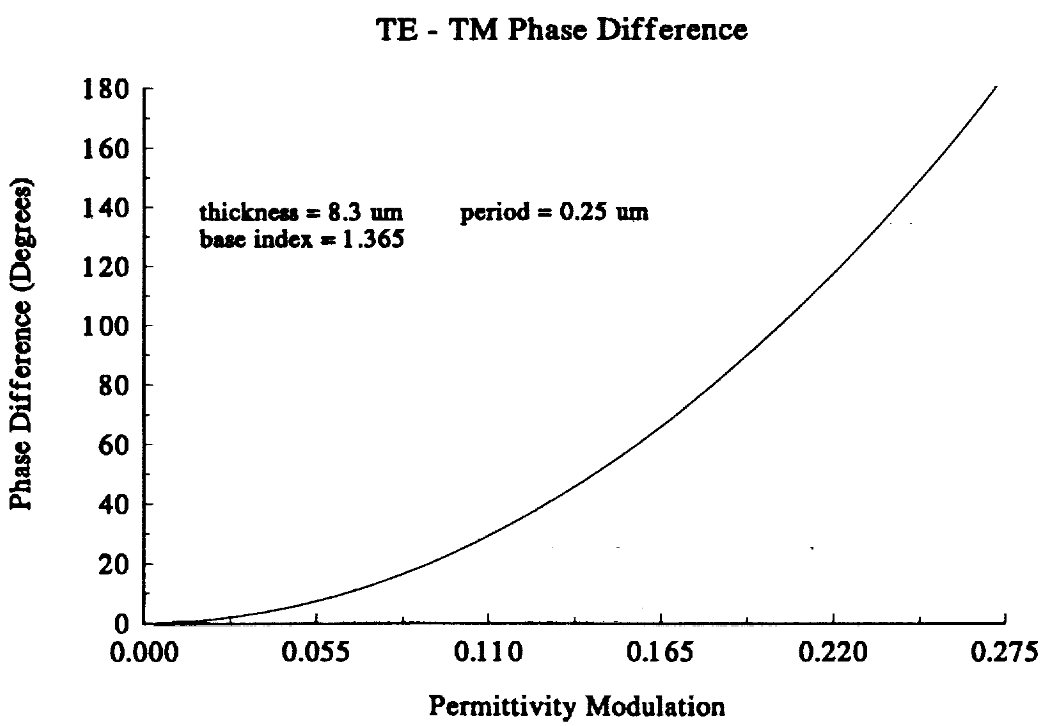

Figure 1. Zero-order holographic waveplate.

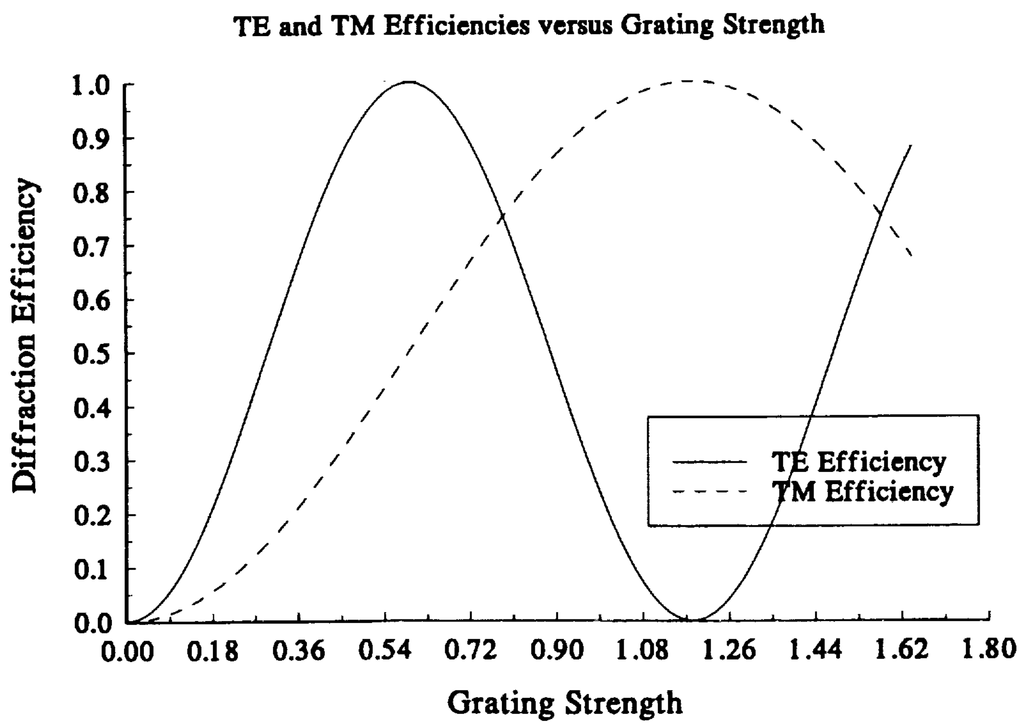

Figure 2. Sixty-degree polarization beam splitter.

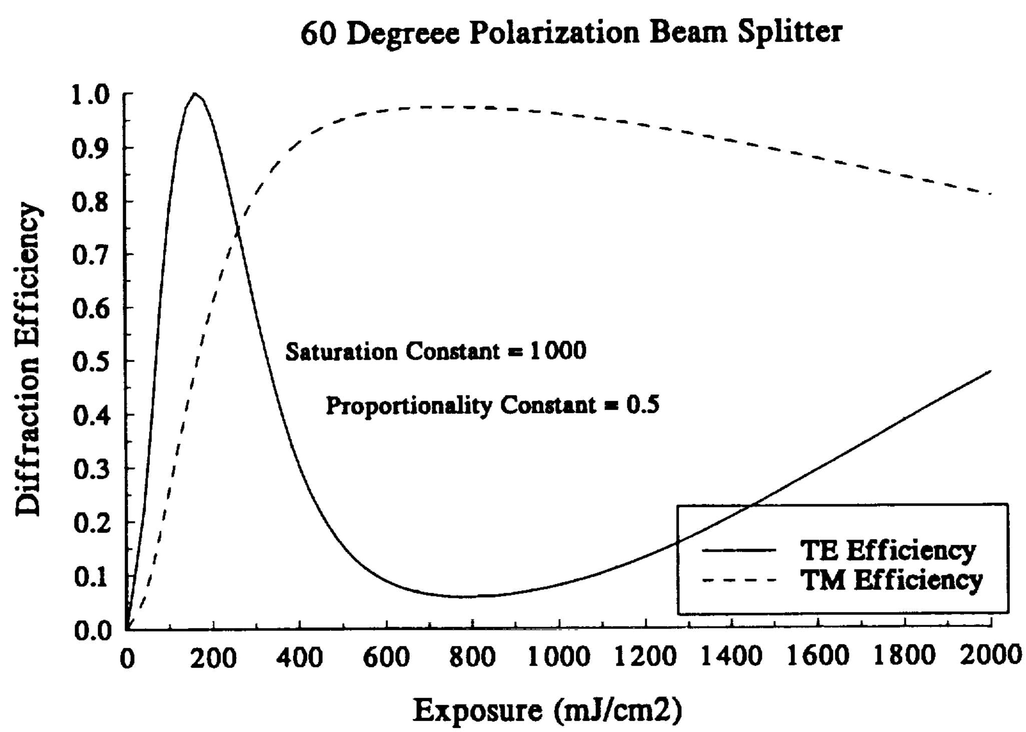

Figure 3. Effect of permittivity modulation saturation.

PLANS

Our future efforts will be directed toward: 1) designing and fabricating phase control components in DCG and surface relief grating elements; 2) helping a new student become familiar with the surface relief grating model developed by Charles Haggans (now at 3M); 3) investigating hybrid diffractive optical components that combine surface relief and volume type gratings; and 4) extending and verifying new modeling efforts that include diffraction of finite beams, converging beams, and cascaded grating systems. We also would like to expand our modeling capability to incorporate finite element analysis techniques, which are important for chirped grating analysis.

We are currently preparing a final report summarizing our grating model work for IBM. The future of this program, however, is unclear since it is no longer supported by ODSC or IBM. We hope to secure funding for this project from other sources that are primarily directed toward optical interconnect applications and that also require the use of diffraction models.

N94-14986

DYNAMIC TESTBED LABORATORY AND MICRO-OPTICS

T. Milster, K. Erwin, F. Froehlich, J. Kann, W. Li, W. Schlichting, R. Shetty, E. Walker and M. Wang

OBJECTIVES

Objectives of this research are as follows:

Understand the three classes of superresolution and their behavior in optical data storage systems;

Investigate new and improved components and techniques in the optical system for data detection and servo control;

Apply micro-optic components to the optical system to reduce size and weight;

Investigate techniques, such as near-field optical probes, for recording data densities beyond that possible with superresolution; and

Understand and find solutions for problems associated with dynamic testing, especially those that arise when evaluating blue-sensitive media.

PROGRESS

Our group has been very busy in several areas. In this progress report, we highlight some of the accomplishments of this quarter. In particular, we include an extended discussion of the superresolution work with the AMC testbed. We also discuss plans for our near-field optical microscope (NSOM) instrument and some theory that describes the NSOM transfer function. The MCD work is proceeding nicely, our static experiments are complete and a paper is ready for submission.

Theory

Our theoretical work this quarter consisted of continuing to develop a simple model for the NSOM work. We are completing a paper that will be submitted to *Optics Letters* on this subject.

Modeling

In the last several ODSC reports, we have described the effects of superresolution by using a shading band in the collection aperture. Our results indicated that both signal and noise are reduced with the shading band, producing no significant change in the carrier-to-noise ratio (CNR) except at high frequencies. However, the transfer function of the system is changed so that we may be able to take advantage of equalizing the frequency response of the system. A summary of our results has been accepted for presentation at the *ISOM* '93 meeting this summer. Appendix E is a copy of the extended abstract.

We are now studying a modification of the simple shading band described in previous ODSC reports. Our configuration is shown in Fig. 1. We shape the shading band into an "X" that is designed to pass the ± first diffracted orders at a specific frequency. In Fig. 1, the shading band is designed for around 4 MHz. The portion of the beam blocked by the shading band only contributes noise. The net effect is an increase in the CNR at this frequency. At lower frequencies, some degradation in signal is observed, but the CNR is improved due to the reduced noise. At higher frequencies, the signal is not affected, but the noise is reduced, again improving the CNR. An additional benefit of the X-band shading is that the transfer function of the system can be somewhat equalized. Our scalar diffraction model was used to determine the effect of X-band shading on the signal. The results are plotted in Fig. 2, which indicates a slight improvement in the transfer function with the shading band. In the *Dynamic Testing* section below we discuss our experimental results.

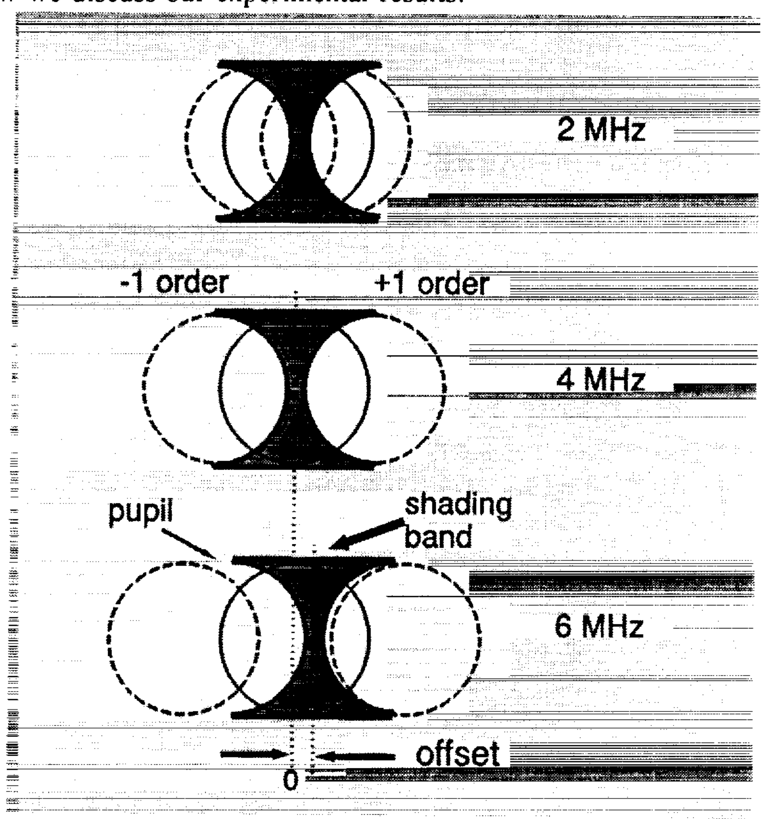

Figure 1. X-band shading. The exit pupil of the optical system used to read out data is shown with the ± first diffracted orders of the signal. The darkened portion of the picture corresponds to the shading band. This shading band is designed to pass most of the signal power at 4 MHz and block excess noise. At lower frequencies, the shading band blocks some of the signal, but the noise is reduced more, resulting in a net CNR increase. At high frequencies, the signal is not blocked, and the shading band only reduces noise. For our dynamic experiments, we tested the shading band at different offsets in the pupil.

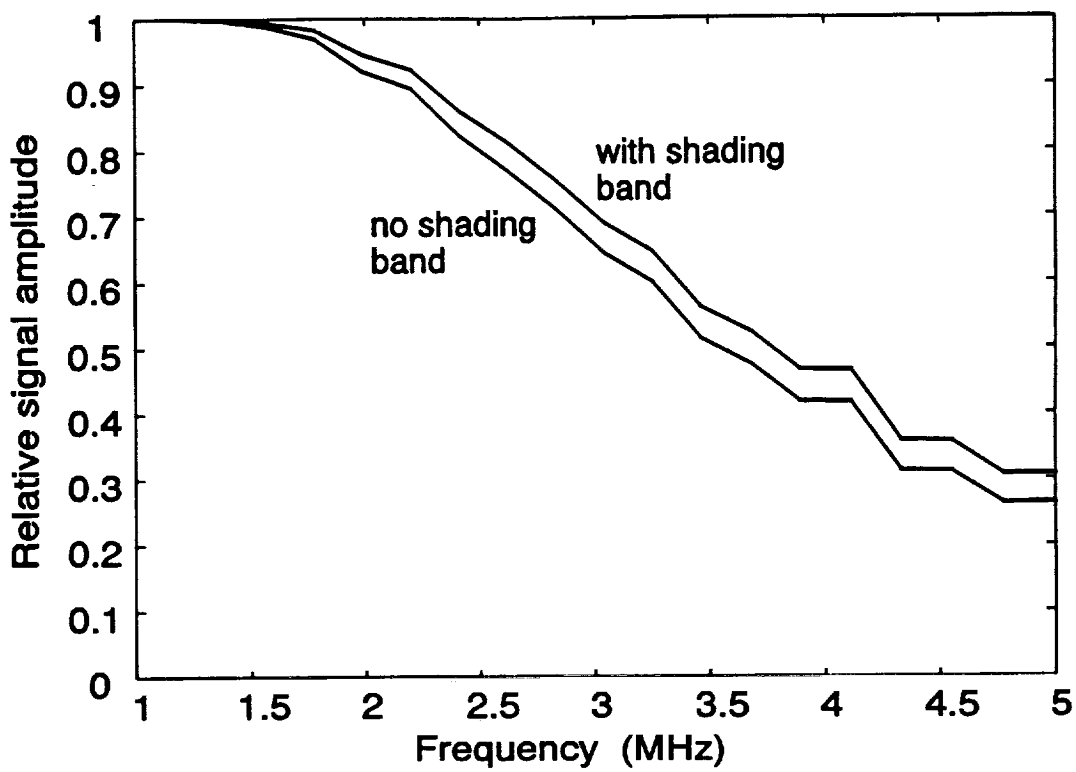

Figure 2. Diffraction model results with and without the X-band shading. A slight improvement in the transfer function is observed when X-band shading is used.

We presented a paper at OPTCON '92 titled "Figures of Merit for Laser Spot Quality," which describes the effects of aberrations on a simple gaussian laser beam that is passed through a diffracting aperture. An interesting observation of Ed Walker's modeling work is that caution should be used when implementing the full-width-at-half-maximum (FWHM) criterion for beam quality because it is very insensitive to aberration. A preprint of the paper appears as Appendix F of this report.

Static Experiments

We are continuing our research program in near-field scanning optical microscopy (NSOM). Fred Froehlich is constructing a sophisticated NSOM instrument to study the application of near-field technology to high-density optical storage. NSOM has been used to write and read MO domains as small as 60 nm (see E. Betzig et al., "Near-field magneto-optics and high density data storage," Appl. Phys. Lett. **61**(2), 1992). Our interest is to analytically model and experimentally characterize the detection of MO domain edges with a near-field tapered fiber-optic probe. WYKO instruments has provided an atomic force microscope (AFM) that we are adapting for NSOM use. Froehlich has submitted the abstract (Appendix G) that will be presented at the ISOM conference this summer.

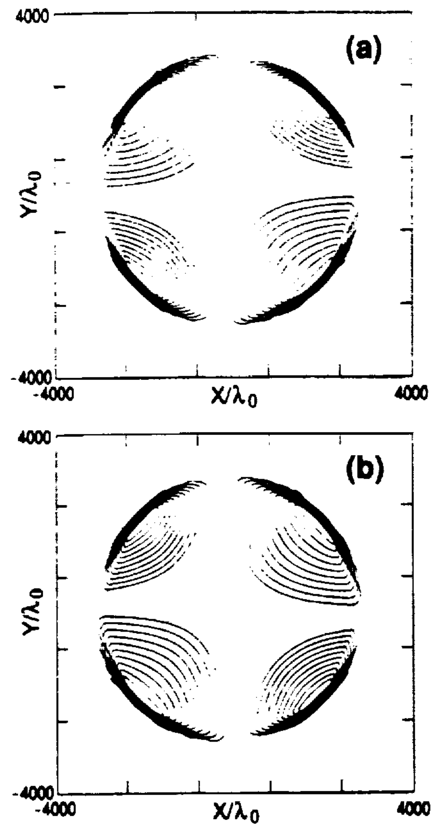

Figure 3. Contour plots of *Iy* for the quadrilayer structure, with the off-diagonal elements of the tensor restored: a) magnetization up; b) magnetization down.

Mark Wang is studying some aspects of superresolution by examining the amplitude and phase of the signal component reflected from MO media. Masud Mansuripur has predicted (Appl. Opt. 30(22), 3154, 1991) that high signal values exist in outer regions of the four quadrants in the pupil, as shown in Fig. 3. Besides trying to experimentally measure this effect, we will try to see the effects of moving the readout spot over a domain edge. The experimental aspects of this problem have proven difficult in the past, but we hope to improve the sensitivity by using a modification of a readout scheme that takes the difference signal optically (Milster and Yao, US Patent No. 4,823,220).

Dynamic Testing

We have configured the AMC testbed for optical equalization experiments, as reported in the December 15, 1992, ODSC report. Weiquan Li and Wang have been performing the tests. Our latest tests are with X-band shading. Figure 4 shows the results for a 3M disk at 3 MHz signal frequency. The graph is plotted versus offset of the shading band (see Fig. 1 for an explanation of offset). At 1.0 mm offset from the center, the CNR increases by about 3 dBm. Improvements in CNR also are observed at other frequencies. The reason that the maximum CNR does not occur in the center of the aperture is that the beam is not centered properly in the testbed. We will report more details on our experiments at the IAB meeting in April.

Wolfgang Schlitching has received an MO disk from Kodak that is optimized for MCD detection. He is evaluating the medium on the dynamic testbed. Since much more light gets back to the detectors with MCD, there are some modifications that need to be made to the electronics to handle the additional power. For example, the focus servo amplifiers saturate during writing and erasing, so their gains must be reduced. Without this adjustment, we can get about 41 dB CNR at low frequencies. More details will be presented at the IAB meeting.

In other dynamic testing news, Wang will be presenting his work on the differential wax-wane focus servo at ISOM '93. (A preprint of his abstract appears as Appendix H). We also are beginning work on the blue-laser head that will be used with the next set of superresolution experiments. These experiments use the air-bearing teststand.

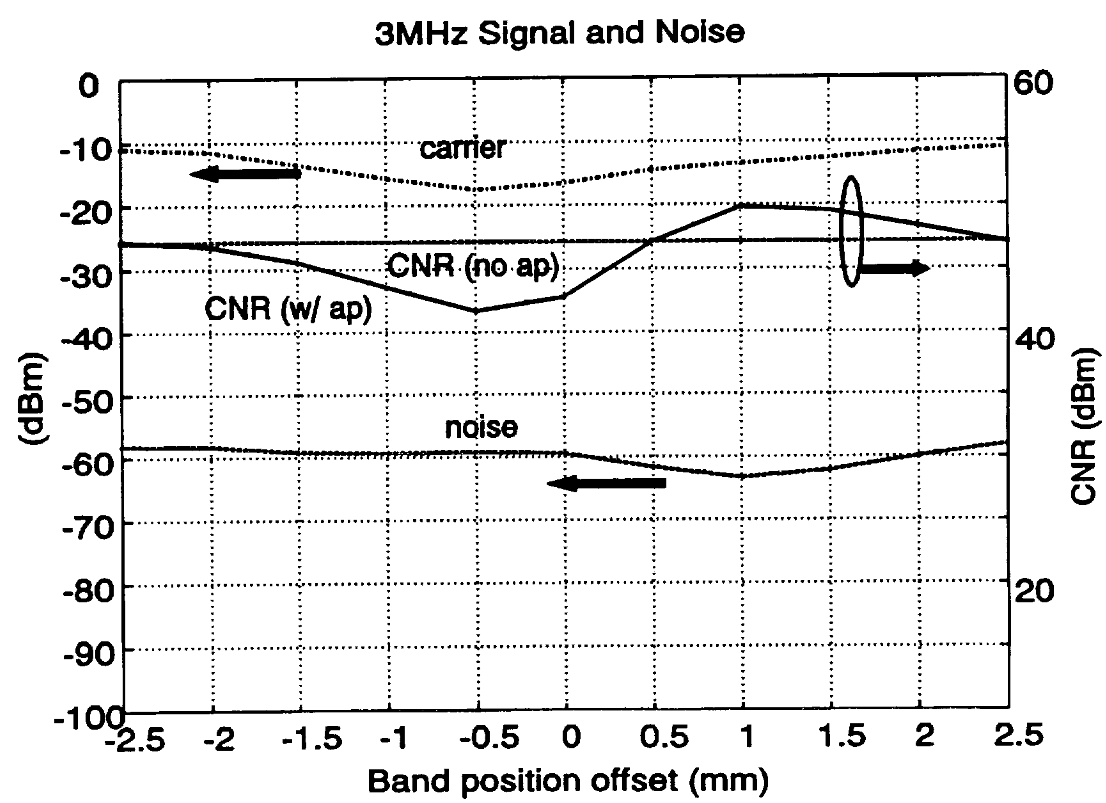

Figure 4. Carrier and noise properties versus X-band shading offset at 3 MHz signal frequency. Notice that the CNR is improved by 3 dB at an offset of 1.0 mm. The offset is necessary due to a slightly decentered beam in the exit pupil of the drive.

N94-14987

GRATINGS AND WAVEGUIDES

K.A. Bates, J.K. Erwin, N. Ramanujam, L. Li and J.J. Burke

OBJECTIVES

Our immediate objective is to understand the limitations of guided-wave and grating coupler devices in their application to optical data storage. Our long-range goal is to develop and validate design codes for integrated optic devices.

PROGRESS

As a member of the short wavelength laser source team (SWAT) our principal research activity has been in the development of numerical models for the design of a blue wavelength integrated optical source for data storage applications. Nanda Ramanujam's research efforts during the last quarter have been focused on designing a polarization-selective Bragg reflector for an extended cavity semiconductor laser using a grating-assisted slab waveguide. This laser acts as a pump for quasi-phasematched second harmonic generation (QPM-SHG) in an indiffused-KTP segmented waveguide. The Bragg reflecting grating is able to effectively discriminate between the TE and TM modal fields and reflects only the TM field, thereby permitting only TM laser operation. Ramanujam is currently exploring designs (such as chirped grating periods) to further increase the reflection bandwidth. During the next quarter, he plans to develop models and design programs for grating-assisted devices on channel waveguides.

Keith Bates continues to work on the variable groove depth grating coupler project. In the past year or so he has made grating couplers that produced near-Gaussian output beams. The fabrication method was based on an idea first suggested by Lifeng Li, i.e., moving a slit with variable dwelling time in front of the resist grating under ion beam bombardment. However, certain imperfections of the stepper motor that was used to drive the slit resulted in some minor intensity fluctuations in the output coupled beam. At the beginning of this year, Kevin Erwin suggested a new method (the invention disclosure is in preparation) to produce the desired variable depth grating. Initial testing of this new idea has shown very promising results. Bates is currently pursuing it.

Despite the advances made during the past 25 years in the electromagnetic theory and numerical modeling of diffraction gratings, certain grating problems remain difficult to solve even on a super-computer. For example, the problem of plane wave diffraction by a highly conducting metallic grating of arbitrary shape in TM (electric vector perpendicular to the grating grooves) polarization cannot be analyzed by any existing method when the ratio of groove depth to period is greater than 2. Many methods develop numerical instability long before the ratio reaches 2.

Recently, Li has constructed a computer program that is based on the classical modal method, its extension to the conical incidence case, and the R-matrix propagation method, which he borrowed from the chemical physics literature. The program approximates an arbitrary grating profile by dividing it into many layers of rectangular gratings. Because of the use of the R-matrix propagation algorithm the program is immune from the usual numerical instabilities associated with the presence of evanescent and anti-evanescent waves in the conventional propagation algorithm. In addition, because of the excellent convergence properties of the classical modal method, Li's new method also exhibits good convergence characteristics when applied to deep metallic gratings in TM polarization. For example, the program can predict diffraction efficiencies of a gold grating of sinusoidal profile and groove depth to period ratio of 100 at a near-infrared wavelength (we realize that such groove depth is not technologically possible.) The program can treat diffraction gratings of arbitrary surface profile, arbitrary refractive index gradients in the direction perpendicular to the grating plane, and arbitrary angle and polarization of the incident plane wave. The program could easily be converted to treat waveguide gratings and, in particular, the segmented planar waveguides of non-rectangular segments and non-uniform index distribution.

This work is being summarized for submission to a journal. The next step will be to extend the model to include anisotropy of the grating material.

N94-14988

COMPACT DISC ERROR MEASUREMENTS

D. Howe, K. Harriman and B. Tehranchi

OBJECTIVES

The objectives of this project are as follows:

Provide hardware and software that will perform simple, real-time, high resolution (single-byte) measurement of the error burst and good data gap statistics *seen by a photoCD player read channel* when recorded CD write-once discs of variable quality (i.e., condition) are being read (9/93);

Extend the above system to enable measurement of the hard decision (i.e., 1-bit error flags) and soft decision (i.e., 2-bit error flags) decoding information that is produced/used by the Cross-Interleaved-Reed-Solomon-Code (CIRC) block decoder employed in the photoCD player read channel (1/94);

Construct a model that uses data obtained via the systems described above to produce meaningful estimates of output error rates (due to both uncorrected ECC words and misdecoded ECC words) when a CD disc having specific (measured) error statistics is read (completion date to be determined); and

Check the hypothesis that current adaptive CIRC block decoders are optimized for pressed (DAD/ROM) CD discs. If warranted, do a conceptual design of an adaptive CIRC decoder that is optimized for write-once CD discs (completion date to be determined).

BACKGROUND

Equipment that determines whether a given CD disc conformans with the Phillips "Red Book" error specifications is commercially available. To make this determination, however, this equipment does not monitor data read from the disc, i.e., it does not directly measure disc errors. Instead, it monitors pin outputs on its CIRC block decoder chip (i.e., the VLSI circuit that performs the decoding of the C1 and C2 ECC words) that indicate when either a one-byte, or two-byte error is corrected, or when an error of length greater than two-bytes is detected, by either the C1 or the C2 ECC decoder. The equipment averages the results of this pin monitoring activity over one-second intervals before reporting them. Although this is adequate for a "yes/no" determination of the disc's conformance to the Red Book error specifications, it is not adequate for high resolution (single byte) mapping of a disc's errors. To see that this is true, consider that at the nominal CD playback scan velocity of 1.3 m/s, one second represents, on average, five full spiral turns of the 120 mm diameter disc, i.e., a surface area of 2.08 mm^2 (since the nominal track-to-track spacing on a CD disc is 1.6 μm). This should be compared to the disc real estate occupied by a single byte; one byte occupies a length of 5.1 μm along the disc's spiral track, which corresponds to a surface area of 8.16×10^{-6} mm^2 on the disc. The coarseness of error event measurements delivered by commercial CD disc evaluation equipment, together with the fact that such equipment does not directly "look at" the data being read from the disc, diminishes the usefulness of this commercial equipment for certain applications. Activities such as disc manufacturing process development/control and disc aging/degradation studies require the observation of small changes in the type and number of errors residing on a disc.

The system identified in the first of the four project goals listed above, which will be completed this summer, will provide high resolution (single-byte) measurement of the error events on specially recorded CD discs (i.e., discs that have a repetitive 24-byte data pattern written to them using the CD-Audio format) that are played on a Phillips Model CCD-461 CD-ROM player. The fact that a particular data pattern must be present on the disc is not a limitation since this system is meant for use with (i.e., studies of) write-once CD discs which can have any specified data written on them for experimental purposes. (Note: we have determined that our hardware could be adapted to high resolution measurement of errors on CD discs containing arbitrary data, e.g., pressed CD-ROM discs.)

PROGRESS

To understand the following description of the CD error measurement system that we are developing, one must know how the various CD data structures, such as C1 and C2 codewords and EFM frames, are organized on (i.e., recorded on) a CD disc. This background information is contained in Appendix I ("Determining the Locations of the Various CIRC Recording Format Information Blocks [User data blocks, C2 & C1 word and EFM frames] on a Recorded Compact Disc"). It is recommended that those interested in the details of our CD error measurement system read that Appendix to facilitate their understanding of what follows.

The scheme we are using to perform high resolution measurement of the errors on CD discs is enabled by the architecture of the Phillips CD3A CIRC block decoder, which is a VLSI circuit that performs data detection, channel data demodulation and C1 & C2 ECC decoding. It is the latest generation CIRC block decoder; it features adaptive data detection, intelligent channel clock synchronization, and soft decision ECC decoding. This chip's C1 ECC decoder will determine how to handle a given received C1 codeword based on the calculated snydrome for that word *and* whether any 1-bit erasure flags are attached to any of the bytes of the word (by the eight-to-fourteen channel data demodulator); its C2 decoder chooses how to treat a given received C2 word based on the calculated syndrome for the word *and* the distribution of 2-bit soft-error flags that accompany the word (a 2-bit flag is attached to every C2 word byte when the byte is output by the C1 decoder). The CD3A chip is used in the Phillips CCD-461 CD-ROM player as well in the Kodak PhotoCD player.

A high level diagram of the CD3A chip is given as Fig. 1. The aspect of this chip's architecture that we exploit is the fact that data are clocked from the chip itself to an external RAM, and back, as illustrated in Fig. 1. This is done to implement the de-interleaving that is required to obtain C1 codewords from the EFM frames that are sequentially read from the disc, and to obtain C2 codewords from the data blocks that are output by the C1 decoder. By monitoring the data traffic marked as "write 1" in Fig. 1 we intercept the serial data stream recovered from the disc after eight-to-fourteen channel data demodulation has occurred, but before any ECC decoding. After appropriate synchronization is obtained, this data stream is organized into individual EFM frames.

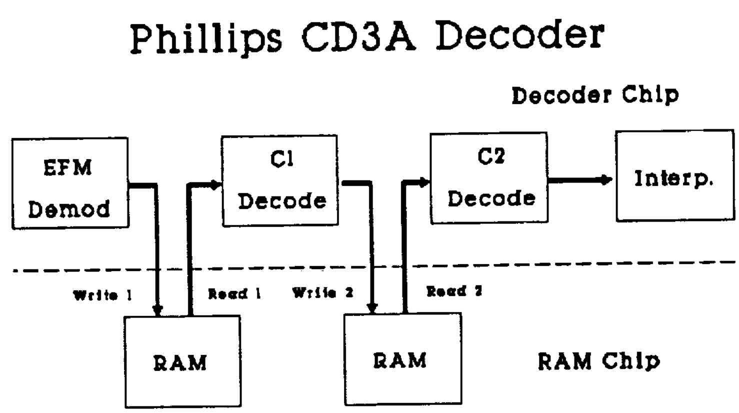

Figure 1.

If a given 24-byte block of user data is repetitively recorded on the disc being read, the lower 32 bytes of each of the recovered EFM frames will be identical, assuming that there are no errors in the block (cf., Appendix I). Therefore, by comparing each recovered EFM frame, byte by byte, with the exact 32-byte pattern that would be present in each EFM frame in the absence of errors, any error that is contained in an EFM frame can be located. Fig. 2 illustrates this; the block labeled "error detector" in that figure represents the 32-byte comparator. This logic element outputs 32 bits in response to each EFM frame comparison operation; a "zero" is output if two compared bytes are identical, a "one" is output if they are not. The hardware will be developed in two phases (versions). Phase I will produce one output byte for each EFM frame in which an error is detected and the output byte will specify the number of erroneous bytes in the contaminated EFM frame. The Phase I hardware will provide intermediate resolution error measurements, i.e., error counts will be averaged over a spatial disc track segment that corresponds to a single EFM frame, which nominally occupies a distance along the track of about 0.176 mm (this distance includes EFM frame overhead). An advantage of the Phase I system

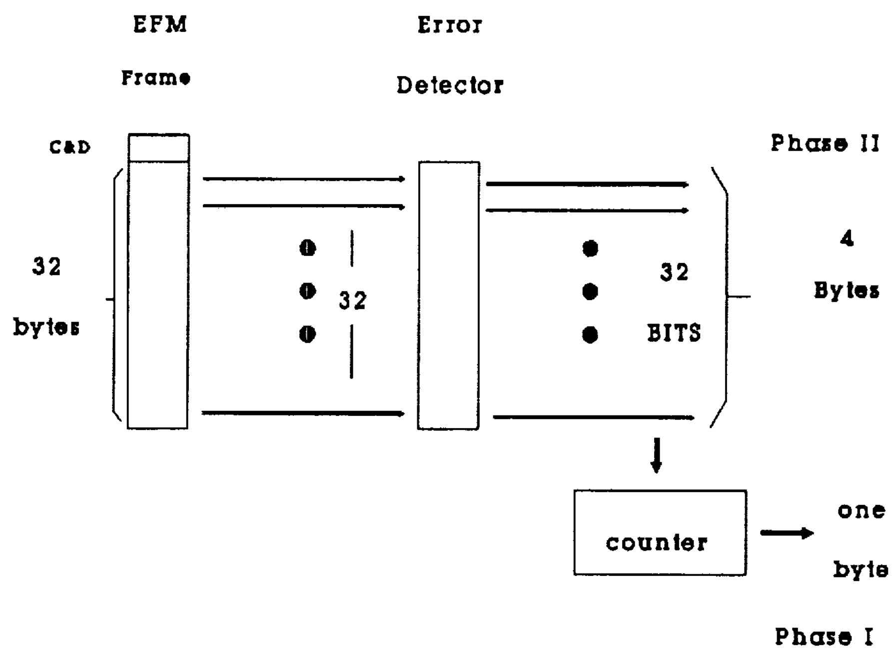

Figure 2.

is that its output data can be processed in real time and we plan to provide polar graph visualizations of the measured error statistics. Phase II hardware, which will produce 4 output bytes for each EFM frame comparison, will provide high resolution (single-byte) error burst and good data gap length measurements. Output data from this system will be stored for post processing.

As an extension to this project , we plan to extend the Phase II hardware's functionality to the collection of the 1-bit erasure flags that are generated by the eight-to-fourteen demodulator in response to channel data run-length violations (cf., the second project goal listed at the beginning of this report). These flags are passed across the CD3A CIRC block decoder RAM interface along with the EFM frame data (cf., Fig. 3). We also will study the possibility of collecting the 2-bit soft decision flags that are generated by the C1 decoder and passed to the C2 decoder for its use in selecting an error handling strategy. These 2-bit flags appear on the CD3A RAM interface at the point labeled "write 2" in Fig. 1.

During the past quarter we have determined the sequencing used for writing and reading both data and error flags to/from the CD3A RAM; we have devised a method of obtaining EFM frame block synch; we have worked out a scheme for relating measured error events to a geometrical location on the disc; and we have completed a high (logical block) level design of the CD error measurement hardware. We are currently designing/constructing the functional system subblocks and writing the system control software.

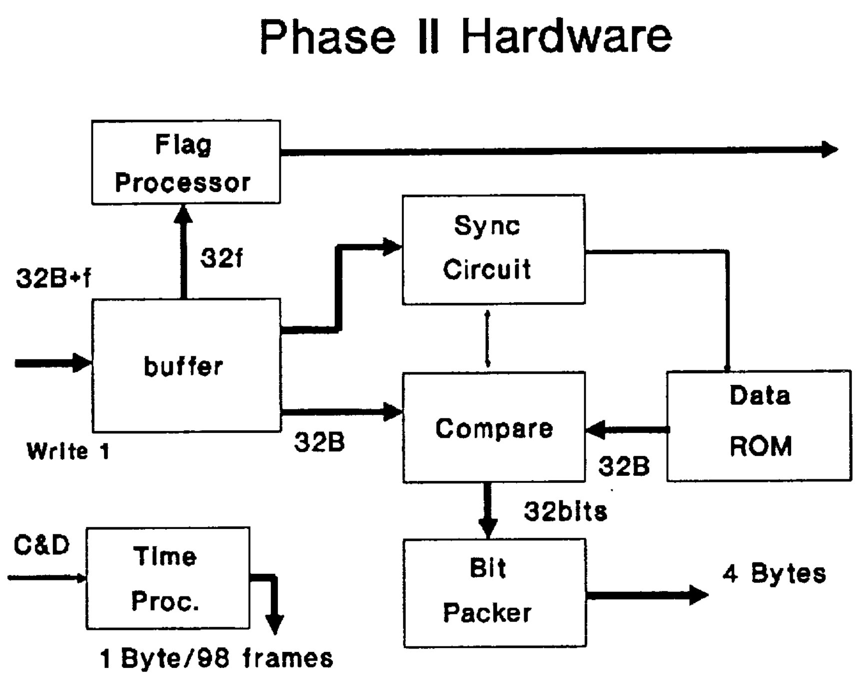
Phase II Hardware
Flag
Processor
32f
32B+f
buffer
Write 1
Sync
Circuit
Compare
32B
Data
ROM
32B
32bits
Bit
Packer
4 Bytes
C&D
Time
Proc.
1 Byte/98 frames

Figure 3.

SECTION 2. APPENDICES

APPENDIX A

PRECEDING PAGE BLANK NOT FILMED

N94-14989

Measurement of Birefringence for Optical Recording Disk Substrates

Hong Fu, S. Sugaya†, J.K. Erwin, T. Goodman, Z. Yan, W.J. Tang and M. Mansuripur

Optical Sciences Center

University of Arizona

Tucson, Arizona 85721

Abstract

The birefringence of bare and coated substrates for magneto-optical recording is experimentally investigated using ellipsometry at the wavelengths of 632.8 nm and 780 nm. We measure the rotation and ellipticity of the polarization state of the reflected or transmitted light for different incident angles and different orientations of the incident linear polarization. The measured data is then fitted by a computer program which solves the Maxwell equations for the plane-wave propagation in a multilayer structure and minimizes the error between the measured and calculated data by adjusting the unknown parameters of the multilayer. This approach enables us to determine orientations of the three principal axes in the substrate and the corresponding refractive indices. A special feature of our ellipsometers is that a glass hemisphere is placed in contact with the substrate, which eliminates the refraction of the incident light and enables a maximum propagation angle of 70° (with respect to the normal) in the substrate. This increases the sensitivity of the measurement. Certain anomalies have been observed, which we believe are associated with the presence of grooves on these substrates.

† Visiting scientist from Functional Devices Research Laboratories, NEC Corporation, Japan.

I. INTRODUCTION

Birefringence is a phenomenon observed in optically anisotropic media in which the refractive indices depend on the polarization direction. The polarization-dependent phase-shifts due to birefringence of the plastic substrates of magneto-optical (MO) disks can easily degrade the performance of MO readout systems [1-7]. As the MO data storage systems progress towards high resolution and ultrafast speeds, the birefringence has become an increasingly important problem.

Birefringence in plastic substrates is due to preferential molecular orientation and internal stresses. The refractive index is higher when the electric field of the light beam is parallel to the molecular chain direction. For injection-molded polycarbonate substrate the fluid shear during the injection molding process acts to align the polycarbonate chains in the plane of the disk. Therefore, the refractive indices n_1 and n_2 for the in-plane electric field components E_1 and E_2 of light are much larger than n_3 for the perpendicular component E_3. The characterization of substrate birefringence has been the subject of several papers [6,8-11], which confirmed the above picture and found that $n_1 - n_3$ is on the order of 10^{-4}, while $|n_1 - n_2|$ is on the order of 10^{-5}. However, the previous work is limited in the following aspects: First, the formula [8,11] by which the experimental data were processed applies only to transparent single-layer media under the assumption that the principal axes of the index ellipsoid are fixed in the radial, track and perpendicular directions. The phase-shifts due to the multilayers and due to the tilt of the index ellipsoid could not be taken into account. Second, due to refraction at the interface between air and substrate, the propagation angle of the light in the substrate is usually small. For example, 70° incident angle in air corresponds to 36.5° propagation angle in the polycarbonate substrate ($n = 1.58$). So the beam possesses only a small E_3 component and the experimental sensitivity to n_3 is limited.

The present paper describes measurements of the substrate birefringence using one ellipsometer with wavelength $\lambda = 632.8$ nm and another with $\lambda = 780$ nm. We remove the first restriction of the previous work by using a computer program which solves the Maxwell equations for a plane-wave propagating in a multilayer structure including the substrate [12]. This approach enables us to determine the three principal axes of the substrate and the corresponding refractive indices. To overcome the second limitation, we have placed a hemispherical glass lens atop the substrate to eliminate refraction. A maximum propagation angle of 70° in the substrate has thus been achieved. We measured the rotation angle and ellipticity of the polarization state of the reflected and/or transmitted light as functions of the incident angle for linearly polarized incident beam. The investigated substrate materials include glass, polycarbonate plastic (bare and coated), and amorphous polyolephin plastic (bare). Measurements were performed on regions with or without grooves. For the former case, the grooves were either filled with index-matching fluid or left empty. Different angles between the plane of incidence and the direction of grooves were used in the measurements. This paper is organized as follows. The two ellipsometer systems and measurement procedures are described in Sec. II, along with a description of the data analysis procedure using the multilayer program. The measurement results are described in Sec. III. Sec. IV contains some concluding remarks.

II. ELLIPSOMETER SYSTEMS AND THE MEASUREMENT METHOD

II.1 The VAE633 System

Figure 1 shows the experimental setup. The light source is a HeNe laser with $\lambda = 632.8$ nm. As the beam first passes through the polarizer and the quarter-wave plate (QWP), whose fast axis is at 45° to the transmission axis of the polarizer, it becomes circularly polarized. The second polarizer selects the linear polarization direction of the incident beam. A hemispherical glass lens is placed in contact (using index-matching fluid) with the surface of the sample. This hemisphere is actually slightly less than one half of a sphere, and is mounted in such a way that the geometric center of the spherical surface is on the back side of the substrate. The light enters normally into the hemisphere, goes through the substrate, and is reflected from the back side of the substrate. After reflection, the beam passes through another QWP with an adjustable fast-axis orientation. The beam then goes through a Wollaston prism which can be rotated about the beam. Finally, the two beams of mutually perpendicular polarization are detected by the photodetectors.

The hemispherical lens eliminates refraction at the air-substrate interface, thus producing a larger propagation angle within the substrate. For example, in polycarbonate substrate with $n = 1.58$, without the glass hemisphere one can reach a maximum angle of 39° at grazing incidence (i.e. $\Theta_{inc} = 90°$), while with the hemisphere in place ($n_{sphere} = 1.52$), the propagation angle inside the substrates is 64° at $\Theta_{inc} = 70°$.

II.2 The VAE780 System

The setup is schematically shown in Fig.2 (a). The operation principle is similar to the VAE633 system. One of the main differences is that all the moving parts are mounted in one arm, which can be rotated in both polar and azimuthal directions. The alignment of the system is thus easier to maintain. The freedom of two-dimensional rotation is particularly valuable to measure the effect of grooves, which are found to be sensitive to both polar incident angle Θ_{inc} and the azimuthal incident angle Φ_{inc} relative to the radial direction. The linearly polarized light from the laser diode (λ = 780 nm) passes through the beam splitter and enters normally through the hemisphere before it reaches the sample. The direction of incident polarization is controlled by rotating the laser in its socket. The hemisphere is used in different ways, depending on whether the sample is transparent or reflective. For transparent samples, two hemispheres are used, see Fig.2 (b). The one on the top is transparent and is used to eliminate refraction. The one at the bottom is coated with aluminum and reflects the beam normally so that the light goes back along the incident path. In this configuration the light passes twice through the substrate. For coated samples, we only need the top hemisphere, see Fig.2 (c). Half of this hemisphere is coated with aluminum. The beam enters from the uncoated side, gets reflected from the bottom of the sample, bounces off the coated side of the hemisphere, and retraces its path. Thus the beam passes four times through the substrate. In both transmission and reflection modes, the use of hemisphere(s) does not introduce phase shift or relative amplitude change between p and s components upon entering and exiting the substrate. Therefore, the measured values of rotation and ellipticity are solely determined by the properties of the sample. As the light beam returns, it is routed by the beam splitter into the detector channel, where its polarization state is determined by the use of the QWP, a Wollaston prism and two detectors.

II.3 The Measurement Principle

The measured quantities are the rotation angle θ and ellipticity angle ε of the reflected beam. The definitions of θ and ε and the corresponding measurement procedures are described below. The p- and s-polarization directions for incident and reflected beams in VAE630 and VAE780 systems are defined in Fig.1 and Fig.2 (a), respectively. The polarization angle ψ_{pol} of the incident beam is measured from the p-direction, Fig.3 (a), and can be read from the setting of the polarizer in VAE633 and the laser diode in VAE780. In general, due to phase retardation between the p- and s-components, the reflected beam is either left- or right-handed elliptically polarized (LEP or REP). Figure 3 (b) shows that the ellipse can be characterized by the orientation of its major axis, θ_{axis}, and the ellipticity angle ε. By definition $|\tan \varepsilon|$ is the ratio of the minor to major axis, and $\varepsilon < 0$ for LEP and $\varepsilon > 0$ for REP. Thus, $-45° \leq \varepsilon \leq 45°$. In particular, $\varepsilon = -45°$ (or $+45°$) corresponds to LCP (or RCP), and $\varepsilon = 0$ corresponds to linearly polarized light. When the fast-axis of the QWP is parallel to the major axis of the ellipse, the beam passing through it becomes linearly polarized. Its polarization angle θ_W can be smaller or greater than θ_{axis}, depending on whether the beam before the QWP is LEP or REP. These two cases are shown in Figs.3 (c) and (d). θ_{axis} and θ_W can be measured simultaneously by adjusting the orientations of QWP and the Wollaston prism, until one of the detectors receives no light. Once extinction is achieved, the orientation of the fast-axis of the QWP gives θ_{axis}, while the Wollaston orientation gives θ_W. The rotation and ellipticity angles of the reflected beam are then given by:

$$\theta = \theta_{axis} - \psi_{pol}\,, \quad \varepsilon = \theta_W - \theta_{axis}\,. \tag{1}$$

In practice, the error for the measured value of ε is less than 1°, as estimated from repeated measurements. The error for θ depends on the value of ε. For $|\varepsilon| < 40°$, error of less than 1° can be achieved. For $|\varepsilon| > 40°$, the ellipse is close to a circle and the orientation of the major axis is hard to measure. The repeatability of θ in such cases is within several degrees.

II.4 Data Fitting with the Multilayer Program

The first part of the multilayer program [12] solves the Maxwell equations for a plane wave obliquely incident upon a multilayer structure consisting of a given number of layers. Each layer is characterized by its dielectric tensor and thickness. With adequate restrictions on the tensor elements, different types of media (isotropic, birefringent, magneto-optic, etc.) can be described. Figure 4(a) shows the quadrilayer structure of a typical MO disk. This structure is used in data fitting for coated substrates. For bare substrates, we consider the substrate alone without additional layers. The hemisphere material (n_{sphere} = 1.52) and the index-matching fluid (n_{fluid} = 1.52) are treated as the medium of incidence. Since the optical paths in VAE633 and that in the transmission and reflection modes of VAE780 are different, three versions of the multilayer program were used in the data analysis. The second part of the program searches the best values of unknown parameters by minimizing the error, defined below, between the measured and the calculated data:

$$\text{error} = \sqrt{\frac{1}{2N}\sum_{i=1}^{N}\left[\left(\theta_i^{(exp)} - \theta_i^{(cal)}\right)^2 + \left(\varepsilon_i^{(exp)} - \varepsilon_i^{(cal)}\right)^2\right]} \; . \tag{2}$$

In this equation, the superscript "exp" stands for experimental data, and "cal" for calculated data, N is the total number of the measurements on a given sample. The unknown parameters are the refractive indices, the orientation angles of the principal axes of the ellipsoid of birefringence and the structure parameters of the multilayer. In our Convex computer system, it takes only a few minutes to search for 10 unknown parameters in fitting 120 data points.

In Fig.4 (a) X and Y denote the in-plane radial and track directions of an optical disk, and Z the normal direction. In addition to the incident angle Θ_{inc}, we use Φ_{inc} to specify the azimuth of the incident k-vector. For all the samples, we found that one principal axis (3) is always along the perpendicular direction, but the in-plane axes (1 and 2) may be rotated in the X-Y plane, see Fig.4 (b). To be specific, we let 1 be the in-plane axis with the larger refractive index, and use $\psi_{in\text{-}plane}$ to denote the in-plane rotation of axis 1 from the radial direction.

There are two aspects of the actual systems that are not taken into account in the multilayer program. One is that the beam is not a plane wave, but a focused beam with 0.5 mm diameter that converges to a 50μm spot at the bottom of the substrate. For thick samples, the two reflected beams from the front and back surfaces are spatially separate and do not interfere with each other, while in the program the two beams overlap. However, since the reflection at the interface between the hemisphere and the substrate is weak, the interference only causes small fluctuation in the calculated curves. Therefore, the plane wave approximation is acceptable. Another aspect is the structure of the grooves on the surface of the substrate, which are usually 0.5 μm wide, 70 nm deep, and have a periodicity of 1.6 μm. The effect of the grooves on polarized light has not been fully investigated. We found that, for bare substrates, the data measured at $\Phi_{inc} = 0°$ can be matched very well, while for coated substrates, good match can be obtained for $\Phi_{inc} = 90°$. For other values of Φ_{inc}, there is usually mismatch between the measured data and theory. In these occasions we are probably witnessing anomalous behavior caused by the grooves.

III. RESULTS

The measured samples include a glass microscope slide, two 3.5" bare polycarbonate substrates (PC3.5B01[1] and PC3.5B02), two 5.25" polycarbonate bare substrates (PC5.25B01 and PC5.25B02), one 5.25" amorphous polyolephin substrate (APO5.25B01), two 3.5" MO disks (PC3.5C01 and PC3.5C02), three 5.25" MO disks (PC5.25C01, PC5.25C02, PC5.25C03). All coated disk substrates are polycarbonate plastic. The main results of these measurements are summarized in Table 1.

III.1 The Glass Sample

To check the VAE633 system, we measured a glass microscope slide with thickness d = 1.2 mm. Glass is believed to be isotropic with a refractive index close to that of the hemisphere and index-matching fluid. So the optical path is simple (e.g. no multiple reflections) and the problem should be well described by the well-known formulas for reflectivity at a single interface [13,14].

Fig.5 shows θ and ε as functions of the incident angle in the range $10° \leq \Theta_{inc} \leq 70°$ for $\psi_{pol} = 45°$. The measured data in (a) and (b) are same. The calculated curves in (a) are obtained by

---

[1]In this notation PC stands for polycarbonate (APO stands for amorphous polyolephin), the number 3.5 for the disk diameter in inches, B for bare substrate (C for coated substrate), and 01 is the serial number.

assuming that the glass is isotropic. The match gives $n_{glass} = 1.54$. We see that the rotation angles can be matched very well, but the non-zero ellipticity for $\Theta_{inc} \leq 41°$ (critical angle of total internal reflection) cannot be matched. The average fitting error is 1.9°. To obtain a better match, we allowed the glass to have a small amount of birefringence. The curves in Fig. 5(b) show the best match with an average error of 0.8°. The fitted refractive indices are $n_1 = 1.54$, $(n_1 - n_2) = 6\times10^{-6}$, $(n_1 - n_3) = -1\times10^{-6}$ and $\psi_{in\text{-}plane} = -9.2°$. In this particular case where the sample has no grooves, X and Y stand for in-plane directions along the two rectangular sides of the microscope slide.

The basic features of the plots of θ and ε versus Θ_{inc} can be understood using the reflectivities for E_p and E_s for dielectric interface [13,14]. Below the critical angle for the total internal reflection ($\Theta_{inc} \leq 41°$), the reflectivities are real and non-equal, i.e. the values of $|E_p|$ and $|E_s|$ will change after reflection but the phase difference should remain zero. Therefore, the reflected beam is still linearly polarized ($\varepsilon = 0$) but in a different direction ($\theta \neq 0$). The measured non-zero ε indicates that there exists a small amount of birefringence. At the critical angle the behavior of θ and ε changes drastically. We mention in passing that the total reflection occurs at the interface between the glass sample and air, but the critical incident angle is determined by the refractive index of the hemisphere, as can be readily seen from Snell's law. In VAE 633, we found that the critical angle is 41.3°, which is in agreement with $n_{sphere} = 1.52$. Above $\Theta_{inc} = 42°$, both E_p and E_s are totally reflected and acquire different phase shift, i.e. $|E_p| = |E_s|$, $\phi_p \neq \phi_s$. So we have $\varepsilon \neq 0$.

III.2 Sample PC3.5B01 and PC3.5B02

The measured point is located at about 3 cm from the center of the disk and at the center of a sector with grooves. To reduce diffraction effects, the groove side of the substrate was placed in contact to the hemisphere and the grooves were thus filled with index matching fluid. The in-plane projection of the plane of incidence is perpendicular to the track direction ($\Phi_{inc} = 0°$).

Figures 7 (a) and (b) show the measurement results and the matched curves for sample PC3.5B01 with $\psi_{pol} = 30°$ and $60°$, respectively. The best fit for the data set with $\psi_{pol} = 30°$ gives $n_1 = 1.58$, $(n_1 - n_2) = 1.5\times10^{-5}$, $(n_1 - n_3) = 5.87\times10^{-4}$ and $\psi_{in\text{-}plane} = -0.3°$. The fitting error is 2.9°. The parameters found for $\psi_{pol} = 60°$ are: $n_1 = 1.58$, $(n_1 - n_2) = 1.3\times10^{-5}$, $(n_1\text{-}n_3) = 5.87\times10^{-4}$, and $\psi_{in\text{-}plane} = -5.3°$. The average error for $\psi_{pol} = 60°$ is 1.7°, smaller than that for $\psi_{pol} = 30°$. We see that the two sets of fitted parameters are nearly identical. Ingnoring the small values of $\psi_{in\text{-}plane}$, one can assert that the principal axes are in fact along the radial, track and perpendicular directions.

Some of the features shown in Fig.6 are common to all the substrates and can be easily explained. First, the absolute values of θ and ε are small at small Θ_{inc}. The reason is that the beam close to normal incidence only experiences the small in-plane birefringence, but not the larger vertical birefringence. The second feature is that the oscillation interval, i.e. the difference between incident angles corresponding to two adjacent peaks, decreases with increasing Θ_{inc}. For example, the peaks of ε in (a) appear at $\Theta_{inc} = 22°, 37°, 49°, 60°$ and $68°$. The corresponding intervals are 15°, 12°, 11° and 8°, and decrease monotonically. This feature could be understood as the change of optical path length per incident angle increases with Θ_{inc}. Another feature is that θ always shows a 90° jump when $\varepsilon = 45°$, see the data points at $\Theta_{inc} = 22°$ in (a). What happens here is that the polarization ellipse is very close to a circle. A slight decrease in the major-axis or increase in the minor-axis causes exchange of the axes and lead to a 90° jump. This transition is shown in Fig.7.

Sample PC3.5B02 is another substrate in the same series of product as PC3.5B01. We measured the same position (3 cm from the center of the disk and center of a sector with grooves) in both VAE633 and VAE780 for $\Phi_{inc} = 0°$ and $\psi_{pol} = 60°$. The data taken with VAE633 has a shape similar to that shown in Fig.6 (b). However, the best fit gives $\psi_{in\text{-}plane} = -50.3°$. In comparison with PC3.5B01, the in-plane birefringence is three times smaller: $(n_1 - n_2) = 0.5\times10^{-5}$ and vertical birefringence is somewhat larger $(n_1 - n_3) = 6.26\times10^{-4}$. PC3.5B02 was also measured with VAE780 in the transmission mode. Figure 8 shows the measured data and the best fit. The best match gives $\psi_{in\text{-}plane} = 56.7°$. The fitted parameters are: $n_1 = 1.58$, $(n_1 - n_2) = 1.9\times10^{-5}$, and $(n_1 - n_3) = 5.83\times10^{-4}$.

III.3 Sample APO5.25B01

The measured position is located 5 cm from the center of the disk and in the middle of a sector with grooves. The groove side is in contact with the hemisphere. The sample was measured with VAE633 at $\Phi_{inc} = 0°$ for $\psi_{pol} = 60°$. The measured data and the best fit are shown in Fig. 9. Both in-plane and vertical birefringence are small: $n_1 = 1.50$, $(n_1 - n_2) = 0.4\times10^{-5}$, $(n_1 - n_3) = 1.3\times10^{-5}$ and $\psi_{in\text{-}plane} = -72.5°$.

III.4 Sample PC5.25B01 and PC5.25B02

These two samples are from the same series of product. The measured point on smaple PC5.25B01 was located 5 cm from the disk center and in the middle of a sector with grooves. The groove side was faced to the hemisphere and filled with index matching fluid. The measurement was performed with $\Phi_{inc} = 0°$ and $\psi_{pol} = 60°$ with VAE780. The measured data and the match are shown in Fig.10. The fitted parameters are: $n_1 = 1.58$, $(n_1 - n_2) = 1.3\times10^{-5}$, $(n_1 - n_3) = 6.22\times10^{-4}$ and $\psi_{in\text{-}plane} = 66°$.

For Sample PC5.25B02 we measured the region without grooves: a point located 2.5 cm from the center of the disk with VAE633 for $\psi_{pol} = 30°$, $45°$, $60°$ and $\Phi_{inc} = 90°$. Figure 11 (a)-(c) show the measured data and the fits. No match has been found for $\Theta_{inc} > 54°$ (not plotted). The fitted parameters based on data taken for $10° \leq \Theta_{inc} \leq 53°$ with $\psi_{pol} = 30°$, $45°$ and $60°$ are: $n_1 = 1.58$, $(n_1 - n_2) = 2.2\times10^{-5}$, $(n_1 - n_3) = 5.83\times10^{-4}$ and $\psi_{in\text{-}plane} = 1.6°$. We also measured a point in the region with grooves. This time we found that, for $\Theta_{inc} \geq 25°$, the measured curves cannot be matched. The measurement was repeated for the same point, but with the side of grooves facing backward, so that the grooves were not filled with the index-matching fluid. In this case there were a series of diffracted beams and we measured the one corresponding to the zeroth order pattern. The measured values for θ and ε in the range of $10° \leq \Theta_{inc} \leq 60°$ were the same as those with the filled grooves.

III.5 Sample PC3.5C01 and PC3.5C02

These two MO disks are from the same series of product with quadrilayer structure. The measured point was located 3 cm from the disk center and in the middle of a sector with grooves. The data were taken with $\Phi_{inc} = 90°$ and $\psi_{pol} = 60°$. The measured data and the best fit are shown in Fig.12. The fitted parameters are: $n_1 = 1.58$, $(n_1 - n_2) = 2.3\times10^{-5}$, $(n_1 - n_3) = 5.34\times10^{-4}$, and $\psi_{in\text{-}plane} = -2.9°$. The principal axes are in fact along the radial and track directions. To obtain the best fit, the quadrilayer structure must be used and adjusted in the calculation. We found that the searched structure parameters were not unique. However, the searched birefringent parameters were always the same and hence are reliable. The reason is that the measured θ and ε contain information about the phase shift contributed by the birefringence, but not much information about the absolute reflectivities which are signatures of the quadrilayer. The same measurement was performed for PC3.5C02. The fitted parameters are: $n_1 = 1.58$, $(n_1 - n_2) = 2\times10^{-5}$, $(n_1 - n_3) = 5.51\times10^{-4}$, and $\psi_{in\text{-}plane} = -6.5°$. Compared with the bare substrates PC3.5B01 and PC3.5B02, we see that the coated substrates have larger in-plane birefringence but smaller vertical birefringence. The decrease of vertical birefringence due to coating was also reported in [11].

III.6 Sample PC5.25C01

The sample is a small section of coated substrate with grooves cut from a 5.25" MO disk. The data were taken with VAE633 at $\Phi_{inc} = 90°$ for $\psi_{pol} = 45°$ and $60°$. As shown in Fig.13, both measured curves can be fitted very well with a fitting error of 1.65°, using the set of parameters: $n_1 = 1.58$, $(n_1 - n_2) = 0.9\times10^{-5}$, and $(n_1 - n_3) = 4.61\times10^{-4}$ and $\psi_{in\text{-}plane} = 8°$.

III.7 Sample PC5.25C02 and PC5.25C03

These two samples are from the same series of product. For PC5.25C02 we measured 4 points, each located at the same radial position (5 cm from the disk center) but in the middle of different sectors. $\Phi_{inc} = 90°$ and $\psi_{pol} = 60°$ were fixed. The measured data were nearly identical for the 4 points, see Fig. 14, indicating that the birefringence property is uniform along the track. The best match for one of the measured points (solid lines in Fig. 14) gives: $n_1 = 1.58$, $(n_1 - n_2) = 0.7\times10^{-5}$, and $(n_1 - n_3) = 3.37\times10^{-4}$ and $\psi_{in\text{-}plane} = -18°$.

For PC5.25C03 we measured one point at 5 cm from the center of the disk and in the middle of a grooved sector. The fitted parameters are: $n_1 = 1.58$, $(n_1 - n_2) = 1.9\times10^{-5}$, $(n_1 - n_3) = 3.47\times10^{-4}$ and $\psi_{in\text{-}plane} = 11.5°$. Figure 15 shows the measured data for both PC5.25C02 and PC5.25C03 with $\psi_{pol} = 60°$, emphasizing the similarity of the two disks.

IV. CONCLUDING REMARKS

In this paper we have described an approach to measuring the birefringence for optical disk substrates using ellipsometry. The procedure consists of measurement of the rotation and ellipticity, and data fitting using a computer program. Using this method we have measured a number of bare and coated substrates. One of the main differences between our method and the previous ones is that we can measure the orientation of the principal axes of the index ellipsoid. Our results confirm that the disk normal direction is always a principal axis (e.g. tilted angle of less than 0.1° was found for all the measured samples). However, rotation of the in-plane axes was found to occur frequently. This rotation has been mentioned previously [9], but our work gives the first quantitative results. Another advantage is due to the use of the glass hemisphere which makes large propagation angles. We found that the grooves in bare (even when filled with index-matching fluid) and coated substrates have different effects on the polarization state of the beam. For bare substrates, the measured data can be matched very well when the plane of incidence is perpendicular to the grooves ($\Phi_{inc} = 0°$). The opposite is true for coated substrates, i.e., $\Phi_{inc} = 90°$ gives the best match. For other values of Φ_{inc} the match is usually poor, especially for data measured at large Θ_{inc}. This dependence on Φ_{inc} shows that the grooves can cause a phase shift, thus producing errors in birefringence measurement. The fact that we can get good match for data taken at $\Phi_{inc} = 0°$ for bare substrates and $\Phi_{inc} = 90°$ for coated substrates may suggest that at these particular angles the grooves have no effect on the beam, and thus the measured birefringence data are more accurate.

REFERENCES

[1] D. Treves and D. S. Bloomberg, "Effect of birefringence on optical memory systems," in Optical Mass Data Storage II, R. P. Freese, A. A. Jamberdino and M. de Haan, eds. Proc. Soc. Photo-Opt. Instrum. Eng. 262-269 (1986).

[2] A. B. Marchant, "Retardation effects in magneto-optic readout," in Optical Mass Data Storage II, R. P. Freese, A. A. Jamberdino and M. de Haan, eds. Proc. Soc. Photo-Opt. Instrum. Eng. 270-276 (1986).

[3] W. A. Challener and T. A. Rinehart, "Jones matrix analysis of magneto-optical media and read-back systems," Appl. Opt. 26, 3974-3980 (1987).

[4] T. Toda, K. Shigematsu, M. Ojima and M. Yoshihiro, "Analysis of signal-to-noise ratio in

magneto-optical disk using a polarization simulator," Electron. Commun. Jpn. Part 2, 72, 49-57 (1989).

[5] A. Yoshizawa and N. Matsubayashi, "Analysis of optical anisotropy of PC substrate for M-O disks and its effect on CNR," in Optical Mass Data Storage II, R. P. Freese, A. A. Jamberdino and M. de Haan, eds. Proc. Soc. Photo-Opt. Instrum. Eng. 91-98 (1986).

[6] W. Siebourg, H. Schmid, F. M. Rateike, S. Abders and U. Grigo, "Birefringence -- an important property of plastic substrates for magneto-optical storage disks," Polym. Eng. Sci. 30, 11133-1139 (1990).

[7] Ivan Prikryl, "Effect of disk birefringence on a differential magneto-optic readout," Appl. Opt. 31, 1853-1862 (1992).

[8] A. Takahashi, M. Mieda, Y. Murakami, K. Ohta and H. Yamaoka, "Influence of birefringence on the signal quality of magneto-optical disks using polycarbonate substrates," Appl. Opt. 27, 2863-2866.

[9] S. Shirouzu, K. Shigematsu, S. Sakamoto, T. Nakagawa and S. Tagami, "Refractive index ellipsiods of a polycarbonate magneto-optical memory disk substrate," Jpn. J. Appl. Phys. 28, 797-800 (1989).

[10] J. E. Hayden and S. D. Jacobs, "Automated spatially scanning ellipsometer for retardation measurements of transparent materials," to appear in Appl. Opt. (1993).

[11] A. Skumanich, "Substrate birefringence in coated optical storage disks," to appear in J. Magn. Soc. Jpn. 17, S1 (1993).

[12] M. Mansuripur, "Analysis of multilayer thin-film structures containing magneto-optic and anisotropic media at oblique incidence using 2 × 2 matrices," J. Appl. Phys. 67, 6466-6475

(1990).

[13] J.D. Jackson, Classical Electrodynamics, 2nd Ed., John Wiley & Sins, New York (1975), p.281.

[14] M.V. Klein and T.E. Furtak, Optics, 2nd Ed., John Wiley & Sons, New York, (1986), p.84.

FIGURE CAPTIONS

FIG.1 The system setup for the variational-angle ellipsometer with wavelength λ = 632.8 nm (The VAE633 system).

FIG.2 (a) The system setup for the variation-angle ellipsometer with wavelength λ = 780 nm (The VAE780 system). (b) The hemisphere setup in transmission mode. (c) The hemisphere setup in reflection mode.

FIG.3 (a) Definition of the incident polarization angle ψ_{pol}. (b) The polarization ellipse of the reflected beam is characterized by θ_{axis} and ε. The sign of ε is "-" for LEP and "+" for REP. (c) and (d): Polarization state of the beam after the QWP when the fast axis is aligned with the major axis.

FIG.4 (a) The quadrilayer structure of MO disk is used in fitting the data for coated substrate. (b) The in-plane principal axes are found rotated for some substrates, but the third one is always perpendicular.

FIG.5 The best fit for glass sample. (a) The medium is forced to be isotropic. (b) Birefringence is allowed. Data were taken with VAE633. The small fluctuations appearing in the calculated curves are due to the interference of beams reflected at the front and the back surfaces of the sample.

FIG.6 The best fit for sample PC3.5B01 measured with (a) ψ_{pol} = 30°, (b)ψ_{pol} = 60°. The discontinuity at Θ_{inc} = 22° in (a) is explained in the text. The jumps at Θ_{inc} = 27° and 39° are not physical, since ±90° stand for the same polarization plane. Data were taken with VAE633. To obtain good match for bare substrates, we found the incident plane must be perpendicular to the track direction (Φ_{inc} = 0°).

FIG.7 The exchange of major axis and minor axis causes a discontinuity of 90° in θ when ε = 45°.

FIG.8 Measured data and the best fit for Sample PC3.5B02. Data were measured with VAE780 in the transmission mode.

FIG.9 Measured data and the best fit for Sample APO5.25B01. Data was taken with VAE633. The fluctuations of the calculated curves are due to the interference between beams reflected from the front and back surfaces of the substrate.

Fig.10 Measured data and the best fit for Sample PC5.25B01. Data were measured with VAE780 in the transmission mode.

FIG.11 Measured data and the best fit for Sample PC5.25B02. The measured point locates in a region without grooves. The polarization angle is (a) ψ_{pol} = 30°, (b) ψ_{pol} = 45°, (c) ψ_{pol} = 60°. No match has been found for Θ_{inc} ≥ 54° (not shown).

FIG.12 Measured data and the best fit for Sample PC3.5C01. The data were measured at Φ_{inc} = 90° and ψ_{pol} = 60° with VAE633. In contrast to bare substrate, we found that, for coated substrates, good match can only be achieved with Φ_{inc} = 90°.

FIG.13 Measured data and the best fit for Sample PC5.25C01. The data were measured at Φ_{inc}

= 90° with VAE633. (a) ψ_{pol} = 45°, (b) ψ_{pol} = 60°.

FIG.14 Comparison of measured data for 4 points at different sectors of Sample PC5.25C02. Solid curves are for sector 1; dashed for sector 2; dotted for sector 3 and dash-dotted for sector 4. The data were taken with VAE633 at Φ_{inc} = 90° and ψ_{pol} = 60°. (a) Rotation angle θ, (b) Ellipticity ε.

FIG.15 Comparison of measured data for the same position at PC5.25C02 (solid lines) and PC5.25C03 (dashed lines). The data are almost the same for $\Theta_{inc} \leq 45°$. This shows the birefringent property in the two samples is very close.

TABLE 1

Summary of measurement results.

Sample	λ	$\psi_{in\text{-}plane}$	n_1	n_1-n_2	n_1-n_3	$d(n_1-n_2)$	$d(n_1-n_3)$	Fitting error
glass slide	633 nm	-9.2°	1.54	0.6×10^{-5}	-1×10^{-6}	7.3 nm	-1.2 nm	0.80°
PC3.5B01	633 nm	-5.3°	1.58	1.3×10^{-5}	5.87×10^{-4}	15.3 nm	704.5 nm	1.73°
PC3.5B02	633 nm	-50.3°	1.58	0.5×10^{-5}	6.26×10^{-4}	5.85 nm	751.4 nm	3.78°
PC3.5B02	780 nm	56.7°	1.58	1.9×10^{-5}	5.83×10^{-4}	22.8 nm	699.6 nm	2.72°
APO5.25B01	633 nm	-72.5°	1.50	0.4×10^{-5}	1.3×10^{-5}	4.8 nm	15.6 nm	0.96°
PC5.25B01	780 nm	66°	1.58	1.3×10^{-5}	6.22×10^{-4}	15.6 nm	746.4 nm	2.96°
PC5.25B02	633 nm	1.6°	1.58	2.2×10^{-5}	5.83×10^{-4}	26.3 nm	699.4 nm	4.67°
PC3.5C01	633 nm	-2.9°	1.58	2.3×10^{-5}	5.34×10^{-4}	27.1 nm	640.9 nm	2.97°
PC3.5C02	633 nm	-6.5°	1.58	2×10^{-5}	5.51×10^{-4}	23.9 nm	661.3 nm	7.17°
PC5.25C01	633 nm	8°	1.58	0.9×10^{-5}	4.61×10^{-4}	11.3 nm	552.6 nm	1.66°
PC5.25C02	633 nm	-18°	1.58	0.7×10^{-5}	3.37×10^{-4}	7.9 nm	404.6 nm	3.6°
PC5.25C03	633 nm	11.5°	1.58	1.9×10^{-5}	3.47×10^{-4}	15.6 nm	406.8 nm	6.6°

The VAE633 System

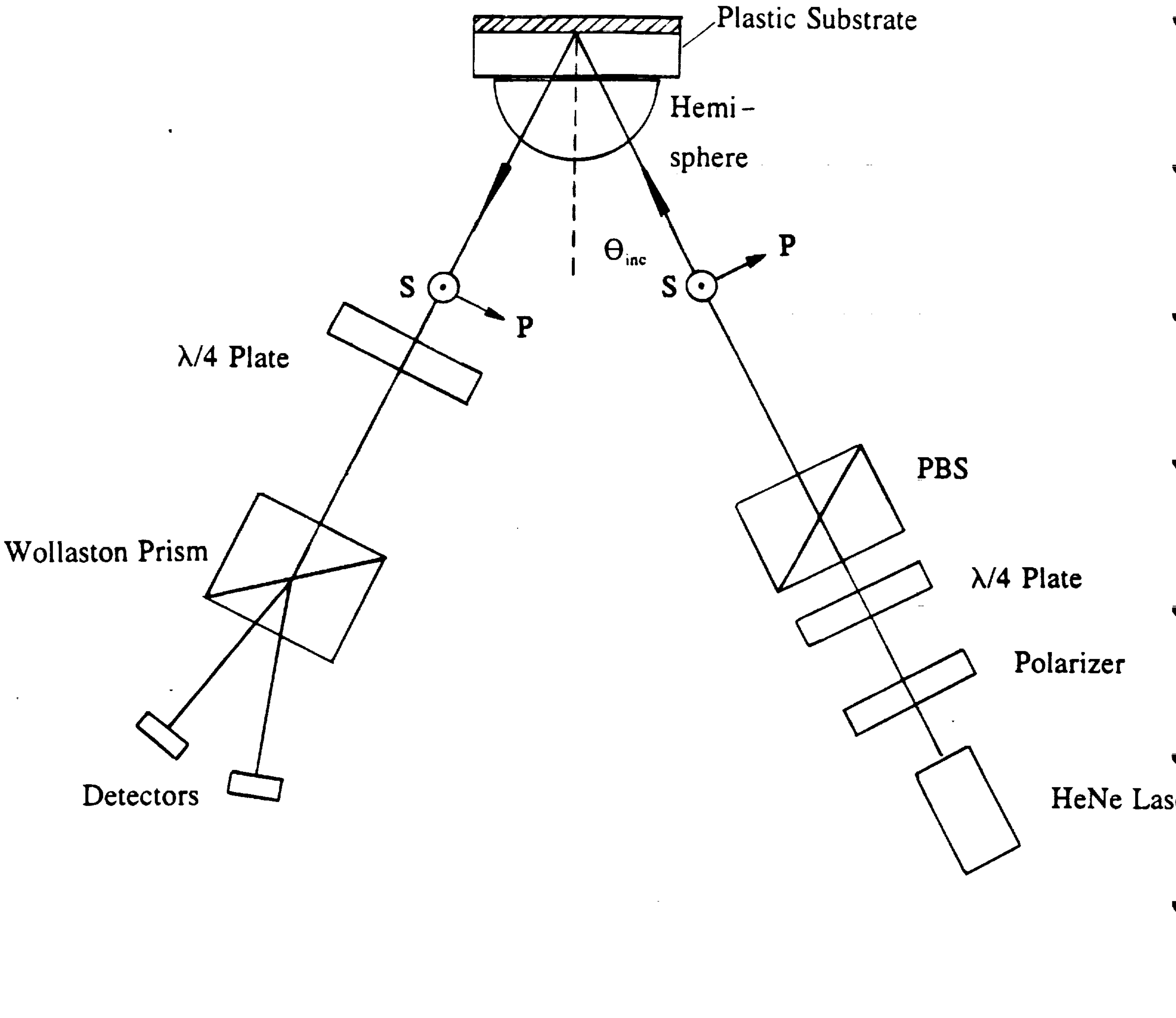

FIG.1

The VAE780 System

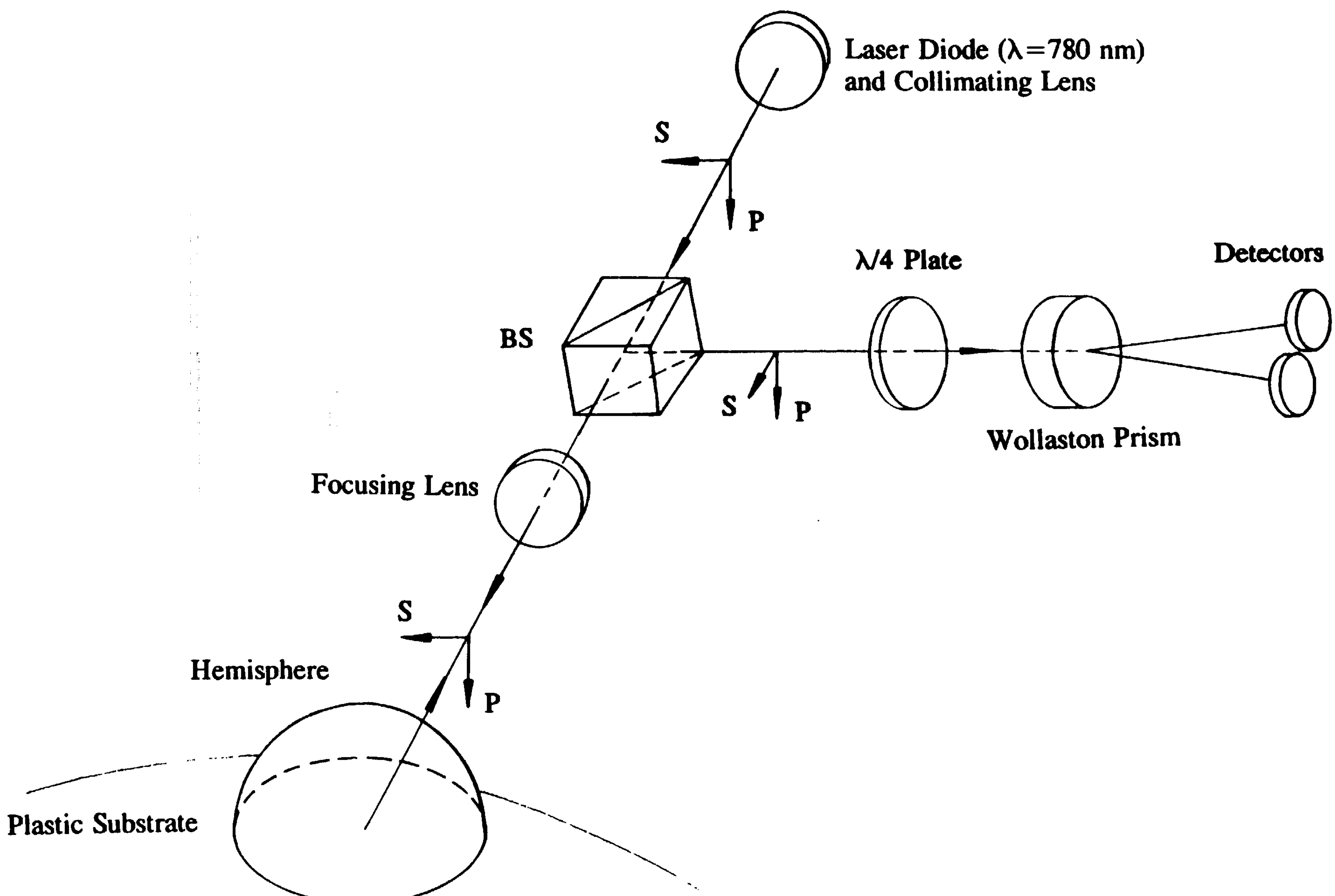

FIG.2(a)

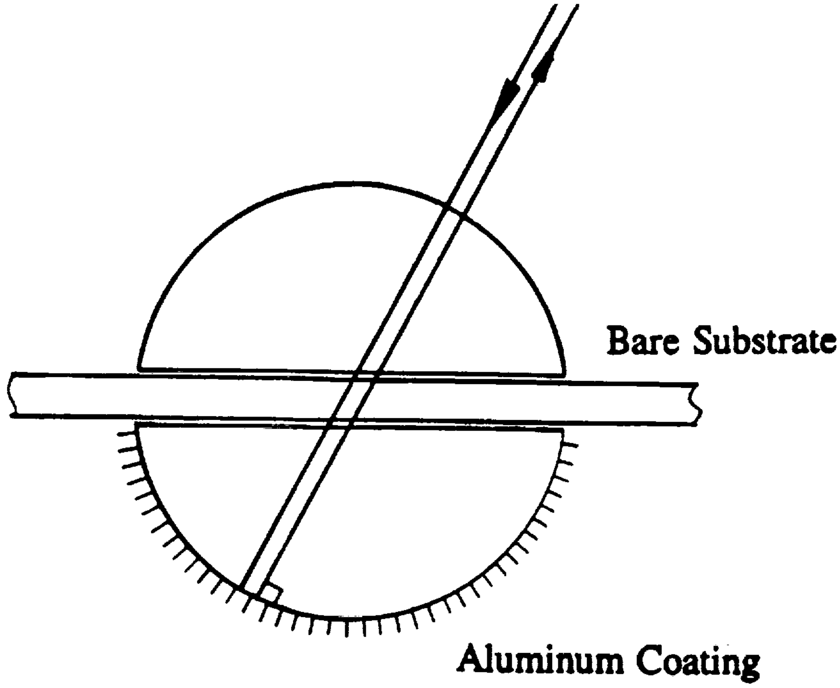
Bare Substrate
Aluminum Coating

FIG.2(b)

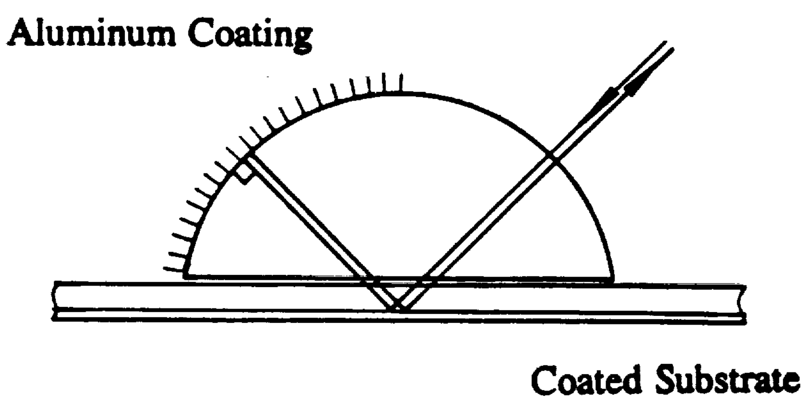
Aluminum Coating
Coated Substrate

FIG.2(c)

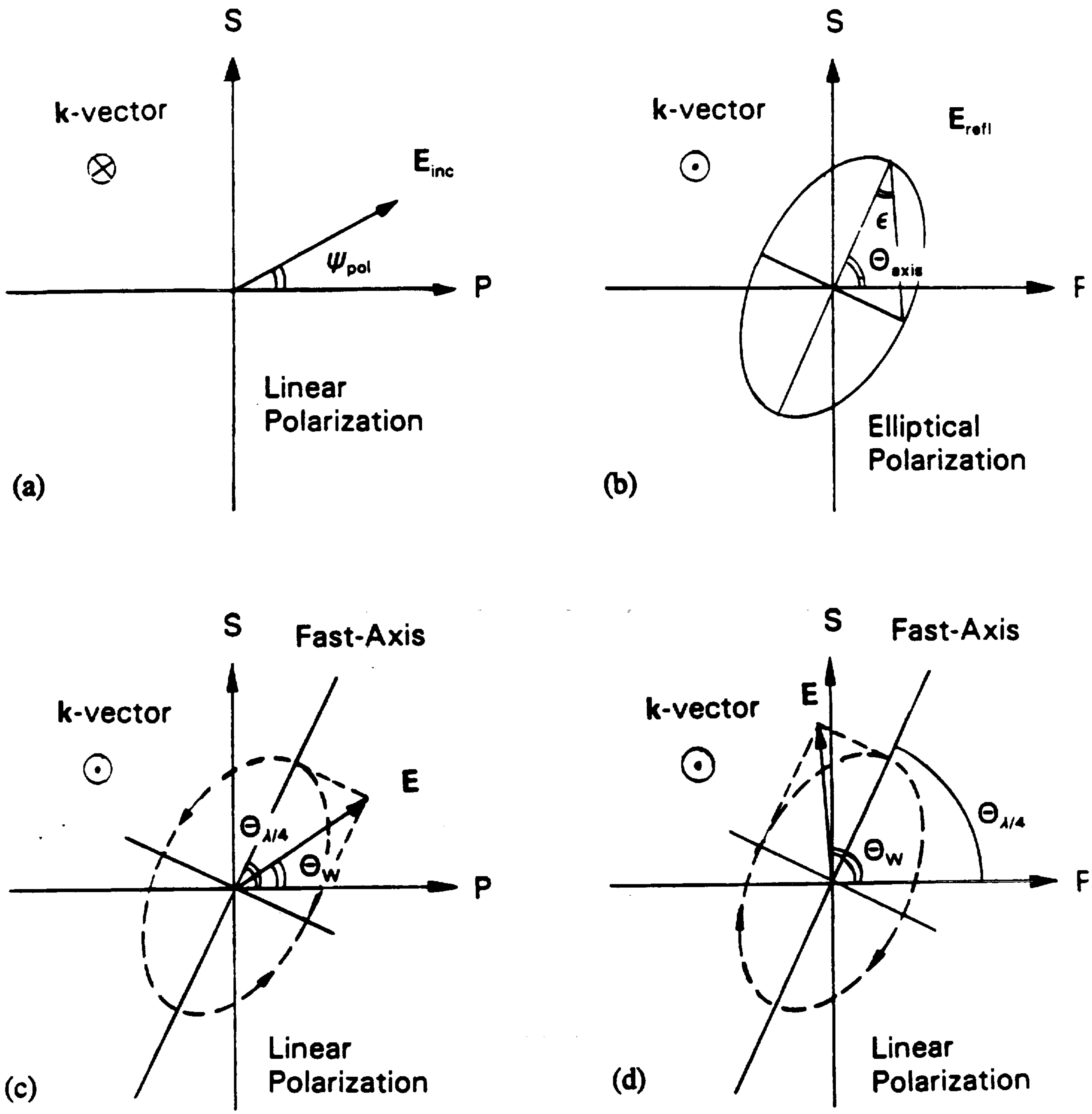

LEP: $\epsilon = \Theta_W - \Theta_{axis} < 0$

REP: $\epsilon = \Theta_W - \Theta_{axis} > 0$

FIG.3

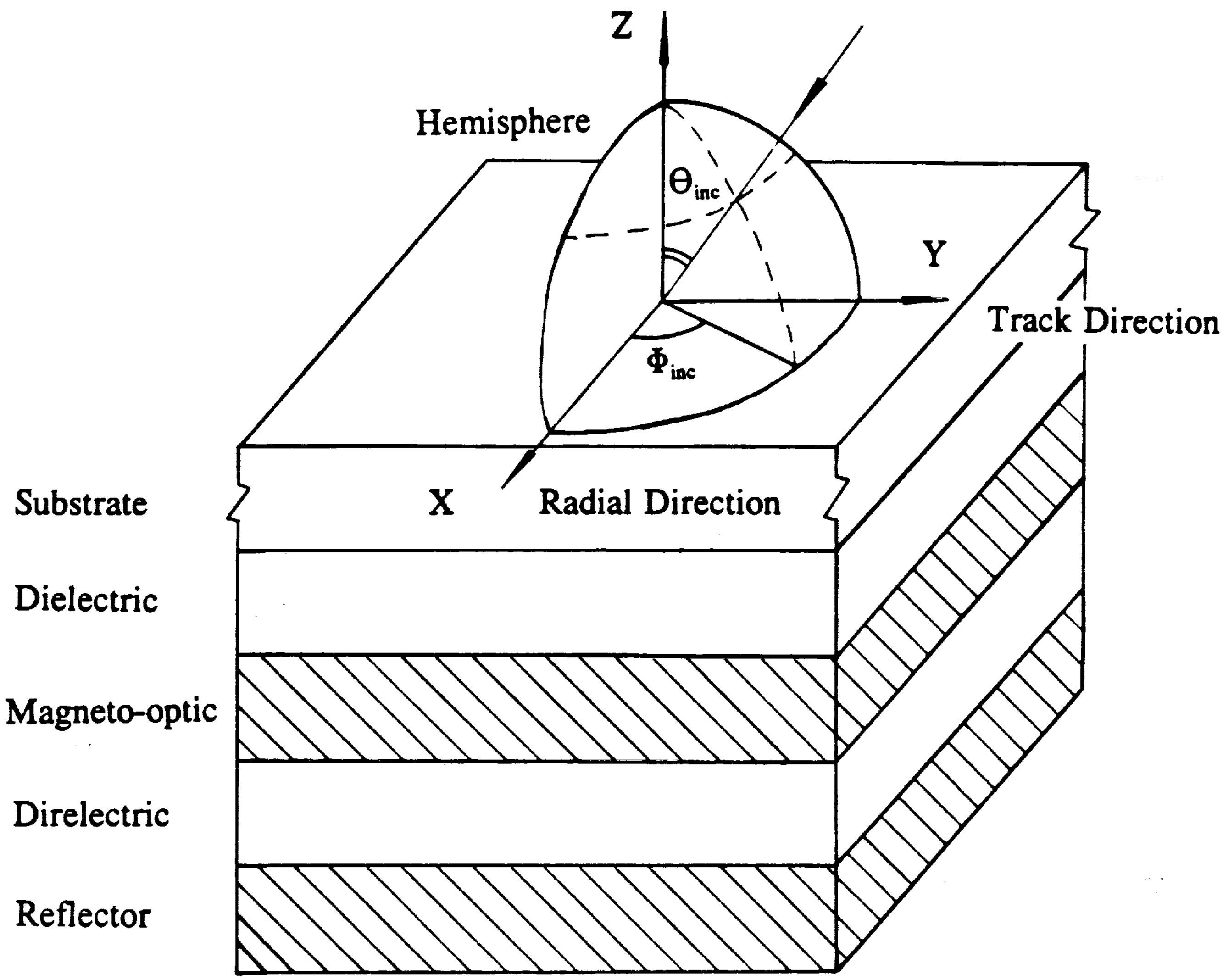
Z
Hemisphere
Θ_{inc}
Y
Track Direction
Φ_{inc}
Substrate
X
Radial Direction
Dielectric
Magneto-optic
Direlectric
Reflector

FIG.4 (a)

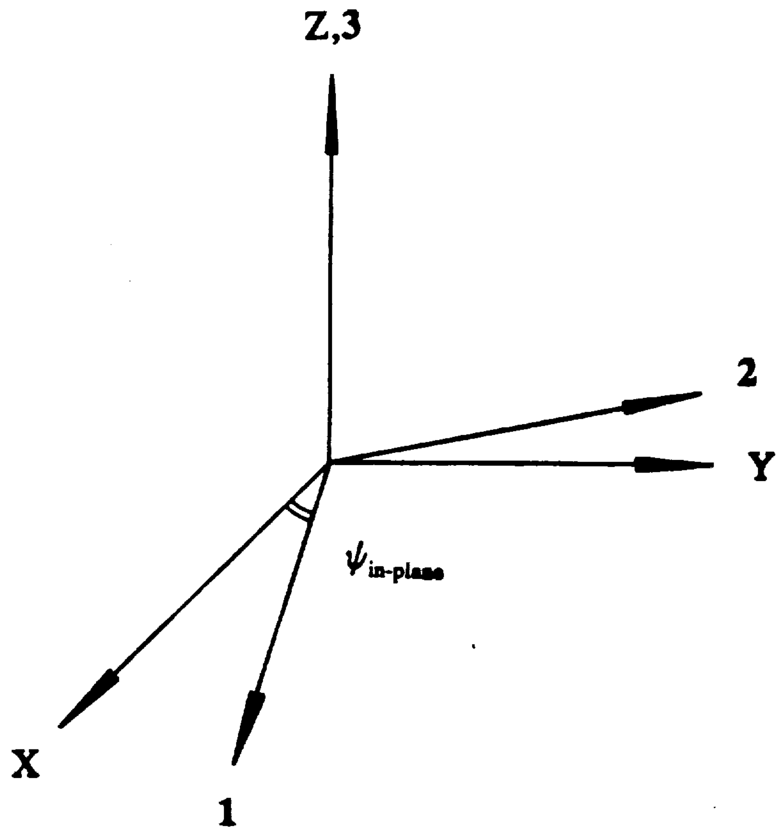

FIG.4 (b)

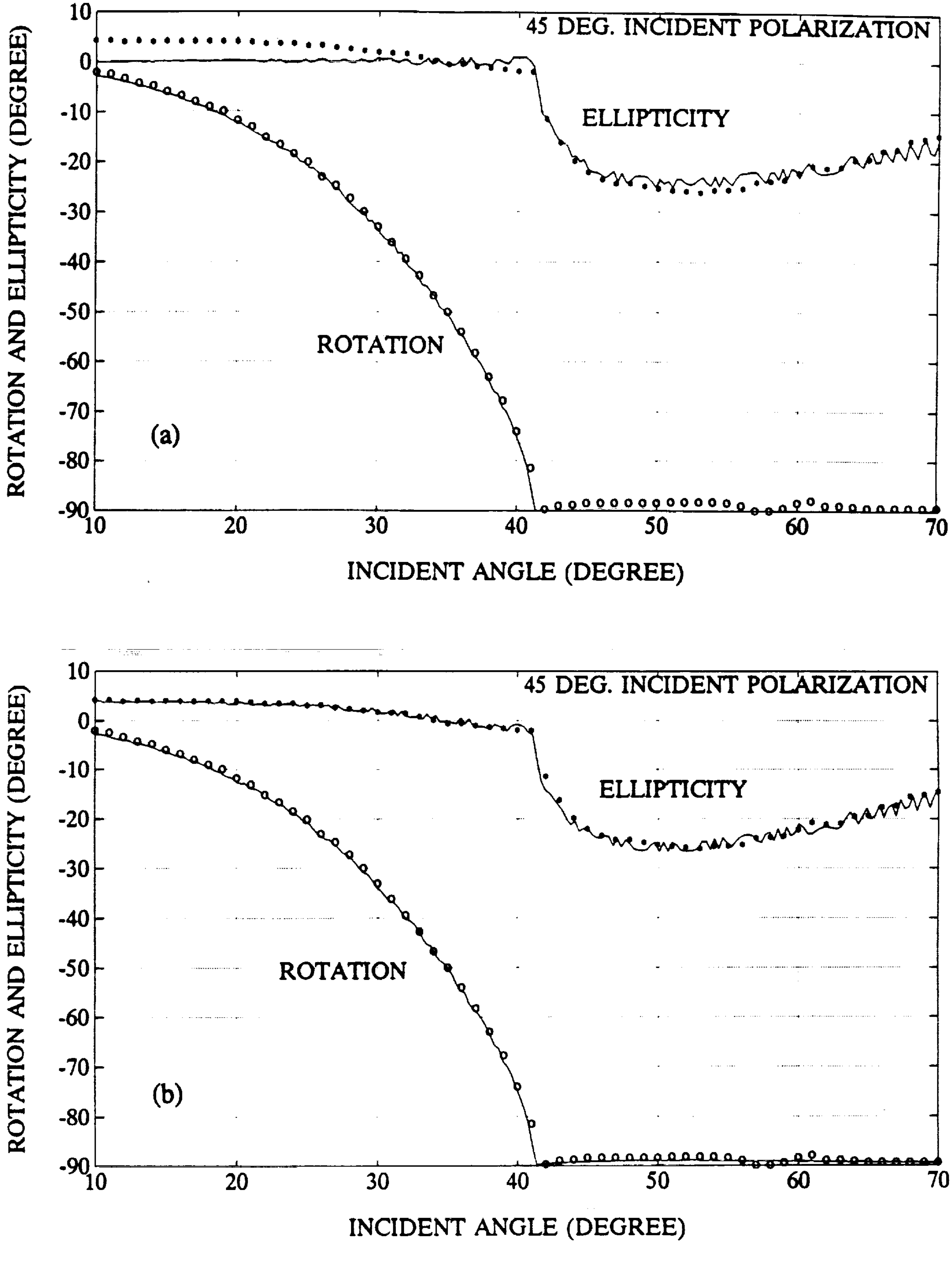

10
0
-10
-20
-30
-40
-50
-60
-70
-80
-90
10
20
30
40
50
60
70
ROTATION AND ELLIPTICITY (DEGREE)
INCIDENT ANGLE (DEGREE)
45 DEG. INCIDENT POLARIZATION
ELLIPTICITY
ROTATION
(a)
45 DEG. INCIDENT POLARIZATION
ELLIPTICITY
ROTATION
(b)

FIG.5

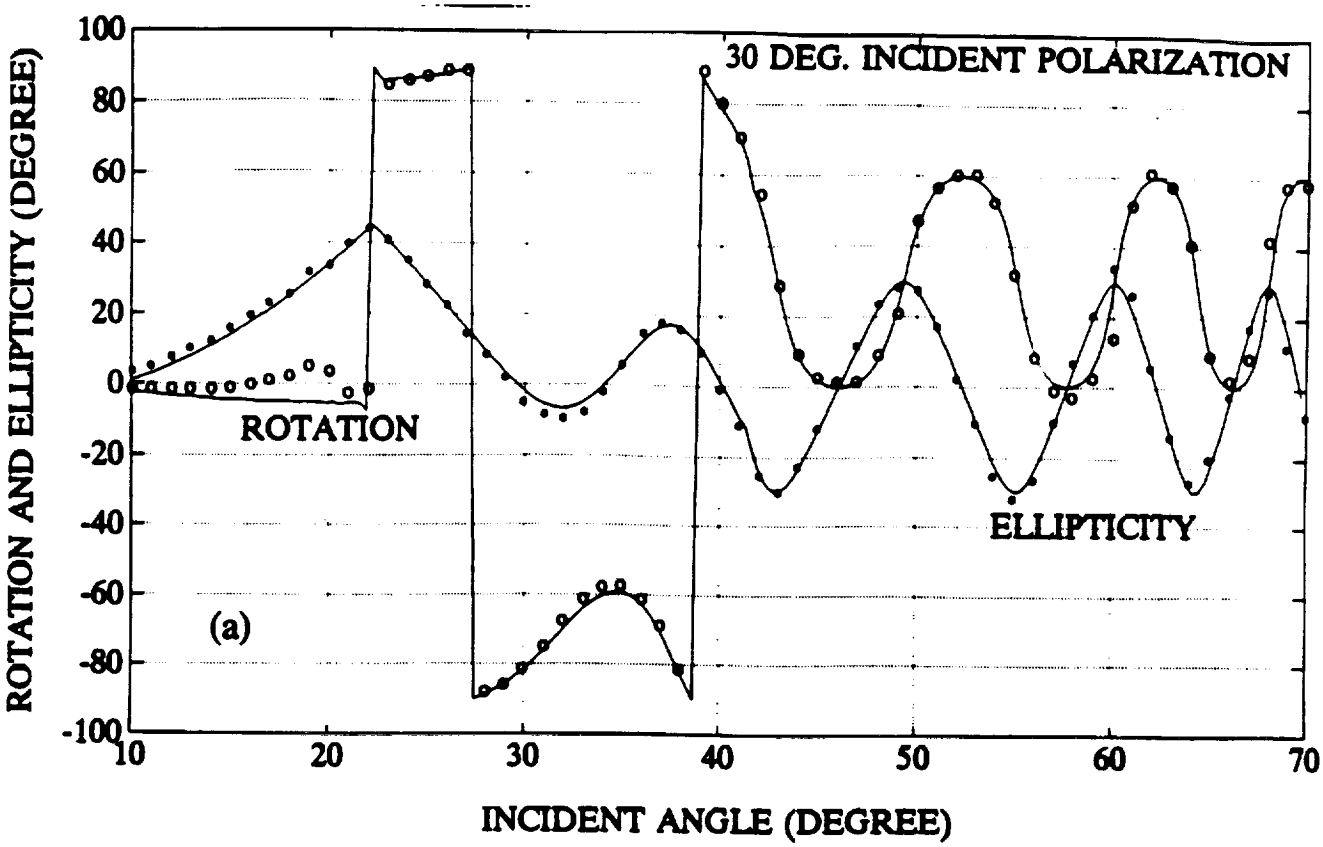

30 DEG. INCIDENT POLARIZATION
ROTATION
ELLIPTICITY
(a)
ROTATION AND ELLIPTICITY (DEGREE)
INCIDENT ANGLE (DEGREE)

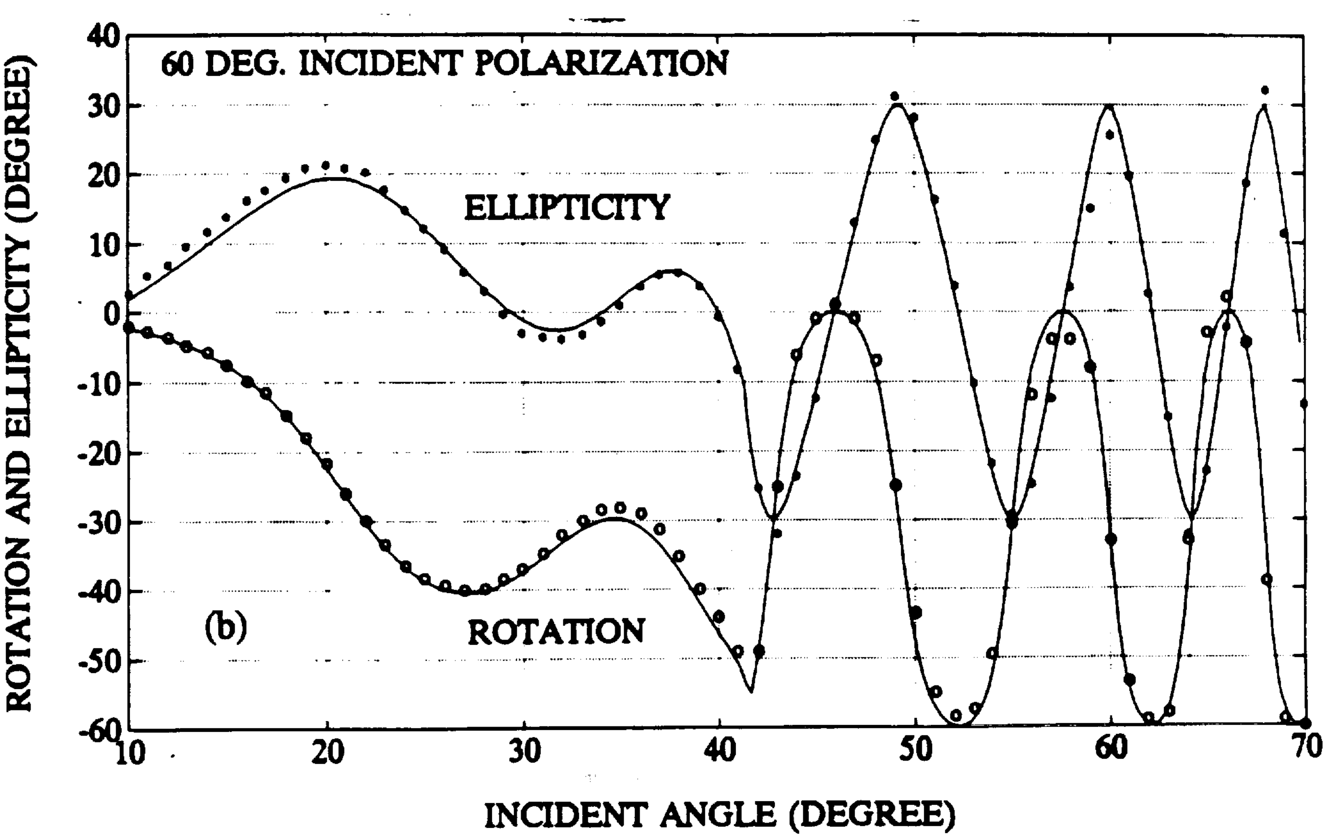

60 DEG. INCIDENT POLARIZATION
ELLIPTICITY
ROTATION
(b)
ROTATION AND ELLIPTICITY (DEGREE)
INCIDENT ANGLE (DEGREE)

FIG.6

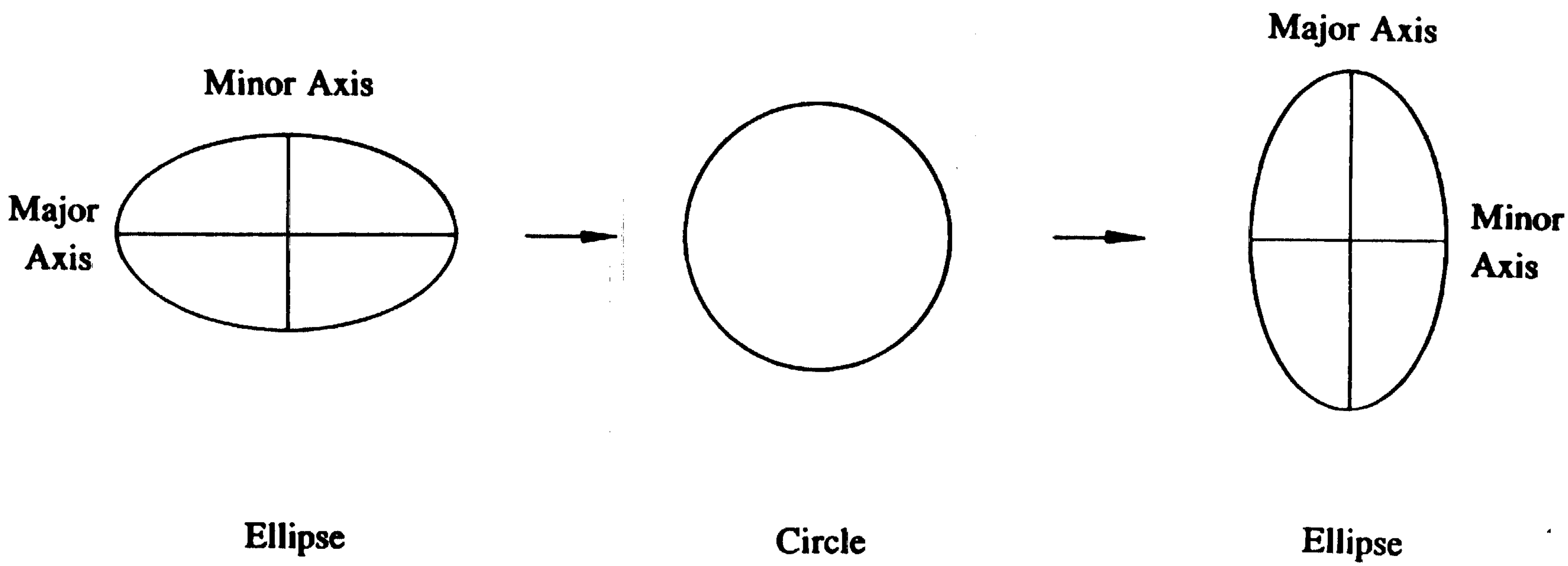
Minor Axis
Major
Axis
Ellipse
Circle
Major Axis
Minor
Axis
Ellipse

FIG.7

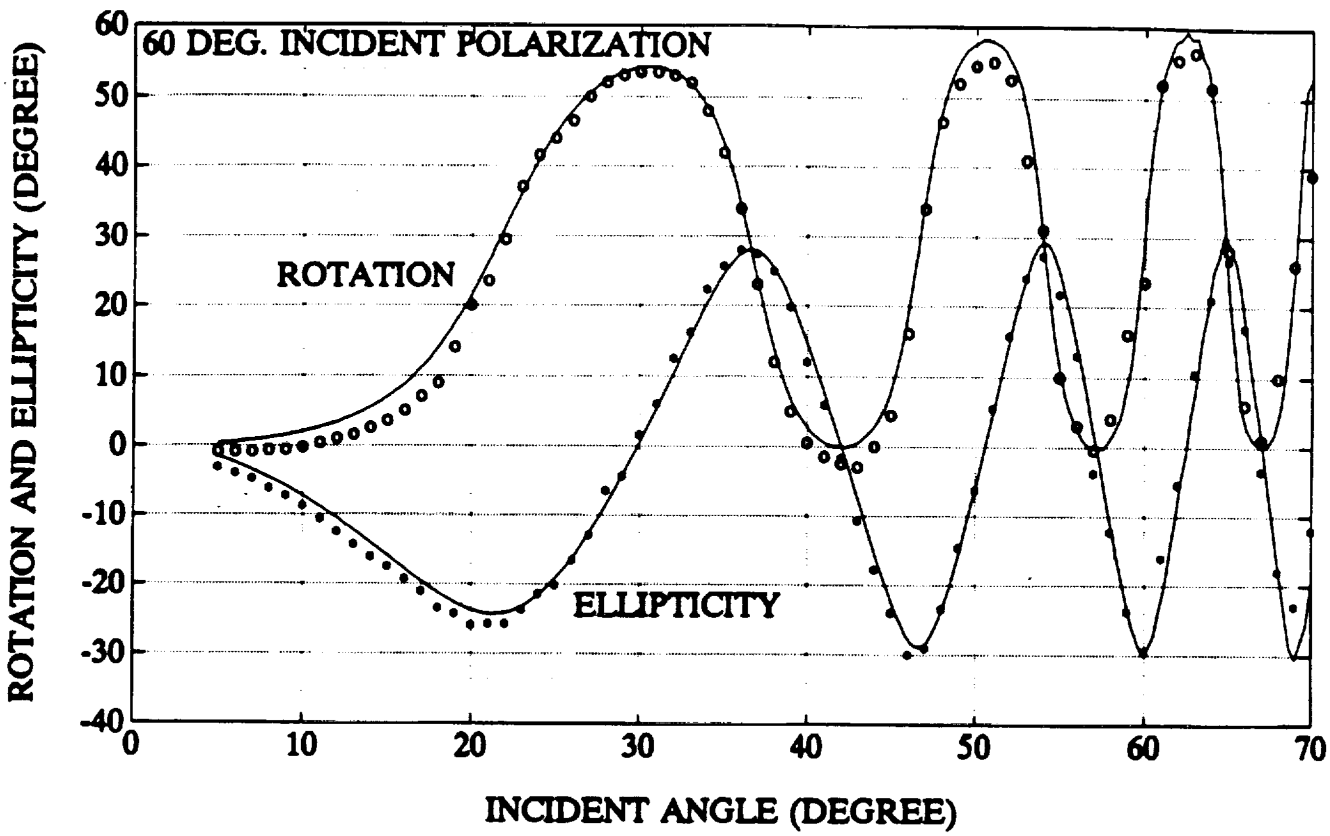
60 DEG. INCIDENT POLARIZATION
ROTATION
ELLIPTICITY
ROTATION AND ELLIPTICITY (DEGREE)
INCIDENT ANGLE (DEGREE)
60
50
40
30
20
10
0
-10
-20
-30
-40
0
10
20
30
40
50
60
70

FIG.8

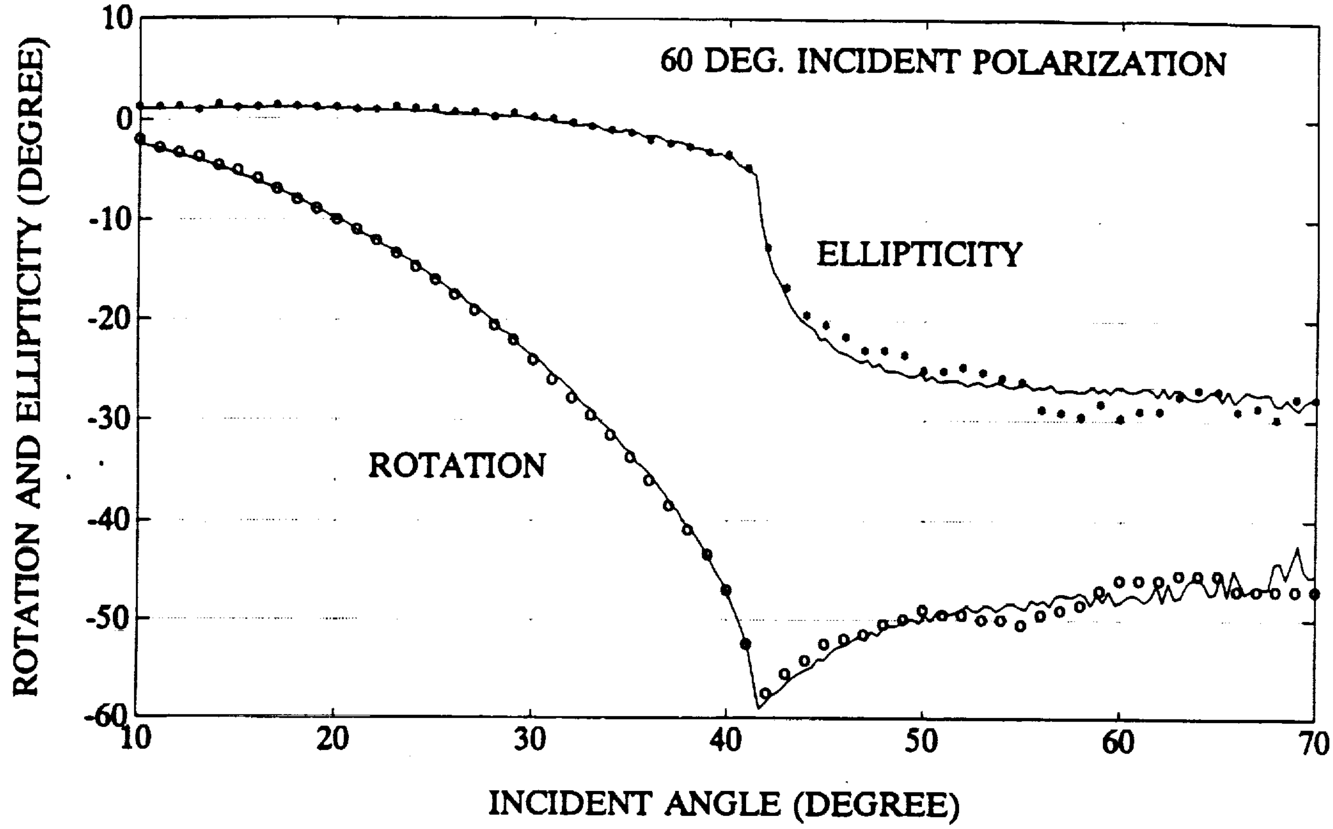
60 DEG. INCIDENT POLARIZATION
ELLIPTICITY
ROTATION
ROTATION AND ELLIPTICITY (DEGREE)
INCIDENT ANGLE (DEGREE)
10
0
-10
-20
-30
-40
-50
-60
10
20
30
40
50
60
70

FIG.9

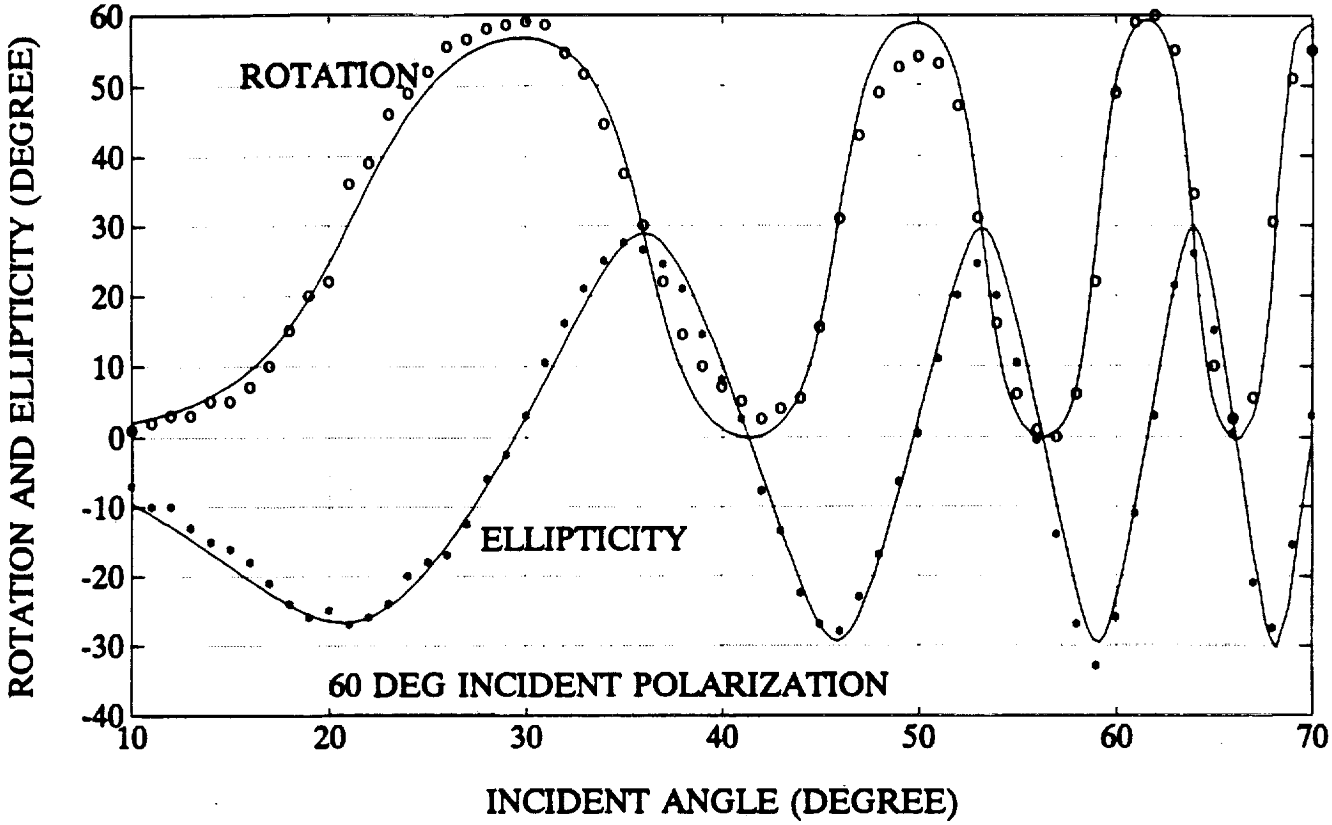
ROTATION
ELLIPTICITY
60 DEG INCIDENT POLARIZATION
ROTATION AND ELLIPTICITY (DEGREE)
INCIDENT ANGLE (DEGREE)
60
50
40
30
20
10
0
-10
-20
-30
-40
10
20
30
40
50
60
70

FIG.10

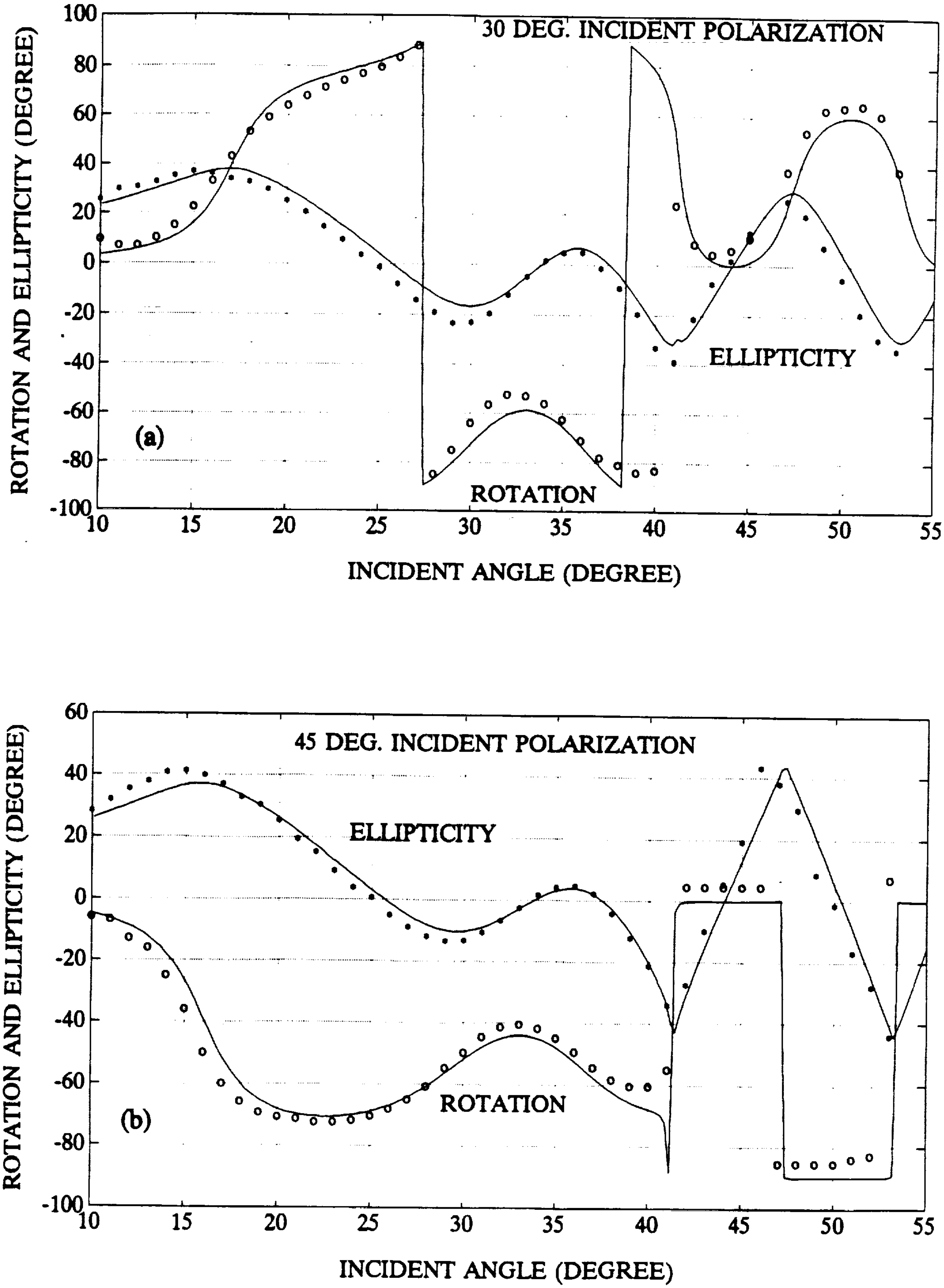
30 DEG. INCIDENT POLARIZATION
ROTATION AND ELLIPTICITY (DEGREE)
ELLIPTICITY
ROTATION
(a)
INCIDENT ANGLE (DEGREE)
45 DEG. INCIDENT POLARIZATION
ROTATION AND ELLIPTICITY (DEGREE)
ELLIPTICITY
ROTATION
(b)
INCIDENT ANGLE (DEGREE)

FIG.11

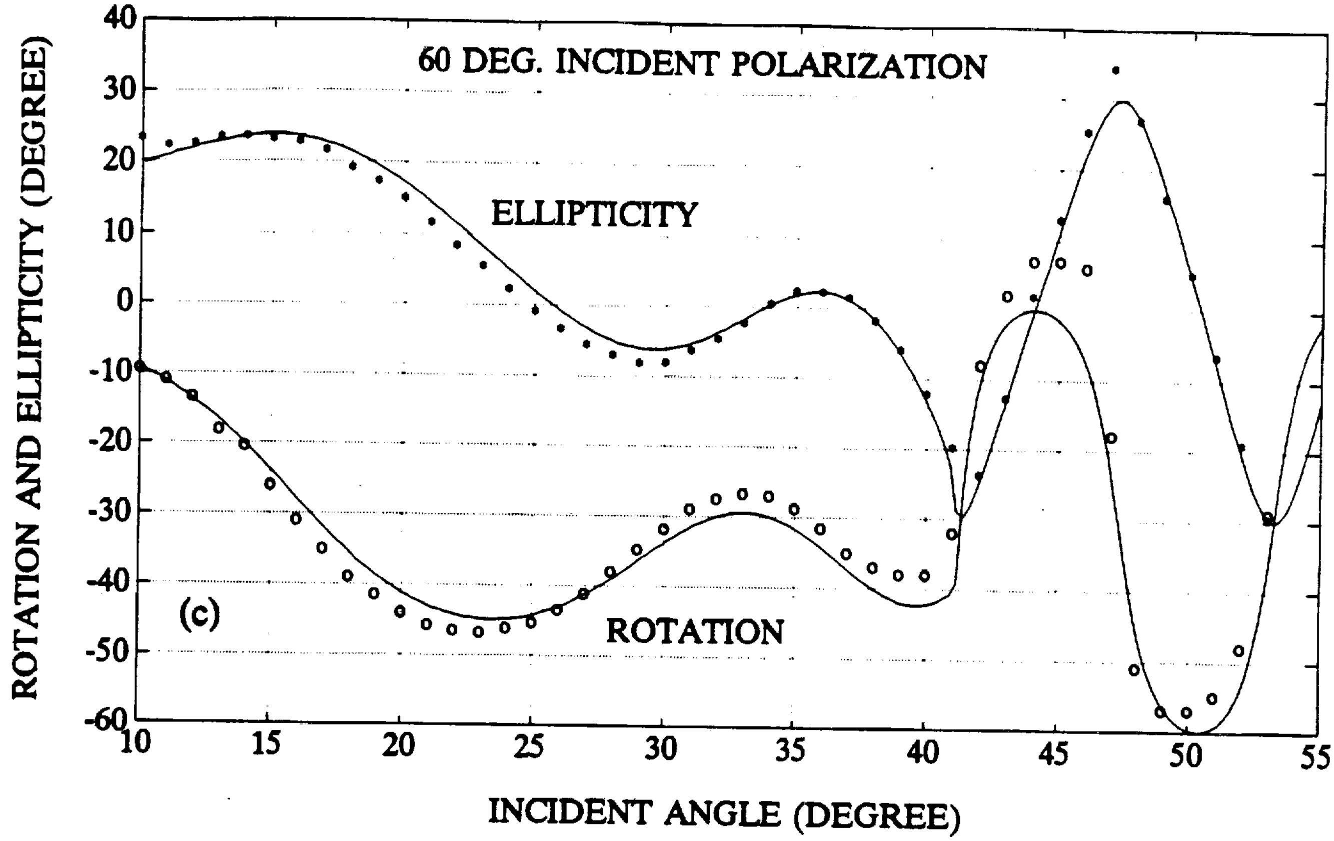

60 DEG. INCIDENT POLARIZATION
ELLIPTICITY
ROTATION
(c)
ROTATION AND ELLIPTICITY (DEGREE)
INCIDENT ANGLE (DEGREE)
40
30
20
10
0
-10
-20
-30
-40
-50
-60
10
15
20
25
30
35
40
45
50
55

FIG.11

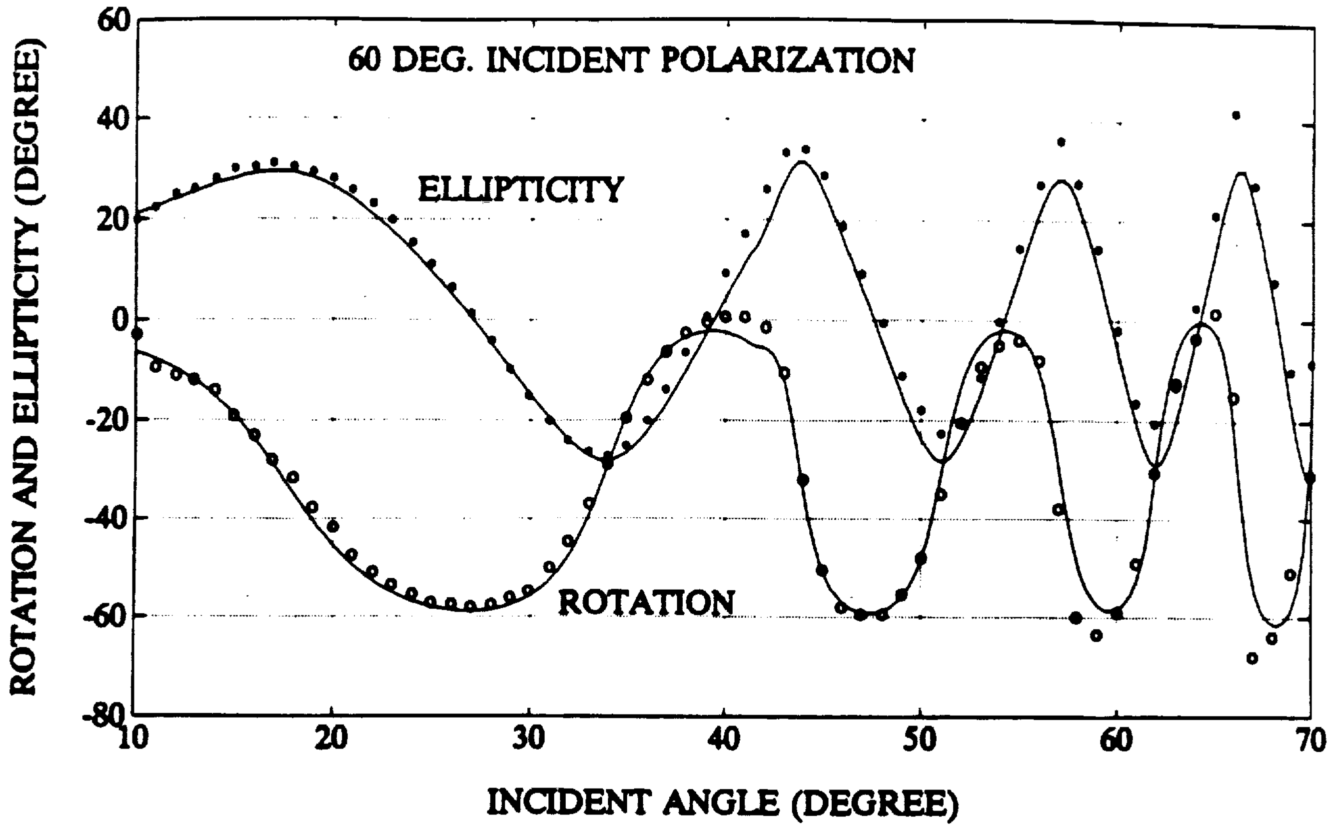
60 DEG. INCIDENT POLARIZATION
ELLIPTICITY
ROTATION
ROTATION AND ELLIPTICITY (DEGREE)
INCIDENT ANGLE (DEGREE)
60
40
20
0
-20
-40
-60
-80
10
20
30
40
50
60
70

FIG.12

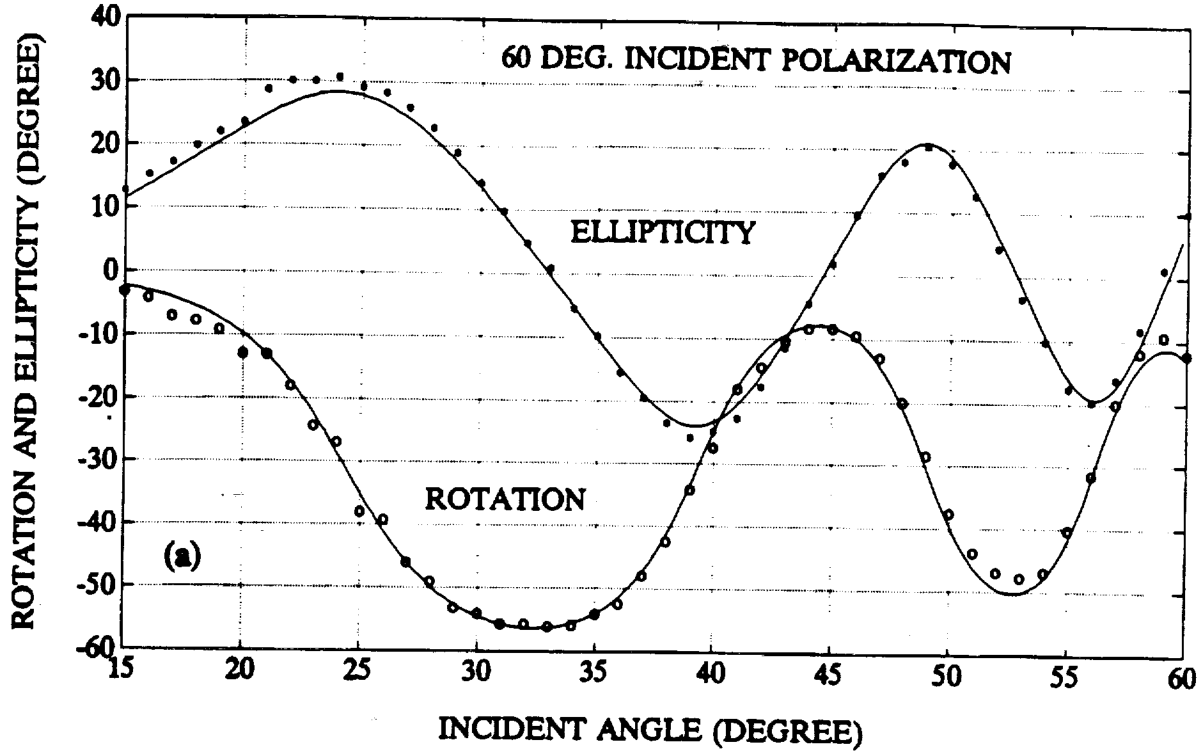
60 DEG. INCIDENT POLARIZATION
ELLIPTICITY
ROTATION
(a)
ROTATION AND ELLIPTICITY (DEGREE)
INCIDENT ANGLE (DEGREE)
40
30
20
10
0
-10
-20
-30
-40
-50
-60
15
20
25
30
35
40
45
50
55
60

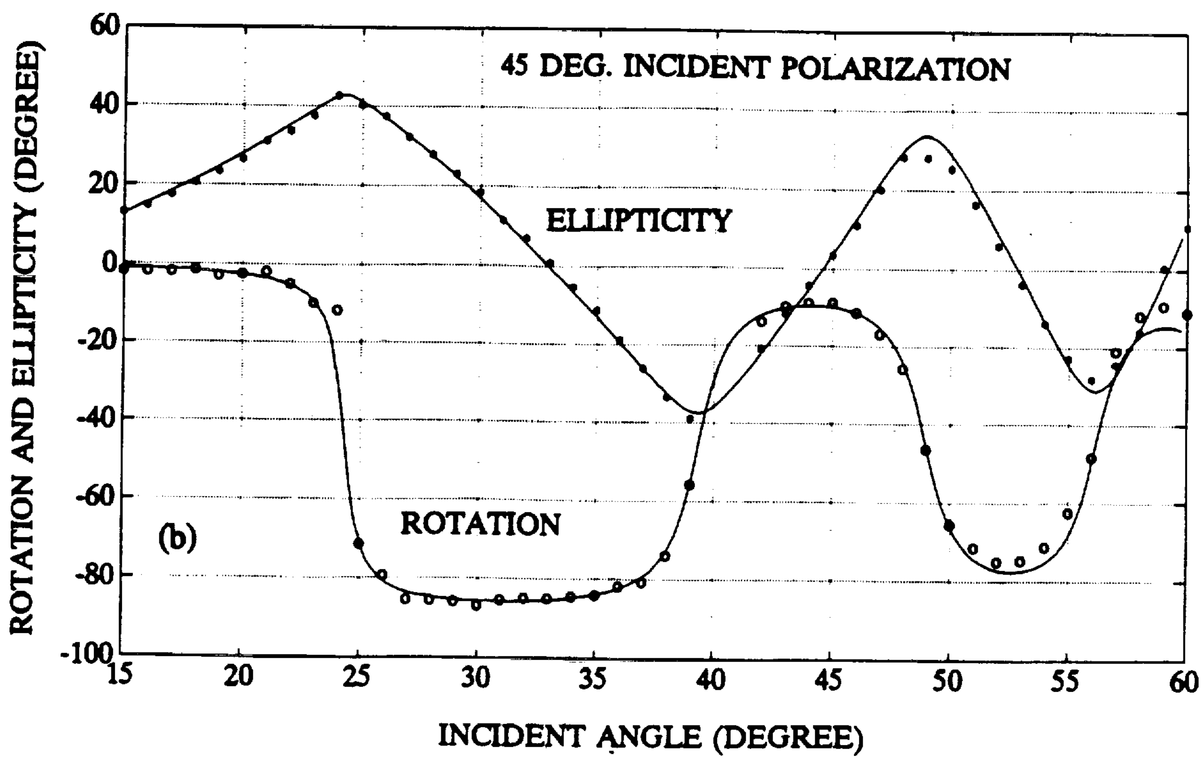
45 DEG. INCIDENT POLARIZATION
ELLIPTICITY
ROTATION
(b)
ROTATION AND ELLIPTICITY (DEGREE)
INCIDENT ANGLE (DEGREE)
60
40
20
0
-20
-40
-60
-80
-100
15
20
25
30
35
40
45
50
55
60

FIG.13

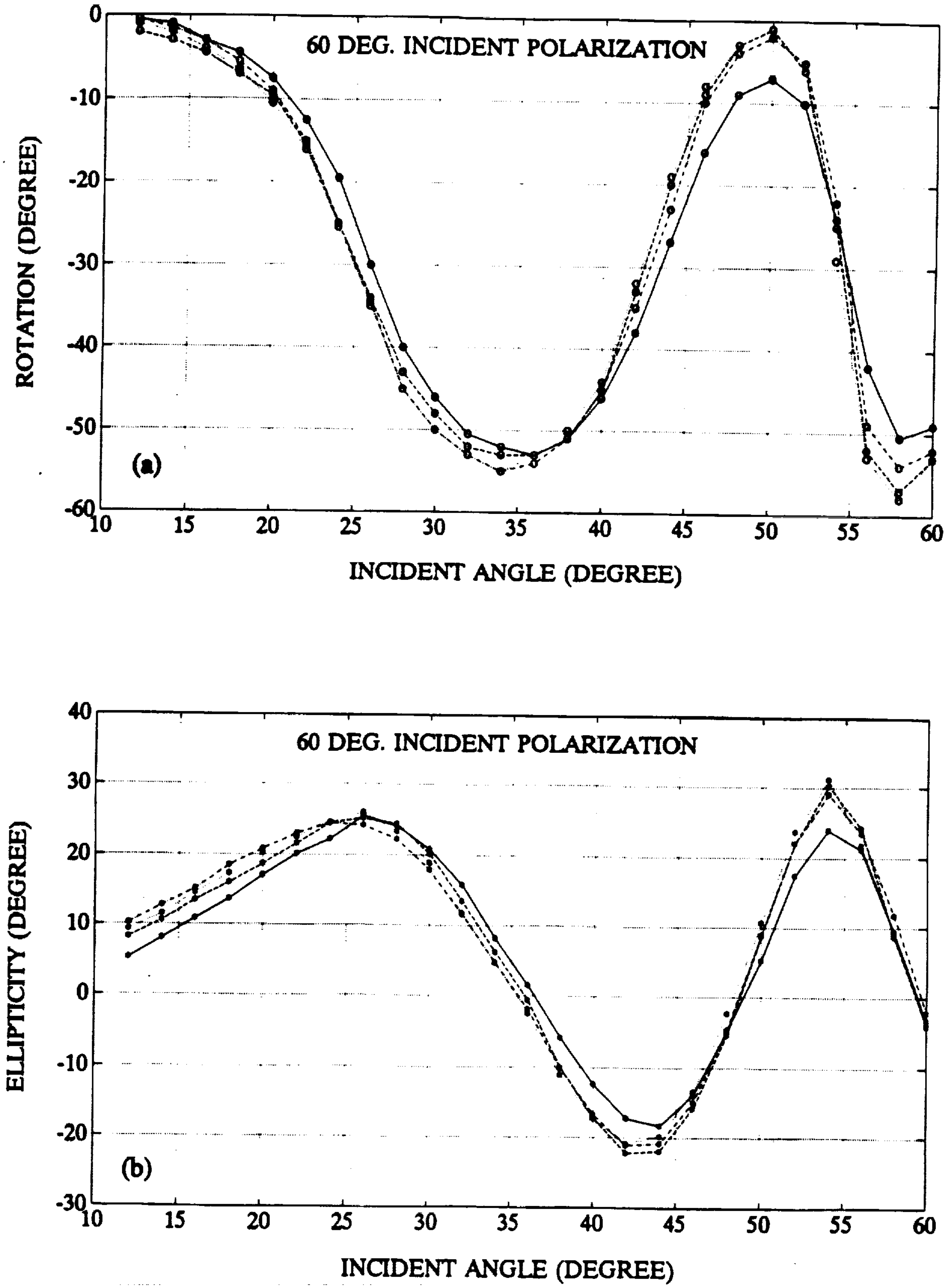

60 DEG. INCIDENT POLARIZATION
ROTATION (DEGREE)
INCIDENT ANGLE (DEGREE)
(a)
0
-10
-20
-30
-40
-50
-60
10
15
20
25
30
35
40
45
50
55
60
60 DEG. INCIDENT POLARIZATION
ELLIPTICITY (DEGREE)
INCIDENT ANGLE (DEGREE)
(b)
40
30
20
10
0
-10
-20
-30
10
15
20
25
30
35
40
45
50
55
60

FIG.14

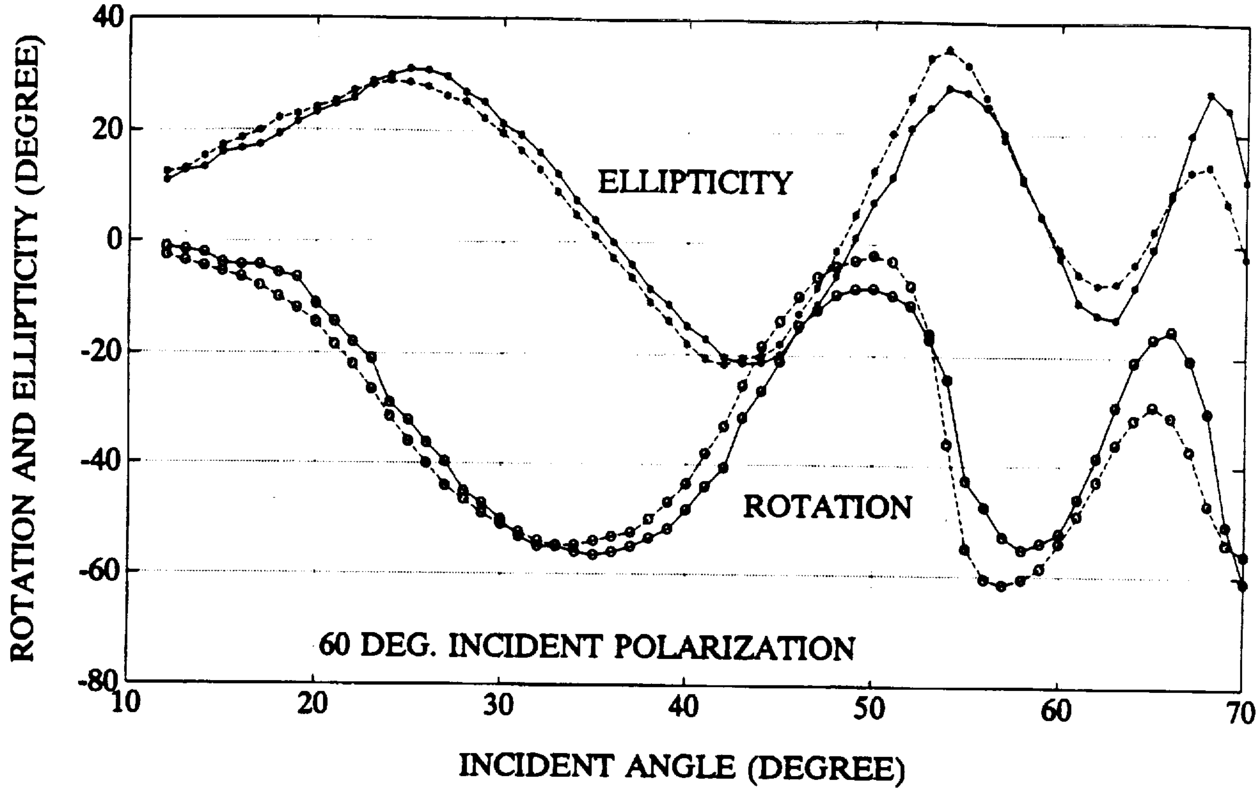

ROTATION AND ELLIPTICITY (DEGREE)
40
20
0
-20
-40
-60
-80
10
20
30
40
50
60
70
ELLIPTICITY
ROTATION
60 DEG. INCIDENT POLARIZATION
INCIDENT ANGLE (DEGREE)

FIG.15

APPENDIX B

PRECEDING PAGE BLANK NOT FILMED

N94-14990

Ring Lens Focusing and Push-Pull Tracking Scheme for Optical Disk Systems

R. Gerber, J. Zambuto, J.K. Erwin, and M. Mansuripur
Optical Sciences Center, University of Arizona, Tucson, Arizona 85721

Abstract

An experimental comparison of the ring lens and the astigmatic techniques of generating focus-error-signal (FES) in optical disk systems reveals that the ring lens generates a FES over two times steeper than that produced by the astigmat. Partly due to this large slope and, in part, because of its diffraction-limited behavior, the ring lens scheme exhibits superior performance characteristics. In particular the undesirable signal known as "feedthrough" (induced on the FES by track-crossings during the seek operation) is lower by a factor of six compared to that observed with the astigmatic method. The ring lens is easy to align and has reasonable tolerance for positioning errors.

Introduction : The ring lens technique of focus error detection and its combination with push-pull tracking was proposed in an earlier paper [1]. Later, based on diffraction calculations, the ring lens was predicted to have superior characteristics over other methods of focus-error detection [2,3]. This superiority stems from the fact that the ring lens produces a large, yet diffraction-limited image at the detector, has circular symmetry which simplifies alignment procedures, and allows focus- and track-error signals as well as data signals to be detected in the same channel. This paper reports the experimental verification of some of the above predictions; in particular, we report that the ring lens produces a steeper FES and has significantly lower feedthrough (i.e., focus error signal generated when moving across tracks) than the astigmatic technique. In the sections that follow we describe a method that has been used successfully to fabricate the ring lens, describe our static testbed for making measurements of the focus- and track-error signals, present the results of these measurements for a ring lens, and compare the results with those obtained for the astigmatic scheme.

Ring Lens Fabrication : The ring lens used in these experiments was formed on a soda-lime glass slide by a thermal process. Initially, a base plate of polished stainless steel with a circular groove carved on its flat surface was prepared. This plate was coated with a thin layer of black ink which serves as mold release agent, and then placed in contact with the glass slide. The assembly was heated in an oven to 735ºC for 2 minutes, then slowly cooled back to the room temperature. During heating, the softened glass sagged into the groove and formed a curved surface in the annulus defined by the groove. The glass slide was subsequently removed from the mold, cleaned, and without further polishing was used in the experiments.

Figure 1 shows various features of the fabricated ring lens. Dimensions of the lens are depicted in *Fig.*1(a) as follows : inner diameter = 2.03mm, outer diameter = 4.35mm, focused ring radius = 1.595mm. The unshaded annular region in the figure corresponds to the section of the lens that has been profiled by the WYKO Corporation's TOPO system and shown in *Fig.*1(b). A scanning electron micrograph of a section of the ring lens appears in (c), and an interferogram showing Newton rings for this lens is reproduced in (d).

It must be emphasized that although the thermal process described above yields reasonably good ring lenses, we do not consider it suitable for the fabrication of highly accurate, aberration-free lenses. Other shortcomings of this technique include the inability to produce lenses with very small ring radii, and also lack of any direct control over the focal length of the lens. Ideally, such lenses must be made by direct molding of glass or plastic, or by the fabrication methods of holographic optics or binary optics.

Testbed for Measurements of Focus/Track Error Signals : The system used to test the various focusing techniques is the static focusing/tracking testbed shown in Fig. 2. This system operates at two HeNe wavelengths (633 nm and 544 nm), and allows either of two linear polarizations (parallel and perpendicular to tracks) to be used for measurements. The paths of the red and green beams are coincident after their combination by the dichroic beamsplitter. The beams are then split into two beams of orthogonal polarizations and recombined by the polarizing beamsplitter. One can readily select a wavelength and a polarization direction by blocking the undesired paths on the testbed. The beam intensity may be controlled by a variable attenuator placed after the dichroic splitter.

After passing through a spatial filter and a collimating lens, the beam goes through a removable shear plate collimation tester, which can detect wavefront errors as low as 0.1λ. The beam emerging from the lens is fairly large in cross-section, and is stopped by a 5 mm diameter aperture. The collimated beam passes through a 50/50 beam-splitter cube which sends half of the light to the disk (or an immitation of the disk) and the other half to a plane mirror, which acts as the reference arm in a Twyman-Green interferometer. The reference arm is used to check the collimation of the beam returning from the disk, and is covered during focus/track error measurements.

In our experiments the grooved surface of an optical disk was simulated by a reflection diffraction grating, placed at the focal plane of a 40×, 0.55 NA, infinity-corrected microscope objective. The grating has 1.1 μm track-pitch, a sinusoidal profile, and peak-to-valley depth of 67 nm. The choice of grating instead of an actual grooved disk eliminates the problem of focusing through the substrate, which would unnecessarily complicate the measurements by introducing aberrations due to misalignment and birefringence. The use of grating also affords us more flexibility in selecting the numerical aperture of the objectives, which are generally not available in a wide variety for 1.2 mm cover slides. The position of the grating is controlled by low-voltage piezoelectric transducers (PZT), mounted in the actuators of an XYZ translation stage. A GPIB-controlled power supply can move the PZT's in 0.003 micron increments over a range of 12 microns.

The focusing/tracking optics are placed after the beam-splitter cube, and form an image on a CCD camera whose pixel spacing is 10 μm. The ring lens forms an image directly on the camera, while the spot formed by the astigmat is small and requires magnification. The image from the camera is fed into a frame-grabber card, which can simulate arbitrarily-shaped detectors in software. The simulated detector for the ring lens scheme is a phi detector (so named because of its resemblance to the Greek letter Φ), while that for the astigmatic method is a quad detector.

Focus-Error Detection and Push-Pull Tracking with the Ring Lens : The ring lens used in our experiments had a focal length of 25 mm, and focused a collimated beam onto a sharp, nearly diffraction-limited ring of diameter 3.19 mm. A section of the focused ring is shown in Fig. 3, as an intensity plot of the light pattern collected by the camera; the width of this ring is roughly 50 μm.

A schematic diagram of the ring lens focusing technique is shown in Fig. 4. As the disk (grating) moves in and out of focus, the beam incident on the ring lens becomes divergent or convergent, and the light at the focal plane of the ring lens moves outside or inside its nominal radius. A focus error signal may thus be generated by subtracting the integrated light intensity outside the nominal ring radius from that inside. The difference signal is subsequently normalized by the sum signal in order to eliminate the effects of laser power and/or reflectivity fluctuations.

During seek operations when the beam scans across the tracks while remaining in focus, diffraction effects produce a so-called "baseball pattern" on the returning beam. This pattern produces bright and dark regions on the focused ring. A track-crossing signal can thus be generated by subtracting the integrated intensity in one half of the image from that in the other half; again the difference signal should be normalized by the sum for reasons that were described earlier.

Focus-Error Detection and Push-Pull Tracking with the Astigmatic Lens : The astigmatic scheme is depicted in Fig. 5. The astigmat used in these experiments had focal lengths 19.75 mm and 20.25 mm, and a clear aperture of about 5mm. The detector was placed at the circle of least confusion, midway between the two line foci, where deviations of the incident beam from collimation produced an elongated image in one of two mutually orthogonal directions. The elongation of the spot is detected by a four-quadrant detector; the FES and TES signals are generated by subtracting the integrated intensity on one pair of quadrants from that on the other, then dividing by the sum signal. Since in our experiments the spot itself was too small to be properly resolved by the CCD array, the plane midway between the foci of the astigmat was magnified by a 40× magnifier and imaged onto the camera. All subsequent processing of the signals was carried out on this magnified image.

Results and Discussion : The ring lens technique was found to produce a steeper FES curve and significantly less feedthrough than the astigmatic method. These findings apply to both wavelengths and both polarization directions employed in this work. The ring lens was also found to be fairly insensitive to misalignments.

Figures 6(a, b) show the FES curves for the ring lens and astigmatic techniques, respectively. The four curves in each group are for different combinations of wavelength and polarization. Neither polarization nor the wavelength seem to have a significant effect on the shape and slope of the FES curve. The slope of the linear region of the FES for the ring lens is 0.5 per micron of defocus, whereas that for the astigmat is only 0.22 per micron.

Plots of TES and spurious FES during track-crossings (i.e., feedthrough) are shown in Fig. 7 for the ring lens and Fig. 8 for the astigmat; important features of these plots are also summarized in Table I. Note that the TES amplitudes are comparable for the two schemes. On the other hand, for both wavelengths and polarizations, the feedthrough (in microns) for the ring lens is between six and eight times lower than that for the astigmat.

The ring lens technique is fairly insensitive to misalignments and imperfections of the system. Figure 9(a) shows several FES curves for various radii of the phi detector. (Recall that the radius of the focused ring is around 1.6 mm, and its width is approximately 50 μm.) An error of $\pm$ 10 μm in detector radius will change the zero-crossing by ± 1.6 microns. In an actual drive, if the radius of the detector happens to deviate from that of the focused ring, the electronic gains of the detectors must be adjusted to offset this error. Figure 9(*a*) also shows that a mismatch of ± 20 μm between the ring radius and the radius of detector can seriously degrade the FES slope. In Fig. 9(*b*) we show FES curves for the best radius but various locations of the phi detector in the focal plane of the ring lens. These plots show a slight decrease in the slope as well as a small shift of the zero-crossing for 10 μm of centering error. The consequences of a 20 μm decenter, however, are much more drastic.

Focusing Scheme	Wavelength (nm)	Polarization (relative to tracks)	Peak-to-valley TES norm. units	Peak-to-valley feedthrough norm. units	microns	wavelengths
Ring lens	544	parallel	1.9	0.12	0.25	0.46
Ring lens	544	perpendicular	1.9	0.12	0.25	0.46
Ring lens	633	parallel	1.5	0.07	0.14	0.23
Ring lens	633	perpendicular	1.5	0.08	0.17	0.27
Astigmat	544	parallel	1.6	0.34	1.5	2.75
Astigmat	544	perpendicular	1.7	0.44	2.0	3.65
Astigmat	633	parallel	1.4	0.22	1.0	1.60
Astigmat	633	perpendicular	1.4	0.22	1.0	1.60

Table I. Summary of track-crossing and feedthrough signals

In comparison with the ring lens results in Fig. 9(*b*), Fig. 10 shows several FES curves for various locations of the quad detector of the astigmatic technique. We observe that 6 μm of centering error has negligible effects on the FES curve, but a decenter of 12 μm is beginning to cause severe problems.

Concluding Remarks : We have presented a comparison of the ring lens and astigmatic methods of generating focus- and track-error signals for optical disk drives. It was found that the ring lens produces an FES curve which is substantially steeper than that produced by the astigmat. Also the cross-talk on the focus error signal from track-crossings was 6-8 times smaller for the ring lens method. In addition, we found the ring lens scheme to be tolerant of small errors in detector positioning and alignment.

Acknowledgements : Thanks are due to Dr. B.E. Bernacki for helpful advice and many valuable discussions. We also thank Mr. J. Corso for his help in fabricating the ring lenses.

References

1. M. Mansuripur and C. Pons, "Diffraction modeling of optical path for magneto-optical disk systems," *Proceedings of the Optical Data Storage Conference*, D.B. Carlin, Y. Tsunoda and A.A. Jamberdino, Eds., SPIE Vol. **899**, pp56-60 (1988).

2. B.E. Bernacki and M. Mansuripur, "Diffraction Analysis and evaluation of several focus- and track-error detection schemes for magneto-optical disk systems," *Proceedings of the Optical Data Storage Conference*, D.B. Carlin and D.B. Kay, Eds., SPIE Vol. **1663**, pp150-156 (1992).

3. B.E. Bernacki, "Characterization of magneto-optical media and systems," PhD dissertation, Optical Sciences Center, University of Arizona (1992).

Figure Captions

Fig. 1. a) Diagram showing dimensions of the ring lens. The apex of the lens occurs at a radius of 1.595mm, which corresponds to the focused ring radius of a collimated incident beam.

b) Surface profile of section of the lens obtained by interferometric measurements. The region captured by the profilometer is the unshaded annular region depicted in (a) with a width of 0.524mm.

c) SEM image of section of the ring lens.

d) Newton's rings observed on a section of the ring lens.

Fig. 2. Schematic diagram of the static focusing/tracking testbed.

Fig. 3. Section of the intensity profile of the focused ring (pixel = $10\mu m \times 10\mu m$).

Fig. 4. Schematic diagram of the method of ring lens focusing and push-pull tracking.

Fig. 5. Schematic diagram of the method of astigmatic focusing and push-pull tracking.

Fig. 6. Measured FES curves for the ring lens (a) and astigmatic (b) scheme of focus error detection. The various symbols in each plot correspond to different wavelengths and polarization orientations used in the experiment.

Fig. 7. Measured TES (dashed) and feedthrough (solid) curves for the ring lens scheme.

a) Green laser with polarization parallel to tracks,

b) Green laser with polarization perpendicular to tracks,

c) Red laser with polarization parallel to tracks,

d) Red laser with polarization perpendicular to tracks.

Fig. 8. Measured TES (dashed) and feedthrough (solid) curves for the astigmatic scheme.

a) Green laser with polarization parallel to tracks,

b) Green laser with polarization perpendicular to tracks,

c) Red laser with polarization parallel to tracks,

d) Red laser with polarization perpendicular to tracks.

Fig. 9. FES curves for the ring lens scheme in the case of red laser with polarization parallel to tracks.

a) Different curves correspond to different detector radii. The solid curve is obtained for best radius, "+" is for ± 10μm and "x" for ± 20μm change in the radius. The curves shift to the left with increasing detector radius.

b) Different curves correspond to various detector locations within the focal plane of the ring lens. The solid curve ("o") is for the best detector position, while the dashed curves are for translations of 10 μm ("+") and 20 μm ("x") relative to this optimum position.

Fig.10. FES curves for the astigmatic scheme in the case of red laser with polarization parallel to tracks; different curves correspond to various detector locations within the midplane between the two astigmatic line foci. The solid curve ("o") is for the best detector position, while the dashed curves are for translations of 6 μm ("+") and 12 μm ("x") relative to this optimum position.

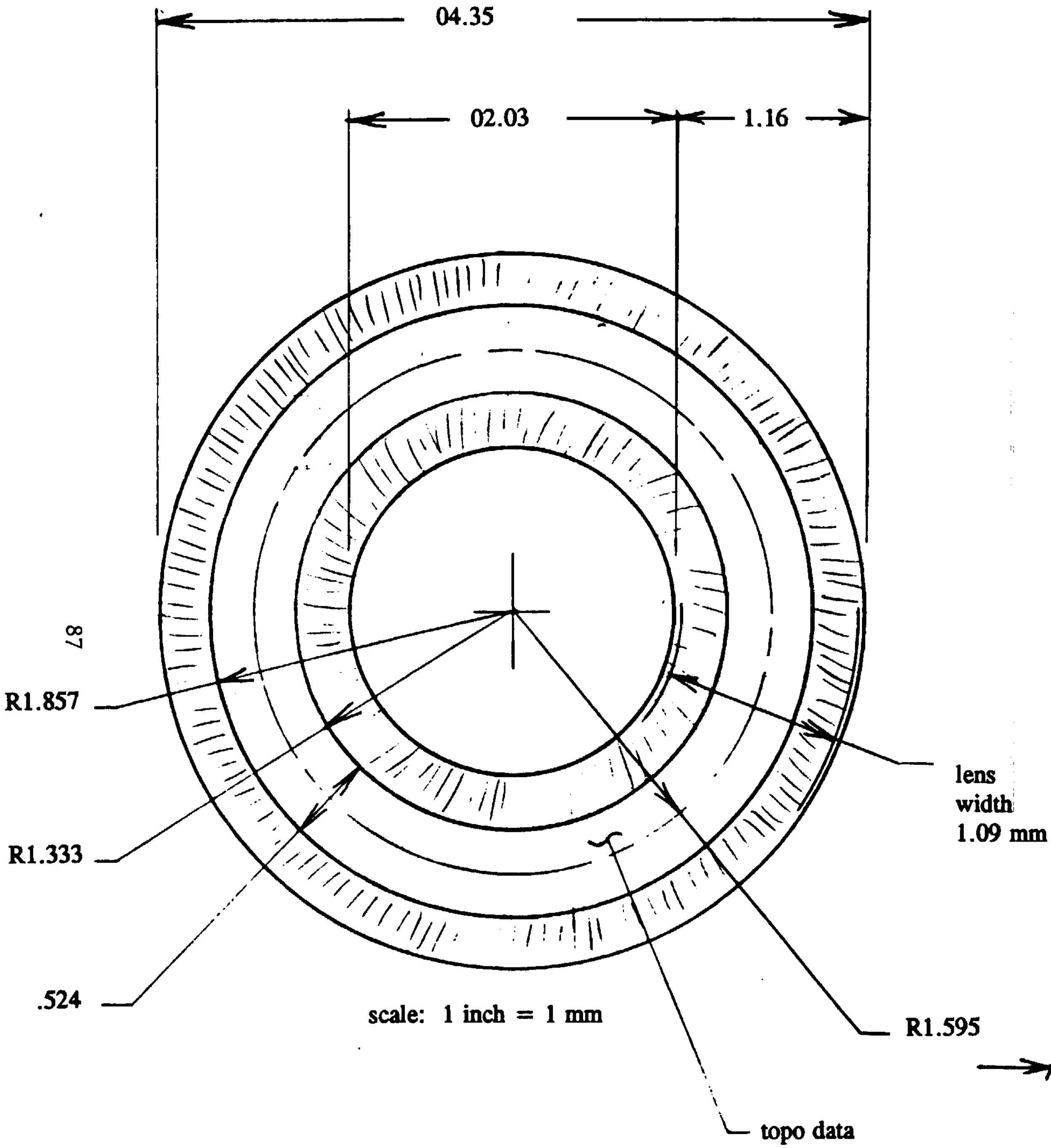

Figure 1(a)

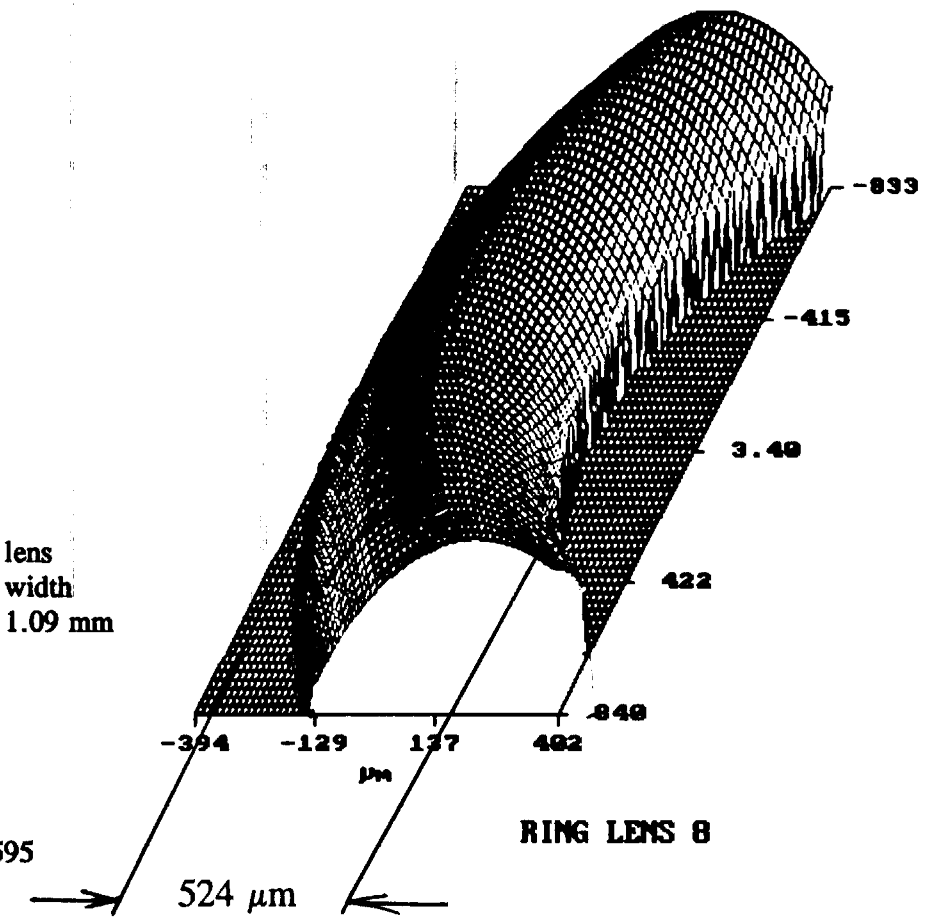

Figure 1(b)

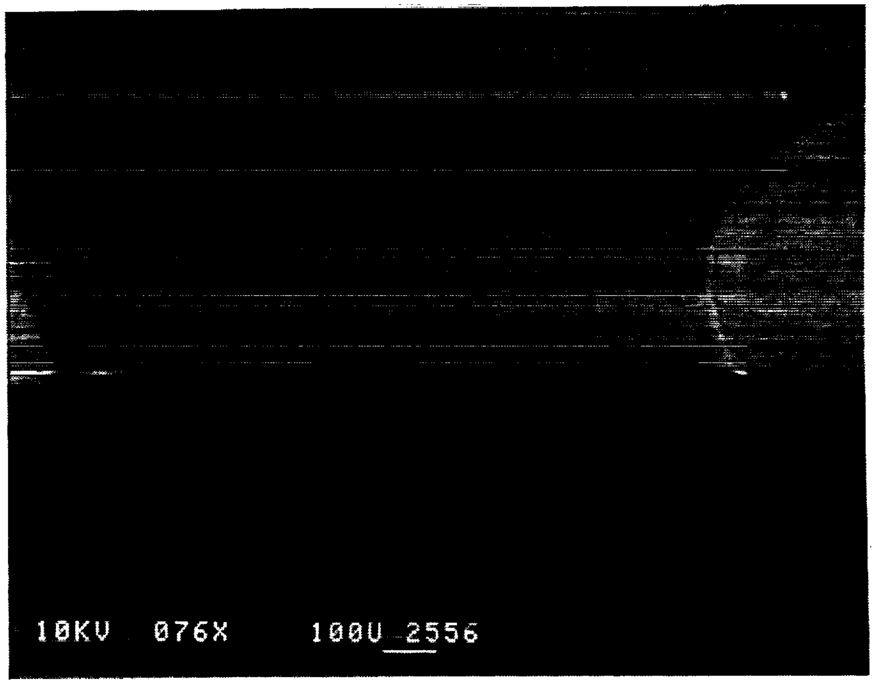

Figure 1(c)

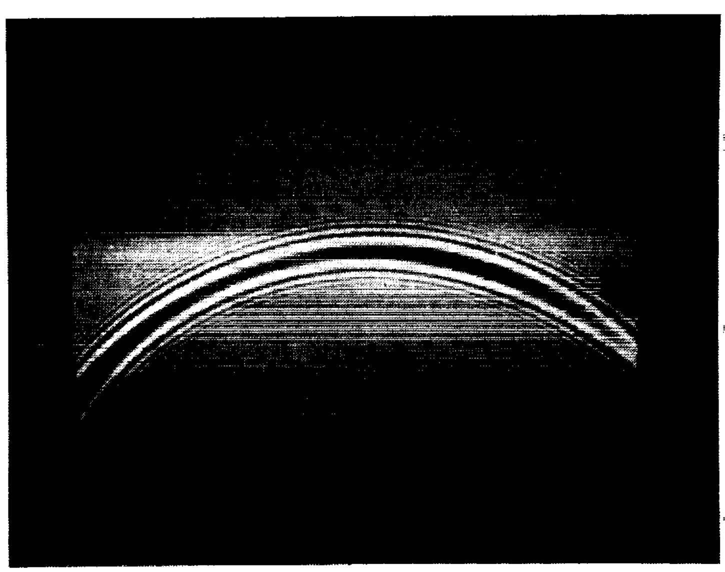

Figure 1(d)

SCHEMATIC DIAGRAM OF
STATIC TESTBED

RG 12/3/92

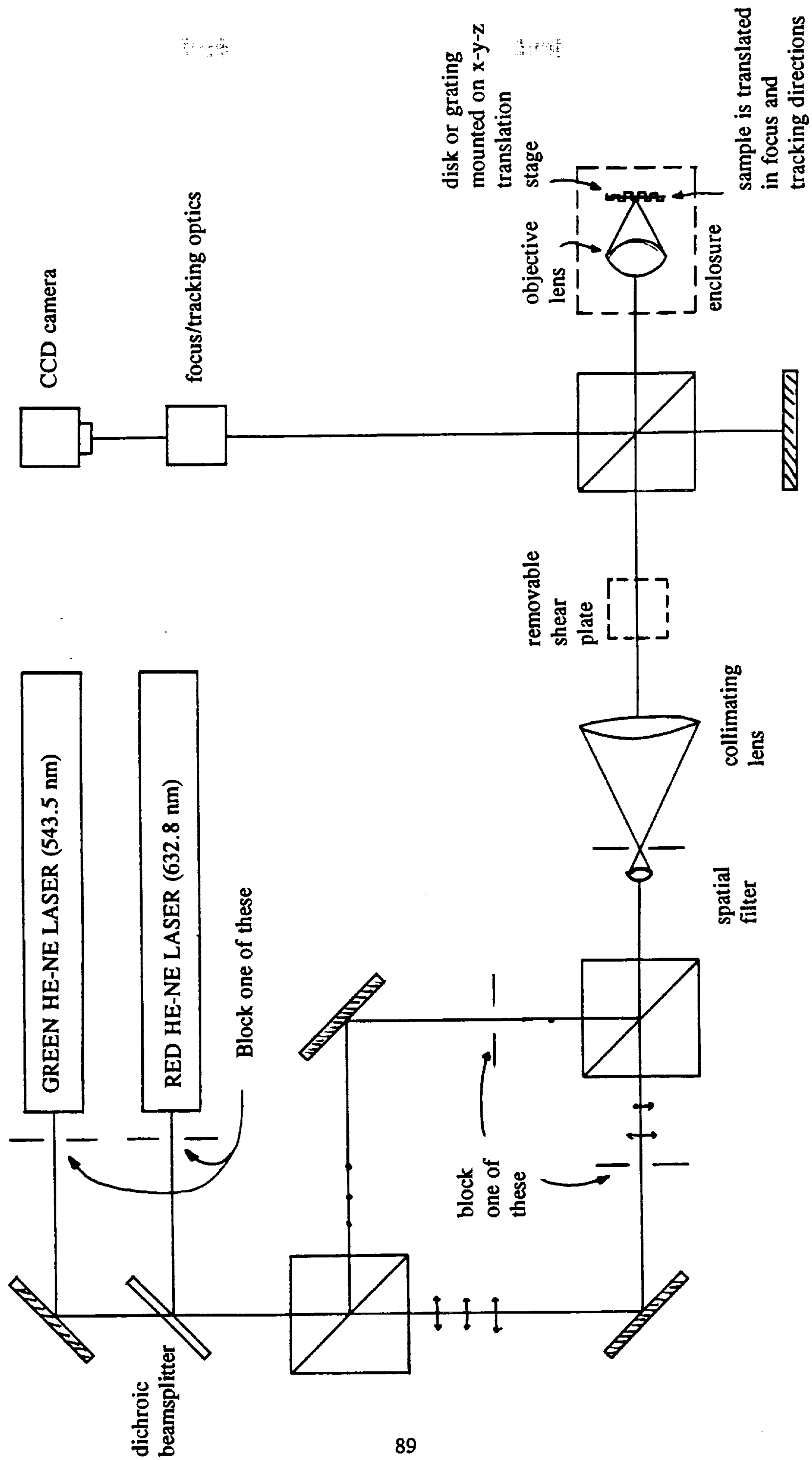

Figure 2 Schematic diagram of static focus/tracking testbed.

Portion of intensity profile of focused ring

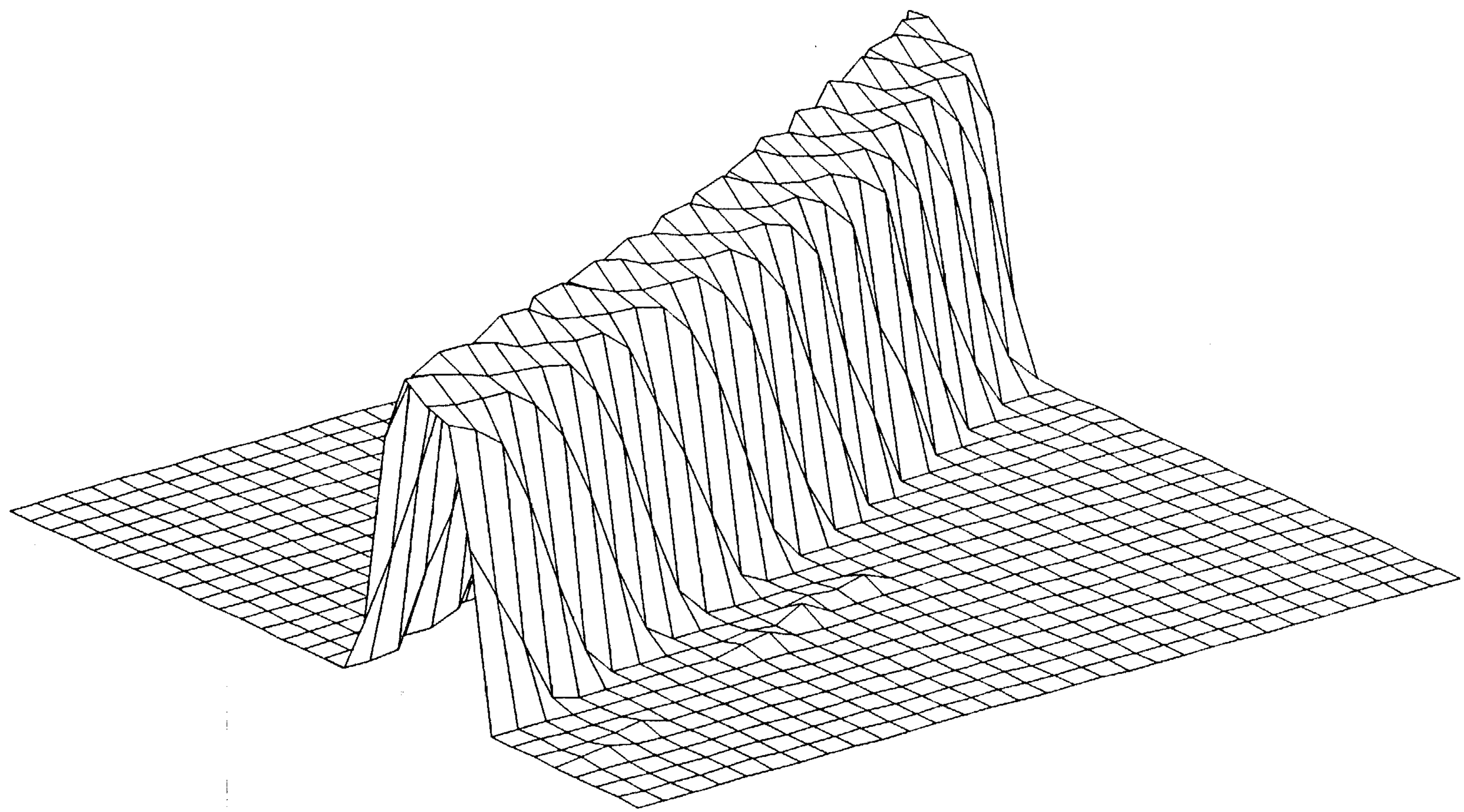

Figure 3

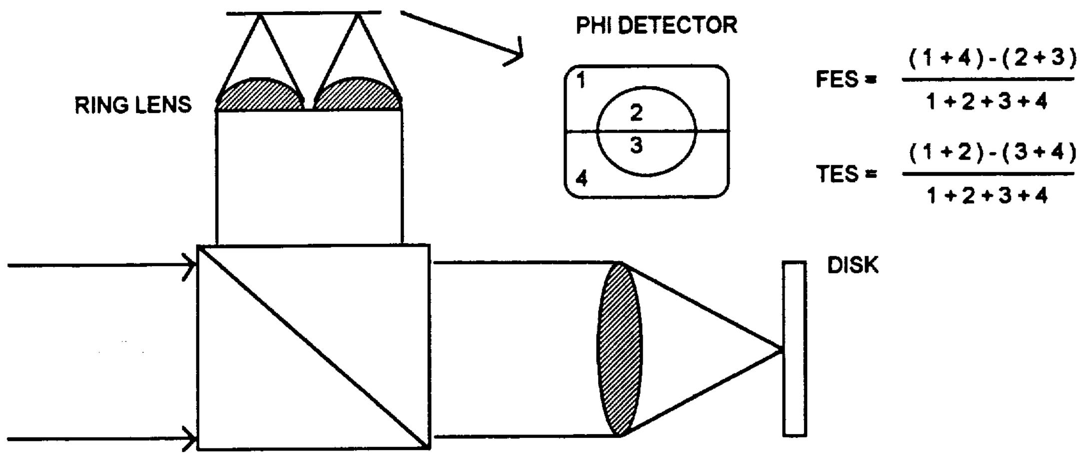

Figure 4

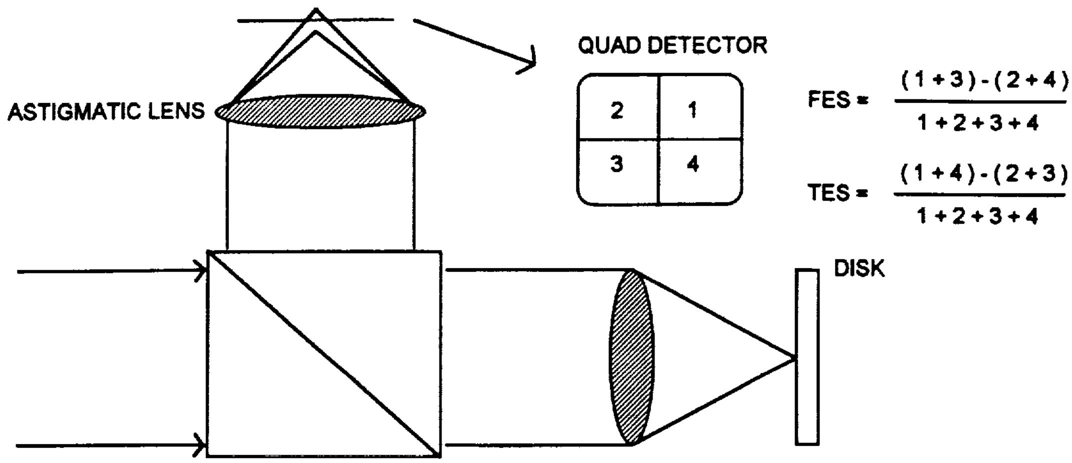
QUAD DETECTOR
ASTIGMATIC LENS
2
1
3
4
FES = (1+3)-(2+4) / 1+2+3+4
TES = (1+4)-(2+3) / 1+2+3+4
DISK

Figure 5

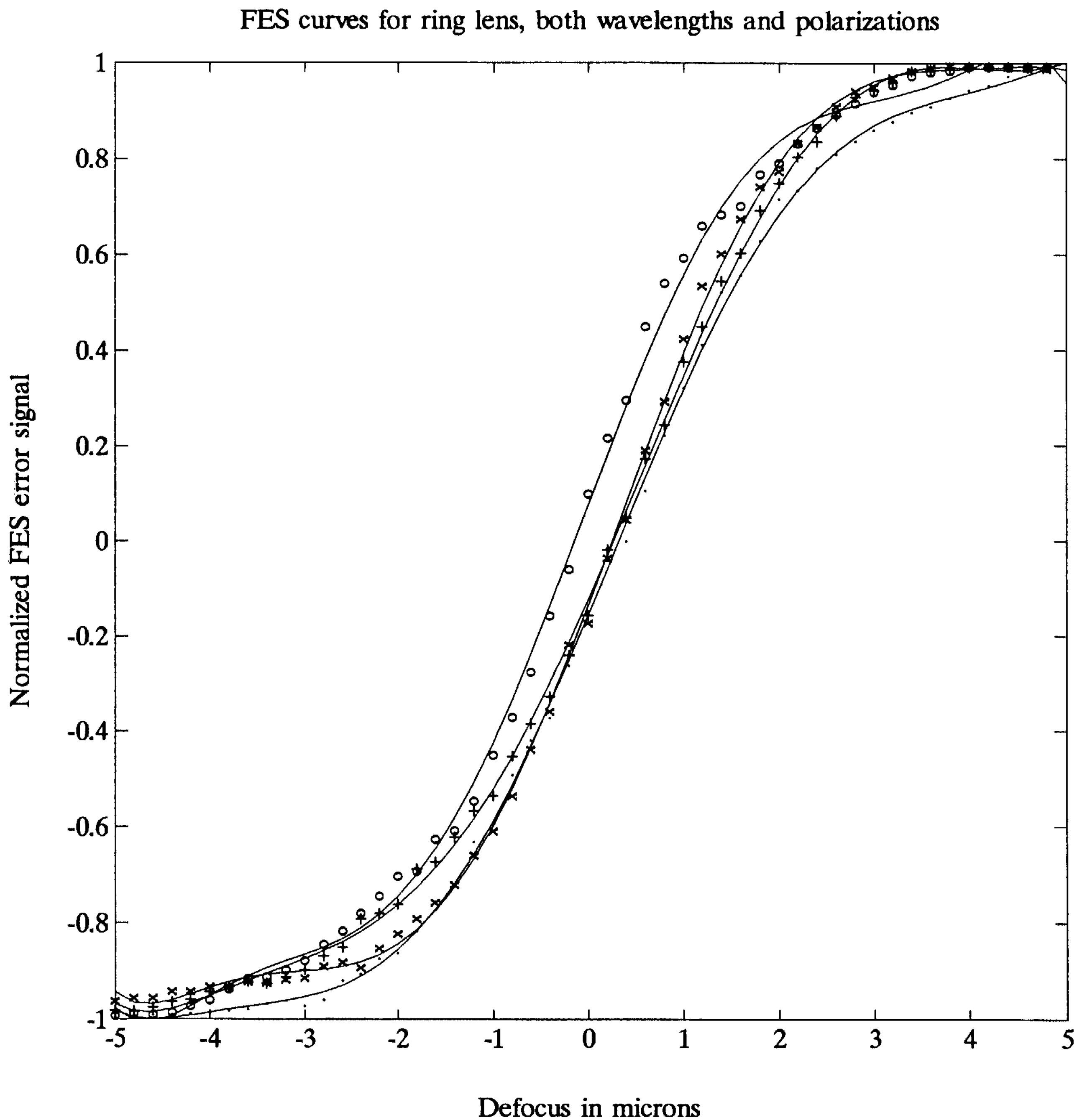
FES curves for ring lens, both wavelengths and polarizations
Normalized FES error signal
Defocus in microns
1
0.8
0.6
0.4
0.2
0
-0.2
-0.4
-0.6
-0.8
-1
-5
-4
-3
-2
-1
0
1
2
3
4
5

Figure 6(a)

FES curves for astigmat, both wavelengths and polarizations

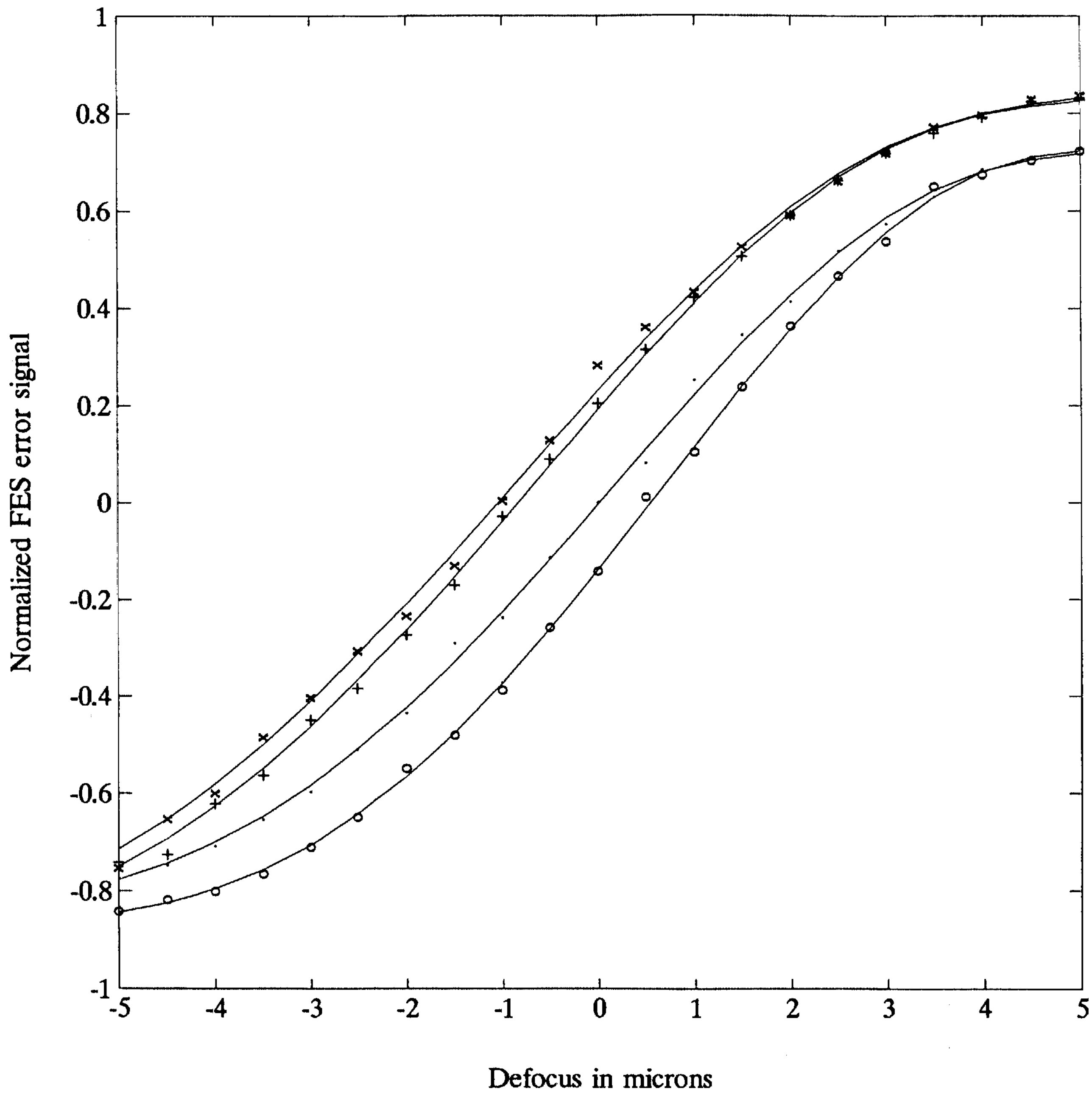

Figure 6(b)

C.2

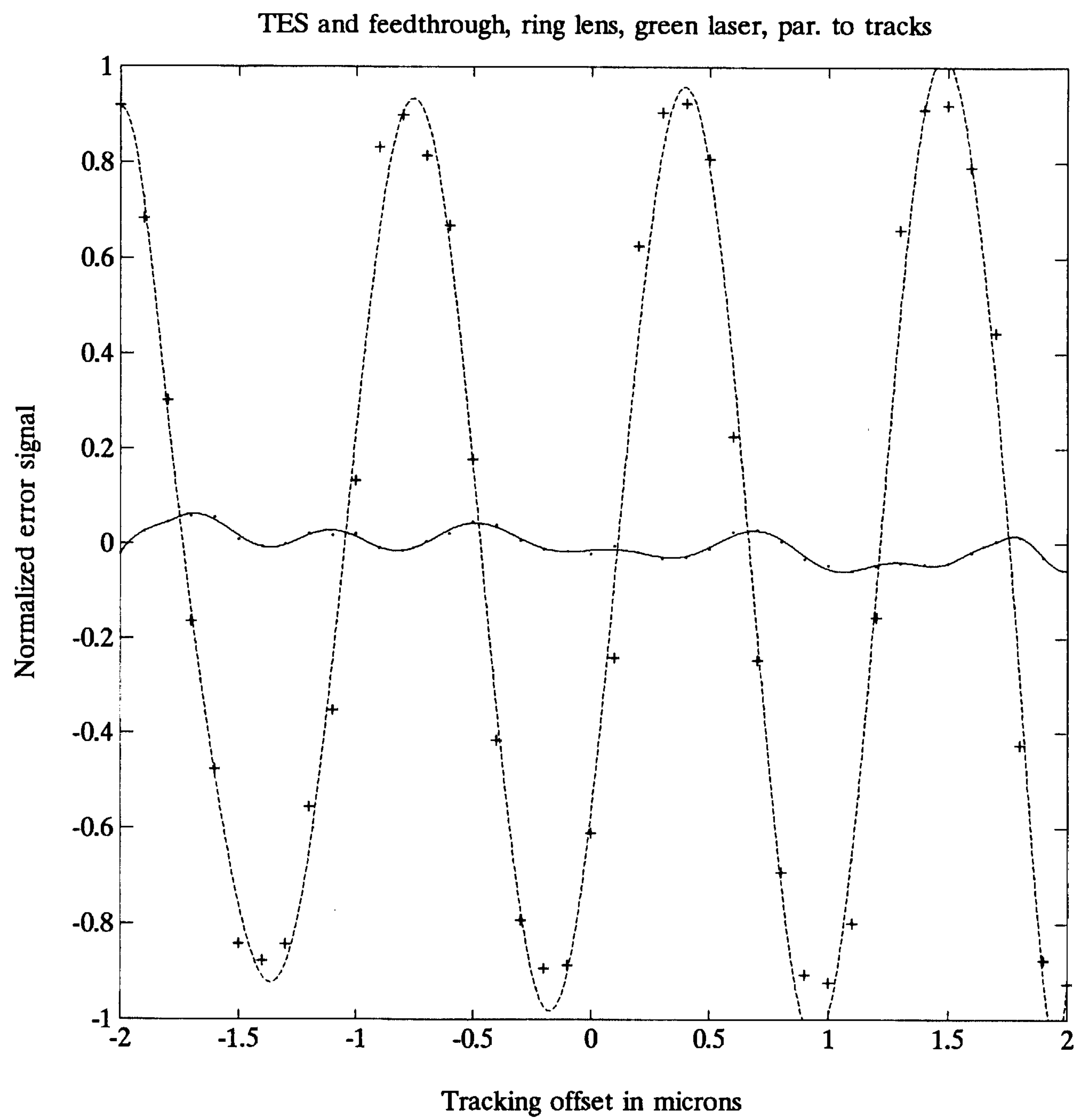
TES and feedthrough, ring lens, green laser, par. to tracks
Normalized error signal
Tracking offset in microns
1
0.8
0.6
0.4
0.2
0
-0.2
-0.4
-0.6
-0.8
-1
-2
-1.5
-1
-0.5
0
0.5
1
1.5
2

Figure 7(a)

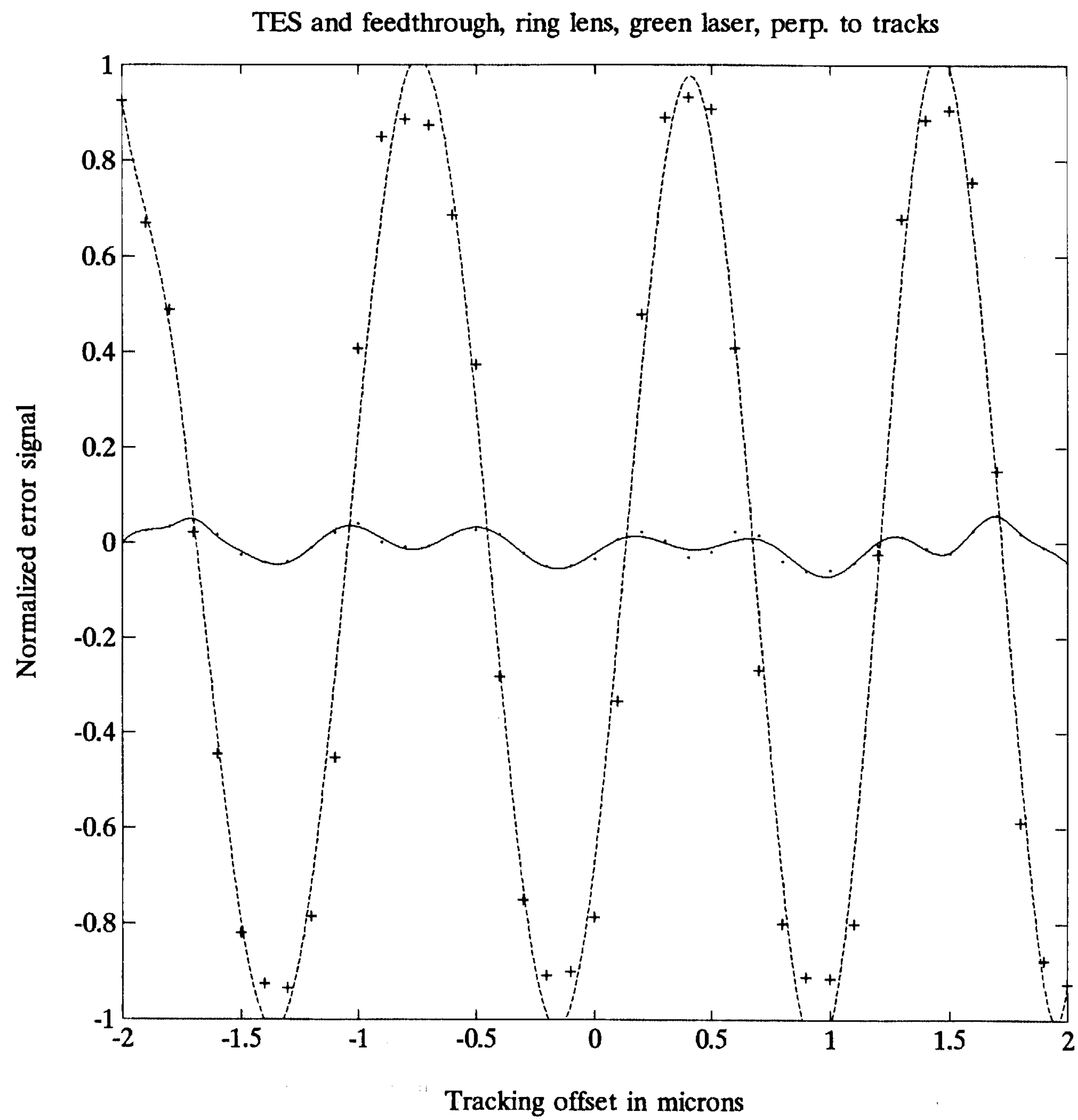
TES and feedthrough, ring lens, green laser, perp. to tracks
Normalized error signal
1
0.8
0.6
0.4
0.2
0
-0.2
-0.4
-0.6
-0.8
-1
-2
-1.5
-1
-0.5
0
0.5
1
1.5
2
Tracking offset in microns

Figure 7(b)

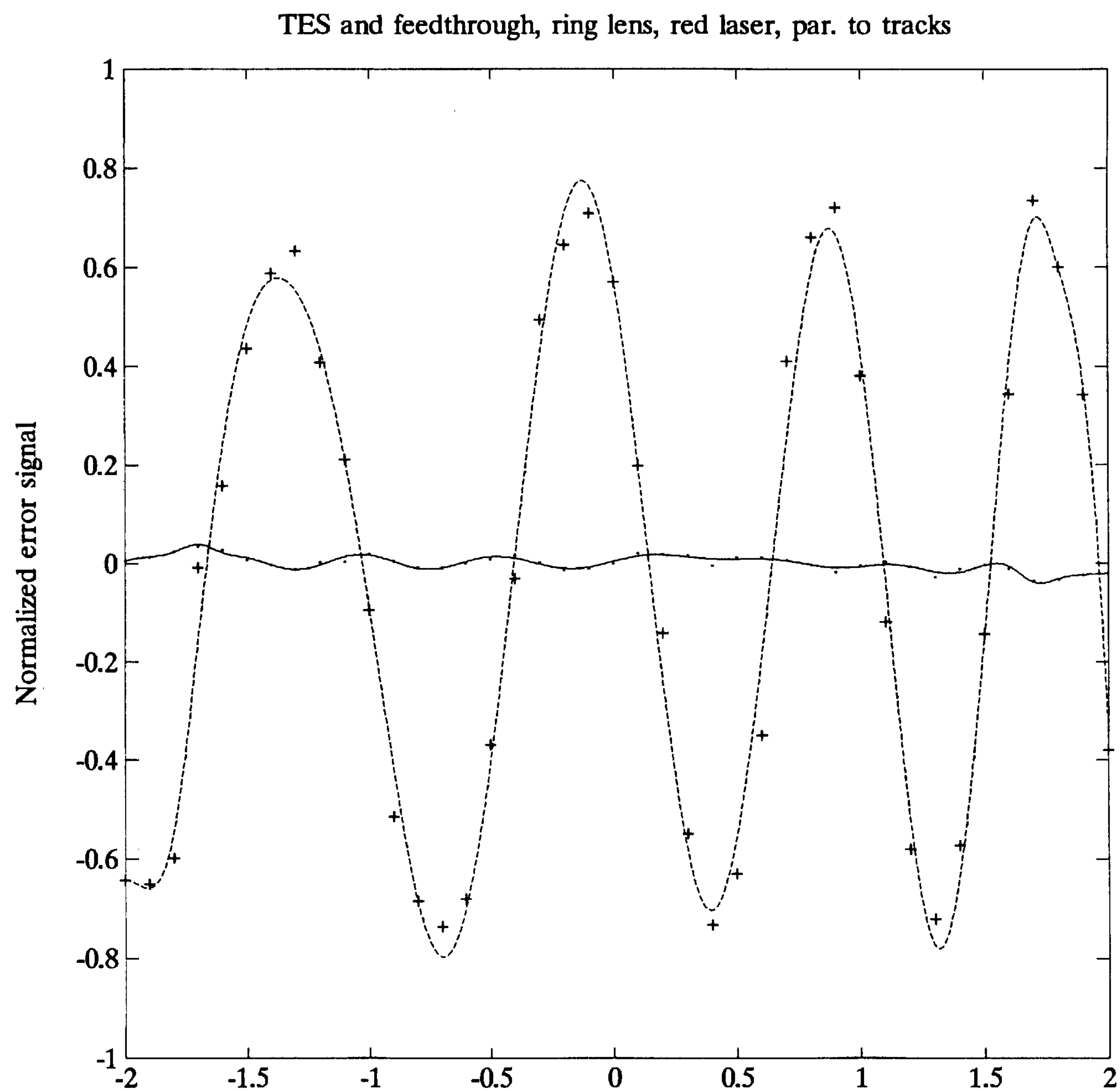

TES and feedthrough, ring lens, red laser, par. to tracks
Normalized error signal
Tracking offset in microns
1
0.8
0.6
0.4
0.2
0
-0.2
-0.4
-0.6
-0.8
-1
-2
-1.5
-1
-0.5
0
0.5
1
1.5
2

Figure 7(c)

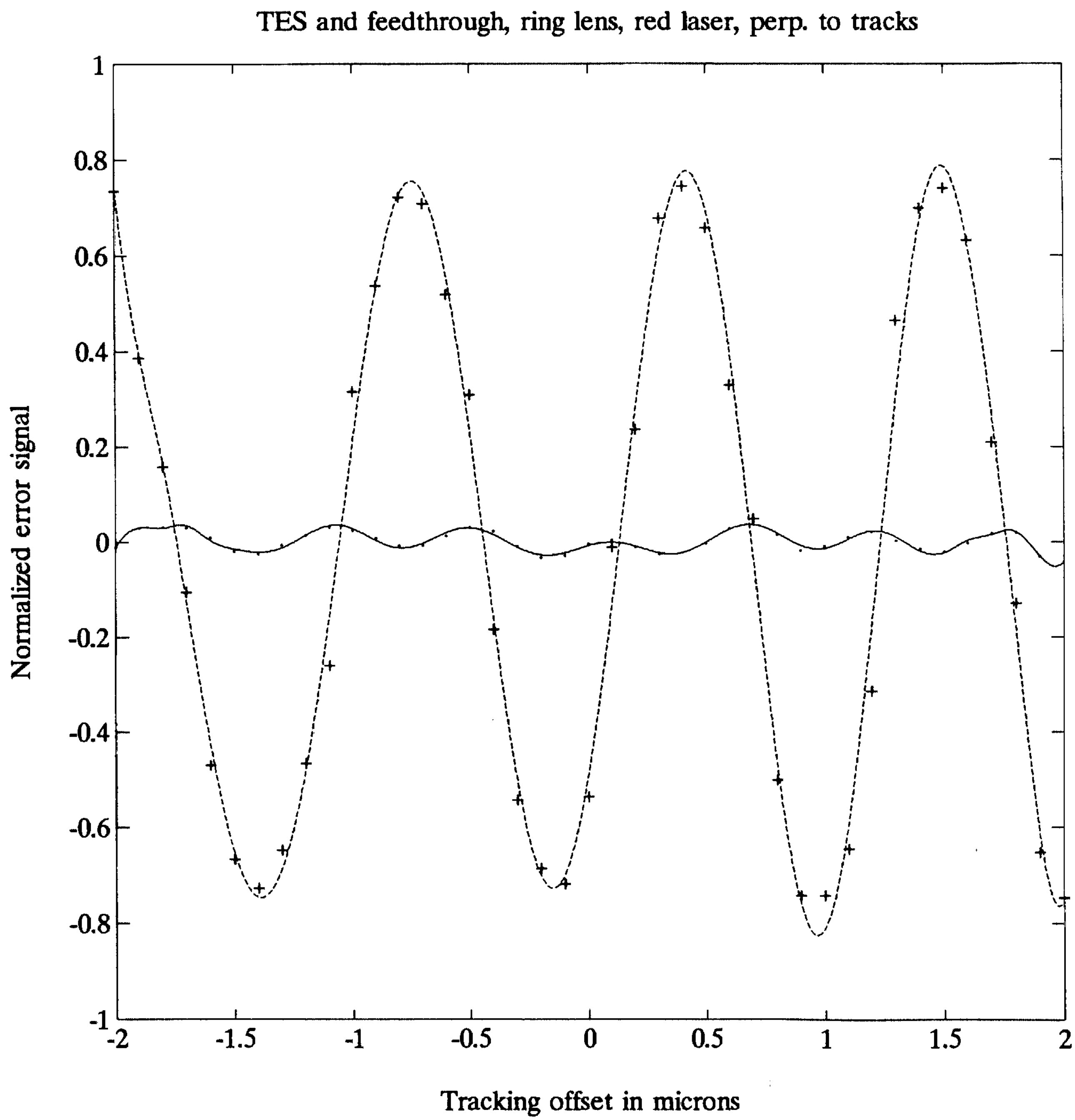
TES and feedthrough, ring lens, red laser, perp. to tracks
Normalized error signal
1
0.8
0.6
0.4
0.2
0
-0.2
-0.4
-0.6
-0.8
-1
-2
-1.5
-1
-0.5
0
0.5
1
1.5
2
Tracking offset in microns

Figure 7(d)

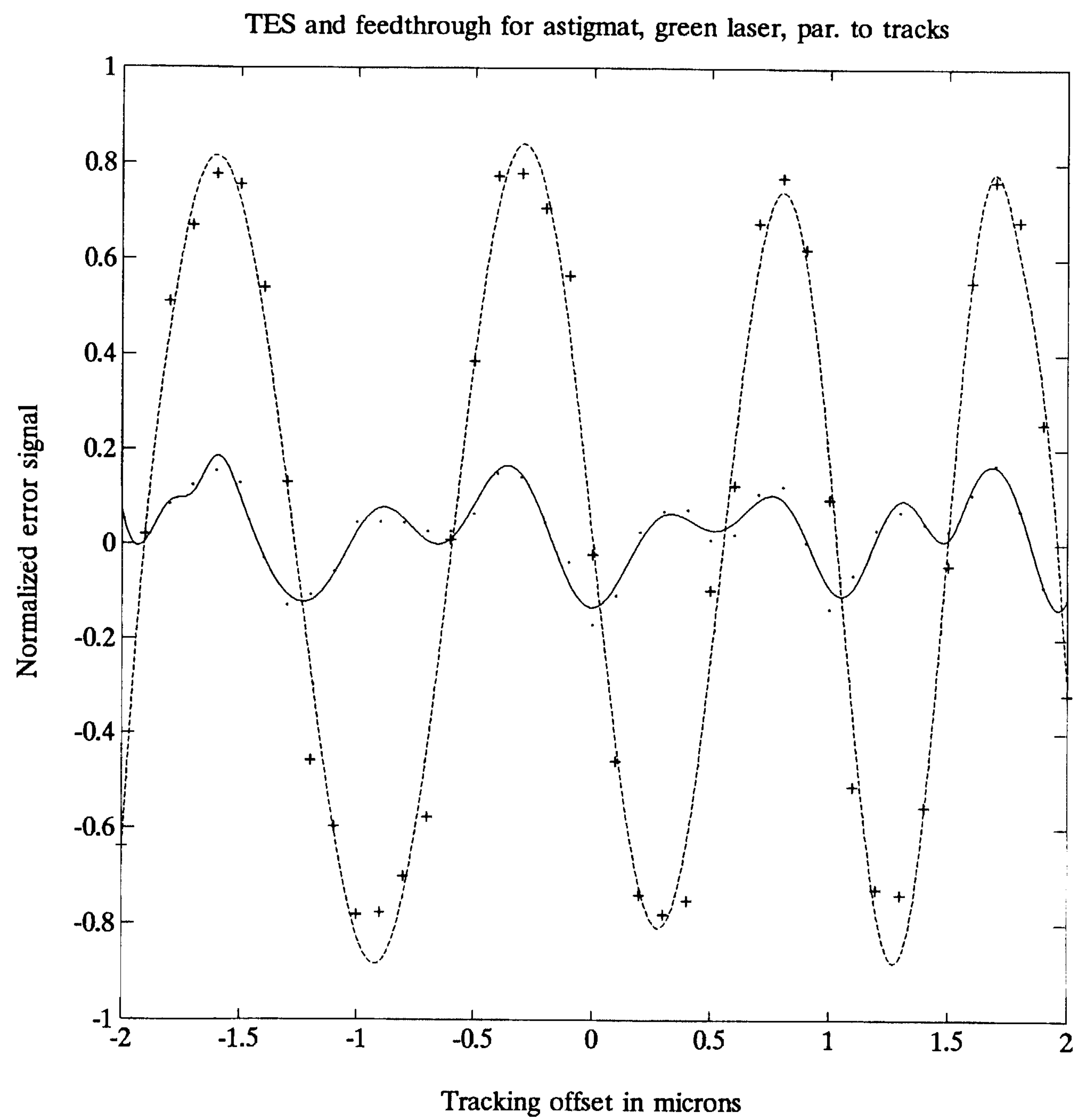
TES and feedthrough for astigmat, green laser, par. to tracks
Normalized error signal
1
0.8
0.6
0.4
0.2
0
-0.2
-0.4
-0.6
-0.8
-1
-2
-1.5
-1
-0.5
0
0.5
1
1.5
2
Tracking offset in microns

Figure 8(a)

TES and feedthrough for astigmat, green laser, perp. to tracks

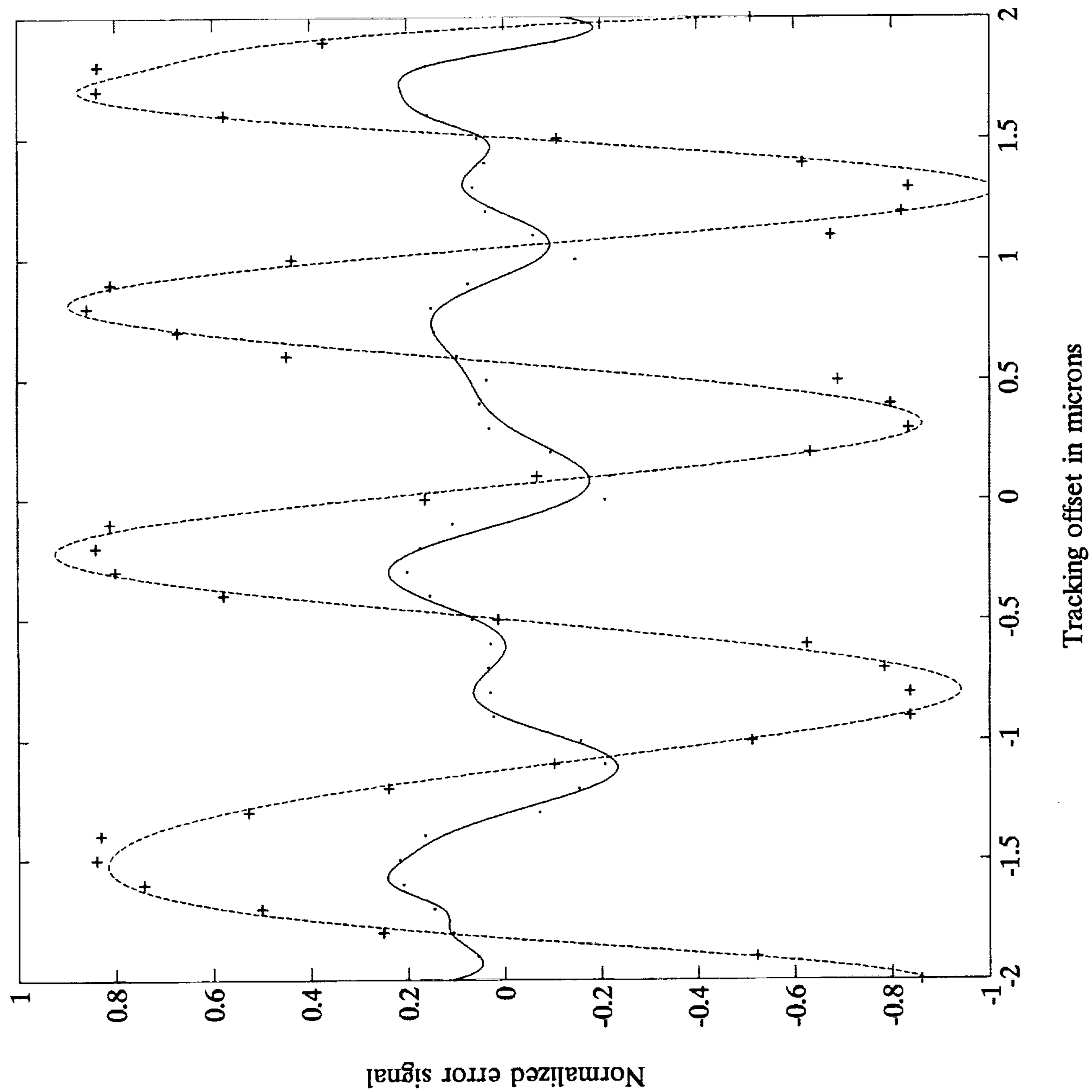

Figure 8(b)

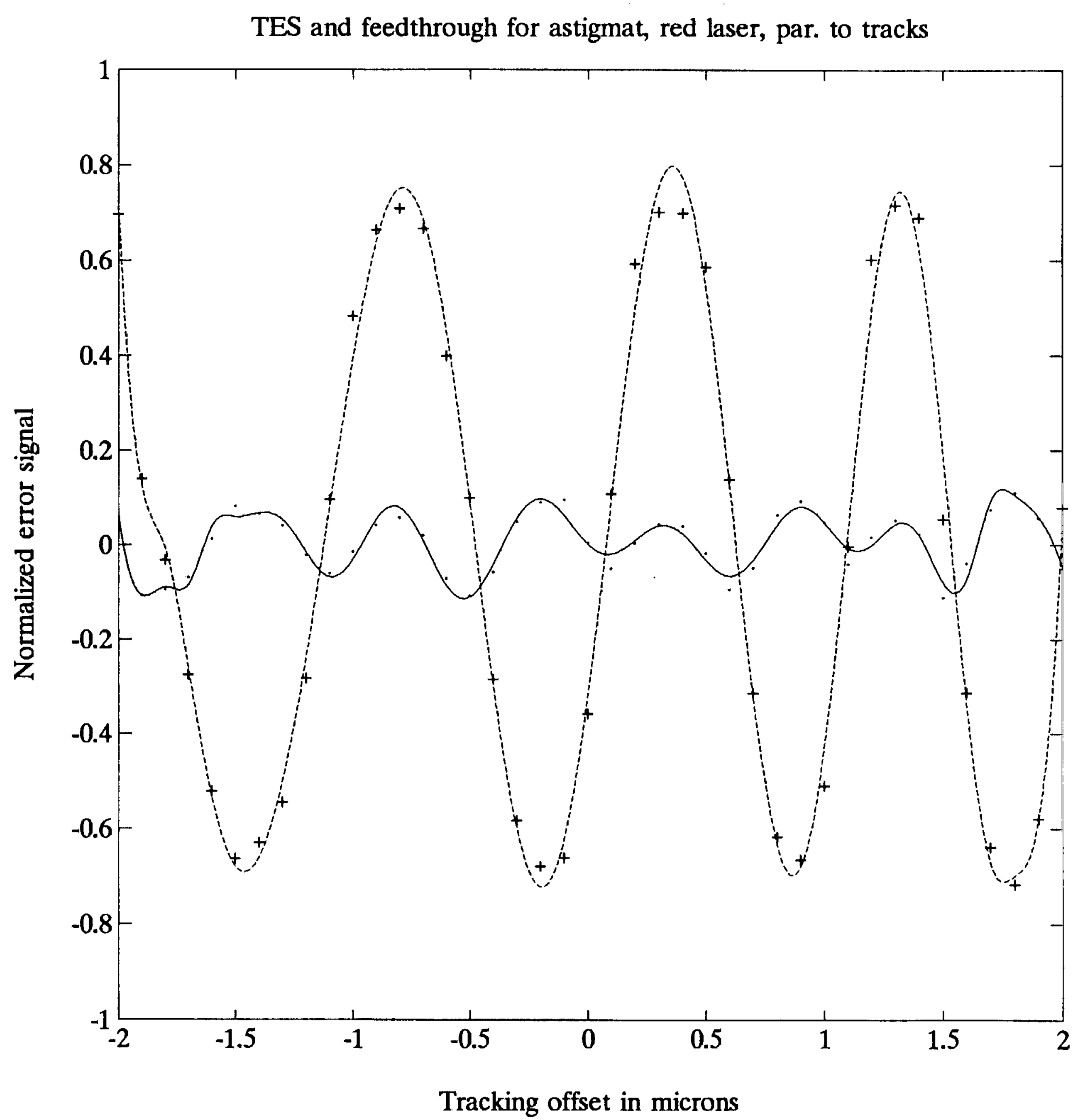

TES and feedthrough for astigmat, red laser, par. to tracks
Normalized error signal
1
0.8
0.6
0.4
0.2
0
-0.2
-0.4
-0.6
-0.8
-1
-2
-1.5
-1
-0.5
0
0.5
1
1.5
2
Tracking offset in microns

Figure 8(c)

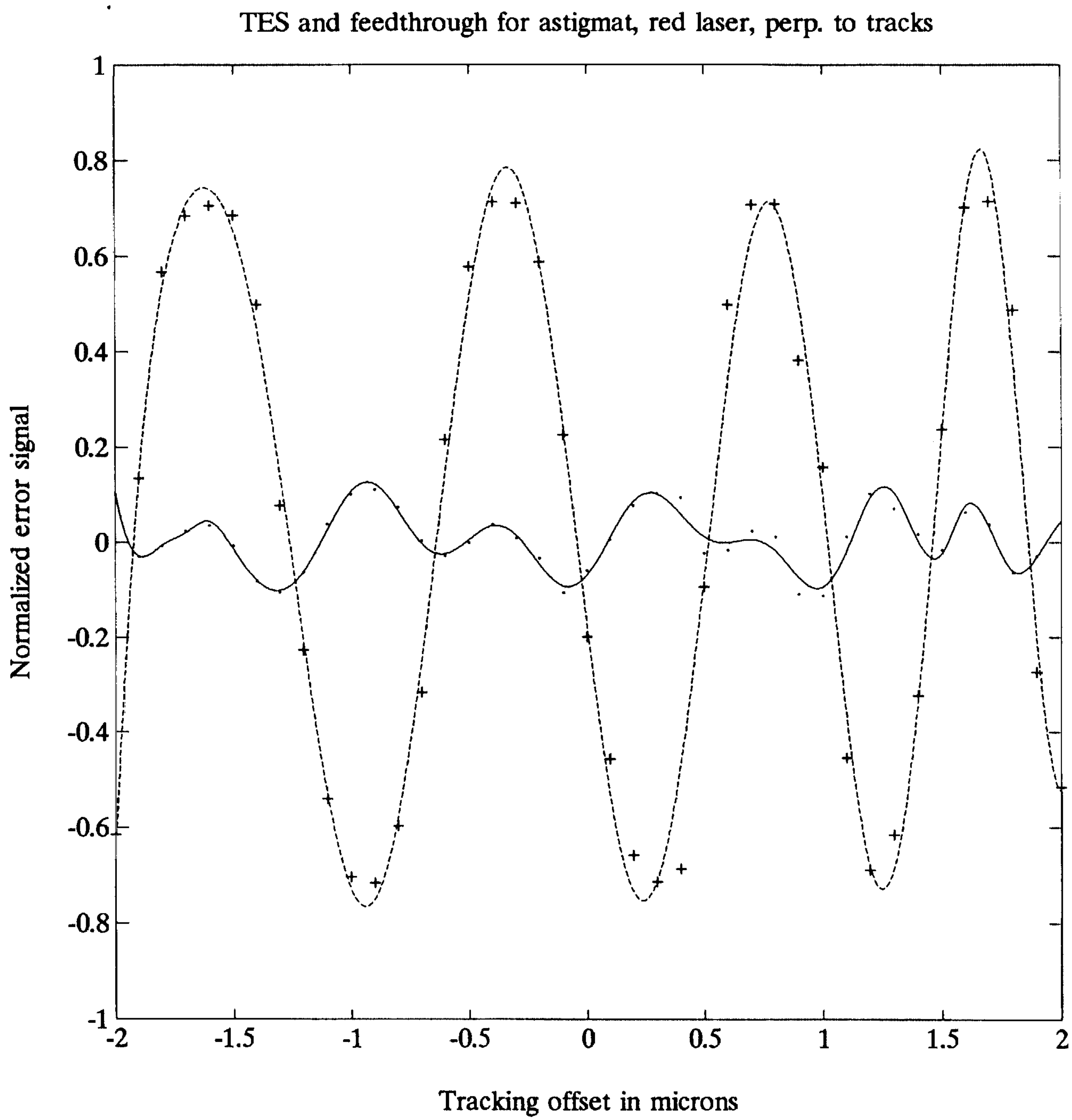

TES and feedthrough for astigmat, red laser, perp. to tracks
Normalized error signal
1
0.8
0.6
0.4
0.2
0
-0.2
-0.4
-0.6
-0.8
-1
-2
-1.5
-1
-0.5
0
0.5
1
1.5
2
Tracking offset in microns

Figure 8(d)

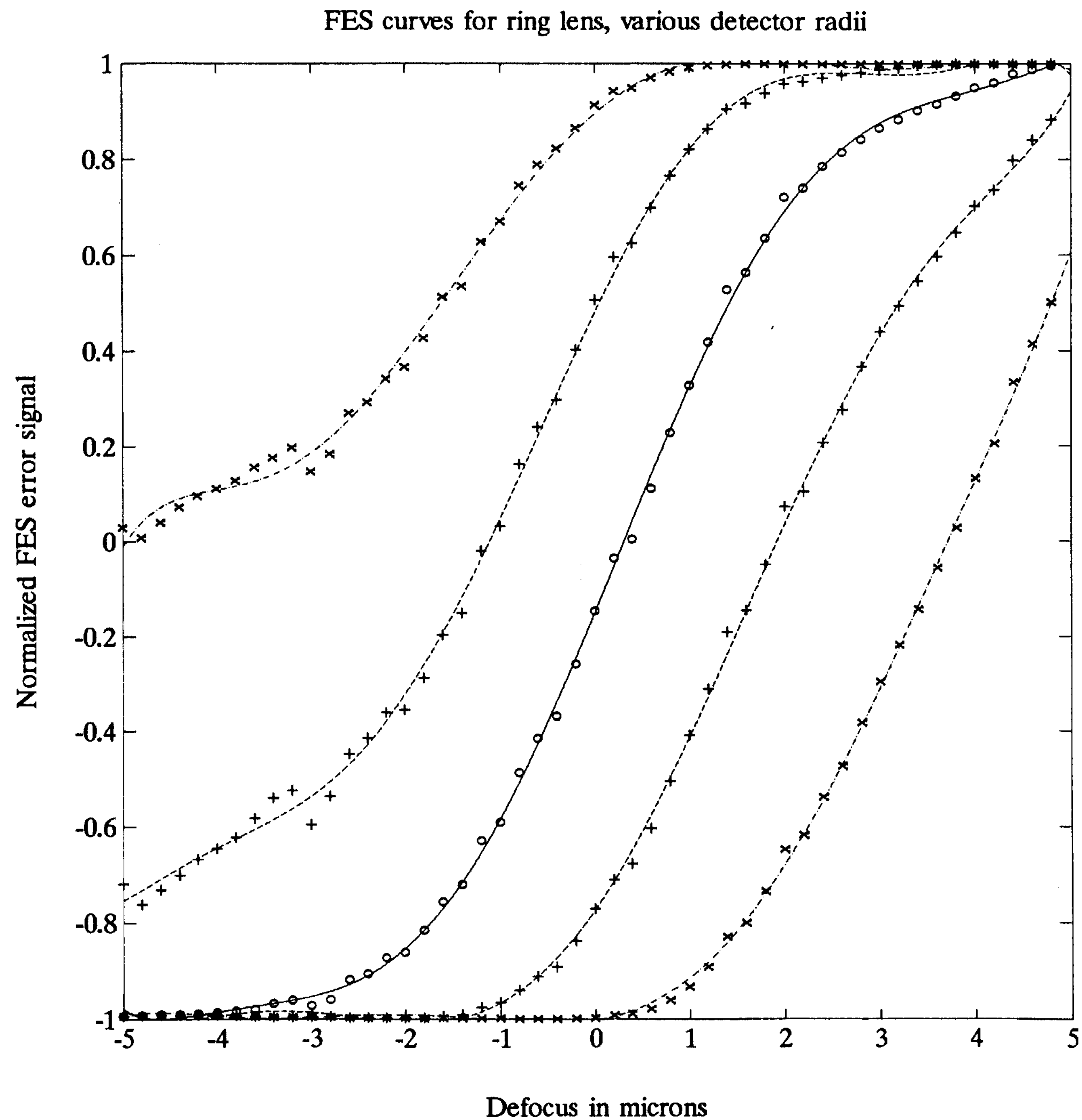
FES curves for ring lens, various detector radii
Normalized FES error signal
1
0.8
0.6
0.4
0.2
0
-0.2
-0.4
-0.6
-0.8
-1
-5
-4
-3
-2
-1
0
1
2
3
4
5
Defocus in microns
Figure 9(a)

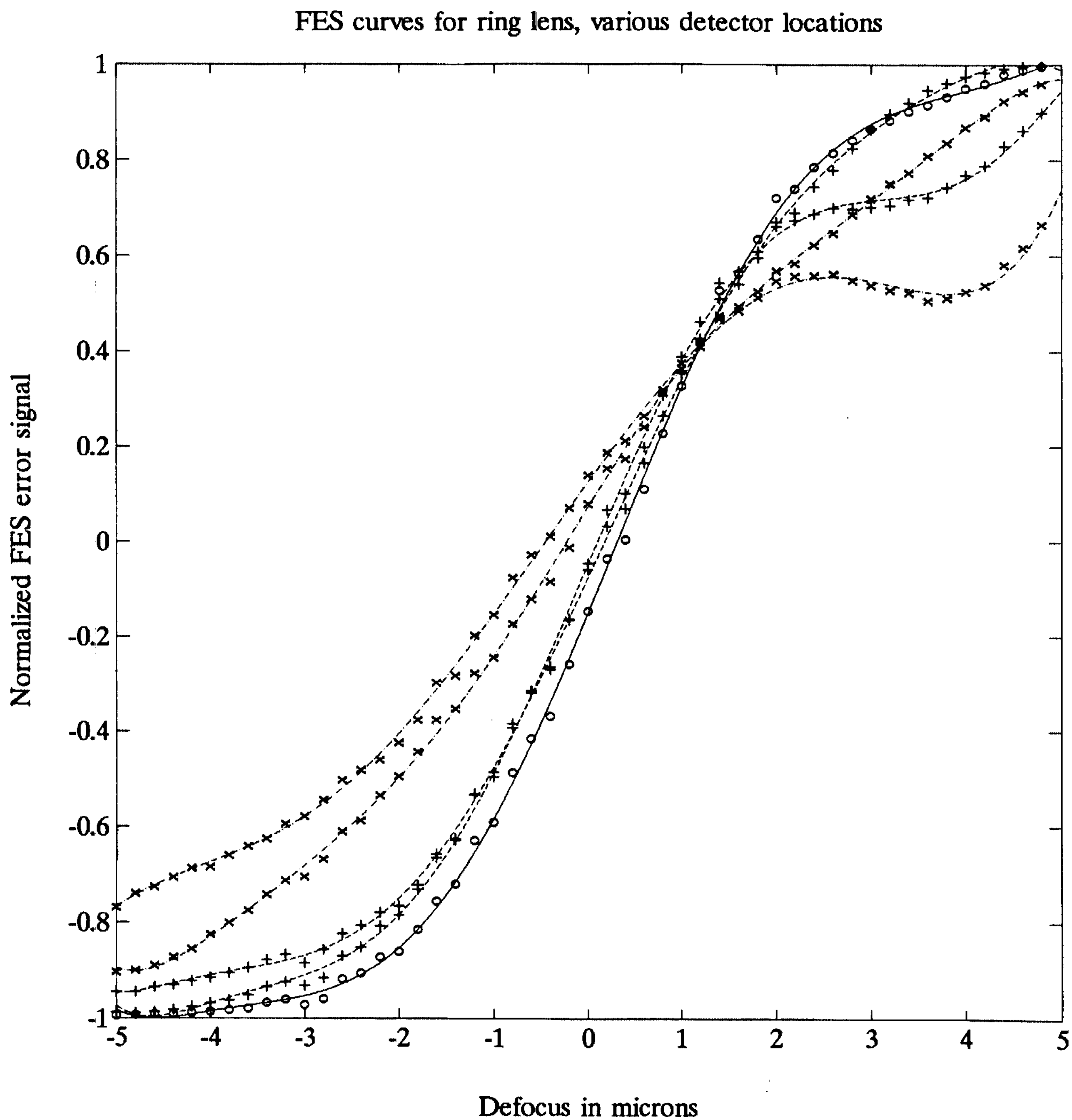
FES curves for ring lens, various detector locations
Normalized FES error signal
1
0.8
0.6
0.4
0.2
0
-0.2
-0.4
-0.6
-0.8
-1
-5
-4
-3
-2
-1
0
1
2
3
4
5
Defocus in microns

Figure 9(b)

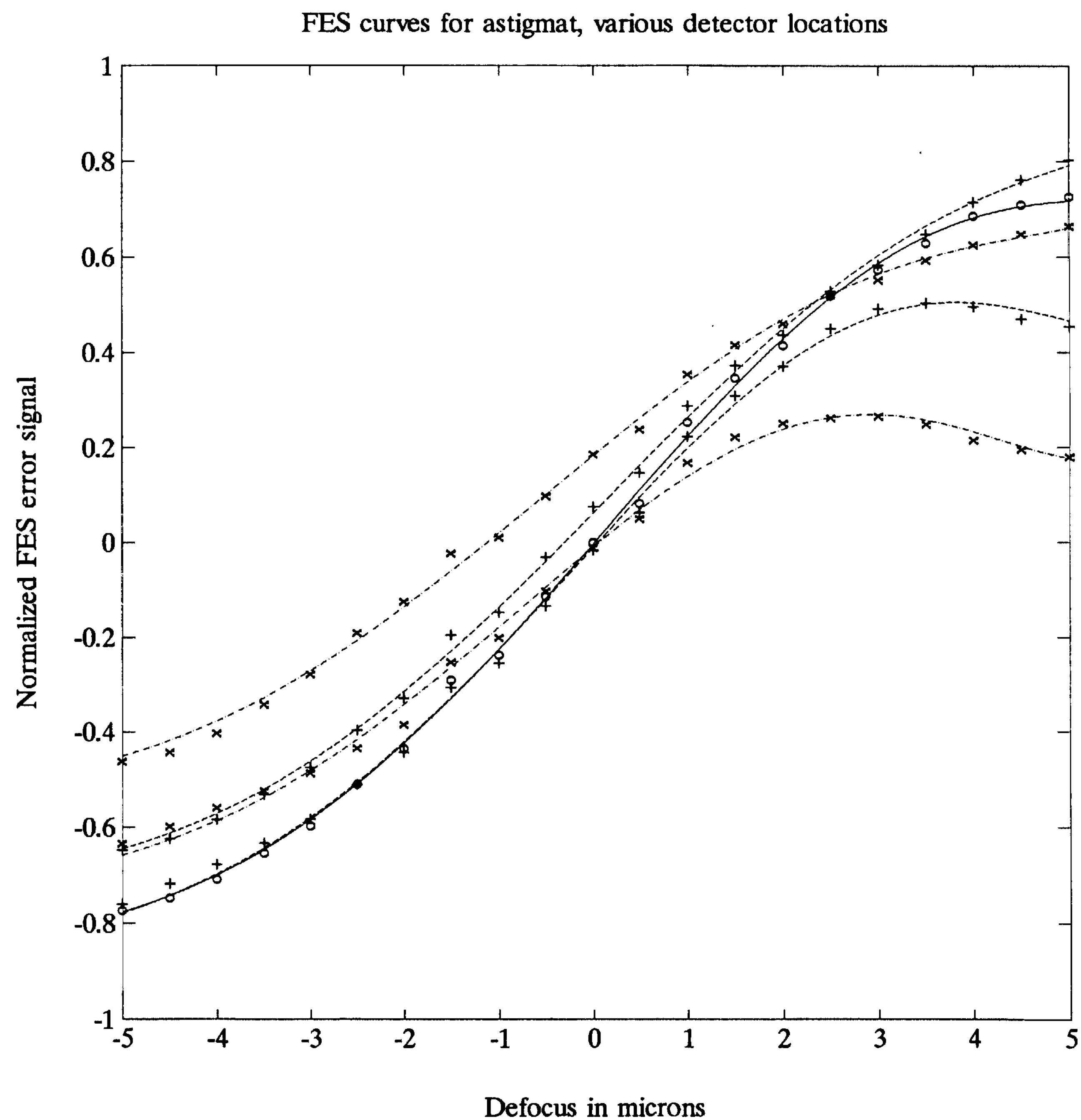
FES curves for astigmat, various detector locations
Normalized FES error signal
1
0.8
0.6
0.4
0.2
0
-0.2
-0.4
-0.6
-0.8
-1
-5
-4
-3
-2
-1
0
1
2
3
4
5
Defocus in microns

Figure 10

APPENDIX C

PRECEDING PAGE BLANK NOT FILMED

N94-14991

Magnetic and magneto-optical properties and domain structure of Co/Pd multilayers

S.Gadetsky*, Teho Wu*, T.Suzuki+ and M.Mansuripur*

* Optical Sciences Center, University of Arizona,Tucson, AZ 85721

+ IBM Research Division, Almaden Research Center, San Jose, California 95120

ABSTRACT

The domain structure of Co/Pd(1.6/6.3 Å)xN multilayers and its relation to the bulk magnetic properties of the samples were studied. The Co/Pd multilayeres were deposited by rf and dc magnetron sputtering onto different substrates. It was found that magnetic and magneto-optical properties and domain structure of the multilayers were affected by total film thickness and substrate condition. Magnetization, coercivity and anisotropy of the films decreased significantly as the film thickness dropped below 100 Å. However, Kerr rotation angle had a maximum at the same thickness. The width of the domain structure increased with the decrease of the film thickness attaining the single domain state at N=10. The initial curves in Co/Pd multilayers were found to depend on demagnetization process. The samples demagnetized by in-plane field showed the largest difference between initial curves and the corresponding parts of the loops. Different domain structures were observed in the samples demagnetized by perpendicular and in-plane magnetic fields.

I. INTRODUCTION

Multilayered films of Co/Pt and Co/Pd are promising materials for magneto-optical (MO) recording[1,2]. Compared to amorphous rare earth-transition metal alloys [3] currently used in commercial MO disks the multilayers are attractive for their superior corrosion resistance [4] and larger Kerr effect signal at short wavelengths [5] (<500 nm), where higher density recording is possible. Co/Pt multilayers have generally been considered more attractive than Co/Pd because of their larger Kerr rotation angle. Co/Pt is deficient, however, in coercivity. The coercivity of Co/Pd multilayers is considerably higher than that for Co/Pt [6]. The coercivity plays an important role in the recording process, since it governs the domain size, shape and stability during readout. Any fluctuations in coercivity may cause an inhomogeneity in domain shape, which in turn contributes to recording noise. The study of coercivity mechanisms in the multilayered structures is also of great importance from the fundamental point of view. The coercivity is closely related to magnetic anisotropy of thin films as well as to the microstructure parameters of the magnetic media such as interface quality, growth orientation, crystallite size, distribution of easy axis for individual crystallites and so forth. The shape of magnetic hysteresis loops, initial curves and domain structure also strongly depend on microstructure of the films. Consequently, the investigation of domain structures in multilayered films and their relation to hysteresis loops and initial curves can help in understanding the origins of coercivity in these films.

The present work is devoted to investigation of domain structures in Co/Pd(1.6/6.3 Å)xN multilayers of varying thickness fabricated on different substrates, and their relation with hysteresis loops and initial magnetization curves.

II. EXPERIMENTAL

Multilayers of Co/Pd were fabricated by sputtering in Ar at a pressure of 20 mTorr onto various substrate conditions. The Co and Pd layers were deposited by rf and dc magnetron sputtering, respectively. Four different conditions were chosen, namely the multilayers were deposited onto Si(111) substrate, Si(111) etched (80A) by Ar, unetched SiN film which was deposited onto Si(111) and etched SiN film on Si(111). The thickness of SiN film was 850 A. For all the cases, individual layer thicknesses of Co and Pd were 1.6 Å and 6.3 Å, respectively. During deposition the substrate was kept at ambient temperature. The Pd layer was the first deposited onto substrate. The number of Co/Pd pairs, N, was 50 for all types of the substrates, and 6, 10, 20, 30, 40 for the etched SiN substrate (see table 1). Last letters in the sample ID mean substrate condition, and a number before the letters is attributable to the number of Co/Pd pairs. For example, sample ID S30ESiN means that substrate is etched SiN layer and the film has 30 Co/Pd pairs.

The measurement of magnetic properties of the samples was carried out by vibrating sample magnetometry in fields up to 14 kOe. The area of the samples for calculation of magnetization was measured using an optical microscope with digitizing image capability. Magneto-optic loops and initial curves were measured in our magneto-optic loop tracer [7] in fields up to 20 kOe. The constants of perpendicular anisotropy were determined using data obtained from the MO loop tracer with in-plane applied field [8]. Domain structures were observed with the help of polarizing optical microscope using a 100x objective (oil immersion type). The observations were recorded with a PC-based frame grabber that allowed image processing for noise reduction, image segmentation and image thresholding [9]. A single-pole, conical tip electromagnet capable of producing a maximum field of 5 kOe, was mounted under the microscope's XY stage to provide the necessary fields for domain growth and contraction.

III. EXPERIMENTAL RESULTS AND DISCUSSION

A. Domain structure and substrate condition

Our observations of domain structure in Co/Pd multilayers indicate that shape of the domains and their growth strongly depends on the substrate conditions and the total thickness of the film. In Fig.1 are shown the domain structures developing in (Co/Pd)x50 multilayered films fabricated on different substrates. The films S50ESi, S50USiN and S50ESiN show domain wall motion dominated magnetization process. Domain structure in the films initially saturated by the field of 20 kOe starts to develop from randomly distributed points. These points are believed to be some defects which facilitate creating a domain wall. Expansion of the domain in the magnetic field close to the coercive field looks like development of maze-like structure with very narrow domains. This behavior proves that DW coercivity is smaller than nucleation coercivity. The domain structure in the film deposited onto unetched Si substrate is quite different (Fig.1d). The remagnetization in this film occurs due to nucleation process. With the increase of the magnetic field the entire film is covered with domains of opposite magnetization; thus the wall coercivity in this film is greater than nucleation coercivity. The magnetic properties of (Co/Pd)x50 multilayers are shown in table 1. It follows from this table that the macromagnetic parameters like M_s and H_c are very similar. K_u is about two times smaller for samples fabricated on unetched substrates. The lower value of K_u in the films on unetched substrates allows to demagnetize the samples with in-plane field of 20 kOe. The same in-plane field, applied to (Co/Pd)x50 films, fabricated on etched Si and SiN substrates, is not able to demagnetize the samples.

The authors of [10] measured the roughness of etched and unetched Si and SiN substrates as well as microstructure of Co/Pt multilayers fabricated on the substrates. They showed that the dispersion angle for $<111>$ orientation of crystallites has the largest value for samples on unetched Si substrates. The presented in [10] magneto-optic loops indicate that the magnetization process in Co/Pt film on unetched Si substrate is nucleation dominated as in our case for Co/Pd film on the similar substrate. So, we can assume, that general microstructural properties of Co/Pt and Co/Pd multilayers on Si and SiN substrates are similar. Hence, the microstructure of the samples seems to be responsible for the type of magnetization process. The film with low perpendicular anisotropy and big dispersion angle of easy axes shows nucleation dominated magnetization. Samples with high anisotropy and low dispersion angle of easy axes show wall-motion dominated magnetization process.

B. Domain structure and film thickness

Figure 2 shows the magnetic and magneto-optic properties of (Co/Pd)xN films of different thicknesses, deposited onto etched SiN substrates, as functions of film thickness. The magnetization of the samples remains the same for N from 50 to 20 decreasing slightly for N=10 and 6. The coercivity decreases starting from 40 layers and reaches very low value of 85 Oe for N=6. Kerr rotation has a maximum for N=10, which is attributable to interference effects [11]. Anisotropy constant K_u decreases with the decrease of film thickness, approaching a value of 7×10^5 erg/cc for N=6. Especially big drop in K_u value occurs at film thicknesses below 120 Å. The authors of [11] showed that this region of film thicknesses corresponds to formation of continuous film structure. For a Co/Pt film with the thickness t of 30 Å the distinct island structure was observed. On the contrary, the film with t= 150 Å had a continuous structure which was formed of very fine crystalline grains with the grain size below 100 Å in diameter.

Figure 3 represents the domain structures in (Co/Pd)xN multilayers of different thicknesses deposited onto etched SiN sublayer. With the decrease of the total thickness of the films the domain width of maze-like structure increases approaching the single domain state at N=10 and dropping again for N=6. The dependence of domain width on film thickness is shown in Fig.4. It is known from the domain theory [12] that the domain structure of the films with uniaxial magnetic anisotropy is effected by film thickness, t, and, in very thin films, single domain structure is attained. In a uniform film with strong perpendicular anisotropy the critical thickness at which the transition from a stripe domain to a single domain occurs is estimated by the formula [11]:

$$t_c = 16.8\sigma/\pi^4 M_s^2$$

where $\sigma=4(AK_u)^{0.5}$ is domain wall energy density, M_s is saturation magnetization, A - exchange stiffness, K_u - anisotropy constant. Using experimental data for K_u and M_s and assuming $A=10^{-7}$ erg/cm we can estimate t_c at about 200 Å. Experimental results indicate that in Co/Pd multilayers this value is about 100 Å. This discrepancy may be attributed to the fact that in the multilayered structures the effective exchange stiffness constant A can be lower than in pure ferromagnet because of the inclusion of nonmagnetic layers of Pd. The appearance of maze-like structure again in (Co/Pd)x6 multilayers can be explained by significant decrease in K_u constant (Fig.2a), so t_c is becoming lower than actual thickness of multilayered film with N=6.

C. Domain structure and initial curves

Measurements of the magneto-optic loops and initial curves have shown that the shape of the initial curve in Co/Pd multilayers strongly depends on the demagnetization procedure (Fig.5). If we demagnetize the sample by a perpendicular field of the same direction as for measuring the initial curve, the initial curve quickly approaches the corresponding point on the magneto-optic loop and goes along it up to saturation value. If we demagnetize the sample by a perpendicular field of opposite sign or by in-plane field the initial curve goes faster than the corresponding part of the magneto-optic loop and approaches the saturation value in lower magnetic fields. This difference between loop and initial curve is greater for samples demagnetized by in-plane magnetic field. In Fig.6 are shown domain structures in S10ESiN and S06ESiN films developed both by perpendicular and in-plane magnetic fields. Usually if we demagnetize by a perpendicular field, the width of the domains is comparable to that for domain structure expanding in the same sample . However if we demagnetize by in-plane fields, the width of domains is noticeably smaller than that for developing domain structure. The most striking difference is observed for S10ESiN film (Fig.6a,b) where single domain state is attained. After demagnetization by in-plane field of 20 kOe the film is covered by submicron domains.

As mentioned earlier, the initial curves for samples demagnetized by perpendicular fields of opposite directions are somewhat different. To determine the source of this difference we performed the following experiment: First, the domain structure was allowed to develop in the magnetic field in one direction (see Fig.7a). Then the reverse magnetic field was applied for several seconds to contract the structure (Fig.7b). The values of both magnetic fields were fixed. Finally, the difference of the two images was obtained (Fig.7c). The experiment has shown that the required field to start shrinking the structure in Fig.7a is lower than the opposite field needed to expand the structure. Figure 7c shows that the contraction occurs along the length of the walls, rather than at domain tips.

The difference in the initial curves for different demagnetized states can originate from pinning of DW on inhomogeneities in the films [13]. If we continue to expand a domain wall we need more field the DW to overcome energy barriers caused by a chain of pinning sites, which the DW has already approached. If the domain shrinks, the DW has some freedom to move between adjacent chains of pinning sites. So, the field required to shrink the DW is lower than that to expand the domain. Demagnetization by in-plane field produces much smaller domains. They arise randomly without any correspondence to pinning sites. In this case the domain walls have even more freedom to move. Moreover, small diameter facilitates collapse of the domains. Therefore the initial curve for the films demagnetized by in-plane field goes much faster than that in the films, demagnetized by perpendicular field.

IV. CONCLUSION

It was found that magnetic and magneto-optical properties and domain structure of Co/Pd multilayers were affected by total film thickness and substrate conditions. Both wall motion- and nucleation-dominated processes were observed in the samples fabricated on different substrates. Magnetization, coercivity and anisotropy of the films decreased significantly as the film thickness dropped below 120 Å. The width of the domain structure increased with the decrease of film thickness, attaining the single domain state at N=10. The initial curves in Co/Pd multilayers were found to depend on the process by which demagnetization had been attained. The samples demagnetized by in-plane field showed the largest difference between initial curve and the corresponding parts of the loop. Different domain structures were observed in the samples demagnetized by perpendicular and in-plane magnetic fields.

REFERENCES

1. P.F.Carcia, W.B.Zeper, F.J.A.M.Greidanus, Materials Research Society Proceedings(Materials Research Society, Pittsburgh, 1989), vol.150, Materials for Magnetooptic Data Storage, p.115

2. S.C.Shin, Jpn.J.Appl.Phys.28,11(1989).

3. T.K.Hatwar, S,C,Shin, D.G.Stinson, IEEE Trans. Magn. 22, 946 (1986).

4. Y.Ochiai, S.Hashimoto, K.Aso, IEEE Trans. Magn. 25, 3755 (1989).

5. S.Hashimoto, Y.Ochiai, J.Magn.Magn. Mater.88, 211 (1990).

6. P.F.Carcia, J. Appl. Phys. 63, 5066 (1988).

7. R.A.Hajjar, T.Wu, M.Mansuripur, J.Appl.Phys.71, 813 (1992).

8. P.Wolniansky, S.Chase, R.Rosenvold, M.Ruane, M.Mansuripur, J.Appl.Phys. 60, 346, (1986).

9. B.E.Bernacki, M.Mansuripur, J.Appl.Phys. 69, 4960, (1991).

10. T.Suzuki, H.Notaris, D.C.Dobbertin, C.-J.Lin, D.Weller, D.C.Miller, G.Gorman, IEEE Trans. Magn. 28, 2754, (1992).

11. S.Hashimoto, Y.Ochiai, K.Aso, J. Appl. Phys. 67, 4429, (1990).

12. C.Kittel, Phys. Rev. 70, 965, (1966).

13. H.Fu, R.Giles, M.Mansuripur, G.Patterson, Computers in Phys., 6, 610, (1992).

Table 1: Co/Pd(1.6/6.3 Å)xN samples

Sample ID	Number of layers	Substrate	M_s(emu/cc)	Θ_k(deg)	H_c(Oe)	K_u(x10^6 erg/cc)
S06ESiN	6	Etched SiN	320	0.23	85	0.7
S10ESiN	10	Etched SiN	374	0.29	636	3.9
S20ESiN	20	Etched SiN	424	0.25	1549	6.2
S30ESiN	30	Etched SiN	408	0.22	2431	6.8
S40ESiN	40	Etched SiN	405	0.19	2995	7.1
S50ESiN	50	Etched SiN	435	0.17	2990	7.5
S50USiN	50	Unetched SiN	402	0.16	2553	3.6
S50ESi	50	Etched Si	404	0.13	3075	5.5
S50USi	50	Unetched Si	392	0.11	3080	3.3

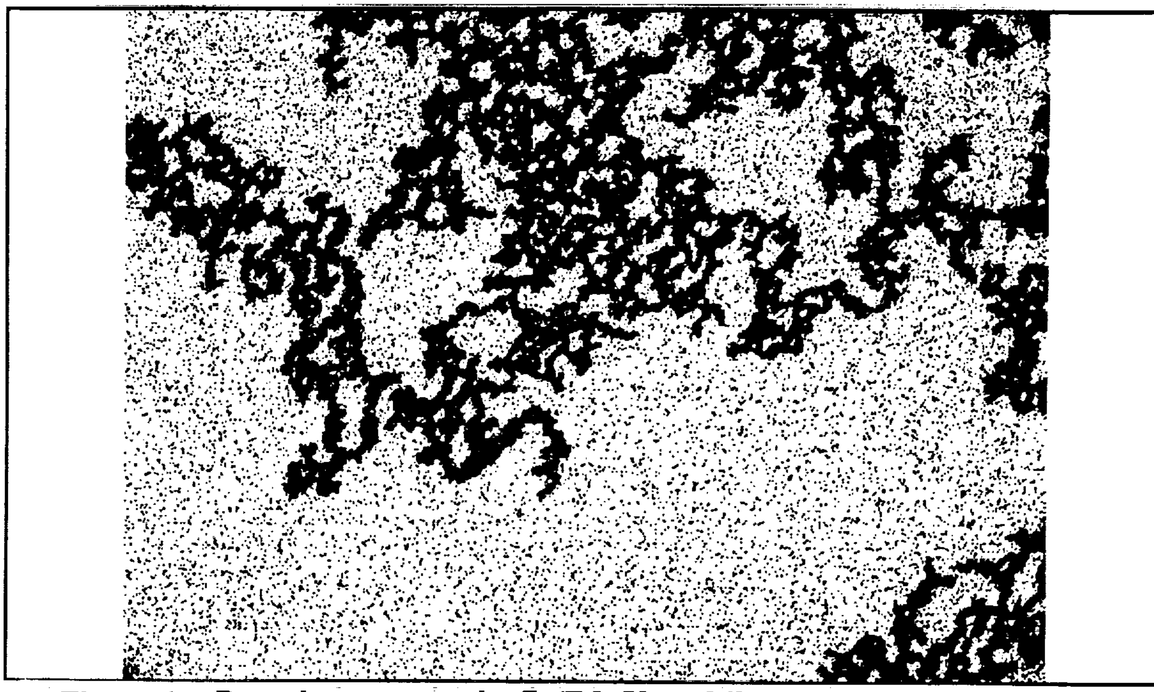

Figure 1a. Domain structure in Co/Pdx50 multilayered film, deposited onto etched SiN layer, developing at H=2.8 kOe.

⊢ 10μm ⊣

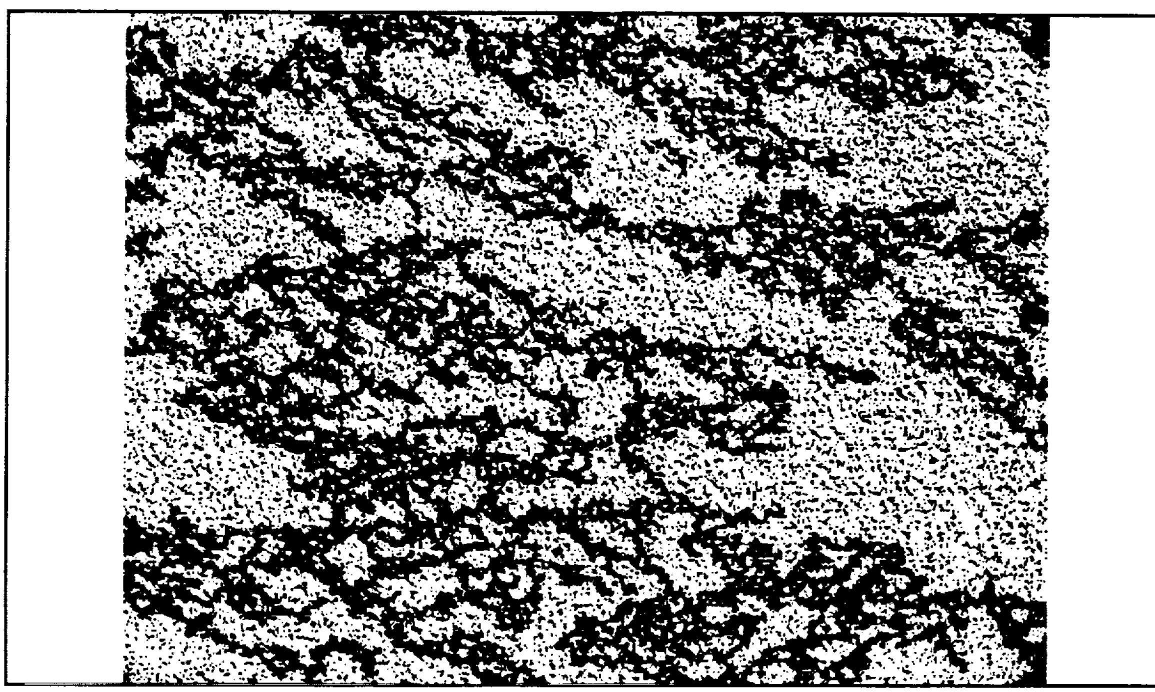

Figure 1b. Domain structure in Co/Pdx50 multilayered film, deposited onto unetched SiN layer, developing at H=2.29 kOe.

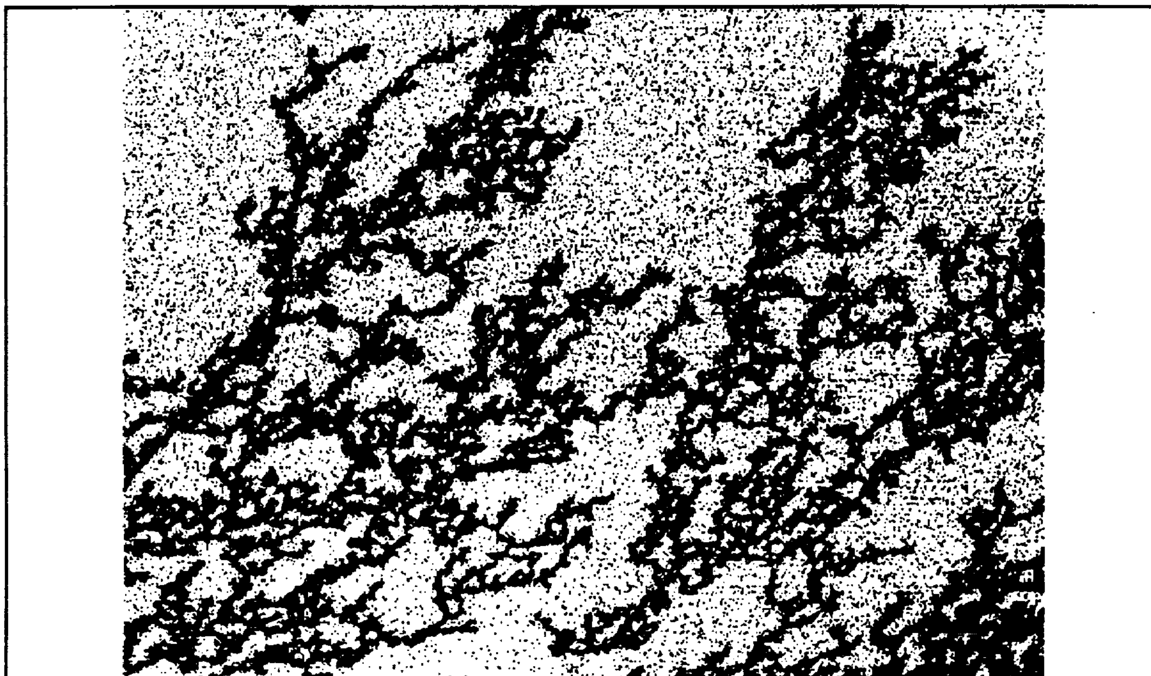

Figure 1c. Domain structure in Co/Pdx50 multilayered film, deposited onto etched Si substrate, developing at H=2.8 kOe.

⊢ 10μm ⊣

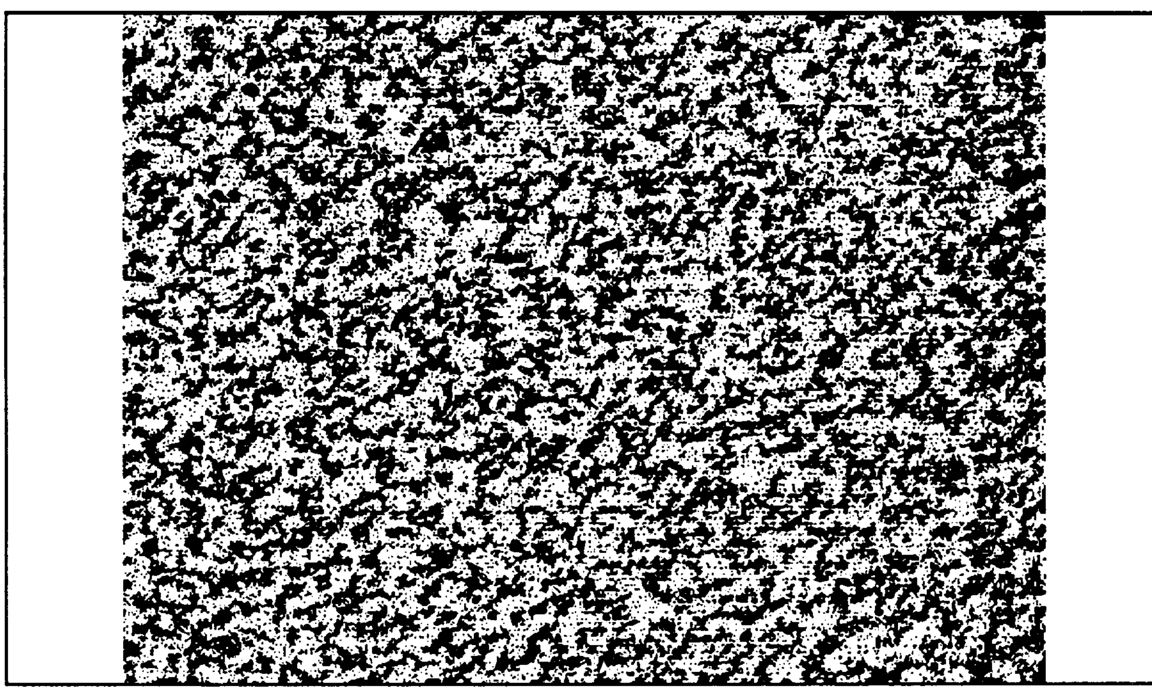

Figure 1d. Domain structure in Co/Pdx50 multilayered film, deposited onto unetched Si substrate, developing at H=2.67 kOe.

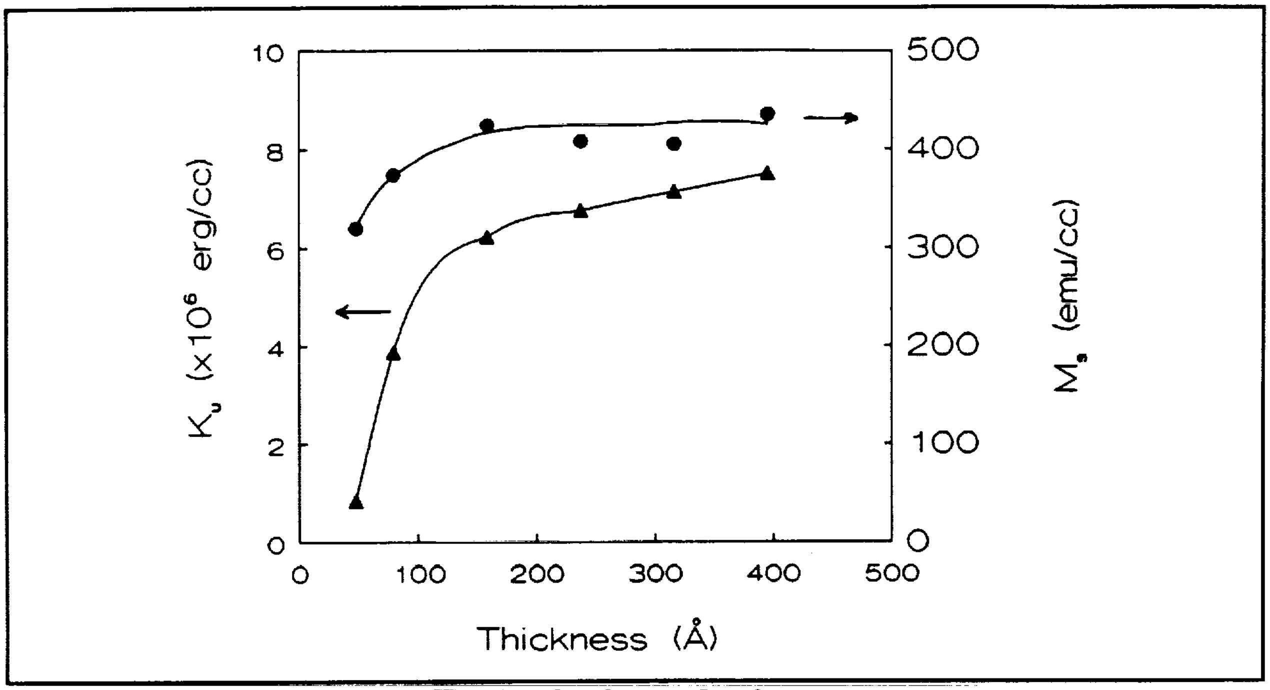

Figure 2a. Dependence of magnetization and anisotropy constant on the thickness of Co/Pd multilayers.

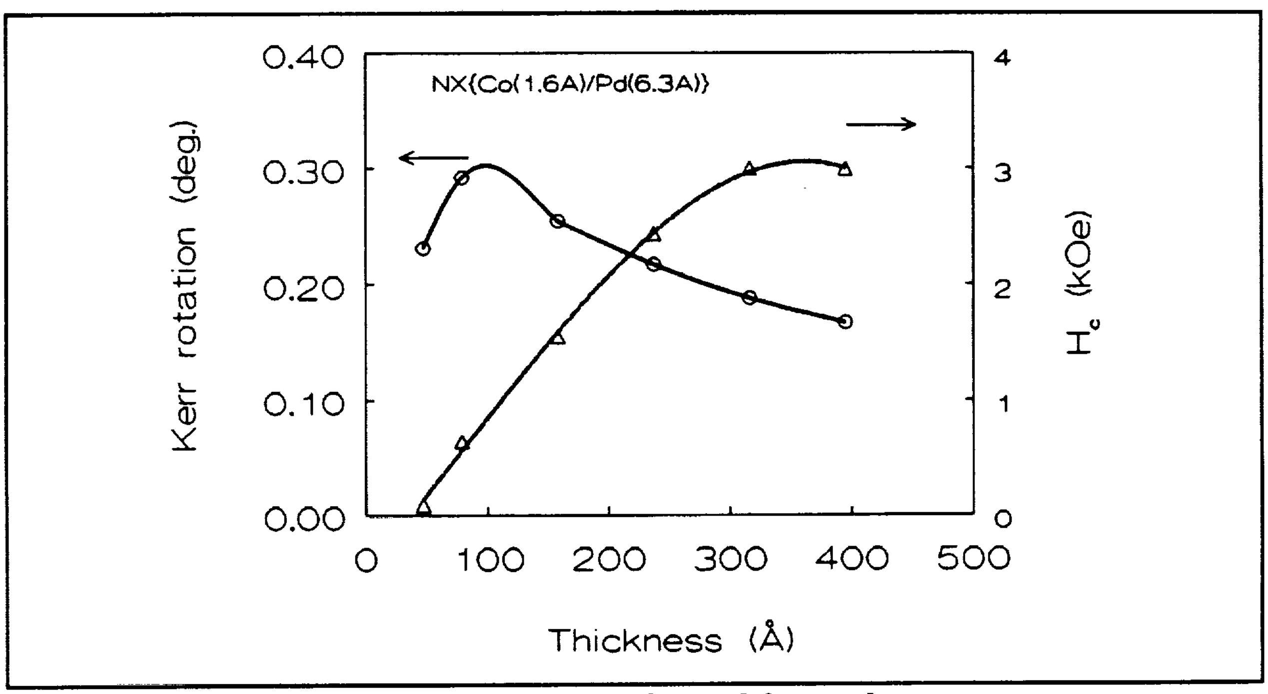

Figure 2b. Dependence of Kerr angle and coercivity on the thickness of Co/Pd multilayers.

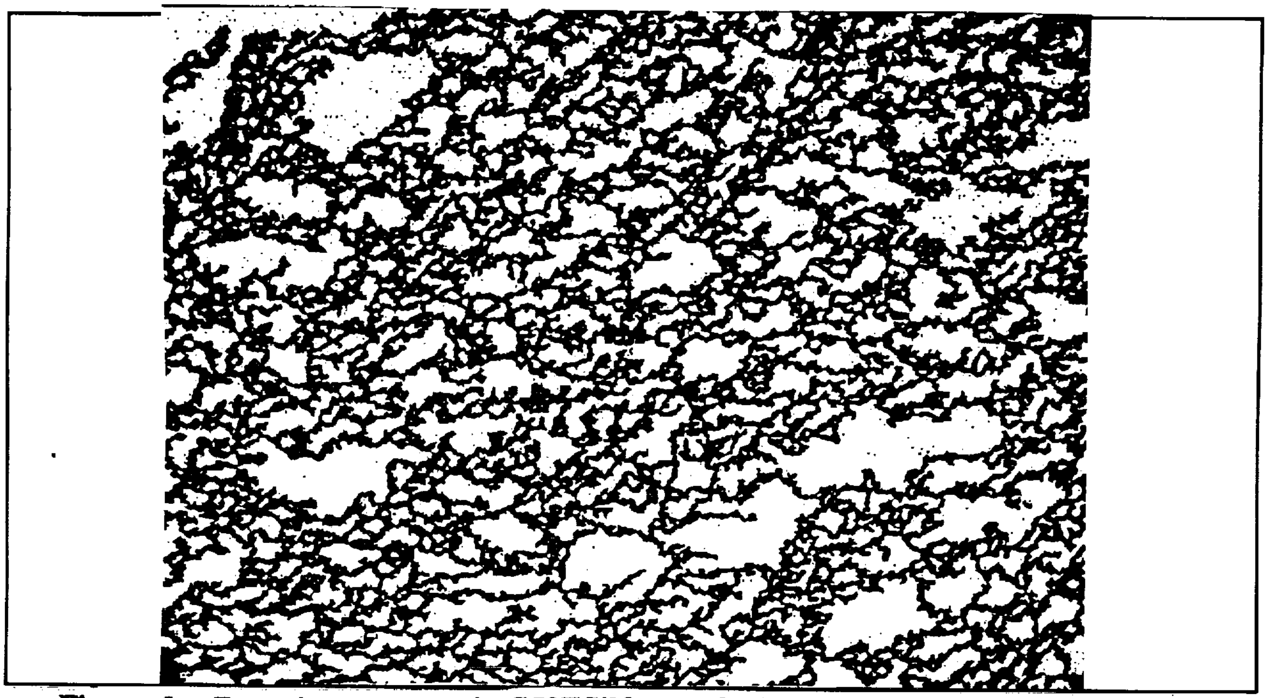

Figure 3a. Domain structure in S50ESiN sample developing at H=2.8 kOe.

⊢ 10μm ⊣

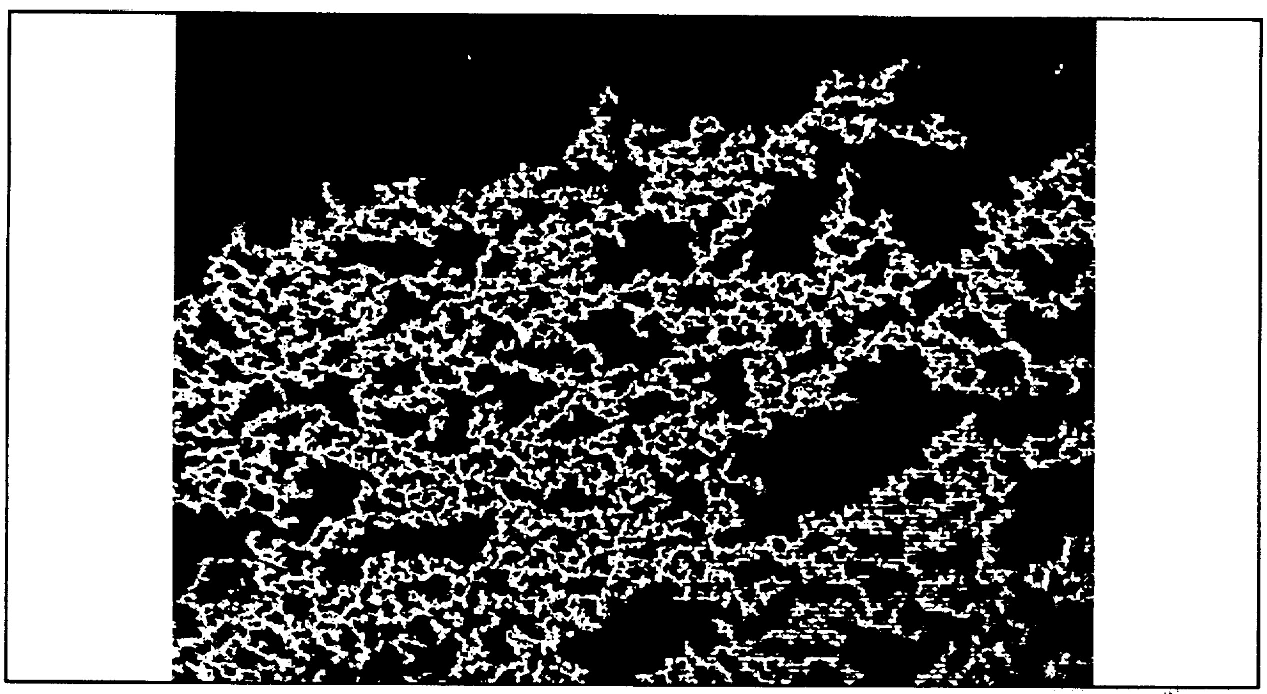

Figure 3b. Domain structure in S40ESiN sample developing at H=2.8 kOe.

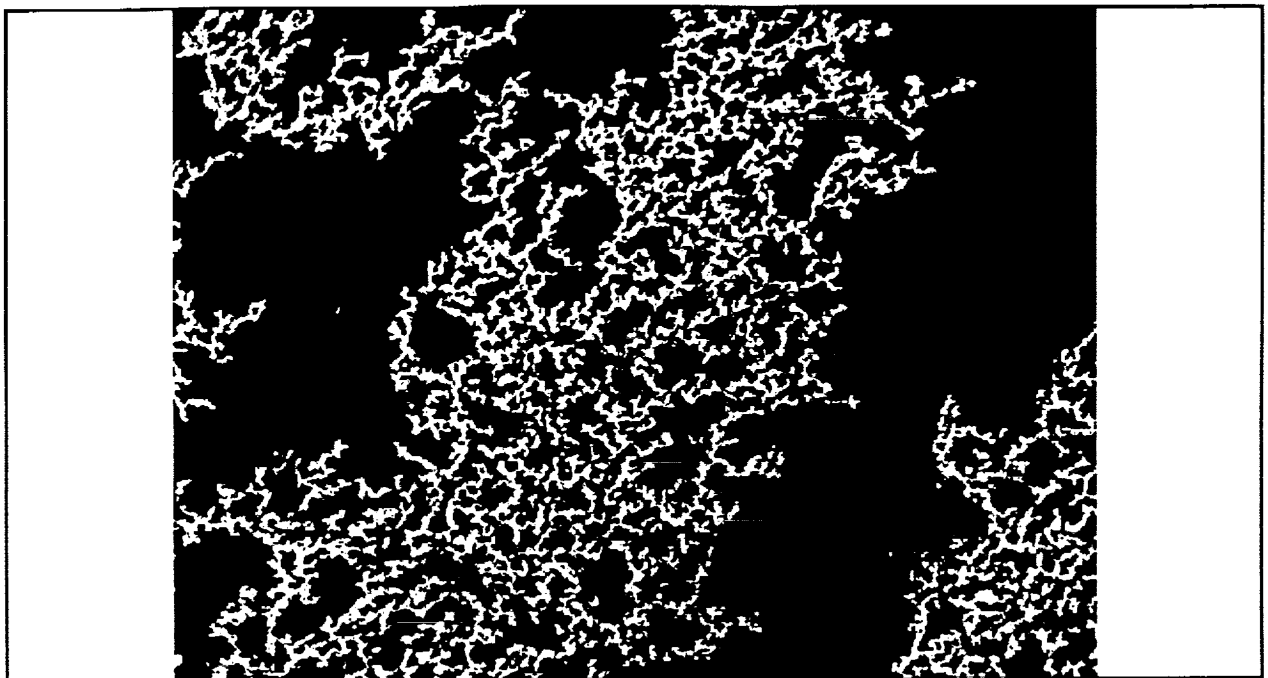

Figure 3c. Domain structure in S30ESiN sample developing at H=2.44 kOe.

⊢ 10μm ⊣

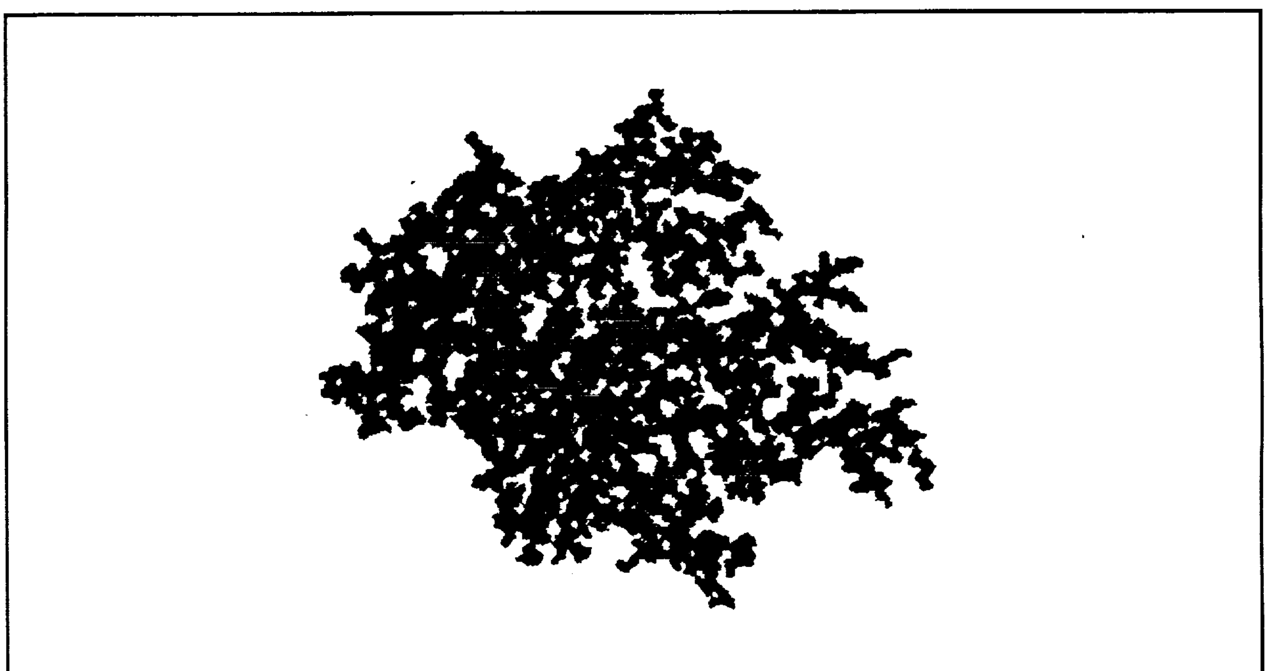

Figure 3d. Domain structure in S20ESiN sample developing at H=1.63 kOe.

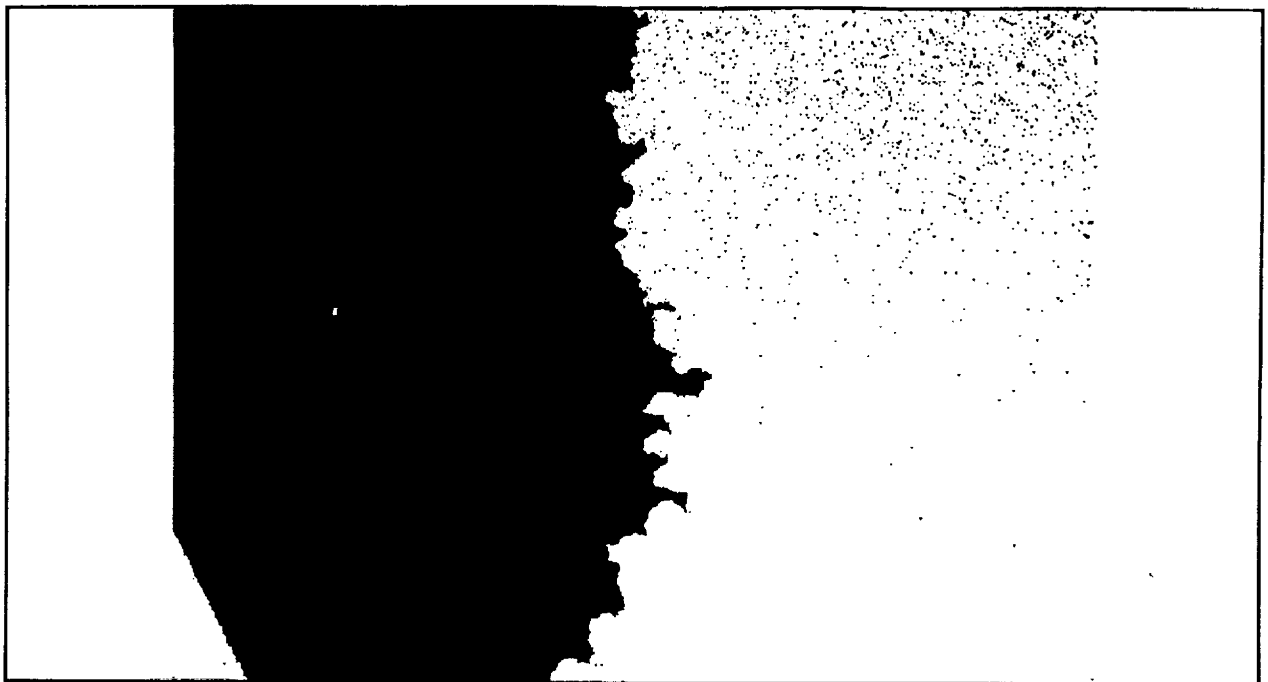

Figure 3e. Domain structure in S10ESiN sample developing at H=0.85 kOe.

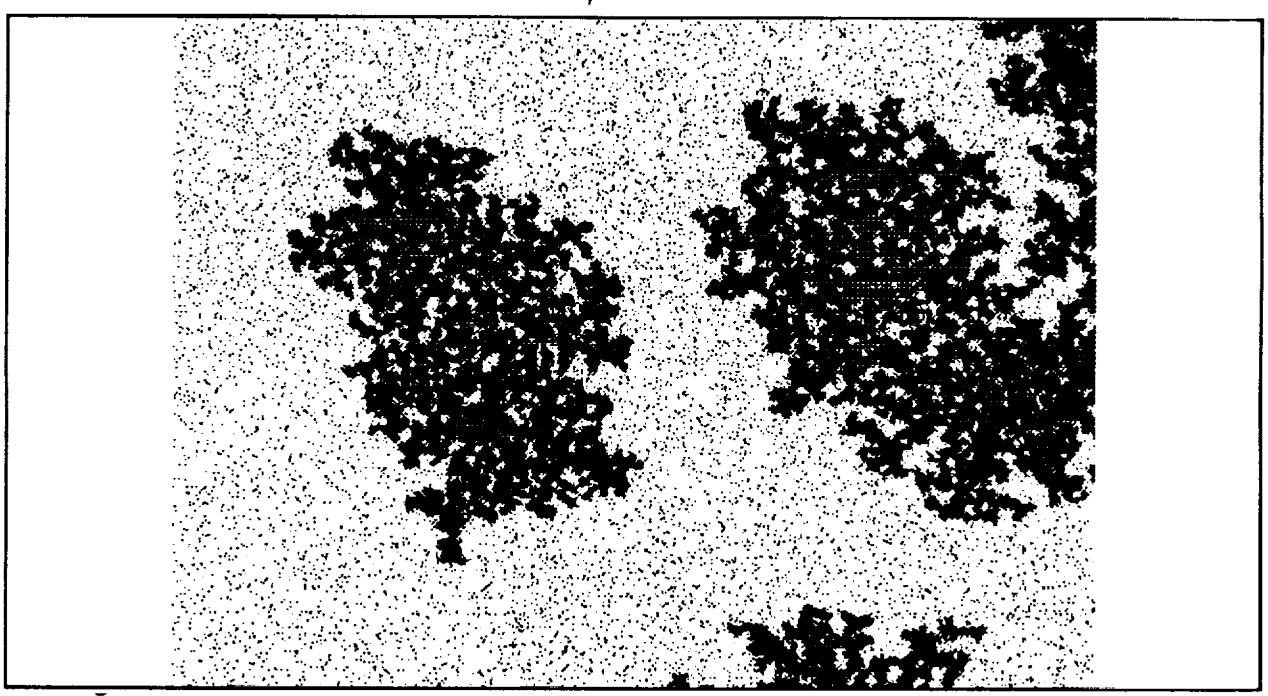

Figure 3f. Domain structure in S06ESiN sample developing at H=0.12 kOe.

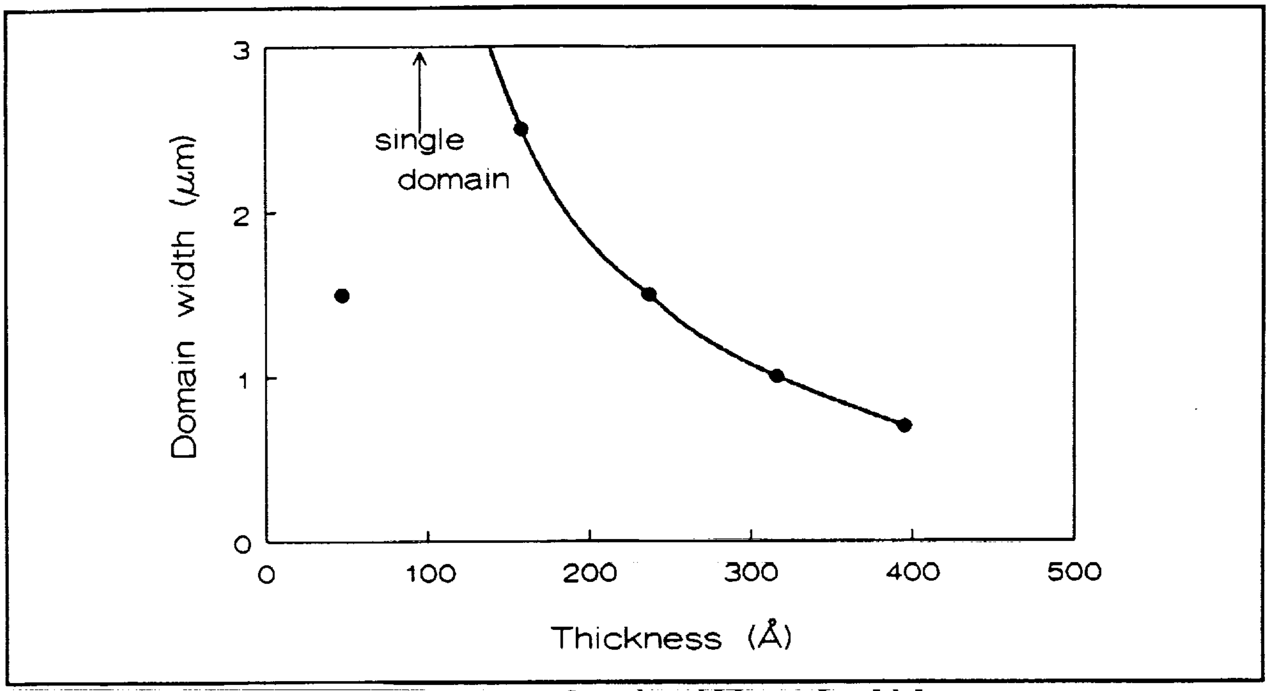

Figure 4. Dependence of average domain width on the thickness of Co/Pd multilayers.

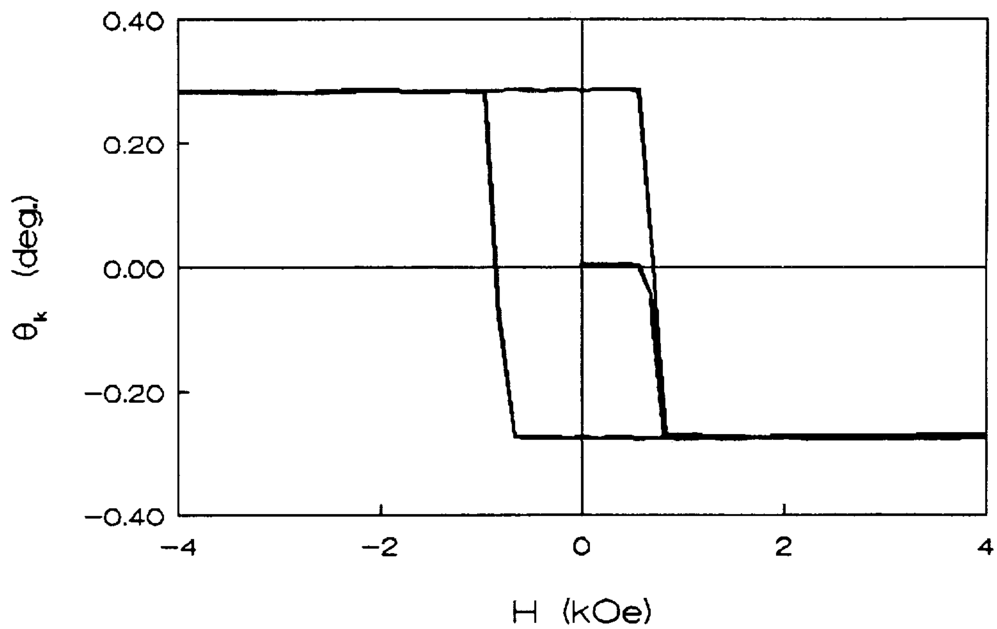

Figure 5a. Sample S10ESiN. Kerr rotation hysteresis loop and initial curve with perpendicular demagnetized field Hd=+580 Oe.

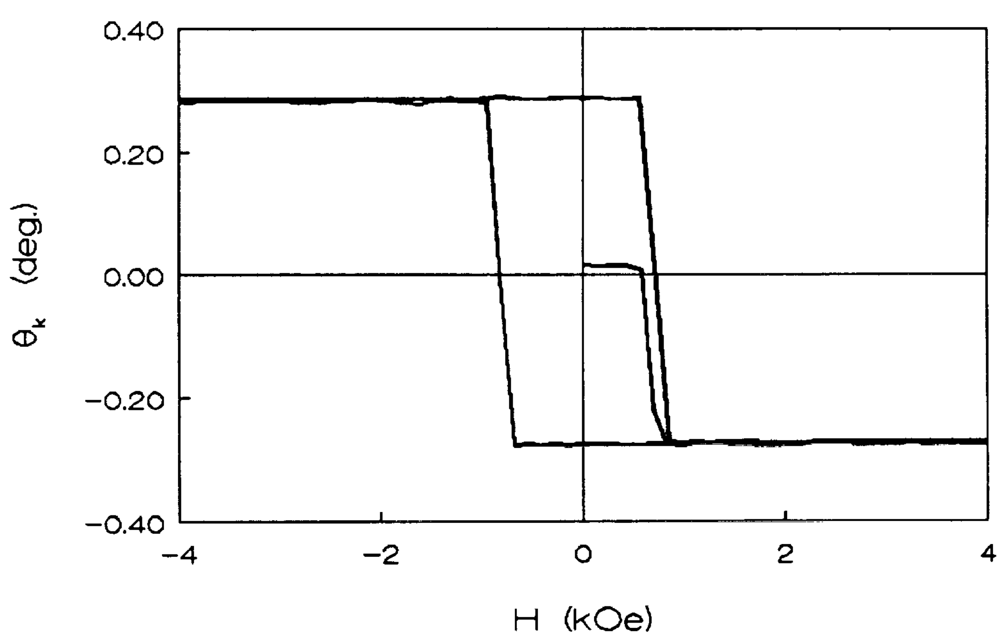

Figure 5b. Sample S10ESiN. Kerr rotation hysteresis loop and initial curve with perpendicular demagnetized field Hd=-620 Oe.

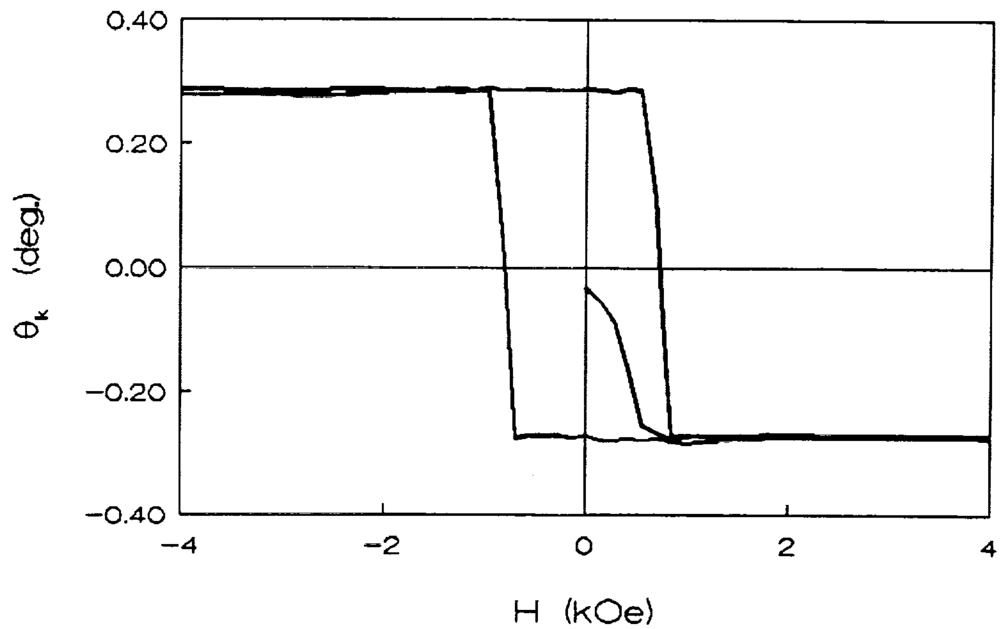

Figure 5c. Sample S10ESiN. Kerr rotation hysteresis loop and initial curve with in-plane demagnetized field.

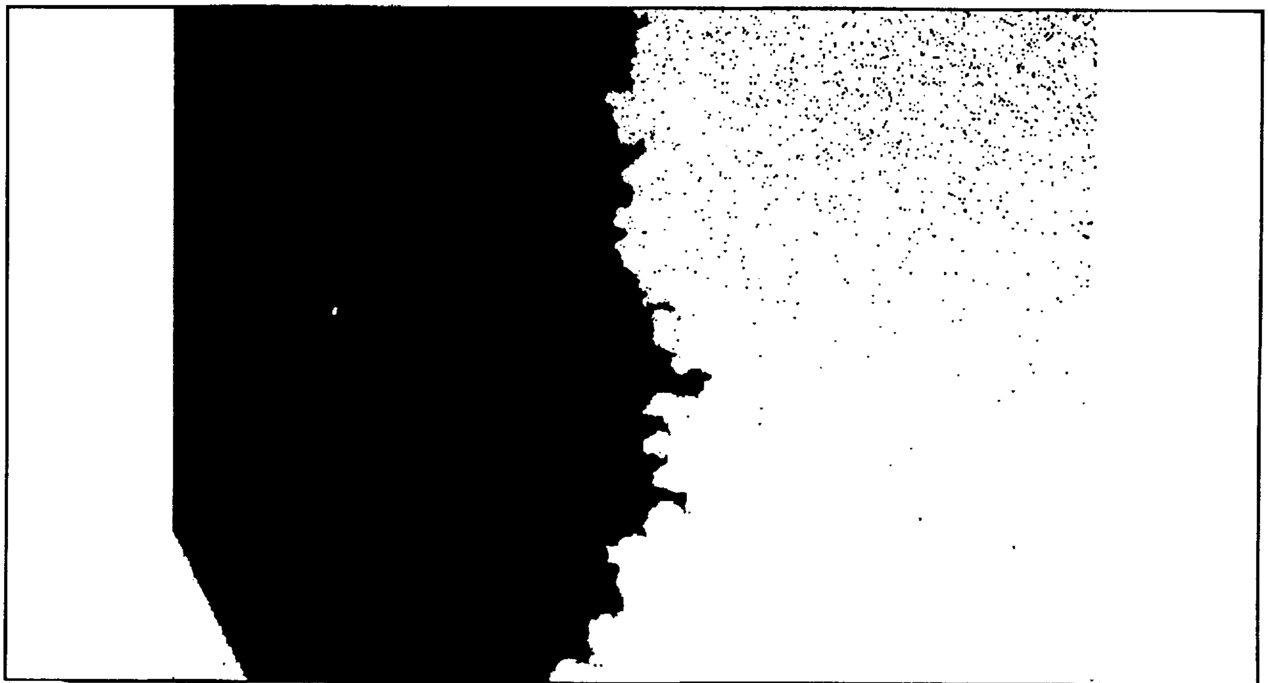

Figure 6a. Domain structure in S10ESiN sample developing at H=0.85 kOe.

⊢ 10μm ⊣

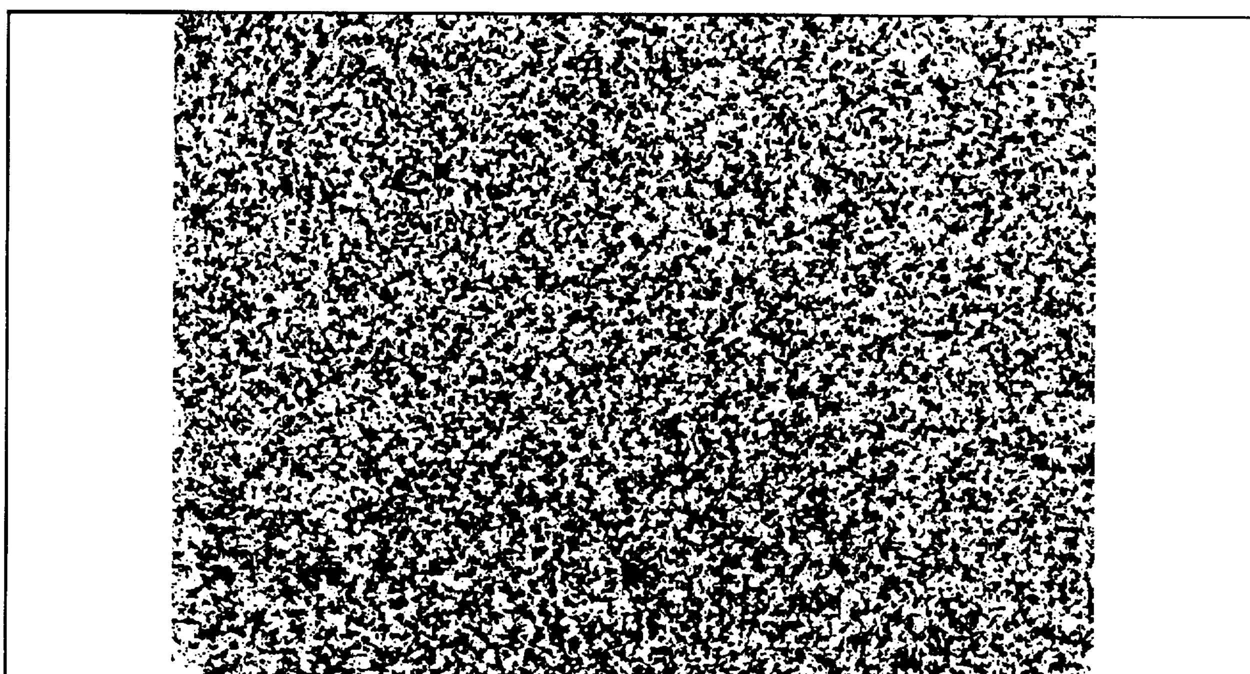

Figure 6b. Domain structure in S10ESiN sample after demagnetization by in-plane magnetic field Hd=20 kOe.

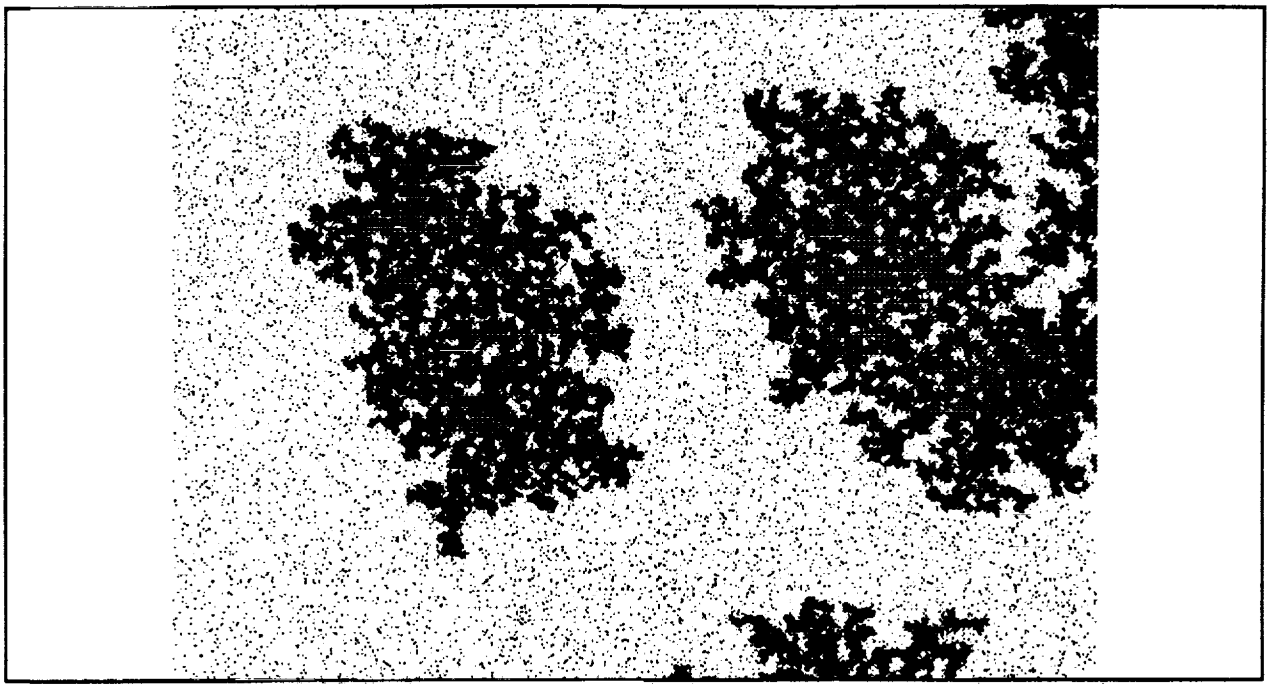

Figure 6c. Domain structure in S06ESiN sample developing at H=0.12 kOe.

⊢ 10μm ⊣

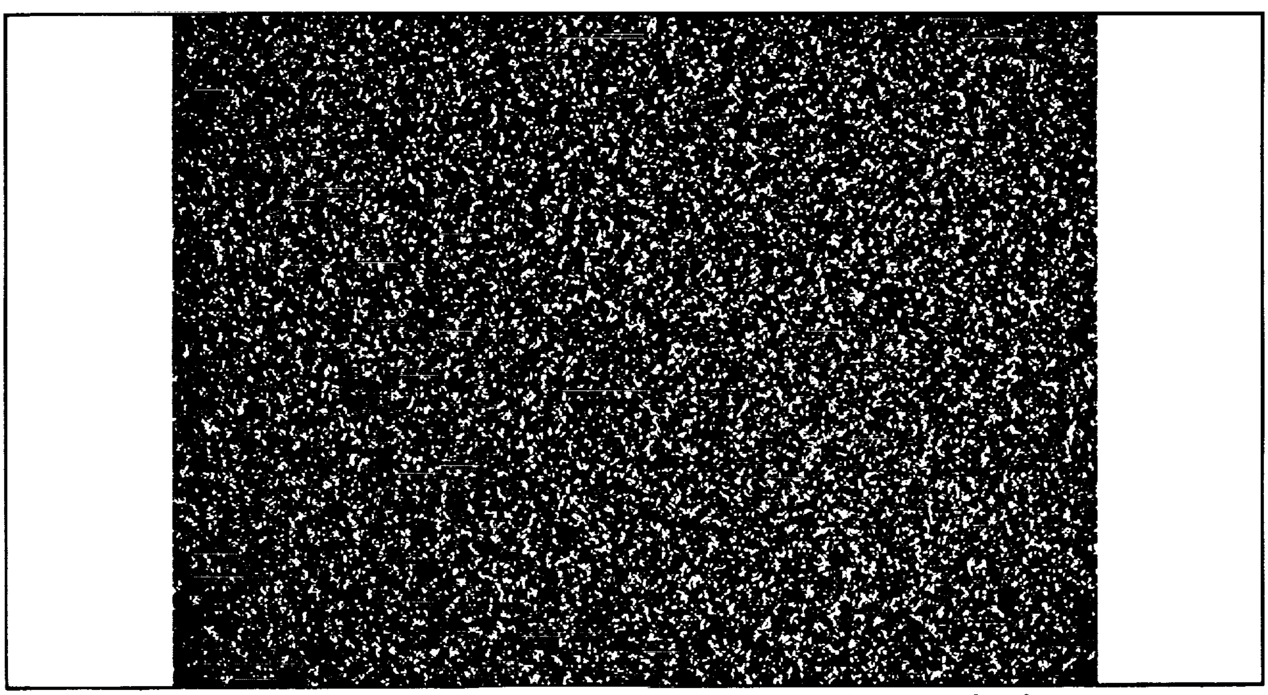

Figure 6d. Domain structure in S06ESiN sample after demagnetization by in-plane magnetic field Hd=20 kOe.

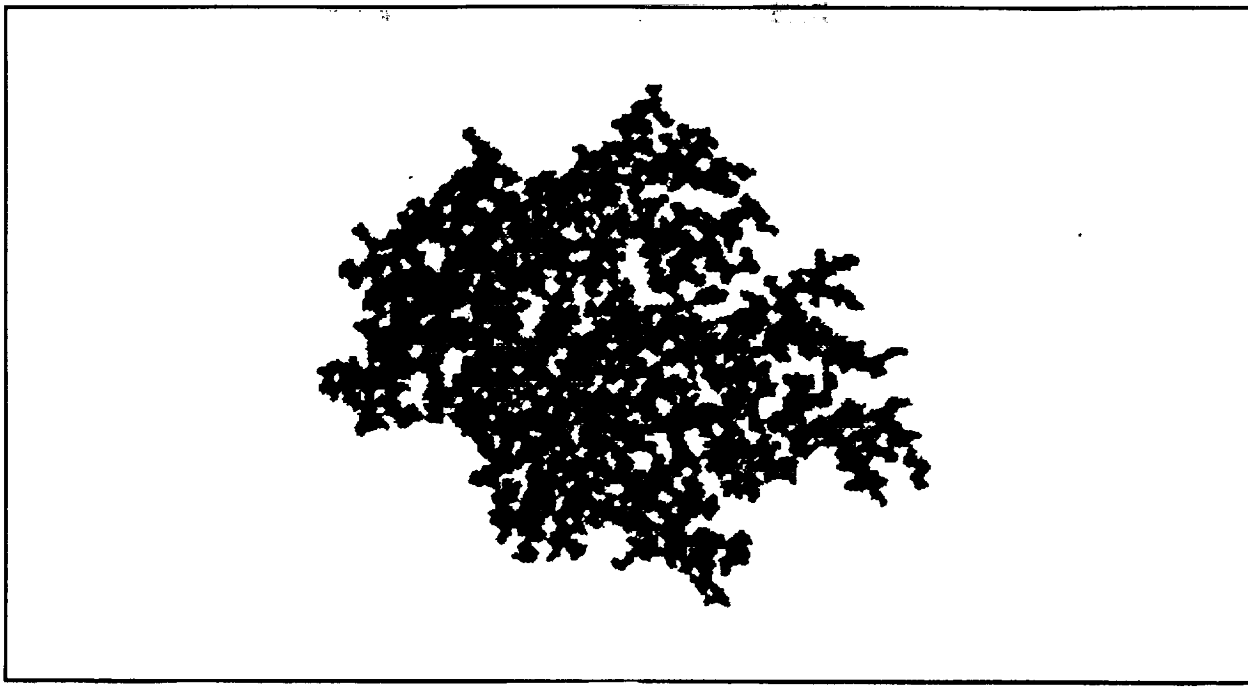

Figure 7a. Domain structure in S20ESiN sample developing at H=1.63 kOe.

⊢ 10μm ⊣

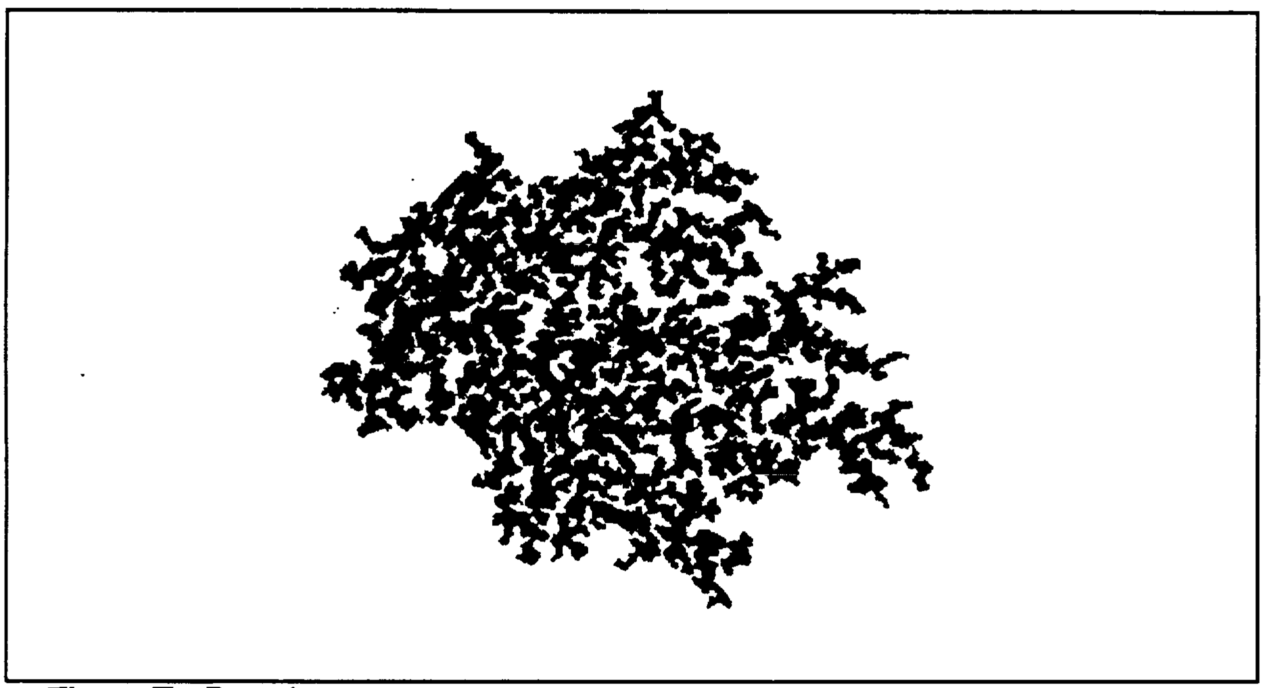

Figure 7b. Domain structure in S20ESiN sample after application of reverse field.The initial domain structure is shown in figure 7a.

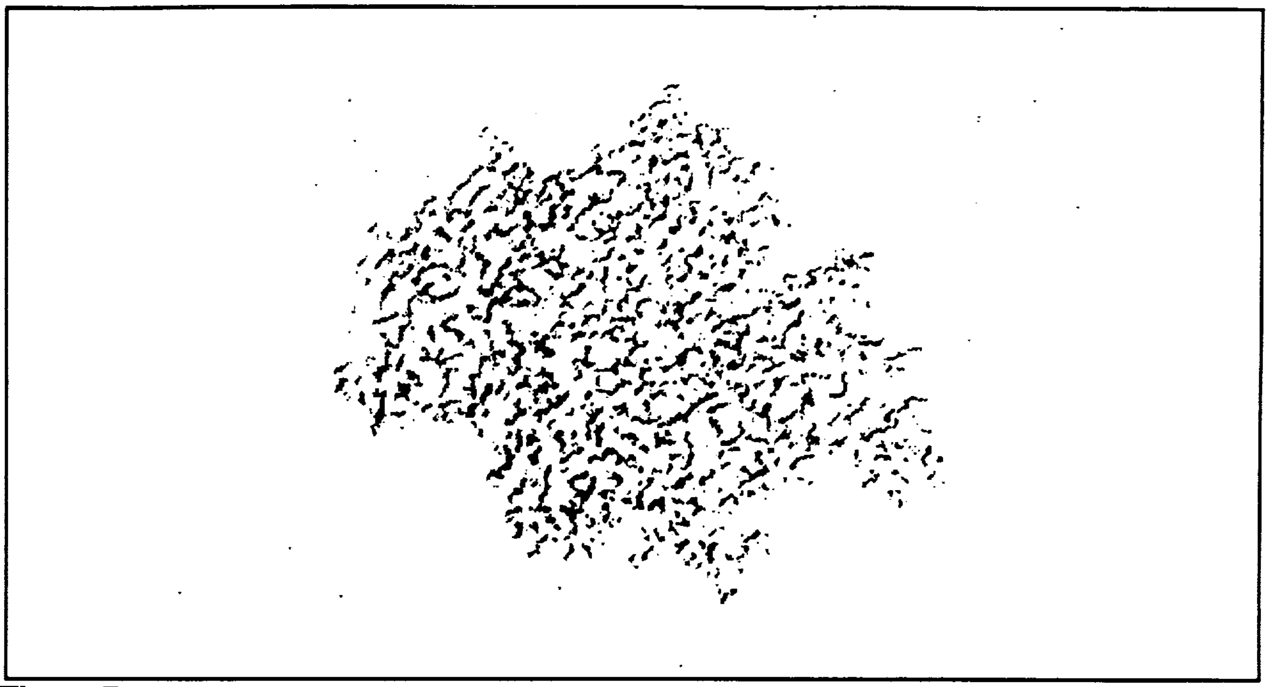

Figure 7c. The black areas show the difference between domain structures, shown in figures 7a and 7b.

⊢ 10μm ⊣

APPENDIX D

N94-14992

Determination of Average Refractive Index of Spin Coated DCG Films for HOE Fabrication

T. J. Kim, Eugene W. Campbell, and Raymond K. Kostuk
Department of Electrical and Computer Engineering
and Optical Sciences Center
University of Arizona
Tucson, AZ, 85721

Abstract

The refractive index of holographic emulsions is an important parameter needed for designing holographic optical elements (HOEs). In this paper theoretical calculations of the accuracy required for the refractive index and thickness of emulsions needed to meet predetermined Bragg angle conditions are presented. A modified interferometric method is used to find average refractive index of the unexposed and the developed dichromated gelatin holographic films. Slanted transmission HOEs are designed considering the index and thickness variations, and used to verify the index measurement results. The Brewster angle method is used to measure surface index of the unexposed and the developed films. The differences between average index and surface index are discussed. Theoretical calculation of the effects of index variation on diffraction efficiency, and experimental results for index modulation variation caused by process changes are also presented.

1.0 Introduction

The refractive index of dichromated gelatin (DCG) film is a function of many parameters. These include gelatin type, dichromate concentration, film thickness, environmental conditions (relative humidity and temperature), hologram construction conditions (exposure energy, construction geometry, wavelength) and chemical development. A number of researchers have previously investigated the refractive index of DCG films[1]-[8]. Several different techniques were used to investigate the index, such as Abbe refractometry, Brewster angle methods, interferometry with index matching oil, and diffraction efficiency measurements with coupled wave analysis. The reported index values range from 1.20 to 1.71. This large uncertainty in index makes it difficult to accurately design holographic optical elements.

In order to design HOEs properly, the average refractive index before exposure and after development must be known within an acceptable range. This paper presents the experimental results for the surface and the average refractive index of spin coated DCG holographic films. It also shows how variations in these values affect the reconstruction angle for slanted volume holograms.

2.0 The Effect of Index Change on Bragg Angle

DCG film can swell or shrink after chemical development. This causes the grating $\underline{K}$ vector to rotate. The Bragg reconstruction angle (or angle for maximum diffraction efficiency) caused by a shift in the $\underline{K}$ vector can be predicted using coupled wave analysis[9]. If the emulsion thickness during construction is t_c and the thickness during reconstruction is t_r a thickness factor can be defined as

$$m = t_r/t_c. \tag{1}$$

The $\underline{K}$ vector will change according to

$$\begin{aligned} \underline{K}_{r_z} &= \frac{1}{m} \cdot \underline{K}_{c_z}, \\ \underline{K}_{r_x} &= \underline{K}_{c_x}. \end{aligned} \tag{2}$$

where the subscripts r and c denote the reconstruction and construction, respectively. The slant angle ϕ will be modified as

$$\tan\phi_r = m \cdot \tan\phi_c. \tag{3}$$

From Bragg angle condition, $\cos(\phi - \varphi) = \mid \underline{K} \mid / 2\beta$[9], the reconstruction angle in the medium can be determined from

$$\varphi_r = \phi_r + \cos^{-1}\left(\frac{\mid \underline{K}_r \mid}{2\beta_r}\right) - \pi, \tag{4}$$

where $\beta_r = 2\pi n_r/\lambda_r$. The shift in the Bragg reconstruction angle is a function of the thickness change (m), and the average refractive index (n_r) after development. It varies with the value for the $\underline{K}$ vector slant angle as shown in Fig. 2 (10°), Fig. 3 (30°), and Fig. 4 (50°). Indices of the surface and the bulk area for the unexposed film were almost the same which were measured using the Brewster angle method (see 3.1) for the surface and using a modified interferometric method (see 3.2) for the bulk area.

When the $\underline{K}$ vector slant angle increases, the shift in Bragg reconstruction angle becomes larger in air for the same average refractive index variation. For example, when the desired reconstruction angle is 9.3° ± 0.5°, the predicted average refractive index of n_r = 1.44, n_c = 1.59, and the thickness swells by 5 % (m=1.05), the allowed average refractive index can range from 1.27 to 1.60 (Fig.2). However, when the desired reconstruction angle is 45.4° ± 0.5° with n_r = 1.44, n_c = 1.59, and m=1.05, the allowed average refractive index range is reduced to 1.415 to 1.465 (Fig.4). Therefore, the range in average refractive index must be reduced for gratings with higher $\underline{K}$ vector slant angles.

3.0 Refractive Index Measurement Techniques

All the DCG spin coated films used for these experiments have a composition consisting of [Ammonium dichromate : Gelatin : DI water = 10 gram : 30 gram : 250 ml]. The film thickness was measured with a Tancor alpha-step 200 with a vertical resolution 0.005 μm. The unexposed DCG film is isotropic and uniform (t_c ± 0.12 μm) over 10 mm. Thus, it is relatively easy to measure the refractive index. However, it is very difficult to measure the refractive index for the developed hologram because the film surface is not as uniform ($t_r \pm 0.32\ \mu m$) and the phase variation through the grating is not linear[7], [8]. Therefore, several refractive index measuring techniques were used to evaluate developed DCG holographic gratings. The Brewster angle measurement technique and Fabry Perot resonant method are used to evaluate for the surface index, a modified interferometric method is used to determine the bulk average index of nongrating region, and the average index of grating region is measured using an analysis of the resultant grating efficiency.

3.1 Brewster Angle Method

This method (Fig.5) was developed by Pawluczyk et al. [4],[7],[8]. It gives only the surface refractive index[10]. Special care is required in measuring the Brewster angle because the interference of light reflected from air-emulsion and emulsion-substrate exists and it becomes dominant around the Brewster angle[4], [8].

The measurement results are, $n_c(\lambda = 514.5nm) = 1.590 \pm 0.005$, $n_c(\lambda = 632.8nm) = 1.570 \pm 0.005$ for the unexposed film and $n_r(\lambda = 514.5nm) = 1.570 \pm 0.005$, $n_r(\lambda = 632.8nm) = 1.540 \pm 0.005$ for the uniformly exposed and developed film.

3.2 Interference Method

This method is very useful for measuring the bulk index of the emulsion, however, the cutting ruins the film (Fig.6). Calibrated Cargille index matching oil is used and the remaining index matching oil between trials is removed with ethyl ether. There is some degree of error if the oil is not completely removed between measurements.

The film is rotated during the measurement by an angle θ_e (Fig. 6) in order to eliminate ambiguities in fringe matching. If the rotating angle inside the medium is θ_e and the index difference between emulsion and index matching oil is Δn, then the relative fringe movement as a function of θ_e follows the relationship

$$2 \cdot \frac{2\pi \Delta n t}{\lambda \cos\theta_e} = 2\pi(q + I), \tag{5}$$

where t is the film thickness, q is integer, and I is the fraction of relative fringe shift. When the shift completes one cycle by increasing the angle θ_e, I = 1, and it is possible to keep track of $|\Delta n|$ variation. When the index of applied matching oil is higher than that of the emulsion, the fringes will either shift up or down with increasing θ_e. When the applied matching oil index is lower than that of the emulsion, the fringe shifts in the opposite direction as θ_e increases. However, Eq. (5) can not be applied in the holographic grating region since the phase variation through grating does not vary linearly with changing θ_e. This method needs more improvements for the index measurement of gratings.

Measured values for the unexposed film were $n_c(\lambda = 632.8nm) = 1.58 \pm 0.01$, for the unexposed and developed film areas $n_r(\lambda = 632.8nm) = 1.46 \pm 0.01$, and $n_r(\lambda = 632.8nm) = 1.48 \pm 0.02$ for the uniformly exposed and developed film areas.

3.3 Grating Efficiency Analysis

In this approach the shift in Bragg angle of a volume grating is compared to data using coupled wave analysis[9]. In previous work[6] polarization selective gratings were used to determine the index n_r, and was found to be in a range from 1.2 to 1.4. The specific value depends on the emulsion thickness and processing technique. This experiment was repeated in our lab with an interbeam construction angle of $2\theta_o = 30°$ within the emulsion. This results gave an index $n_r \cong 1.38$.

By measuring the Bragg angle shift and thickness change factor (m), the average refractive index can be deduced from the angular tolerance calculation as discussed in section 2.0. Transmission gratings with large slant angles (50° in air) were used since they produce larger shifts in Bragg angle. Pre and post processed film thickness measurements were obtained from different 2×2.5 inch^2 samples taken from the same 4×5 inch^2 plate. The plates were dehydrated with isopropanol/water concentrations of (25-50-75-100-100 %). The maximum efficiency of the hologram used for Bragg angle shift measurements was 88.4 %. The Bragg angle shift was determined from the change in the center of the FWHM values of the efficiency vs. angle measurements and found to change by 5° (see the Exp. data curve in Fig. 7). This corresponds to an average index $n_r = 1.360$ (Fig. 4).

Theoretical calculation based on the rigorous coupled wave analysis[11] was performed and compared with the experimental data in Fig.7. The measured thickness (t_r) is 8.698 μm, however, the effective thickness for the curve fit is 5.0 μm. This lower effective thickness may be caused by the gradual change of index modulation with depth which may be caused by nonuniform chemical dehydration. The difference of index between surface (1.54) and the average value (1.46) is a good evidence for this. More research needs to be done to explain this effect.

3.4 Fabry Perot Resonant Method

Another method examined to determine the refractive index of the emulsion was by comparing the measured reflected beam intensity to calculated reflection values. In the case of a uniform thin emulsion on glass the interference of beam reflected from the air-emulsion and emulsion-glass surfaces give rise to a Fabry Pero effect[12]. Information from the modulated beam intensity can be used to determine the effective index of the emulsion. However, the DCG samples used in our experiment had a high level of surface reticulation in the exposed areas. This resulted in high levels of scatter from the air-emulsion surface which obscured the Fabry Perot effect.

In spite of these difficulties the average index of the emulsion surface could be determined, and was found to be 1.54 for a uniformly exposed region of film and 1.50 for a grating region at 632.8 nm.

4.0 Effect of Dehydration Rate on Index Modulation

The index modulation depends on the exposed energy and the chemical process. Gradual dehydration with isopropyl alcohol concentration of (25-50-75-100-100%) were compared to a rapid dehydration (50-100-100%).

The 1st peak of diffraction efficiency (DE) occurs with an exposure energy of about 70 mJ/cm^2 for the rapid dehydration and with approximately 220 mJ/cm^2 for the gradual dehydration. Normalized curves for DE vs. angle are given in Fig. 8. All measurements were performed as explained in 3.3. For rapid dehydration the Bragg angle shift is about 7.08° and the thickness factor is about m = 1.07. The resultant average refractive index n_r is about 1.348. For the gradual dehydration process the Bragg angle shift is about 5.10°, and the thickness factor is about m = 0.992. This gives an average refractive index n_r of about 1.355. The angular band width at full width - half maximum is $\Delta\theta \cong 13^o$ for the gradual dehydration process and $\Delta\theta \cong 9^o$ for the rapid dehydration. This implies that the effective thickness of the grating is greater for the rapidly dehydrated emulsion.

5.0 Conclusions

In this report several techniques for measuring the change in the average refractive index were evaluated. The effect of inaccuracies in values used for the pre and post processed average index on the diffraction angle from transmission gratings were also determined.

The grating efficiency analysis method was the only method found which give consistent results for the effective index of holographic gratings. The surface refractive index for the holographic gratings was found to be considerably higher than the effective index (i.e. 1.50 vs 1.35). The effect of changing the rate dehydration did not appear to significantly change the effective refractive index.

6.0 Acknowledgments

The authors wish to thank the Optical Circuitry Cooperative at the University of Arizona and the National Science Foundation Grant No. ECS-9109954 for supporting this work. One of us (EWC) also wish to thank Eastman Kodak for a fellowship during this period.

References

[1] Shankoff, T. A., "Phase holograms in dichromated gelatin," *Applied Optics*, V7 N10, p2101, (1968).

[2] Meyerhofer, D., "Dichromated Gelatin," from a book Holographic recording materials, ed. by Smith, H. M., *Springer-Verlag, Berlin Heidelberg, New York*, p74 (1977).

[3] Newell, J. C. W., "Optical holography in dichromated gelatin," D. Phil. Thesis, Oxford University (1987).

[4] Pawluczyk, R., "Modified Brewster angle technique for the measurement of the refractive index of a DCG layer," *Applied Optics*, V29 N4, p589 (1990).

[5] O'Connor, B., "Polarization properties of high numerical apeture holographic optical elements," MS Thesis, Univ. of Arizona (1989).

[6] Rallison, R. D. and Schicker, S. R., "Polarization properties of gelatin holograms," *SPIE Vol. 1667*, (1992).

[7] Pawluczyk, R., et al., "Characterization of DCG holograms during the production process: some practical aspects," *SPIE Vol. 954, Optical Testing and Metrology II*, 40 (1988).

[8] Kim, T. J., "Optimization of dichromated film coatings for holographic recordings," MS Thesis, Univ. of Arizona (1991).

[9] Kogelnik, H., "Coupled wave theory for thick hologram gratings," *Bell Sys. Tech. J.*, V48 N9, p2909 (1969).

[10] Hecht, E., "Optics," 2nd ed., Addison-Wesley Publishing Co., (1987).

[11] Gaylord, T. K., and Moharam, M. G., "Analysis and applications of optical diffraction by gratings," *Proceedings of IEEE*, V73 N5, p894 (1985).

[12] Yariv, A., "Optical Electronics," 4th ed., ch. 4, Holt, Rinehart and Winston Inc., Philadelphia, (1991).

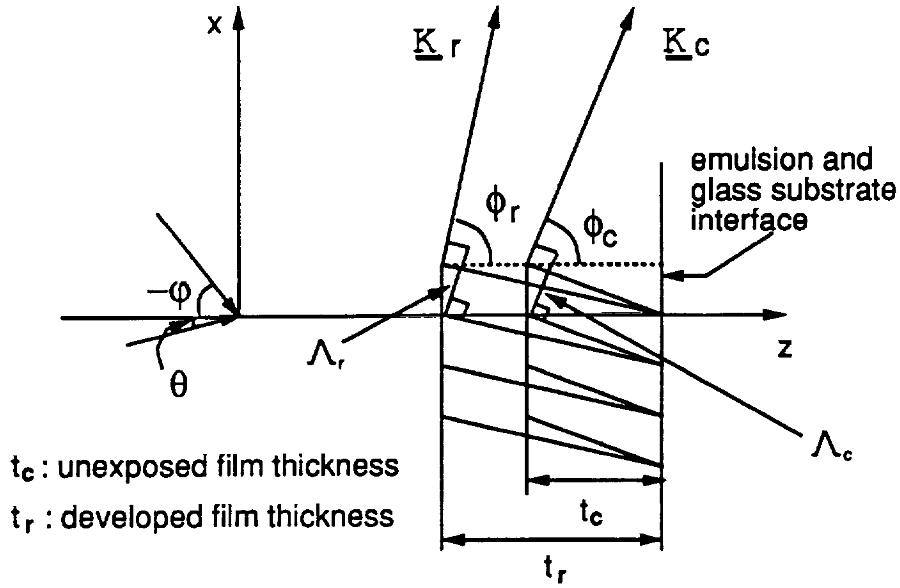

Figure 1: Schematic diagram for the $\underline{K}$ vector shift where r denotes reconstruction and c construction. Λ_r and Λ_c are grating spacings.

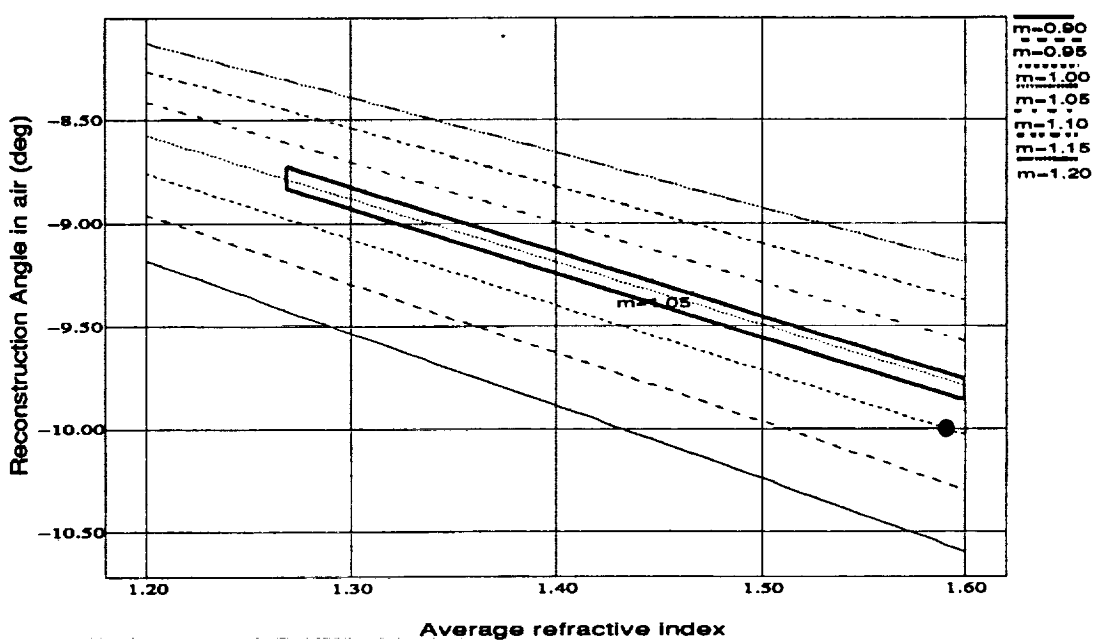

Figure 2: The Bragg angle shift with different thickness change factors as a function of average refractive index. Values given are for a slanted transmission grating; $\theta = 0°$, $-\varphi = 10°$ in air, $\lambda_c = \lambda_r = 514.5$nm. The point • denotes $n_c = n_r = 1.59$ and no thickness variation.

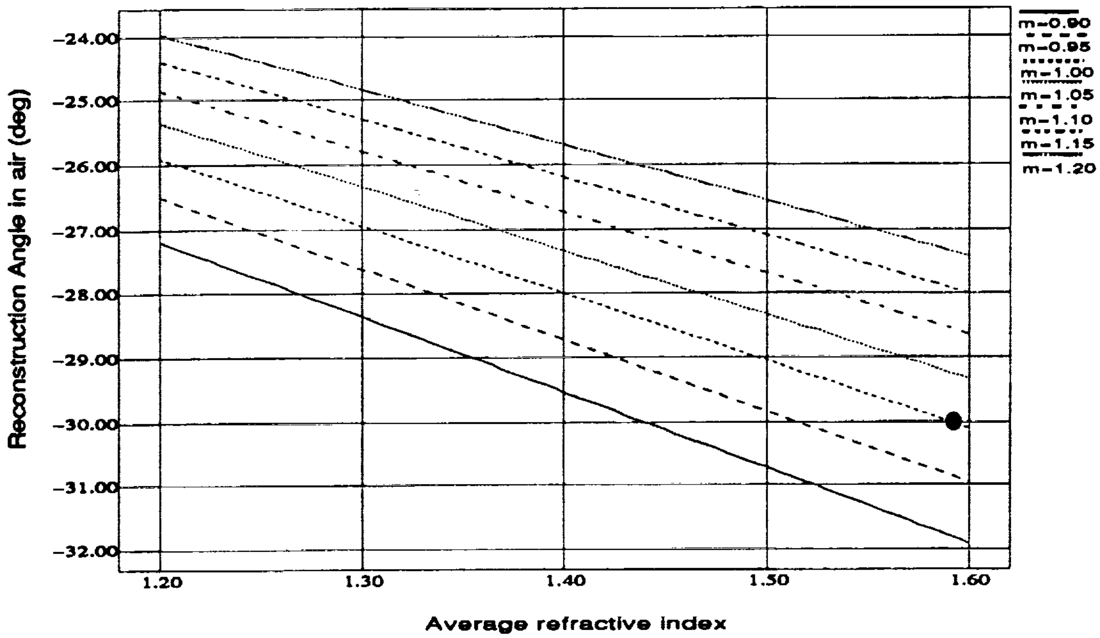

Figure 3: The Bragg angle shift with different thickness change factors as a function of average refractive index. Values given are for a slanted transmission grating; $\theta = 0°$, $-\varphi = 30°$ in air, $\lambda_c = \lambda_r = 514.5$nm. The point • denotes $n_c = n_r = 1.59$ and no thickness variation.

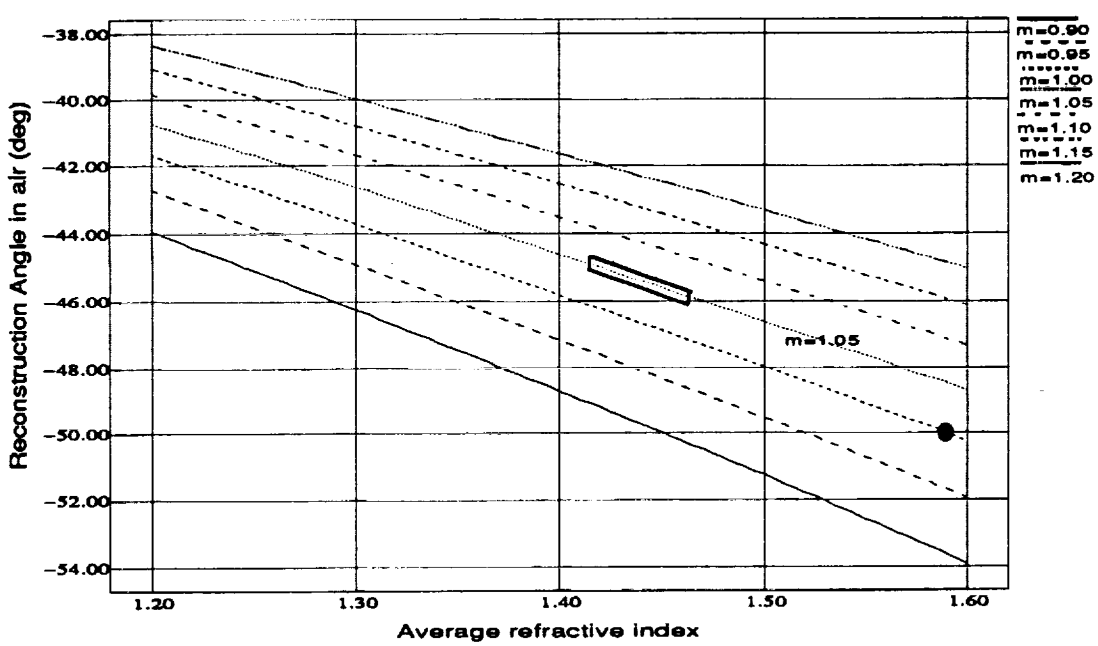

Figure 4: The Bragg angle shift with different thickness change factors as a function of average refractive index. Values given are for a slanted transmission grating; $\theta = 0°$, $-\varphi = 50°$ in air, $\lambda_c = \lambda_r = 514.5$nm. The point • denotes $n_c = n_r = 1.59$ and no thickness variation.

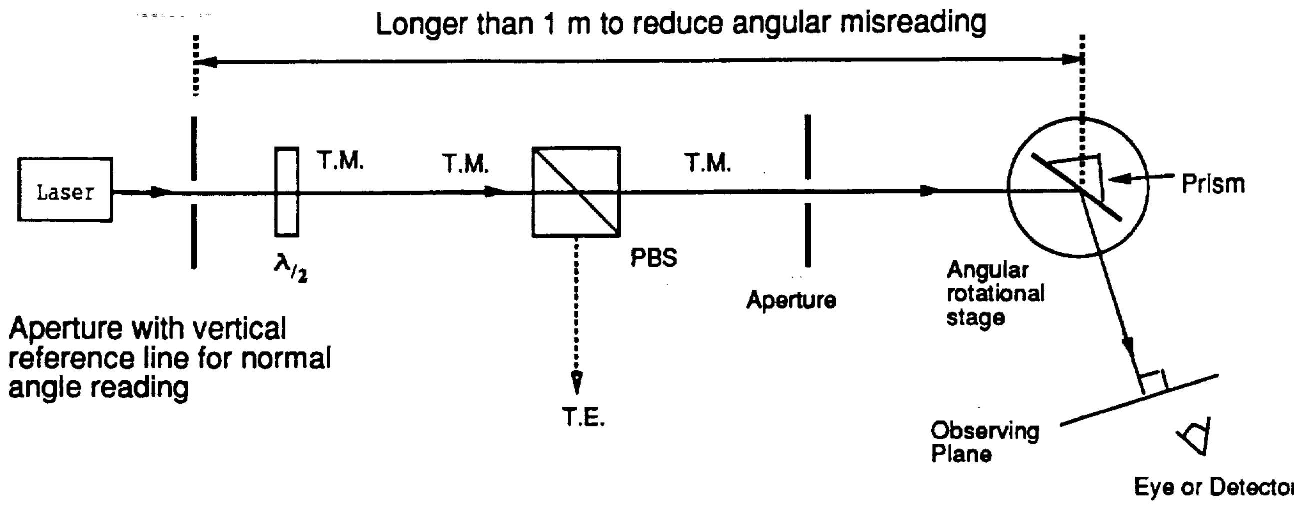

Figure 5: Optical set-up for Brewster angle measurement technique.

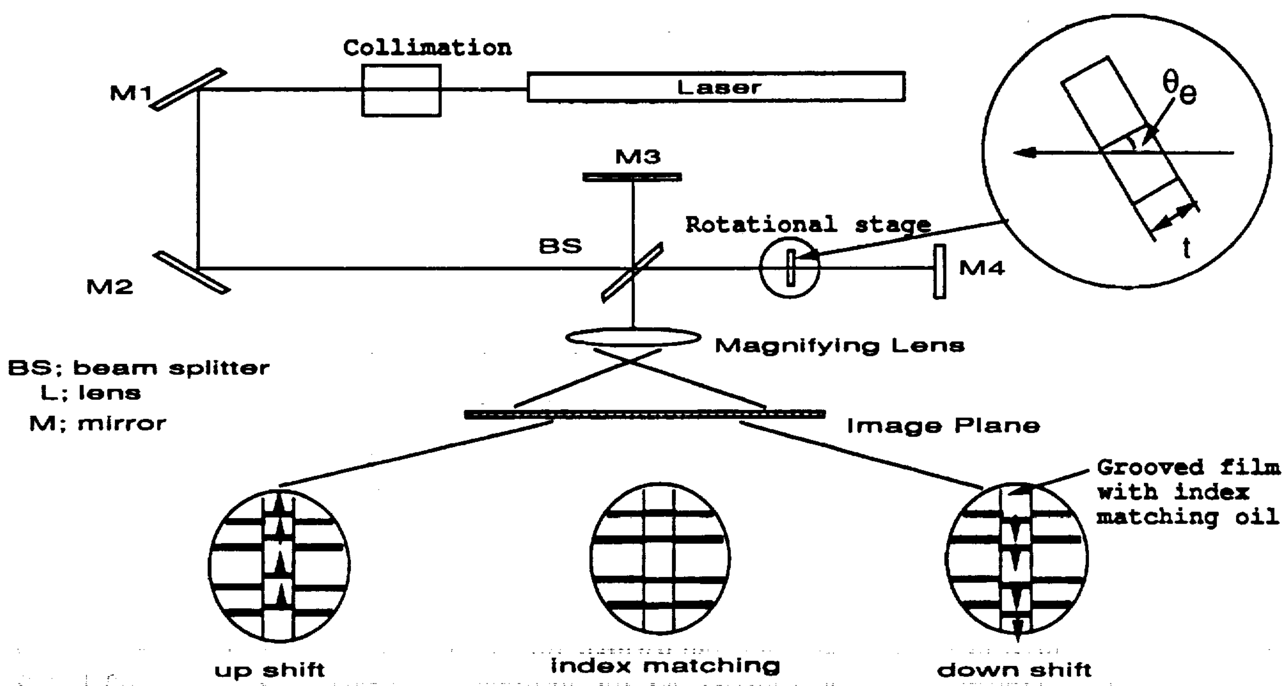

Figure 6: Optical set-up of modified interferometric technique for index matching measurement.

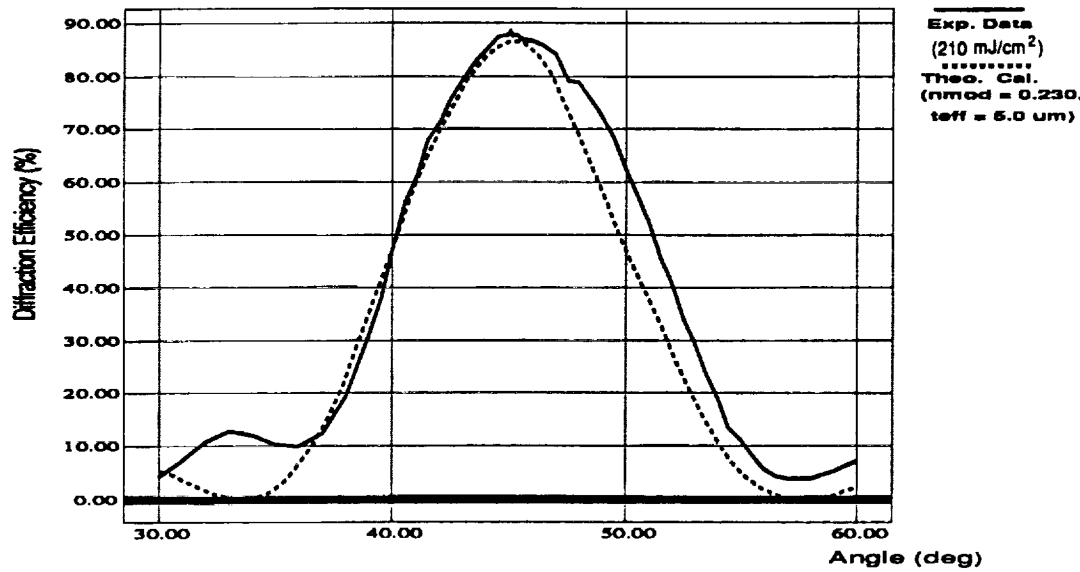

Figure 7: Comparison between experimental data and theoretical calculation. Values given are for a slanted transmission grating; $\theta = 0°$, $-\varphi = 50°$ in air, m = 0.998; construction and reconstruction at $\lambda_c = \lambda_r = 514.5$nm.

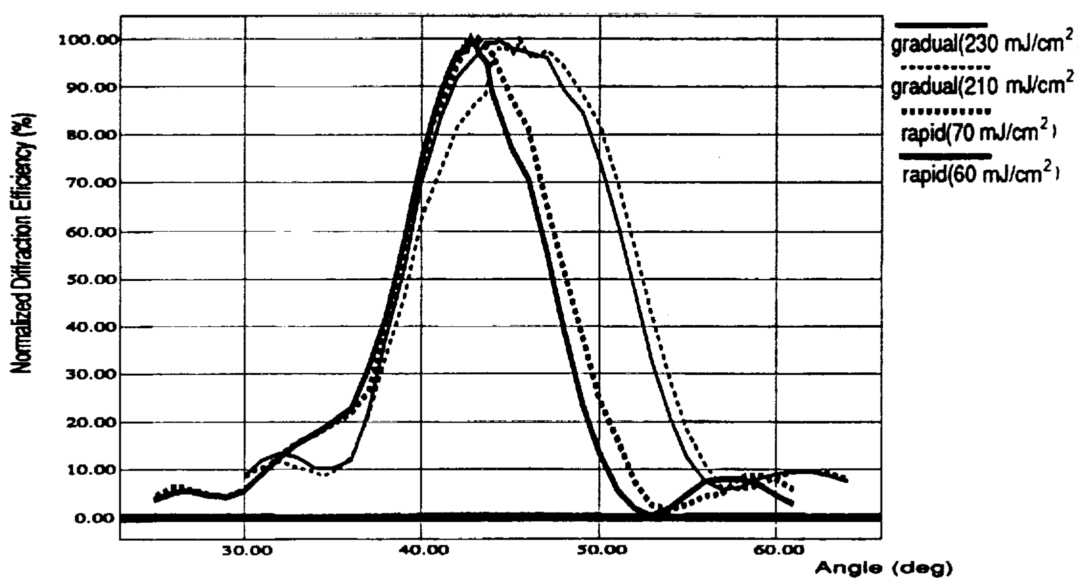

Figure 8: Experimental data of angular bandwidth for the comparison between rapid dehydration (Isopropyl alcohol concentration 50-100-100 %) and gradual dehydration (25-50-75-100-100 %). The exposure energy to obtain maximum diffraction efficiency is about 70mJ/cm^2 for the rapid dehydration process and about 230 mJ/cm^2 for the gradual dehydration process. Values given are for a slanted transmission grating; $\theta = 0°$, $-\varphi = 50°$ in air; construction and reconstruction at $\lambda_c = \lambda_r = 514.5$nm.

APPENDIX E

N94-14993

Effects of a Shading Band in the Data Path of an Optical Drive

T.D. Milster and M.S. Wang
Optical Sciences Center / Optical Data Storage Center
University of Arizona, Tucson, Arizona, 85721, USA

(602) 621-8280

Weiquan Li
Shanghai Institute of Metallurgy
865 Changning Road, Shanghai 200050, China

Abstract

A shading band can alter the system transfer function. In our theory and experiment, both contast improvement and enhanced carrier-to-noise ratio are investigated.

Effects of a Shading Band in the Data Path of an Optical Drive

T.D. Milster and M.S. Wang
Optical Sciences Center / Optical Data Storage Center
University of Arizona, Tucson, Arizona, 85721, USA

Weiquan Li
Shanghai Institute of Metallurgy
865 Changning Road, Shanghai 200050, China

1. Introduction

Efforts to improve the density of data recorded onto optical media have included shaping the transfer function of the optical system. Several authors have described various methods for shaping the transfer function. Reference 1 contains a summary of the various techniques and plots of the transfer functions. In this paper, we describe the effects of a simple shading band in the data path of an optical drive. One effect of the shading band is to shape the transfer function of the optical system. This is similar to the technique of applying electronic equalizing filters for better frequency response. A second effect of the shading band is to decrease the noise associated with the laser and the medium. In our work, we implement a shading band in a commercial optical disk drive. The relevant parameters to this study are: shading band width = 30% of the pupil diameter, medium velocity = 5.7 m/s, NA = 0.55, and λ = 0.78 nm. We used a standard 130 mm magneto-optic disk with a plastic substrate. The following sections briefly describe the theory associated with using the shading band and the results of our experiments.

2. Theory

The data pattern can be considered a collection of gratings. Large bit spacings correspond to low frequencies and small bit spacings correspond to high frequencies. When the laser beam is focused onto the medium, the reflected light contains diffracted orders from the data-pattern gratings. The signal light is contained primarily in the ± 1st diffracted orders reflected from the disk. The amount of signal power that is retrieved by the data detectors depends on how much signal light is passed through the pupil of the objective lens. With reference to Figure 1, at low (2 Mhz) frequency the ± 1st orders are almost completely contained within the pupil, so signal amplitude is high. The shading band reduces the signal light by reducing the amount of ± 1st orders passed by the pupil. As the recording frequency is increased, thereby reducing the bit spacing, the ± 1st orders become more widely separated and the shading band mainly reduces the background light, and hence reduces the noise, in the data signal.

The calculated transfer functions for our system with and without a shading band are shown in Figure 2. In our calculations, we assume that the data pattern consists of wide marks in the direction perpendicular to the tracks. When the shading band is used, the signal amplitude is reduced at low frequencies, but not at high frequencies. This modification of the transfer function partially equalizes the frequency response of the system, thereby providing improved contrast. Reduction of the signal is detrimental unless the noise is reduced as well. Our experiments, which are described in the next section, were designed to investigate the properties of signal and noise with the shading band.

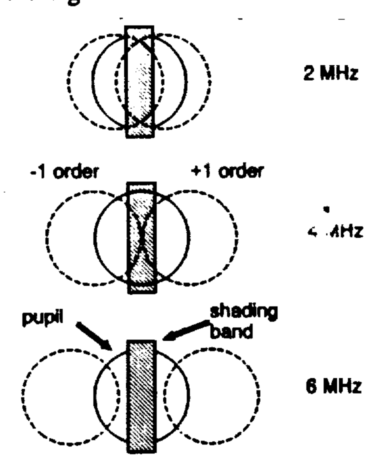

Figure 1. Pupil of the objective lens, shading band, and ± 1st diffracted orders of the data signal for three recording frequencies.

3. Experiment

The optical drive was modified to accept the shading band in its data path. The most convenient location of the shading band is after the partially polarizing beam splitter and before the lens that focuses light onto the data detectors.

Figure 3 displays the noise behavior of the system with and without the shading band. The electronic noise floor was measured with the data detectors blocked. It is not a function of the shading band. The detectors were unblocked, and the disk was stopped to measure the laser noise floor. Note that the laser noise includes the electronic noise contribution. With the shading band, the laser noise is only 1 dB above the electronic noise floor. Then, with the disk spinning, we measured the medium noise floor on an erased track. The medium noise is reduced 4 dB at low (0 to 1 MHz) frequencies, and 1 to 2 dB at high (5 to 7 MHz) frequencies.

Figure 4 displays the narrow-band carrier and noise behavior. In the low (0 to 3 MHz) frequency region, the carrier is reduced about 2 dB more than the noise, resulting in a decrease in the carrier-to-noise ratio (CNR). In the mid (3 to 5 MHz) frequency range, the carrier and noise are reduced equally with no loss in CNR. In the high (5 to 6 MHz) frequency range, the carrier is not reduced, the noise is reduced significantly, and the resulting CNR is increased about 2 dB.

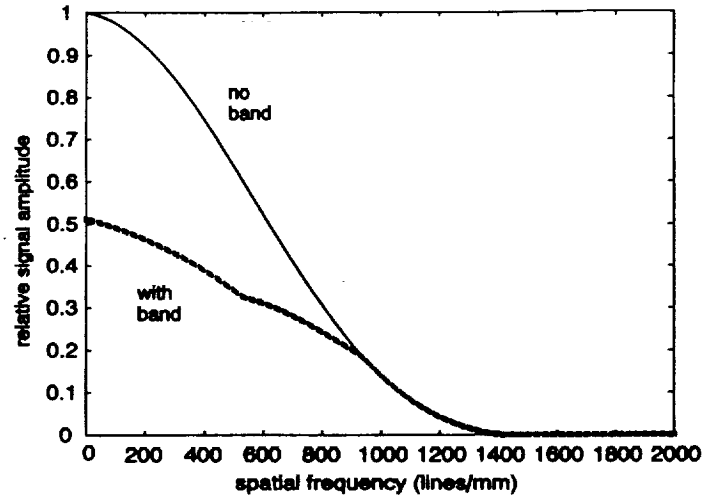

Figure 2. Optical transfer function without and with the shading band.

4. Conclusions

We have shown how a simple shading band modifies the optical transfer function of a data storage drive. This could improve contrast in the data signal. With the shading band, both laser and medium noise levels are reduced. With the particular shading band we choose, the CNR is reduced at low frequencies, unchanged for mid-range frequencies, and improved for high frequencies. Due to the property of reducing the noise floor, further improvements in CNR might be realized by a more clever design of the shading band.

5. References

1. T. Milster and C. Curtis, Applied Optics, 31, pp. 6272-6279 (1992).

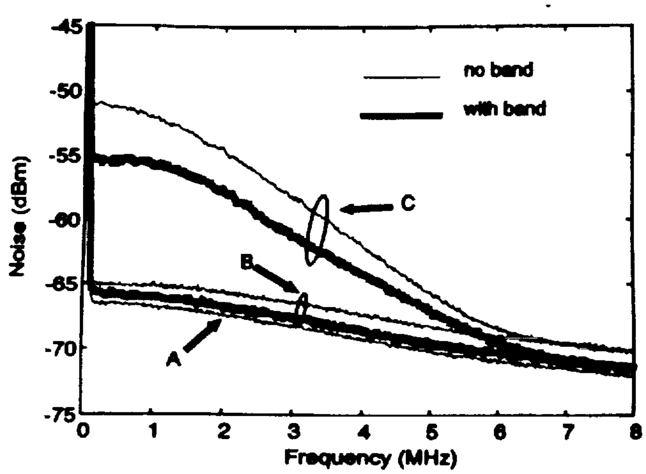

Figure 3. A) electronic noise floor, B) laser + electronic noise floor, and C) medium + laser + electronic noise floors for our system with and without the shading band.

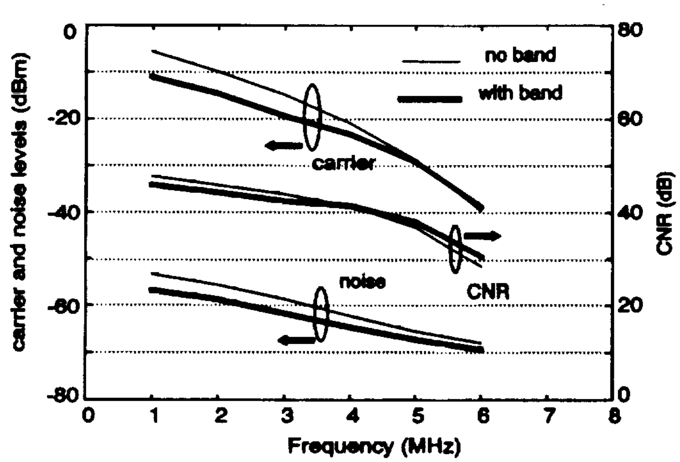

Figure 4. carrier, total noise, and narrow-band carrier-to-noise (CNR) measurements for our system. Note that, with the shading band, the CNR is reduced at low frequencies, unchanged for mid frequencies, and improved at high frequencies.

APPENDIX F

N94-14994

Figures of merit for laser beam quality

T.D. Milster and E.P. Walker
Optical Sciences Center
University of Arizona, Tucson, Arizona 85721

ABSTRACT

We show how FWHM, FW1/e^2, Strehl ratio, and encircled energy figures of merit vary with different types of aberration and measurement methods. We examine in detail the array sampling method and the slit-scan method. Our irradiance in the exit pupil of the optical system is a simple gaussian. We found that in general the slit-scan method and the array method do not yield the same result. The width measurements for the central lobe of the diffraction pattern are very insensitive to aberration.

2. INTRODUCTION

As has been known since opticists started making lenses, aberrations redistribute energy from the central lobe of the Airy pattern into the sidelobes. However, the study of the effects of aberrations in laser beam systems with nonuniform irradiance profiles is a relatively new topic [1][2][3]. For example, a full-width at half maximum (FWHM) of the central lobe in a focused beam that is near the value obtained with an unaberrated system is often used as justification that the beam is "diffraction limited." In this paper, we show that caution must be used in drawing this conclusion because of the effects third-order aberrations have on the FWHM. We also describe how several figures of merit vary with aberrations and measurement technique.

Two methods used to measure laser beam quality are sampling an array of data points and measuring with a scanning slit [3]. We can obtain a two-dimensional array of sample points by inserting a CCD camera or a scanning pinhole directly into the beam. Line profile and edge response data are obtained by scanning a slit across the beam. Instruments used to obtain array and scanning slit data are typically much simpler and less expensive than interferometers, which is a third alternative to measure beam quality. In this paper, we concentrate on the properties of array and slit-scan measurements of a focused laser beam.

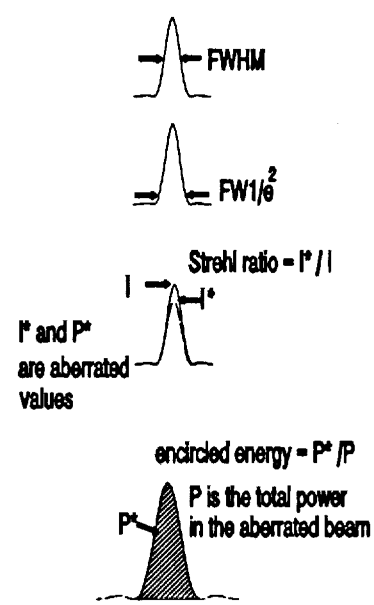

Figure 1. Figures of merit.

Common figures of merit for laser beam quality include width measurements, Strehl ratio, and encircled energy, as shown in Figure 1. FWHM and full-width at $1/e^2$ (FW1/e^2) are self explanatory. The Strehl ratio is defined as the ratio of the peak irradiance of the aberrated beam, I^*, to the peak irradiance, I, of a system with no aberrations. Encircled energy is defined as the ratio of the power, P^*, contained in a small circular region around the peak of the aberrated beam to the total power, P, in the beam. Our circular region is equal to the diameter of the first ring of the Airy pattern in an aberration-free and uniformly illuminated system. This diameter is 1.22 λ/NA, where λ is the laser wavelength and NA is the numerical aperture of the focused beam. A related figure of merit is the energy ratio of the power outside the circular area to

Preprint from SPIE 1834 10

the total power in the beam, which can be calculated from: energy ratio = $1 - P'/P$.

Our optical system model is shown in Figure 2. A simple gaussian laser beam is reimaged through an optical system so that the waist is located a distance R from the exit pupil. The laser beam irradiance in the exit pupil has a FW$1/e^2$ of $2w$. The stop has diameter d. We assume that $d >> \lambda$ and that the NA is large enough so that focus shifts due to the properties of the gaussian beam are insignificant. We also assume that the NA is small enough so that vector diffraction effects are not significant. We model the effects of aberrations by adding a phase error, ΔW, to the wavefront in the exit pupil. The phase errors take the form of astigmatism (W_{222}), spherical (W_{040}) and coma (W_{131}).

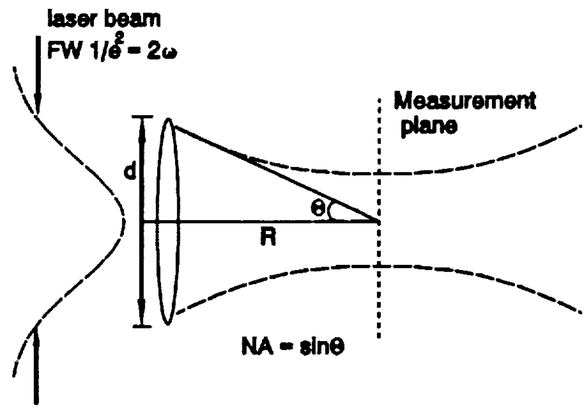

Figure 2. Optical system model.

In the following paragraphs we review array and slit-scan methods. Then we discuss effects of individual third-order aberrations on various figures of merit. Next we discuss effects of random combinations of third-order aberrations. We then summarize and present our conclusions.

3. REVIEW OF ARRAY AND SLIT-SCAN METHODS

Array methods include scanning a pinhole over the measurement plane or using a two-dimensional array of detectors, like those found in a charge-coupled device (CCD) camera. In either case, a two-dimensional data set is acquired from which the figures of merit are calculated. The data are discrete samples of the irradiance incident onto the measurement plane. In order to provide sufficient sampling, the spacing between detector elements must be small compared to the beam size. Typically, CCD cameras have pixel sizes on the order of 10 μm on a side. This limits the practical beam sizes that can be measured to several hundred microns. An auxiliary lens may be used to produce a magnified image of a smaller beam onto the detector plane, but additional aberrations are often introduced that affect the measurement. Also, care must be taken in interpreting metric information from the array, because pixels in CCD cameras are often not square nor do they have the same interval in the horizontal and vertical directions. In our study we assume that the pixels are square and uniformly spaced.

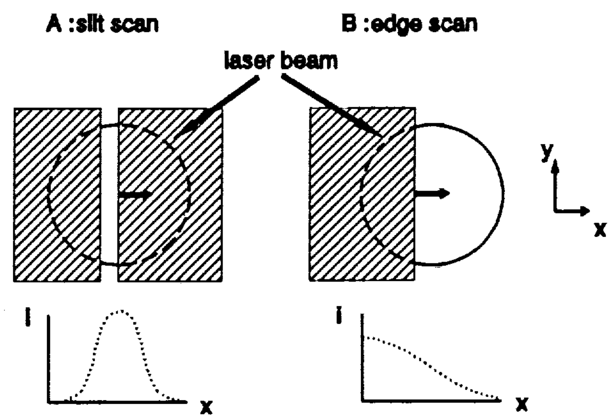

Figure 3. (a) slit-scan method. (b) edge scan method.

Slit-scan methods are used to derive one-dimensional information from the laser beam. As shown in Figure 3A, a narrow slit is used to scan the measurement plane in the x direction. The slit integrates the irradiance in the y direction, so data do not represent true beam profiles, but rather they represent projections along the y axis. The width of the slit determines the resolution of the measurement. Ideally, an infinitely narrow slit would be used, but as the slit becomes too narrow the signal-to-noise degrades.

Another way to obtain slit-scan data is from a moving knife edge, as shown in Figure 3B. In this case, an opaque surface with a sharp edge is scanned across the measurement plane in the x direction. The data from the edge scan are differentiated, and the result is equivalent to an infinitely narrow slit scan, except that the signal-to-noise is improved because more signal light is available.

4. EFFECTS OF INDIVIDUAL THIRD-ORDER ABERRATIONS

In this section we examine the effects of astigmatism, spherical aberration and coma on several figures of merit. Both array data and slit-scan methods are implemented. In our study, we use a simple scalar diffraction modeling code. The optical system is such that $2w/d = 0.89$, which corresponds to the optimum overfill in terms of maximum peak irradiance in the focused beam [4]. In a real optical system, defocus and tilt can be adjusted to give a higher beam quality by canceling some of the effects of aberrations. In our modeling we add the appropriate amount of defocus and tilt to minimize the root-mean-square (rms) wavefront error. The amount of phase error, ΔW, added to the ideal wavefront for each aberration is described by the peak error at the edge of the exit pupil before correction. Width measurements are normalized with respect to NA and λ. For a specific optical system, the physical width is found by multiplying the normalized value by λ/NA.

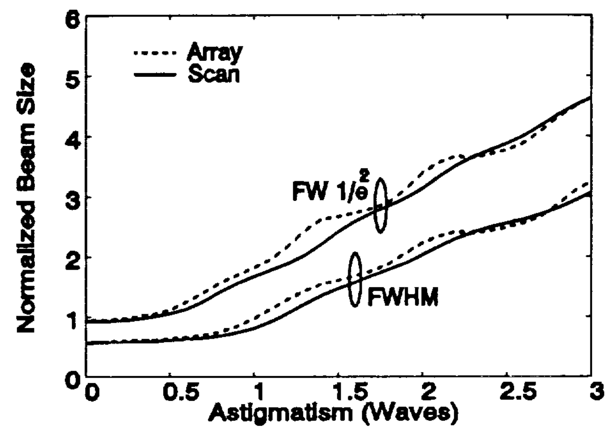

Figure 4. Normalized FWHM and FW $1/e^2$ of the array and slit-scan methods as a function of astigmatism.

We consider the FWHM figure of merit first. Figure 4 displays the normalized FWHM versus astigmatism for the array and slit-scan methods. The laser beam exhibits a symmetric profile in the measurement plane because defocus has been added to minimize the rms wavefront error. There is little change in the FWHM measurement for less than one wave of astigmatism. The array method and the slit-scan method produce similar results. Figure 5 displays the normalized FWHM versus spherical aberration. Sidelobes due to more than two waves of spherical aberration affect width measurements significantly. Lobe widths plotted in Figure 5 include the maximum FWHM (that including all of the sidelobes), central-lobe FWHM and side-lobe FWHM. As the amount of aberration increases, the FWHM of the central lobe actually decreases for the array method. The slit-scan method is slightly more sensitive. The jump in the FWHM around 2.4 waves is due to the shape of the sidelobes in the slit-scan method. As shown in Figure 6A, the slit scan of a beam having 2.4 waves of spherical aberration has sidelobes that increase

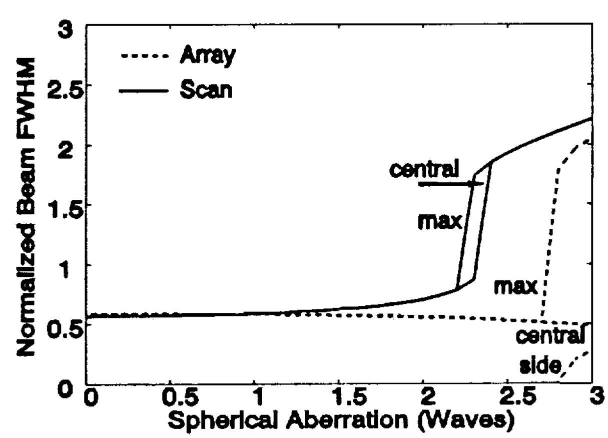

Figure 5. Normalized FWHM of the array and slit-scan methods as a function of spherical aberration.

the FWHM. With 2.3 waves of spherical aberration, the sidelobes are below the half-maximum of the irradiance peak. In Figure 6B, we show the array profile of the beam with 2.4 waves of spherical aberration. Note that the central lobe is well defined, and the sidelobes are well below the half-maximum of the peak irradiance. Figure 7 displays the normalized FWHM versus coma. Coma is not a symmetric aberration, so we consider profiles and slit-scans in both the x and y directions. Again, FWHM is insensitive below one wave of aberration. Sidelobes affect the FWHM measurement at about 2.6 waves of coma. An oscillatory property is observed for the FWHM of the central peak in the x direction, which is also the direction of the maximum wavefront error in the uncorrected system.

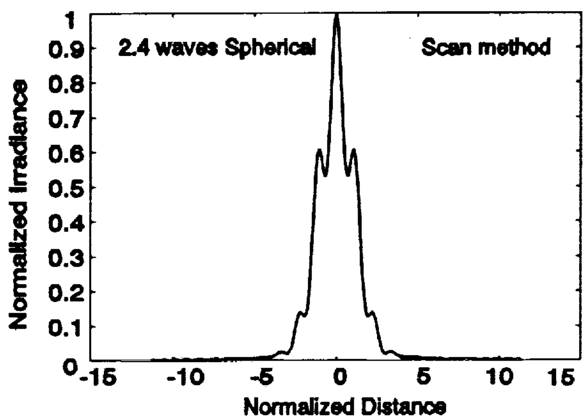

Figure 6a. Irradiance profile of the slit-scan method with 2.4 waves of spherical aberration.

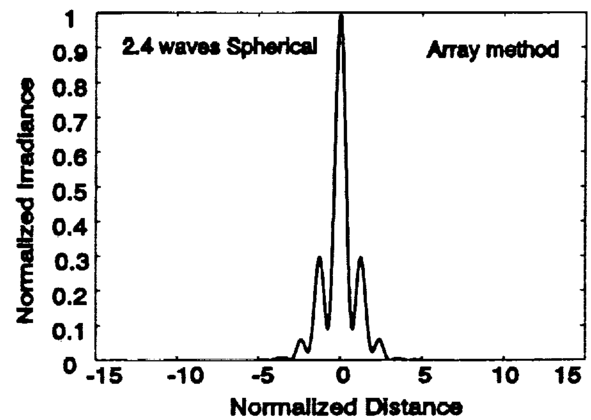

Figure 6b. Irradiance profile of the array method with 2.4 waves of spherical aberration.

Next we consider FW1/e^2. Figure 4 displays the FW1/e^2 for astigmatism. A monotonically increasing curve is observed for the slit-scan method, and the array method is more oscillatory, but it is well behaved. Figure 8 displays FW1/e^2 for spherical aberration. As was observed for FWHM, the sidelobes affect the FW1/e^2 figure of merit dramatically. Note that, for the central lobe in the array method, the FW1/e^2 actually decreases with increased spherical aberration. Sidelobes increase the maximum FW1/e^2 at 1.9 waves for the array method and at 1.2 waves for the slit-scan method. Figure 9 displays FW1/e^2 versus coma. Due to the asymmetric behavior of the focused beam the FW1/e^2 figure of merit becomes complicated to interpret above one wave of coma. In general, the slit-scan method is more sensitive. Note that for all three aberrations the FW1/e^2 figure of merit is not sensitive below 0.5 wave of aberration.

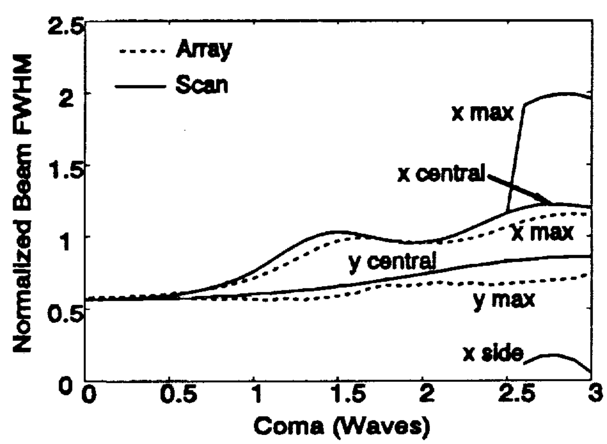

Figure 7. Normalized FWHM of the array and the slit-scan methods as a function of coma.

We now discuss Strehl ratio. Figure 10 displays the Strehl ratio for all three aberrations and both measurement methods. For the array method , Strehl ratio is a very sensitive figure of merit. For the slit-scan method, Strehl ratio is not as sensitive, but it does provide a monotonically decreasing figure of merit with increased aberration. Both methods, Strehl ratio is most sensitive to astigmatism.

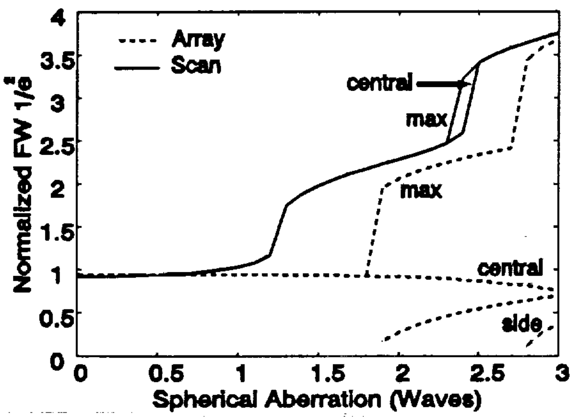

Figure 8. Normalized FW $1/e^2$ of the array and slit-scan methods as a function of spherical aberration.

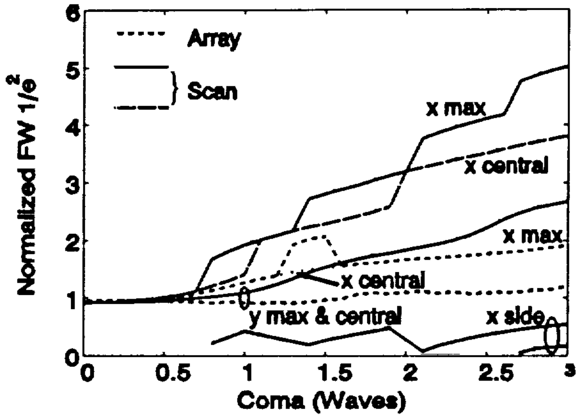

Figure 9. Normalized FW $1/e^2$ of the array and the slit-scan method as a function of coma.

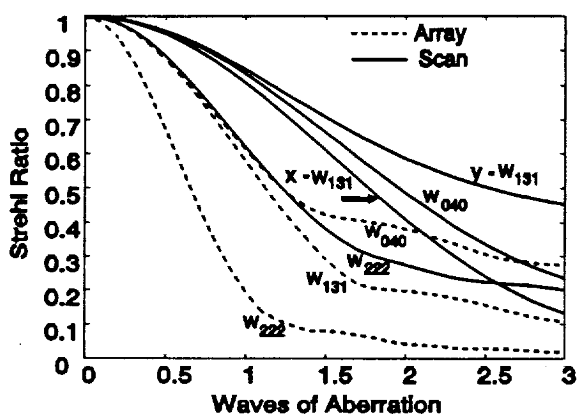

Figure 10. Strehl ratios of the array and slit-scan methods as a function of waves of aberration.

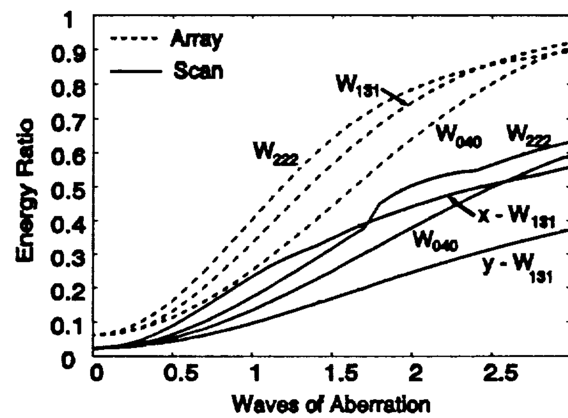

Figure 11. Energy ratio of the power outside of the central lobe to the total power in the beam.

Figure 11 displays the energy ratio for all three aberrations and both measurement methods. Like we observed in the Strehl ratio calculations, the energy ratio is a smooth monotonic function versus aberration. The array method is more sensitive than the slit-scan method. Coma and astigmatism are more easily detected than spherical aberration. When data in Figure 11 is compared to the width data in Figures 4, 5, and 7-9, we observe that the insensitivity of the FWHM can be a severe problem. For example, up to 40% of the total spot energy is contained outside the central lobe for one wave of aberration. Although $FW1/e^2$ is slightly more sensitive, up to 18% of the total spot energy is contained outside of the central lobe for one-half wave of aberration.

5. EFFECTS OF COMBINED ABERRATIONS

We study the effects of combined aberrations with a simple extension to our basic model. Instead of a single aberration, we included random amounts of astigmatism, spherical, and coma. In addition, the coma rotation angle and the astigmatism rotation angle were included as random variables. Tilt and defocus were added in order to minimize the rms wavefront departure. Standard deviation of the wavefront, σ, was kept between the limits : $0 \le \sigma \le 0.10$. The overfill of the laser beam in the exit pupil was slightly different in the x and y directions. A total of 2000 trials were performed. The figures of merit for both the array method and the slit-scan method were calculated for each trial. The result of the average FWHM versus σ is shown in Figure 12, which displays similar characteristics to Figures 5 and 7 for low values of aberration. The difference between the focused beam width in the x and y directions is due to the difference in overfill in the exit pupil. The slit-scan method produces smaller beam widths than the array method for $\sigma < 0.07$ and larger beam widths for $\sigma > 0.08$. The relation between σ and the peak ΔW depends on the type of aberration present. For example, one wave of astigmatism has $\sigma = 0.200$, one wave of spherical has $\sigma = 0.074$, and one wave of coma has $\sigma = 0.116$.

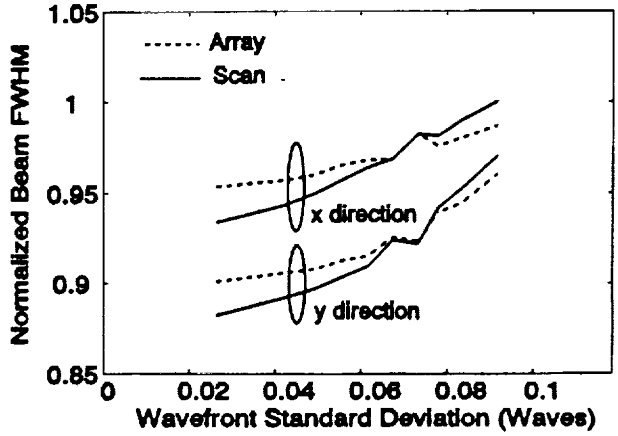

Figure 12. Normalized FWHM of the array and slit-scan methods as a function of wavefront standard deviation.

6. SUMMARY AND CONCLUSIONS

We have shown how FWHM, FW1/e^2, Strehl ratio, and encircled energy figures of merit vary with different types of aberration and measurement methods. We found that in general the slit-scan method and the array method do not yield the same result because the slit-scan method measures an integrated line profile of the beam while the array method measures a profile. The FWHM and FW1/e^2 values for the central lobe of the diffraction pattern are very insensitive to aberration. Therefore, one should use caution when claiming that an optical system is "diffraction limited" based solely on the these criteria. In the case of spherical aberration the central lobe width actually decreases with increased aberration. The slit-scan method width measurements are typically more sensitive to aberration than the array method. The most sensitive figure of merit is the array method Strehl ratio. The array method energy ratio is a useful figure of merit because is it describes the ratio of the power outside the central lobe to the total power in the beam. The numeric values for the energy ratio from a slit-scan are always lower than the corresponding array method. Both the Strehl ratio and the energy ratio are smooth, monotonic functions versus aberration. A computer experiment in which random combinations of aberration are added to the exit pupil indicates that the average FWHM is different for slit-scan and array methods. Our results for individual aberrations are based on one condition of overfill in the exit pupil. Other overfill ratios (2w/d) could yield different results.

7. ACKNOWLEDGEMENTS

This work was sponsored by the Joint Services Optical Program and the Optical Data Storage Center.

8. REFERENCES

1. A. Siegman, "Effects of spherical aberration on laser beam quality," SPIE 1834, in press.

2. T.D. Milster, M.K. Benedict, and R.P. Stahl, " Laser diode requirements for magneto-optical storage devices," SPIE 1316, pp. 143-149 (1990).

3. T.D. Milster and J.P. Treptau, "Measurement of laser spot quality," SPIE 1414, pp. 91-96 (1991).

4. H.M. Haskill, "Laser recording with truncated gaussian beams," Appl. Opt., vol. 18, no. 3, pp. 2143-2146 (1979).

APPENDIX G

N94-14995

A Near-field Scanning Optical Microscope for Analysis of Magneto-optic Media

Fred F. Froehlich and Tom D. Milster

Optical Sciences Center
University of Arizona
Tucson, AZ 85721

602-621-8263

Abstract

The design of a near-field scanning optical microscope (NSOM) is described. Applications to the study of magneto-optic media and domain detection are discussed.

A Near-field Scanning Optical Microscope for Analysis of Magneto-optic Media

Fred F. Froehlich and Tom D. Milster

Optical Sciences Center
University of Arizona
Tucson, AZ 85721
602-621-8263

The ability to achieve subwavelength optical resolution for microscopy through the use of a mechanically scanned near-field optical probe has recently been reported.[1] This technique provides a means of exceeding the far-field diffraction limit associated with the use of an objective lens in conventional optical microscopy, and is known as near-field scanning optical microscopy (NSOM). The near-field probe may be realized by forming a subwavelength-sized aperture in an opaque screen. Such a probe may be implemented in practice by tapering an optical fiber down to the desired diameter and coating its exterior (except for the very tip) with aluminum. The spatial resolution achieved is dependent on the aperture diameter and the tip-to-sample separation, and the resolution is approximately equal to the aperture diameter for separations less than one aperture radius.

NSOM is capable of providing imagery with polarization contrast and is, therefore, a potentially useful tool for the study and analysis of magneto-optic materials. NSOM also provides a means of performing very high-density MO data storage, and domains as small as 60 nm have been successfully written and detected.[2] High-resolution lithography on a submicron scale has also been demonstrated.[3]

Our NSOM instrument has been designed for the examination of MO thin film samples and is illustrated in Figure 1. The instrument consists of three optical subsystems: a conventional visual polarization microscope, a servo subsystem for maintaining the fiber probe position relative to the sample, and a characterization subsystem for obtaining the MO signal. The sample is mounted on a piezo-driven x-y flexure stage, and characterization is performed in transmission. The probe tip may be coarsely prealigned to sample features, such as domain structures, with the visual subsystem. The visual polarization microscope operates in reflection and consists of the lamp, polarizer, beamsplitter, objective, prism, analyzer, and eyepiece. The servo subsystem regulates the separation (typically less than 20 nm) of the tip and sample with a hybrid shear atomic force/optical technique. A small dither is applied to the fiber tip (parallel to the sample surface), and light from the HeNe laser is scattered from the tip and imaged to the pinhole. The dither produces a modulated signal on the PMT. Atomic forces between the tip and sample perturb the amplitude and phase of the dither, which can be detected and used as a feedback signal to regulate tip position. The characterization subsystem operates at blue wavelengths and generates an MO signal in transmission. Light from the Ar^+ laser is launched into the fiber probe with the aid of waveplates to produce any arbitrary state of incident polarization. The beamsplitter and prism are removed from the visual subsystem, and polarization-sensitive optics detect the signal light as the sample is scanned to create an image.

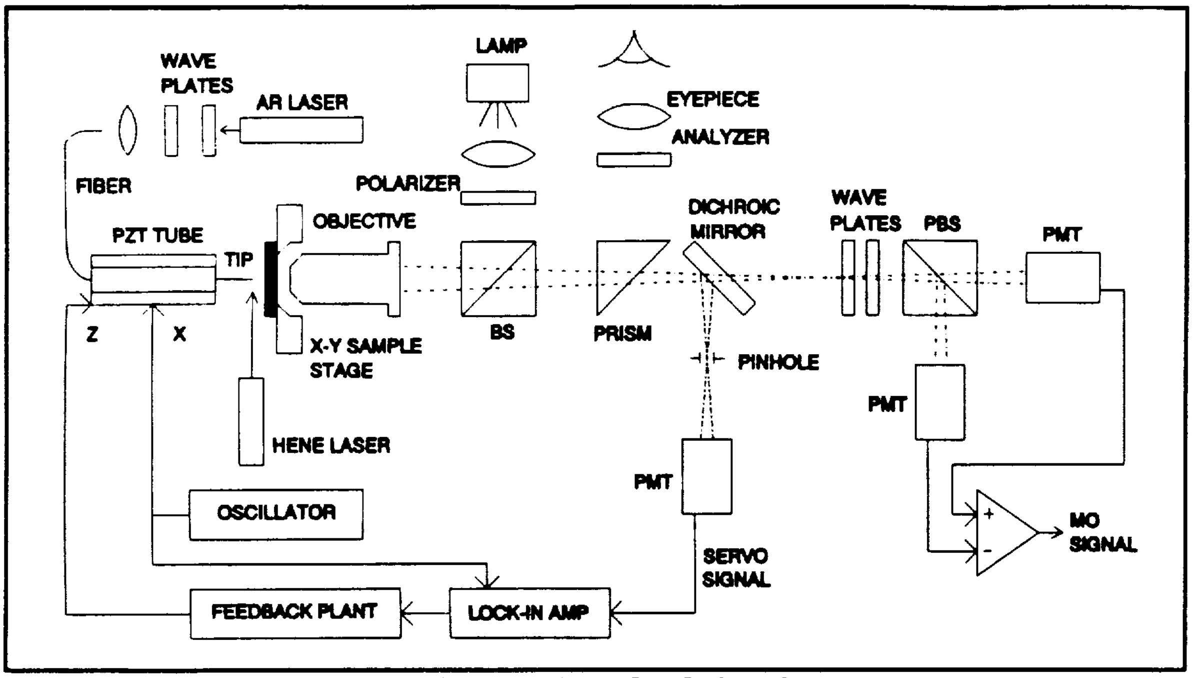

Figure 1. NSOM system layout for detection of MO domain structures.

A typical differential detection scheme is shown consisting of waveplates, a polarizing beamsplitter, two PMTs, and a difference amplifier, but other schemes are possible as well.

The samples used in this study are Co/Pt multilayers prepared by sputtering. The design is 13 bilayers of 3.5 Å Co and 8 Å Pt, yielding a total MO film thickness of 149.5 Å, on a Pyrex substrate. No cover layer is used because the probe tip must be in proximity to the MO layer surface to obtain the resolution afforded by the near-field interaction. Domains were prewritten on the samples by conventional far-field means using an Olympus polarization microscope fitted with a focused laser diode source and an electromagnet.

NSOM may be applied to a variety of studies of MO materials and data storage problems. The high spatial resolution of NSOM (down to 12 nm) can be utilized to study domain wall jaggedness. Depolarization effects due to disk grooves and surface roughness can be examined on a subwavelength scale. The interaction of the near-field probe and MO domain structures can be characterized with various detection schemes. Domain-sensitive methods such as differential detection with linearly polarized light, and edge-sensitive methods using split detectors and circularly polarized light are two techniques of particular interest.

References

1. E. Betzig and J. K. Trautman, "Near-field optics: microscopy, spectroscopy, and surface modification beyond the diffraction limit," Science, vol. 257, pp. 189-195, 10 July 1992, and references contained therein.

2. E. Betzig, et al, "Near-field magneto-optics and high density data storage," Appl. Phys. Lett., 61 (2), 13 July 1992.

3. F. Froehlich, T. Milster, and R. Uber, "High-resolution optical lithography with a near-field scanning subwavelength aperture," Proc. of the SPIE, vol. 1751, July 1992.

APPENDIX H

N94-14996

A Complete Study of Differential Wax-wane Focus Servo Technique

Mark S. Wang
Optical Sciences Center
University of Arizona
Tucson, Arizona 85721
(602) 621-8263

Tom D. Milster
Optical Sciences Center
University of Arizona
Tucson, Arizona 85721
(602) 621-8280

ABSTRACT

We present a thorough study of differential wax-wane focus servo technique including effects of aberration and cancellation of crosstalk.

A Complete Study of Differential Wax-wane Focus Servo Technique

Mark S. Wang and Tom D. Milster
Optical Sciences Center, University of Arizona
Tucson, Arizona 85721, (602) 621-8280

Summary

We concentrate on differential wax-wane focus servo technique[1] that is insensitive to many of the errors found in other schemes. Servo optics are illustrated in Figure 1. The beam reflected from optical disk is focused by the detector lens onto two detectors, detector 1 is slightly inside focus, and detector 2 is slightly beyond focus. The quad detector is offset from the center of the beam to give the FES algebra, where α is an electronic gain factor that can be any number larger than one.

We used scalar diffraction model to study its performance. We studied beam propagation in the optical system, the focus error signal, the detector alignment tolerance, the tracking error signal and crosstalk. The effect of aberration on the above parameters is modeled in detailed.

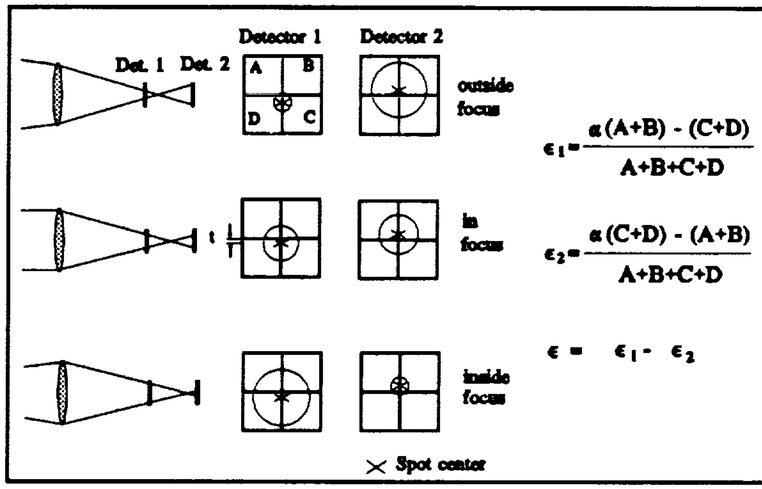

Figure 1 The differential wax-wane focus servo technique. α is an electronic gain factor.

The differential wax-wane technique has several advantages over a single wax-wane focus servo technique. The gain is two times higher, the lock-on-range is better defined, and the linearity is ten times better in terms of *RMS* deviation. It is also insensitive to track rotation and disk tilt.

One important performance parameter is sensitivity to *pattern noise*, which is a false focus error caused by small changes in the spatial distribution of optical power on the detectors. The most common type of pattern noise is due to diffraction from tracks. It is also referred as tracking crosstalk.

The effect of aberration varies depending on where the aberration is introduced and what kind of aberration it is. The focus offset in differential channel is the same as in a single channel. Crosstalk, change of gain, and nonlinearity are improved in the differential channel. $W_{222}(\perp)$ and $W_{131}(\perp)$ generate no focus offset and don't change the gain or linearity, but they change the amplitude and phase of track crosstalk significantly. $W_{131}(\|)$ has minimal effect on any parameter if it is disk aberration, but changes focus offset, gain, and crosstalk amplitude if it is source or detection-optics aberration. The most significant effect of $W_{222}(\|)$ and W_{040} is the focus offset.

The case of combined aberrations (in which we measured the aberrations on our optical system) generates a large focus offset that is a strong function of the electronic gain factor α. There is about 0.7 μm of track crosstalk in a single channel, and the amplitude and phase are different between the two individual channels. Thus, crosstalk is not canceled in differential channel. The crosstalk amplitude of individual channels differs by a factor of about 2, and the relative phase is also different. Total cancellation is not achieved in the differential FES. However, we found that, by rotating the detector, the phase of crosstalk can be adjusted so that the individual crosstalks are 90° out of phase with the tracking signal. The crosstalk phase of detector 1 is then the same as detector 2. We can also change the electronic gain to compensate for the amplitude differences. By reducing the electronic gain of detector 1 by a factor of 2, the crosstalk amplitude become the same. The crosstalk in the differential channel is canceled very well. Theoretically, the crosstalk can be reduced to zero by fine tuning the electronic gain factor and rotating the quad detectors. The residual crosstalk is less than 0.1 μm. Figure 3 shows the measured crosstalk. Note that, by changing the electronic gain, the differential FES is $\epsilon = \epsilon_1/2 - \epsilon_2$.

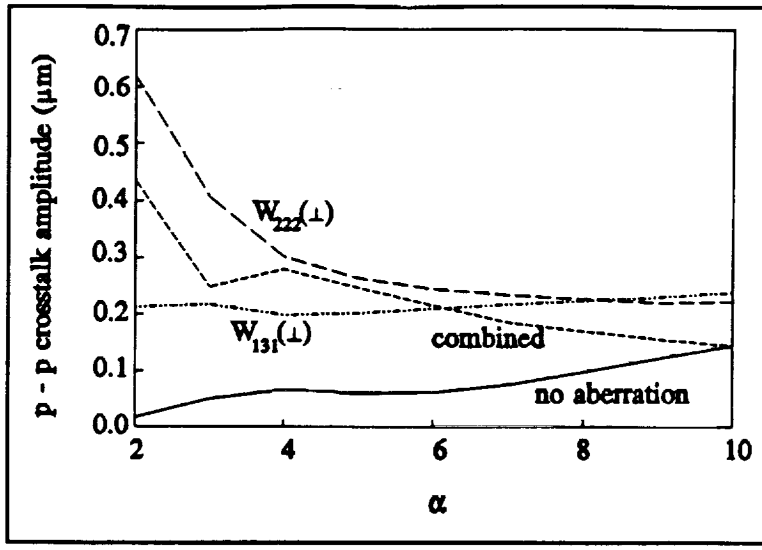

Figure 2 Crosstalk amplitude as a function of the electronic gain factor α when various aberrations are present in the optical system.

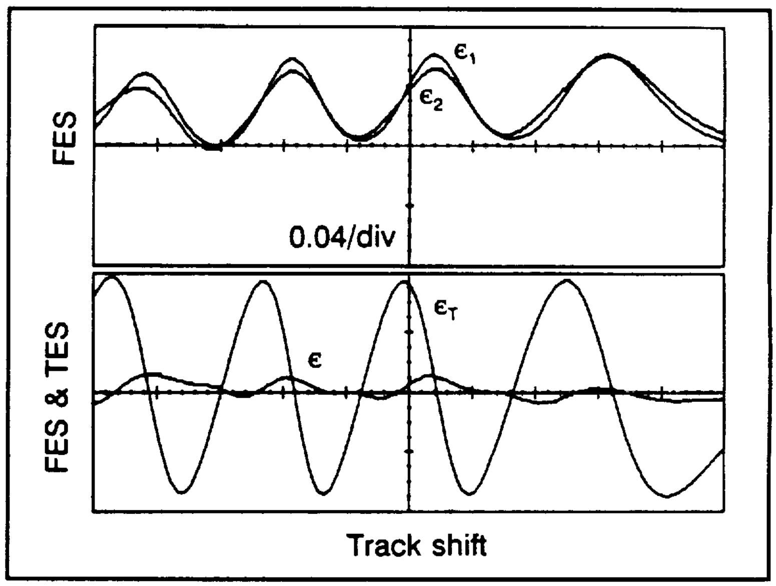

Figure 3 Measured FES crosstalk and TES as a function of track shift. $\epsilon = \epsilon_1/2 - \epsilon_2$.

Conclusion: We presented a complete study of the differential wax-wane focus servo technique including both scalar diffraction modeling and experimental measurements. The crosstalk was reduced from 0.7 μm in a single channel to less than 0.1 μm in the optimized differential channel. This gives the differential wax-wane technique a clear advantage over several techniques we compared.

Reference:

1. T. D. Milster, M. S. Wang, F. F. Froehlich, J. L. Kann, J. P. Treptau, and J. K. Erwin, "Differential Spot-Size Focus Servo," Proc. SPIE v. **1499** 348-353 (1991).

APPENDIX I

PRECEDING PAGE BLANK NOT FILMED

DETERMINING THE LOCATIONS OF THE VARIOUS CIRC RECORDING FORMAT INFORMATION BLOCKS (User data blocks, C2 & C1 words and EFM frames) ON A RECORDED COMPACT DISC

Dennis G. Howe
Optical Sciences Center
University of Arizona
Tucson, AZ 85721

January 28, 1993

Introduction:

Just prior to its being EFM modulated (i.e., converted to eight-to-fourteen channel data by the EFM encoder) and written to a Compact Disc (CD), information that passes through the CIRC Block Encoder is grouped into 33-byte blocks referred to as EFM frames. 24 of the bytes that make up a given EFM frame are user data that was input into the CIRC encoder at various (different) times, 4 of the bytes of this same EFM frame were created by the C2 ECC encoder (each at a different time), and another 4 were created by the C1 ECC encoder (again, each at a different time). The one remaining byte of the given EFM frame, which is known as the EFM frame C&D (for Control & Display) byte, carries information that identifies which portion of the current disc program track the given EFM frame belongs to and also specifies the location of the given EFM frame on the disc (in terms of a time stamp that has a resolution of 1/75th second, or 98 EFM frames). (Note: since the program track and time information is stored as a 98-byte word, a logical group consisting of 98 consecutive EFM frames must be read, and their respective C&D bytes must be catenated and decoded, before the program track identification and time position information that pertains to the entire block of 98 EFM frames can be obtained.) The C&D byte is put at the start (0th byte) of an EFM frame in real time; its placement completes the construction of the EFM frame - it is assigned just before the EFM frame enters the EFM encoder. In Fig. 1., the 33 x 1 column vector $EFM^{<i>}$ represents EFM frame No. "i"; the byte labeled as $F_{0,i}$ in this column vector is the C&D byte of EFM frame No. "i".

In the 134 (row) x 33 (column) array that accompanies this text, each row represents an EFM frame and each EFM frame's identification number is given by the value of the first element of each row, i.e., these values are found in the column identified as F_0 at the top of the 134 x 33 array. The numerical value of these (column F_0) array elements corresponds to the value of the second subscript ("i") of the element $F_{0,i}$ in the column vector $EFM^{<i>}$ of Fig. 1. EFM frames are written sequentially to the CD disc when it is recorded. Thus, byte F_0 of EFM frame No. 0 is recorded first, followed by byte D_1 of EFM frame No. 0, ..., and the 33rd byte written to the disc is byte $C1_3$ of EFM frame No. 0. As EFM frame No. 1 directly follows EFM frame No. 0, the 34th byte written to the disc is byte F_0 of EFM frame No. 1, etc. The 134 x 33 array is therefore a map of how data is written to the disc; the first row (i.e., the top row) of the array is written first, left to right, followed by the next row, again left to right, etc.

In the following discussion we will refer to four distinct blocks of data: (i) 24-byte User Input Data blocks, (ii) 28-byte C2 words, (iii) 32-byte C1 words and (iv) 33-byte EFM frames. In order to track the location on the recorded CD disc of the various data bytes, we shall "tag" (or identify) each data byte that is recorded on the disc with a number, or index, that corresponds either to the instant in time at which the particular byte entered the CIRC encoder (in the case of User Input Data), or to the instant in time at which the data byte was created by the CIRC encoder (as is the case with C2 parity bytes, C1 parity bytes and EFM frame C&D bytes). Once a byte is "tagged", the number it is tagged with will be kept, i.e., that number will not change, even when the particular byte becomes a member of other CIRC information blocks (which will occur as the byte flows through the CIRC encoder). In order to assign numerical values to the byte "tags", we shall think of information flowing through the CIRC encoder in expanding-size blocks, namely, the User Input Data blocks, C2 and C1 words, and EFM frames mentioned above.

The User Input Data Blocks:

24 bytes of sequential user data is input to the CIRC encoder as a single 24-byte User Input Data block. A User Input Data block that enters the CIRC encoder at instant "k" is represented by the column vector $D^{<k>}$ of Fig. 1. The sequence in which user data bytes filled the User Input Data block is indicated by the first subscript of each data byte (i.e., element) of $D^{<k>}$; the instant at which the block entered the CIRC encoder is denoted by the second subscript of the various bytes of $D^{<k>}$. Thus, $D_{1,k}$ denotes the first byte of the 24-byte User Input Data block that entered the CIRC encoder at instant "k" and $D_{24,k}$ denotes the 24th (and last) byte of the User Input Data block that entered the CIRC encoder at instant "k". Sometimes we shall refer to blocks that enter the CIRC encoder at instant "k" as block No. "k", and vice versa.

The C2 Words:

Directly after they enter the CIRC encoder, the bytes of a 24-byte User Input Data block are reordered (or swapped) such that the sequence $\{D_{1,k}, D_{2,k}, D_{3,k}, \ldots, D_{23,k}, D_{24,k}\}$ becomes the sequence $\{D_{1,k}, D_{2,k}, D_{9,k}, D_{10,k}, D_{17,k}, D_{18,k}, D_{3,k}, D_{4,k}, D_{11,k}, D_{12,k}, D_{19,k}, D_{20,k}, D_{5,k}, D_{6,k}, D_{13,k}, D_{14,k}, D_{21,k}, D_{22,k}, D_{7,k}, D_{8,k}, D_{15,k}, D_{16,k}, D_{23,k}, D_{24,k}\}$. Then, after delaying the first 12 bytes of the reordered User Input Data block by 48 bytes (which amounts to interleaving the first half of the reordered User Input Data block by two reordered User Input Data blocks) the resultant (reordered, two-block interleaved) 24-byte block is encoded by the C2 ECC coder. This encoding process involves the computation of four C2 parity bytes and the subsequent addition of them to the reordered and doubly-interleaved 24-byte block between bytes $D_{20,k-2}$ and $D_{5,k}$. This results in a 28-byte C2 word such as the one represented by the column vector $C2^{<p>}$ in Fig. 1. Four new bytes, namely the C2 parity bytes $C2p_0$, $C2p_1$, $C2p_2$, and $C2p_3$ are created by the CIRC encoder when the C2 word is formed; we therefore "tag" these four parity bytes with a numerical value that corresponds to the instant at which these parity bytes were created. In addition, we "tag" the C2 word itself with this same numerical value. This is illustrated in Fig. 1, where it is shown that the column vector $C2^{<p>}$, which represents C2 word No. "p", contains the four parity bytes $C2p_{0,p}$, $C2p_{1,p}$, $C2p_{2,p}$ and $C2p_{3,p}$ (recall our convention is that the second byte subscript contains the numerical value that corresponds to the instant at which the C2 word is created, or equivalently, to the C2 word's No. "value"). This same C2 word (i.e., C2 word No. "p") also contains bytes from User Input Data block No. "p-2" as its first 12 information bytes (these 12 bytes experienced a delay of 2 User Input Data blocks prior to entering the C2 ECC encoder), as well as bytes from User Input Data block No. "p" as its last 12 information bytes (these 12 bytes experienced no delay between the time they entered the CIRC encoder and the time at which they entered the C2 encoder - in effect these 12 bytes were input directly into the C2 encoder).

The C1 Words:

Next, the 28-byte block output by the C2 coder is interleaved again, this time on a byte-by-byte basis. Here, the 2nd byte of a given C2 word is delayed by four C2 words (112 bytes) relative to the first byte, the 3rd byte of the given word is delayed by eight C2 words (224 bytes) relative to the first byte, ..., and the 28th byte of the given word is delayed by one-hundred-and-eight C2 words (3,024 bytes) relative to the first byte. A 28-byte block of data that has been variably-interleaved in this manner is input to the C1 ECC encoder, which computes four C1 parity bytes and adds them to the end of the variably-interleaved 28-byte block that was input to it. This is illustrated in Fig. 1, where it is shown that column vector $C1^{<n>}$, which represents C1 word No. "n", has C1 parity bytes $C1p_{0,n}$, $C1p_{1,n}$, $C1p_{2,n}$ and $C1p_{3,p}$ as its last four bytes. From Fig. 1 we also see that the 28 information bytes of C1 word No. "n" (i.e., its first 28 bytes) consist of user data bytes taken from User Input Data blocks that entered the CIRC encoder at various times ranging from two C1 word-times prior to the time of the current word (cf., the first byte of $C1^{<n>}$, namely $D_{1,n-2}$, which entered the CIRC encoder as a member of User Input Data block No. "n-2") to one-hundred-and-eight C1 word-times prior to the current word (cf., the 28th byte of $C1^{<n>}$, namely $D_{24,n-108}$, which entered the CIRC encoder as a member of User Input Data block No. "n-108"). It can also be seen from Fig. 1 that the information portion of a C1 word contains parity bytes that belong to four different C2 words (namely, bytes $C2p_{0,n-48}$ through $C2p_{3,n-60}$ of column vector $C1^{<n>}$).

The EFM frames:

A final interleaving follows the C1 encoding. The odd bytes, namely the 1st, 3rd, 5th, ..., 31st bytes, of the 32-byte block that is output by the C1 coder are each delayed by one C1 word (i.e., by 32-bytes) relative to the even bytes of the same C1 word. And lastly, a single EFM C&D byte is appended to the beginning of each of the resultant, singly-interleaved 32-byte blocks to form the 33-byte EFM frames. The column vector $EFM^{<i>}$ in Fig. 1 is a representation of EFM frame No. "i". Note that this EFM frame's C&D byte, namely byte $F_{0,i}$, and the two C1 parity bytes $C1p_{1,i}$ and $C1p_{3,i}$, are the only bytes in EFM frame No. "i" that were created (by the CIRC encoder) at instant "i". The EFM frame C&D byte $F_{0,i}$ is created by the CIRC encoder at the instant the EFM frame No. "i" is formed, and the two C1 parity bytes mentioned directly above, were created by the C1 encoder at this same time, which is why they are labeled as parity bytes that belong to C1 word No."i".

Locating Specific Information Bytes and CIRC Data Structures on the Recorded Disc:

In order to keep track of the various processing steps outlined above, we can use an index that increments once each time a new EFM frame is created. Concurrent with that event (i.e., the creation of an EFM frame), a new 24-byte User Input Data block is input to the CIRC encoding system, a new C2 word is encoded by the C2 coder, and a new C1 word is encoded by the C1 coder. Thus, we tag all 24 bytes of a single User Input Data block with a common index, the four C2 parity bytes that correspond to a given C2 word share a common index (since they were all created at a particular time), and the four C1 parities of a given C1 word are given a common index (again, since they were simultaneously created). Specifically, the 24 bytes of a given User Input Data block are all given the index value assigned to the EFM frame C&D byte that was current when the first byte of the 24-byte User Input Data block entered the CIRC encoding system. Similarly, the group of four C2 parity bytes, and the group of four C1 parities that were each created via single encoding operations, are each given the index value of the EFM frame C&D byte that was current when those groups of parities were computed and assigned by the respective ECC coders.

It is these index values that are listed in the 134 x 33 array, which is our map of the recorded CD disc. From that array we see that the C&D byte of EFM frame No. 0 (byte F_0 in the first, i.e., top, row of the array) is assigned an index = 0, that user data byte #1 of EFM frame No. 0 (byte D_1 in row 1) came from the User Input Data block having index = -3 (i.e., this byte came from the User Input Data block that was input while the EFM frame with index = -3 was current), that user data byte #2 (byte D_2 in row 1) came from the User Input Data block having index = -6 (i.e., the User Input Data block that was input while the EFM frame with index = -6 was current), that user data byte #9 (byte D_9 in row 1) came from the User Input Data block having index = -11, ..., that C2 parity byte number 0 (byte $C2_0$ in row 1) was created by the C2 coder when the EFM frame with index = -49 was current, ..., and that C1 parity byte number 3 (byte $C1_3$ in row 1) was created by the C1 coder when the EFM frame with index = 0 was current.

The data in a given EFM frame is sequentially recorded on the disc and sequentially indexed EFM frames are recorded in sequence. Thus, the 134 x 33 array is essentially a map of how data is recorded (laid out) on the disc. Byte F_0 of EFM frame No. 0 is recorded first, followed by byte D_1 of EFM frame No. 0, etc. Byte $C1_3$ of EFM frame No. 0 is the last byte of that frame to be recorded and it is directly followed by byte F_0 of EFM frame No. 1. Because of this, the array can be used to determine the location of all the data from a specific User Input Data block, or from a specific C2 or C1 word. For example, the 24 data bytes located in columns 2 through 13 and in columns 18 through 29 that have the same index value all came from the same User Input Data block (e.g., byte D_1 in EFM frame No. 0, byte D_2 in EFM frame No. 3 and byte D_9 in EFM frame No. 8 all are members of the User Input Data block having index = -3). With the help of the column vectors given in Fig. 1, the locations on the disc of all the bytes of specific C2 and C1 ECC words can also be determined.

Using the column vector representations for an arbitrary EFM frame, an arbitrary C2 word and an arbitrary C1 word that are given in Fig. 1, we see that C2 word No. "p" (i.e., the C2 word that was created when EFM frame No. "p" was current) has data bytes that were input as part of User Input Data block No. "p-2" as its first 12 bytes and data bytes that were input as part of User Input Data block No. "p" as its last 12 bytes. Thus, if one wanted to read the disc and retrieve, for example, all the data (24 bytes) that were input as

User Input Data block No. 0, one would have to read a length of disc track which contains the entire 56 bytes that make up C2 words No. 0 and No. 2 (since the last 12 bytes of C2 word No. 0 and the first 12 bytes of C2 word No. 2 contain the 24 bytes that were input as User Input Data block No. 0). To acquire C2 word No. 0 one would have to read all those bytes in columns 2 - 13 (bytes D_1 through D_{20}) of the 134 x 33 array that have index = -2 and all those bytes in columns 14 - 29 (bytes $C2_0$ through D_{24}) that have index = 0. Similarly, to acquire C2 word No. 2, one must read all those bytes in columns 2 - 13 that have index = 0 and all those bytes in columns 14 - 29 that have index = 2. From the 134 x 33 array we see that this means that EFM frames No. 1 through No. 110 must be read. However, note that byte D_{24} of EFM frame No. 110 (which is the last byte of C2 word No. 2) is also part of C1 word No. 110, which has all of its odd-numbered bytes in EFM frame No. 111 (the column vector representation of an arbitrary C1 word given in Fig. 1 shows that the 2nd, 4th, 6th, ..., 32nd bytes of C1 word No. "n", i.e., bytes $D_{2,n-6}$, $D_{10,n-14}$, $D_{18,n-22}$, ..., $C1p_{2,n}$ are part of EFM frame No. "n", while the 1st, 3rd, 5th, ..., 31st bytes of C1 word "n", i.e., bytes $D_{1,n-2}$, $D_{9,n-10}$, $D_{17,n-18}$, ..., $C1p_{3,n}$ are part of EFM frame No. "n+1"). This means that EFM frame No. 111 must be read too, so that C1 word No. 110 can be acquired and decoded (because C1 decoding must be accomplished before C2 decoding). In total, then, 111 EFM frames must be read from the disc in order to retrieve the 24 data bytes that were input as a single User Input Data block...

To augment the understanding of how to use the 134 x 33 array to determine the locations of CIRC-encoding data structures on a recorded CD disc, on that array we have drawn circles around the locations of all 28 bytes of C2 word No. 0, and drawn squares around the locations of all 32 bytes of C1 word No. 110. Triangles have also been drawn around the locations of all 24 bytes of User Input Data block No.5. (These CIRC information blocks were arbitrarily chosen.)

CD Audio Interpolation:

The above analysis sheds light on the purpose for performing the byte reordering (swapping) that is done on the Input User Data block prior to C2 encoding. The CD system is designed, at its lowest level, as a serial (tape-like) digital audio recorder - audio program material is sampled at a rate of 44.1 KHz and those samples are digitized as 32-bit words (each 4-byte digital audio sample consists of a 16-bit right-channel audel and a 16-bit left-channel audel). Thus, a given 24-byte User Input Data block contains exactly 6 audio samples; the first four bytes (bytes $D_{1,j}$ - $D_{4,j}$, in the case of Input User frame No. "j") constitute the first audio sample, the next four bytes ($D_{5,j}$ - $D_{8,j}$) make up the second audio sample, etc. The column vector representation of a C2 word in Fig. 1 shows that the first 12 bytes of C2 word No. "p" (which consist of bytes $D_{1,p-2}$ to $D_{4,p-2}$, $D_{9,p-2}$ to $D_{12,p-2}$ and $D_{17,p-2}$ to $D_{20,p-2}$ in scrambled form) would carry the 1st, 3rd and 5th audio samples from User Input Data block No. "p-2", while the last 12 bytes of that same C2 word (which consist of bytes $D_{5,p}$ to $D_{8,p}$, $D_{13,p}$ to $D_{16,p}$ and $D_{21,p}$ to $D_{24,p}$ in scrambled form) would carry the 2nd, 4th and 6th audio samples from User Input Data block No. "p". This means that the audio samples carried in a single undecodable C2 word could be interpolated from their "neighbor" audio samples, which are carried by two other C2 words, one of which is recorded at a distance of two C2 words earlier than the non-decodable word and the other at a distance of two C2 words later than the non-decodable word. For example, if C2 word No. 10 could not be decoded, one could interpolate values for audio samples 1, 3, and 5 that belong to User Input Data block No. 8 (and which are carried as the first 12 information bytes of C2 word No. 10) using the audio samples 2, 4, and 6 of User Input Data block No. 8 (which are carried as the last 12 information bytes of C2 word No. 8). Similarly, values for the audio samples 2, 4, and 6 from User Input Data block No. 10 (which are carried as the last 12 information bytes of C2 word No. 10) could be interpolated using the audio samples 1, 3, and 5 from User Input Data block No. 10 (which are carried as the first 12 information bytes of C2 word No. 12).

Note that the byte reordering that is done prior to C2 encoding also causes the interleaving of the left and right stereo audels that constitute the 1st, 3rd and 5th digital audio samples from a given User Input Data block. For example, from the Fig. 1 column vector representation of a C2 word, note that the first two bytes (i.e., the left channel audel) of digital audio sample 1, viz., D_1 and D_2, are followed by the first two bytes (again, the left channel audel) of digital audio sample 3, viz., D_9 and D_{10}, which are followed by the first two bytes of digital audio sample 5, viz., D_{17} and D_{18}; these are followed, in sequence, by the last two bytes (i.e., the right channel audel) of digital audio samples 1, 3 and 5 from the same User Input Data block. Digital audio samples 2, 4, and 6 from a given User Input Data block are treated similarly. This feature allows independent (separate) interpolation of values for either left channel or right channel audels using "neighbor" left channel or right channel information that is carried in another C2 word.

Handling of Long Burst Errors:

From the 134 x 33 array of recorded byte index values, we see that a burst error having minimum length of 100 bytes would be required cause two errors to occur in a single C2 word. For example, an error burst extending from byte $D_{1,3}$ (the second byte of EFM frame No. 3) to byte $D_{2,6}$ (the third byte of EFM frame No. 6) would contaminate two bytes of C2 word No. 2. We can also see that an error burst that has a minimum length of 166 bytes would be required to cause two errors in both of the two C2 words that carry "neighbor" audio samples. For example, a burst extending from byte $D_{1,3}$ to byte $D_{2,8}$ would be required to cause two errors in both C2 word No. 2 and C2 word No. 4. Clearly, very long burst errors can be corrected by the highly-interleaved C2 code, and extremely long burst errors are required to defeat the concealment of audio information errors via interpolation.

The C2 code's immunity to long burst errors, however, can readily be compromised if there is a high number of short random errors. For example, suppose that a 20-byte long burst error occurs; it will cause (only) one byte to be erroneous in each of twenty different C2 words. Then, the probability that a short random error will contaminate a second byte of any one of these same C2 words is roughly 20 x 27 x P_B = 540 P_B, where P_B is the byte error rate that describes the occurrence of short random errors. Similarly, if a long burst error that contaminates two bytes of a given C2 word has occurred, then the probability that a short random error will contaminate a third byte of that same C2 word is roughly 26 x P_B. Clearly, if the short random error rate at the input to the C2 decoder is as high as, say $P_B = 10^{-5}$ to 10^{-3} erroneous bytes/byte (a range of rate values that may well be representative of the short random error rate of an aged, well-used CD disc), then there would be an unacceptably high probability of occurrence of uncorrectable C2 words (i.e., C2 words having more than two or three flagged errors), and/or misdecodable C2 words (i.e., C2 words having more than two unflagged errors). It is the job of the C1 code, which is decoded prior to C2 decoding, to reduce the short random error rate at the input of the C2 decoder to an acceptable level.

Correction of Short (Random) Errors:

The purpose of the single-frame interleaving that is done just prior to C1 encoding is to enhance the short random error correcting capability of the C1 code. Specifically, since the conditional probability (conditioned on the occurrence of an uncorrectable error pattern) of C1 misdecoding, i.e., having the C1 decoder unknowingly output incorrect data, is about 1% when a C1 decoder is configured to correct two errors, versus about 0.0002% when a C1 decoder is configured to correct only one error, it is desirable to use single-error correction at the C1 decoding level. (Since the Hamming distance of both the C1 and C2 codes is five, when a codeword of either of these codes is misdecoded the data block output by the decoder will have a minimum of five incorrect bytes; thus an uncorrectable error pattern that contains, say, only three erroneous bytes will be enlarged to a five, or more, byte error if erroneous decoding occurs.) The one-word interleaving done at the C1 level allows a single-error-correcting C1 decoder to correct two-byte long errors (since such errors will contaminate only one byte in each of two successive C1 words). This is important since it has been observed that the average length of the short random errors that occur in injection molded CD Digital Audio Discs and CD-ROM discs is about 11 bits in length.

The C1 block error rate (BLER) is equal to the fraction of C1 words (at the input to the C1 decoder) that contain one or more single or multiple-byte errors. If the occurrence of any type of error event is a relatively rare event, e.g., if only 0.1%, or less, of the bytes on a disc are erroneous, then the BLER provides a reasonable estimate of the rate of occurrence of error events (of any type). However, a long burst error that has length BL only increments the BLER count by at most [BL/32], where [x] represents the least integer $\geq$ x. Therefore, the BLER is essentially a measure of the rate of occurance of short random errors.

The Red Book BLER specification is BLER < 0.03. Since there are (at 1x playback speed) 7,350 C1 blocks/second, this translates to

BLER < 220 contaminated C1 words/second.

In what follows, we shall assume that an error-contaminated EFM frame experiences, on average, a single short random error event (i.e., that the short random error rate is sufficiently low that the probability of two error events occurring in a single EFM frame is very small relative to the probability of occurrence of only one error event). We shall also assume that the average length of a short random error is 1.375 bytes (11 bits). Such an average length error may start at any one of eight locations in an arbitrary byte of a depth-one interleaved C1 word. Thus, the 1.375-byte error event will contaminate only one byte in each of the two depth-one interleaved C1 words with probability 5/8 and will contaminate two bytes in one, but only one byte in the other, of the pair of interleaved C1 words with probability 3/8.

Random short error rate at the input of the C1 decoder: Since, on average, a random short error event always contaminates two C1 words, the short error event rate can be approximated by

$$\frac{BLER}{2}\ \frac{\text{short error events}}{\text{sec}}\ .$$

The coresponding byte error rate is

$$P_B \approx \left(\frac{BLER}{2}\right)\frac{\text{events}}{\text{sec}} \times (1.375)\ \frac{\text{erroneous bytes}}{\text{event}} \times \left(\frac{1}{7350}\right)\frac{\text{sec}}{\text{C1 word}} \times \left(\frac{1}{32}\right)\frac{\text{C1 word}}{\text{byte}}$$

or

$$P_B \approx \frac{BLER}{34{,}211}\ \frac{\text{erroneous bytes}}{\text{byte}}\ .$$

Taking BLER < 220 error events/sec, the random short error rate at the input of the C1 decoder is found to be

$$P_B < 6.5 \times 10^{-4}\ \frac{\text{erroneous bytes}}{\text{byte}}\ .$$

Random short error rate at the output of the C1 decoder: We saw earlier that, on average, a short random error event will always cause two C1 words to be contaminated and that 3/8 ths of the time one of the two contaminated words will have two bytes in error. That is, on average, only one-half of three-eighths of the contaminated C1 words will contain more than one erroneous byte. Thus, the byte error rate (due to short random errors having an average length of 11 bits) at the output of a single-error-correcting C1 decoder is given by

$$P_B \approx \left(\frac{3}{8}\right) \times \left(\frac{BLER}{2}\right) \frac{\text{undecodables}}{\text{sec}} \times \left(\frac{2}{32 \times 7350}\right) \frac{\text{erroneous bytes / undecodable}}{\text{bytes / sec}}$$

When the BLER is at its maximum specified (in the Red Book) value of 220 C1 words/second, a single-error correcting C1 decoder will fail to correct about 41 C1 words/second. And if a CD disc that is just within the Red Book BLER specification is played, the short random error rate at the output of a single-error-correcting C1 decoder is estimated to be

$$P_B \approx \left[\frac{41 \times 2}{32 \times 7350}\right] \frac{\text{erroneous bytes / sec}}{\text{bytes / sec}} = 3.5 \times 10^{-4} \ \frac{\text{erroneous bytes}}{\text{byte}} \quad .$$

The short random error rate at the output of a more aggressive C1 decoder, e.g., a double-error corrector, would be substantially lower since only those C1 words that have more than two bytes in error would remain uncorrected (but, keep in mind that such a decoder will have a relatively high probability of misdecoding when an uncorrectable error pattern is encountered). Other alternatives for more powerful C1 decoding would be to use the C1 decoder to correct a single error together with one erasure per C1 input word (assuming, of course, that a means of reliably erasing bytes in the input C1 word is available), or to use the C1 decoder to correct zero (or one) errors per input C1 word and simultaneously detect up to four (two) errors and mark them as erasures for subsequent correction by an erasure-correcting C2 decoder.

The purpose of the preceding discussion of the short random error rates at both the input and output of the C1 decoder was to illustrate how the singly-interleaved C1 code contributes to the overall data reliability of the CIRC coding system, and to make the point that multiple (> 2) byte errors in C2 words (i.e., at the input to the C2 decoder) become highly probable when a long burst error occurs in conjunction with a moderately high rate of short random error events (i.e., a moderately high BLER value).

User Input Data Block No. "k"...

$$D^{<k>} := \begin{bmatrix} D_{1,k} \\ D_{2,k} \\ D_{3,k} \\ D_{4,k} \\ D_{5,k} \\ D_{6,k} \\ D_{7,k} \\ D_{8,k} \\ D_{9,k} \\ D_{10,k} \\ D_{11,k} \\ D_{12,k} \\ D_{13,k} \\ D_{14,k} \\ D_{15,k} \\ D_{16,k} \\ D_{17,k} \\ D_{18,k} \\ D_{19,k} \\ D_{20,k} \\ D_{21,k} \\ D_{22,k} \\ D_{23,k} \\ D_{24,k} \end{bmatrix}$$

C2 word No. "p"...

$$C2^{<p>} := \begin{bmatrix} D_{1,p-2} \\ D_{2,p-2} \\ D_{9,p-2} \\ D_{10,p-2} \\ D_{17,p-2} \\ D_{18,p-2} \\ D_{3,p-2} \\ D_{4,p-2} \\ D_{11,p-2} \\ D_{12,p-2} \\ D_{19,p-2} \\ D_{20,p-2} \\ C2p_{0,p} \\ C2p_{1,p} \\ C2p_{2,p} \\ C2p_{3,p} \\ D_{5,p} \\ D_{6,p} \\ D_{13,p} \\ D_{14,p} \\ D_{21,p} \\ D_{22,p} \\ D_{7,p} \\ D_{8,p} \\ D_{15,p} \\ D_{16,p} \\ D_{23,p} \\ D_{24,p} \end{bmatrix}$$

C1 word No. "n"...

$$C1^{<n>} := \begin{bmatrix} D_{1,n-2} \\ D_{2,n-6} \\ D_{9,n-10} \\ D_{10,n-14} \\ D_{17,n-18} \\ D_{18,n-22} \\ D_{3,n-26} \\ D_{4,n-30} \\ D_{11,n-34} \\ D_{12,n-38} \\ D_{19,n-42} \\ D_{20,n-46} \\ C2p_{0,n-48} \\ C2p_{1,n-52} \\ C2p_{2,n-56} \\ C2p_{3,n-60} \\ D_{5,n-64} \\ D_{6,n-68} \\ D_{13,n-72} \\ D_{14,n-76} \\ D_{21,n-80} \\ D_{22,n-84} \\ D_{7,n-88} \\ D_{8,n-92} \\ D_{15,n-96} \\ D_{16,n-100} \\ D_{23,n-104} \\ D_{24,n-108} \\ C1p_{0,n} \\ C1p_{1,n} \\ C1p_{2,n} \\ C1p_{3,n} \end{bmatrix}$$

EFM frame No. "i"..

$$EFM^{<i>} := \begin{bmatrix} F_{0,i} \\ D_{1,i-3} \\ D_{2,i-6} \\ D_{9,i-11} \\ D_{10,i-14} \\ D_{17,i-19} \\ D_{18,i-22} \\ D_{3,i-27} \\ D_{4,i-30} \\ D_{11,i-35} \\ D_{12,i-38} \\ D_{19,i-43} \\ D_{20,i-46} \\ C2p_{0,i-49} \\ C2p_{1,i-52} \\ C2p_{2,i-57} \\ C2p_{3,i-60} \\ D_{5,i-65} \\ D_{6,i-68} \\ D_{13,i-73} \\ D_{14,i-76} \\ D_{21,i-81} \\ D_{22,i-84} \\ D_{7,i-89} \\ D_{8,i-92} \\ D_{15,i-97} \\ D_{16,i-100} \\ D_{23,i-105} \\ D_{24,i-108} \\ C1p_{0,i-1} \\ C1p_{1,i} \\ C1p_{2,i-1} \\ C1p_{3,i} \end{bmatrix}$$

Figure 1. The CIRC encoder blocks

i 0..32

j 0..[illegible]

EFM Frame byte identifiers

EFM frame byte F_0 = EFM frame C&D byte

EFM frame bytes D_1 - D_{24} = user input data

EFM frame bytes $C2_0$ - $C2_3$ = C2 parity bytes

EFM frame bytes $C1_0$ - $C1_3$ = C1 parity bytes

$EFM^{\langle i \rangle}$

EFM^{T} =

F_0	D_1	D_2	D_9	D_{10}	D_{17}	D_{18}	D_3	D_4	D_{11}	D_{12}	D_{19}	D_{20}	$C2_0$	$C2_1$	$C2_2$	$C2_3$	D_5	D_6	D_{13}	D_{14}	D_{21}	D_{22}	D_7	D_8	D_{15}	D_{16}	D_{23}	D_{24}	$C1_0$	$C1_1$	$C1_2$	$C1_3$
[illegible]	[illegible]	[illegible]	[illegible]	[illegible]	[illegible]	[illegible]	[illegible]	[illegible]	[illegible]	[illegible]	[illegible]	[illegible]	[illegible]	[illegible]	[illegible]	[illegible]	[illegible]	[illegible]	[illegible]	[illegible]	[illegible]	[illegible]	[illegible]	[illegible]	[illegible]	[illegible]	[illegible]	[illegible]	[illegible]	[illegible]	[illegible]	[illegible]